THE LONGITUDINAL DISTRIBUTION OF ENERGETIC PARTICLES IN THE INNER HELIOSPHERE
-MULTI-POINT OBSERVATIONS WITH STEREO-

Dissertation
zur Erlangung des Doktorgrades
der Mathematisch-Naturwissenschaftlichen Fakultät
der Christian-Albrechts-Universität zu Kiel
vorgelegt von

NINA DRESING

– Kiel, April 2014 –

Nina Dresing:
The Longitudinal Distribution of Energetic Particles in the Inner Heliosphere
-Multi-Point Observations With STEREO-

ERSTER GUTACHTER (SUPERVISOR):
Prof. Dr. B. Heber

ZWEITER GUTACHTER (ADVISOR):
Dr. Silvia Dalla

TAG DER MÜNDLICHEN PRÜFUNG:
19.05.2014

ZUM DRUCK GENEHMIGT:

gez. Prof. Dr. W. J. Duschl, Dekan

ABSTRACT

The datasets of the STEREO spacecraft, utilized in this thesis, built an unprecedented platform to investigate longitudinal particle distributions in the inner heliosphere. In contrast to previous space missions these two nearly identical spacecraft fly on Earth-like orbits around the Sun with successively increasing longitudinal separation to Earth. One spacecraft, therefore, runs ahead of the Earth, STEREO A, while the other one, STEREO B, trails behind. Beside plenty of up to date instruments carried by the STEREO spacecraft, one of the main advantages of the mission is the radial distance to the Sun which is nearly the same as that of the Earth. This is of great use when investigating energetic particles because radial effects can almost be neglected. Another important advance is that both spacecraft do not orbit the Sun 'blindly': In addition to a number of in-situ experiments they are also equipped with several remote sensing instruments. These provide optical observations of the Sun and the corona at different wavelengths which were only available from the Earth's viewpoint previous to the STEREO mission.
In the region of STEREO's orbit, two energetic particle populations lend themselves for longitudinal investigations: Energetic particles associated with corotating interaction regions (CIRs), and solar energetic particles (SEPs). The first part of this thesis deals with the former and the different effects which can cause variable CIR observations and associated particle increases. For this purpose, the special configuration of the STEREO spacecraft enables us to disentangle temporal and spatial effects. Furthermore, local interactions with transient structures were observed which obviously favor the local particle acceleration.
The second part of this thesis presents investigations of solar energetic particle events which show remarkably wide particle spreads of up to 360 degrees in longitude in the inner heliosphere. These so-called wide-spread events are of special interest because the processes, yielding to these unexpectedly wide distributions, are not completely understood yet. On the basis of a detailed study of such an event and comparison with a 3D propagation model, we conclude that particle transport perpendicular to the mean magnetic field in the interplanetary medium cannot be neglected for wide spread events. In a second study we identified 21 of such wide-spread events and investigate these in a statistical manner. As a key characteristic the longitudinal anisotropy distribution is also investigated. By means of this information different types of events could be distinguished. In contrast to the first study where strong perpendicular diffusion was supposed to play the main role, several observations require a pre-distribution of the particles over large angular ranges close to the Sun. The second study, therefore, concludes that it is likely that both processes, perpendicular diffusion in the interplanetary medium as well as a lateral distribution in the corona (due to coronal transport, a shock or another so far unknown process) must be present at the same time to explain the majority of our observations.

ZUSAMMENFASSUNG

Die in dieser Arbeit verwendeten Daten der STEREO-Sonden bilden eine nie dagewesene Plattform um longitudinale Teilchen-Verteilungen in der inneren Heliosphäre zu untersuchen. Im Gegensatz zu vorigen Raum-Missionen beschreiben diese zwei baugleichen Sonden Erd-ähnliche Orbits um die Sonne, wobei sie sich sukzessiv von der Erde entfernen. Dabei fliegt die eine Raumsonde, STEREO A, der Erde auf ihrem Orbit vorweg, und die andere Sonde, STEREO B, folgt der Erde. Neben einer vielzahl zeitgemäßer Instrumente besteht ein Hauptvorteil der STEREO-Mission darin, dass die beiden Sonden sich in etwa bei dem gleichen Abstand zur Sonne befinden wie die Erde, was bei der Untersuchung energiereicher Teilchen von großem Nutzen ist, da radiale Effekte nahezu ausgeschlossen werden können. Ein weiterer wichtiger Forschritt ist, dass beide Raumsonden nicht "blind" um die Sonne kreisen, sondern neben den vielen In-situ-Experimenten auch mit einer Reihe sog. Remote-Sensing-Instrumente ausgestattet sind. Diese liefern optische Beobachtungen von der Sonne und der Korona in verschiedenen Wellenlängenbereichen, die vor dem Beginn der STEREO-Mission nur vom Blickwinkel der Erde aus verfügbar waren.
In dem Bereich, den die STEREO-Sonden durchfliegen, bieten sich zwei verschiedene Teilchenpopulationen für longitudinale Untersuchungen an: Energiereiche Teilchen, die in korotierenden Wechselwirkungsregionen (CIRs) entstehen, und solare energiereiche Teilchen (SEPs). Der erste Teil dieser Arbeit beschäftigt sich mit ersteren und den verschiedenen Faktoren, die für variable CIR-Beobachtungen und den damit verbundenen Teilchenanstiegen verantwortlich sind. Dabei bietet die besondere Konstellation der STEREO-Sonden die Möglichkeit zeitliche von räumlichen Effekten zu unterscheiden. Weiterhin konnten lokale Wechselwirkungen mit vorbeifliegenden Strukturen beobachtet werden, die offensichtlich die lokale Teilchenbeschleunigung begünstigen.
Der zweite Teil dieser Arbeit präsentiert Untersuchungen von solaren Teilchenereignissen (SEP events), die besonders breite Teilchenverteilungen bis zu 360 Grad heliographischer Länge in der inneren Heliosphäre aufweisen. Solche sog. Wide-Spread-Events sind von besonderem Interesse, da die Prozesse, die diese unerwartet breiten Verteilungen hervorrufen, bislang nicht vollständig geklärt sind. Anhand einer detaillierten Untersuchung eines solchen Ereignisses und dem Vergleich mit einem 3D-Ausbreitungs-Modell folgern wir, dass zum Magnetfeld senkrechter Transport im interplanetaren Medium für die beobachtete breite Teilchenverteilung verantwortlich sein könnte. In einer zweiten Studie wurden 21 solcher Wide-Spread-Events identifiziert und statistisch untersucht. Als Schlüsselinformation wird hierbei auch die longitudinale Anisotropie-Verteilung untersucht. Anhand dieser Information können verschiedene Typen von Ereignissen unterschieden werden. Im Gegensatz zur ersten Studie, in der angenommen wurde, dass starke Senkrecht-Diffusion den Haupt-Prozess bildet, erfordern eine Reihe von Beobachtungen eine Vorverteilung der Teilchen über große Winkelberei-

che schon nahe der Sonne. Die zweite Studie folgert daher, dass es wahrscheinlich ist, dass zwei verschiedene Prozesse, nämlich Senkrecht-Diffusion im interplanetaren Medium und eine laterale Ausbreitung in der Korona (durch koronalen Transport, einen Schock oder weitere bislang nicht geklärte Prozesse) zusammen beteiligt sein müssen, um die Großzahl der Beobachtungen zu erklären.

PUBLICATIONS

Multi-spacecraft Observations of CIR-Associated Ion Increases During the Ulysses 2007 Ecliptic Crossing
N. Dresing, R. Gómez-Herrero, B. Heber, R. Müller-Mellin, and R. Wimmer-Schweingruber, Solar Physics 256, 409-425 (2009), DOI:10.1007/s11207-009-9356-3

The Large Longitudinal Spread of Solar Energetic Particles During the 17 January 2010 Solar Event
N. Dresing, R. Gómez-Herrero, B. Heber, A. Klassen, Y. Kartavykh, and W. Dröge, Solar Physics 281, 281-300 (2012), DOI:10.1007/s11207-012-0049-y

A statistical survey of wide-spread solar electron events observed with STEREO and ACE with special attention on anisotropies
N. Dresing, R. Gómez-Herrero, B. Heber, A. Klassen, O. Malandraki, Y. Kartavykh, and W. Dröge, Astron. Astrophys., submitted March 2014

Spatial and temporal variations of CIRs: Multi-point observations by STEREO
R. Gómez-Herrero, O. Malandraki, N. Dresing, E. Kilpua, B. Heber, A. Klassen, R. Müller-Mellin, and R. Wimmer-Schweingruber, Journal of Atmospheric and Solar-Terrestrial Physics 73, 551-565 (2010), DOI:10.1016/j.jastp.2010.11.017

Longitudinal and Radial Dependence of Solar Energetic Particle Peak Intentsities: STEREO, ACE, SOHO, GOES, and Messenger Observations
D. Lario, A. Aran, R. Gómez-Herrero, N. Dresing, B. Heber, G.C.Ho, R. B. Decker, and E. C. Roelof, The Astrophysical Journal 767, 41 (2013), DOI:10.1088/0004-637X/767/1/41

Wide longitudinal distribution of interplanetary electrons following the 7 February 2010 solar event: observations and transport modeling
W. Dröge, Y. Kartavykh, N. Dresing, B. Heber, A. Klassen, Journal of Geophysical Research, submitted January 2014

SEPServer Catalogues of Solar Energetic Particle events at 1 AU based on STEREO recordings: 2007-2012
A. Papaioannou , O.E. Malandraki, N. Dresing, B. Heber, K.-L. Klein, R. Vainio, R. Rodríguez-Gasén, A. Klassen, A. Nindos, D. Heynderickx, R. Gómez-Herrero, N. Vilmer, A. Kouloumvakos, R. A. Mewaldt, K. Tziotziou, and G. Tsiropoula, Astron. Astrophys., accepted March 2014

CONFERENCE PROCEEDINGS

Multi-point observations of CIR-associated energetic ions during Ulysses' ecliptic crossing in 2007

N. Dresing, R. Gómez-Herrero, B. Heber, R. Müller-Mellin, R. Wimmer-Schweingruber, A. Klassen, Proc. 31st Internat. Cosmic Ray Conf. (Lodz, Poland), paper 0325 (2009)

Multi-spacecraft observations during a series of three solar energetic particle events in May, 2009

N. Dresing, R. Gómez-Herrero, Y. Kartavykh, W. Dröge, A. Klassen, B. Heber, B. Klecker, Proc. 32nd Internat. Cosmic Ray Conf. (Beijing, China), paper 0918 (2011)

A statistical analysis of wide-spread solar electron events observed with STEREO and close to Earth spacecraft

N. Dresing, R. Gómez-Herrero, A. Klassen, B. Heber, O. Malandraki, Y. Kartavykh, and W. Dröge, Proc. 33rd Internat. Cosmic Ray Conf. (Rio de Janeiro, Brazil), paper 0611 (2013)

Approaching solar maximum 24 with STEREO - Multi-point observations of solar energetic particle events

N. Dresing, C. Cohen, R. Gómez-Herrero, B. Heber, A. Klassen, R. Leske, G. Mason, R. Mewaldt, and T. von Rosenvinge, Proc. 33rd Internat. Cosmic Ray Conf. (Rio de Janeiro, Brazil), paper 1275 (2013)

The First Ground Level Event of Solar Cycle 24 and its longitudinal distribution in the inner heliosphere

B. Heber, N. Dresing, W. Dröge, R. Gómez-Herrero, K. Herbst, Y. Kartavykh, A. Klassen, J. Labrenz, O. Malandraki, and R. Müller-Mellin, Proc. 33rd Internat. Cosmic Ray Conf. (Rio de Janeiro, Brazil), paper 746 (2013)

CONTENTS

ACRONYMS

3D	Three-dimensional
ACR	Anomalous Cosmic Rays
AR	Active Region
CIR	Corotating Interaction Region
CME	Coronal Mass Ejection
EUV	Extreme Ultraviolet
FS	Forwad Shock
GCR	Galactic Cosmic Rays
GLE	Ground Level Enhancement
ICME	Interplanetary Coronal Mass Ejection
IP	Interplanetary
PFSS	Potential Field Source Surface
RS	Reverse Shock
SEP	Solar Energetic Particle
SI	Stream Interface
SIR	Stream Interaction Region

1

INTRODUCTION AND MOTIVATION

1.1 THE SUN AND THE HELIOSPHERE

The solar wind plasma which is emitted from the Sun forms a cavity in the interstellar medium which we call the heliosphere. This space is governed by the solar wind and the solar magnetic field; it expands as far as ∼100 AU (depending on the direction) and contains our complete planetary system. The extent of the *inner* heliosphere is not clearly defined, however, the part comprising the planets up to Mars may be considered as the inner heliosphere. Because the solar wind plasma pressure dominates the magnetic field pressure, the magnetic field can be considered as frozen-in in the solar wind plasma. Therefore, the mixture of different plasma streams originating from neighboring regions on the Sun is not possible. Due to the solar rotation, the frozen-in magnetic field forms a spiral pattern in the heliosphere when carried out by the solar wind. The curvature of these so-called Parker magnetic field spirals, therefore, depends on the heliocentric distance and the solar wind speed with low speed forming stronger curvatures than high speeds.
The magnetic field of the Sun can be described in a first approach as a dipolar field that reverses in a 11-year cycle. During the time of the magnetic field reversal a strong quadrupole component adds to the dipole leading to a complex and variable structure. Magnetic stresses evolve which release their energy in strong reconnection processes. These phenomena are summarized as solar activity. Periods of strong activity are called solar maximum times while periods of low activity are called solar minimum. Because the activity is strongest during the magnetic field reversal and low when the magnetic field shows a dipolar structure, an 11-year solar activity cycle is observed. This activity cycle is reflected in the sunspot number (see lower panel of Fig. 1) as well as in the occurrence rate of solar eruptions but also the heliospheric solar wind structure is affected. Figure 1 shows solar wind measurements by the Ulysses spacecraft during each of its three polar orbits around the Sun in the top panel. The first and third orbit (right and left hand figures) during solar minimum show a well ordered solar wind structure with respect to heliographic latitude: High speed solar wind is observed over the poles while slow solar wind dominates in the low latitude range between ca ±30 degrees around the heliospheric current sheet. Also the magnetic field polarity (positive and negative, marked by red or blue color, respectively) is well ordered with opposite polarities on both sides of the current sheet. The middle figure shows measurements during solar maximum where slow and fast wind streams and varying magnetic field polarity can be observed at any latitude. The bottom panel of Fig. 1 shows the smoothed sunspot number as well as the tilt angle of the solar current sheet indicating the solar activity cycle (*McComas et al.*, 2008).

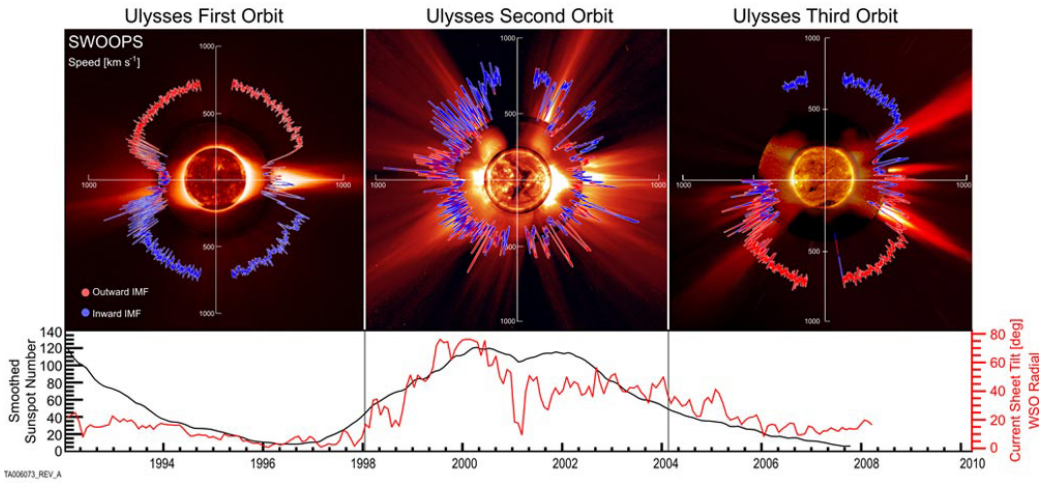

Figure 1: Top panel: Solar wind speed as measured by Ulysses during its three polar orbits around the Sun in a polar representation. Different magnetic field polarities are marked by red and blue color, respectively. Bottom panel: Smoothed sunspot number (black) and tilt angle of the solar current sheet with respect to the solar rotation axis. High values on both parameters mark solar maximum periods, while low values are observed during solar minimum. The first and third orbit of Ulysses during solar minimum periods show an undisturbed solar wind pattern with high speed solar wind observed over the solar poles and low speed observed around the ecliptic (see left and right hand figures). The middle figure of the top panel shows the highly variable solar wind speed during solar maximum observed in the second orbit of Ulysses. Figure from *McComas et al.* (2008)

The solar activity also determines and strongly influences the particle populations present in the heliosphere which will be introduced in the next section.

1.2 PARTICLE POPULATIONS IN THE HELIOSPHERE

Figure 2 shows a sketch of the inner heliosphere with the Sun (yellow circle) and some representative magnetic field lines. An 1-AU ring (dashed arc) indicates the Earth's orbit. The figure shows a summary of the energetic particle populations which are present in the inner heliosphere. The Galactic Cosmic Rays (GCR), consisting mainly of protons, α-particles, and electrons, build the high energy part and are not produced inside the heliosphere but at galactic sources, i.e. supernovae shocks, and can reach energies up to the TeV-range. These particles penetrate the heliosphere isotropically from outside and propagate through the heliosphere and towards the Sun. The same is true for the Anomalous Cosmic Rays (ACR) which presumably have their source close to the boundary of our heliosphere. They can be distinguished from the GCRs by their different elemental abundances, charge states, and energy spectra (*Garcia-Munoz et al.*, 1977; *Cummings et al.*, 1995; *Fichtner*, 2001). Planetary particles, such as Jovian electrons or particles accelerated at the Earth's bow shock, form non-centered point sources in the heliosphere.

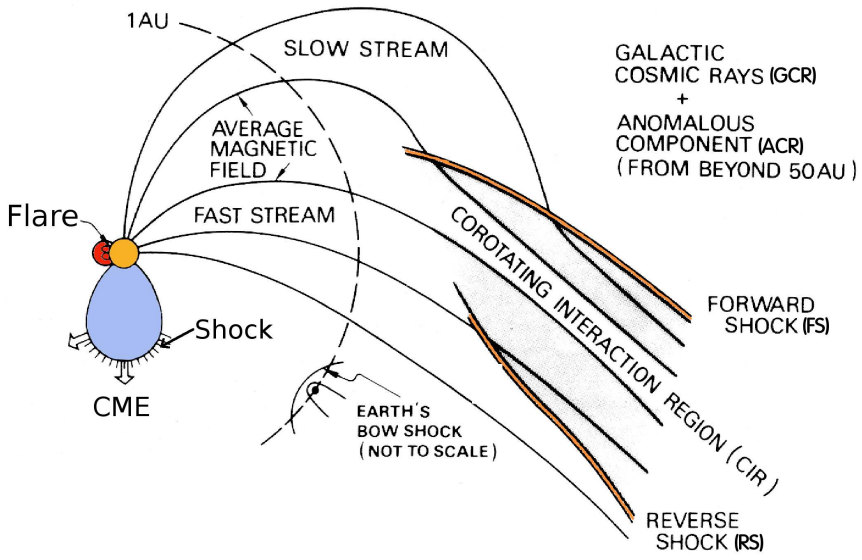

Figure 2: Particle populations in the inner heliosphere. Galactic Cosmic Rays (GCRs) and Anomalous Cosmic Rays (ACR) enter the inner heliosphere isotropically. Propagating shock waves, such as Forward (FS) and Reverse Shocks (RS) associated to a Corotating Interaction Region (CIR) as well as shocks driven by Coronal Mass Ejections (CME) build moving sources of energetic particles. Solar Flares at the Sun produce Solar Energetic Particles (SEP), while planetary particles as for example accelerated at the Earth's bow shock build non-centered point sources in the heliosphere. Figure adapted from *Kunow et al.* (1991).

As mentioned above, the solar cycle has a strong influence on the particle populations in the heliosphere. Because the solar wind and magnetic field structure affect the particle propagation, the 11-year solar cycle causes a modulation of cosmic rays. The production of other particle populations is naturally linked to the activity of the Sun itself: Large plasma bulks are ejected from the Sun which propagate outwards with high speeds of $\sim$2000 km/s or more. These so-called Coronal Mass Ejections (CME, marked in blue in Fig. 2) can drive shock fronts which accelerate mainly ions up to energies of tens of MeV. Another manifestation of solar activity are the solar flares (marked by a red arc in Fig. 2, not to scale) which are strong reconnection processes in which particles can be accelerated up to high energies of even hundreds of MeV or sometimes more. Flare events are known to be electron-rich, however, also protons and heavy ions are accelerated and propagate outwards into the InterPlanetary (IP) magnetic field. These so-called solar Energetic Particles (SEP) which comprise both, flare-accelerated and CME shock-associated particles, occur during the rising and declining phase of the solar cycle and predominantly during solar maximum. Another particle population is dominant during periods of the solar cycle when the solar wind is rather stable and undisturbed: So called Stream Interaction Regions (SIR) form due to the interaction of slow and fast solar wind streams (see Section 2.1). If these solar wind streams are stable over one or more solar rotations, the same SIR can be observed in the following solar rotations and is called a Corotating Interaction Region (CIR). The two shock fronts which form at the borders of the CIR accelerate

mainly ions up to a few MeV. As a result, the energetic-ion increases also corotate with the Sun and can consecutively be observed over wide longitudinal ranges of 360 degrees around the Sun. The positions of the so-called Forward (FS) and Reverse Shocks (RS), respectively, are marked in Fig. 2 by orange lines. For a comprehensive overview of the particle populations in the inner heliosphere see e.g *Kunow et al.* (1991); *Reames* (1999); *Fichtner* (2001); *Richardson* (2004); *Heber* and *Potgieter* (2006).
In the energy range of tens of keV up to tens of MeV, both the CIR-associated particles and the SEPs are the dominant particle populations in the inner heliosphere. Although they occur primarily during different periods of the solar cycle, an overlap exists making it necessary to be able to distinguish between both when studying CIRs or SEPs. The observations of the STEREO mission (see Section 1.4.1 used in this thesis cover the period from solar minimum in 2007 up to solar maximum in 2013. Therefore, the longitudinal distribution of both, CIR-accelerated particles and SEPs could be investigated.

1.3 PURPOSE OF THIS THESIS

Still, all of the particle populations mentioned above and their sources remain the subject of intensive research. The focus of this thesis lies on the longitudinal distribution of CIR-accelerated and solar energetic particles. To fully describe these energetic particle observations different aspects determining the event have to be taken into account. Therefore, the following three questions have to be answered:

1. How and where have the particles been accelerated?

2. How and where were the particles injected into the IP magnetic field?

3. How did the particles propagate through the interplanetary field?

Each of these questions alone can be as complex as filling a whole field of research. The details of energetic charged particle acceleration are beyond the scope of this thesis, however, the location of the acceleration region at the Sun will be discussed. The same applies to question 2: The physical processes of energetic charged particle injection from their acceleration region at the Sun or at a shock wave into the interplanetary magnetic field is not analyzed in this work. But the question on the location, injection, and its extent will be addressed and compared to the remote-sensing results. To shed some light on the propagation conditions is also subject of this thesis. The following questions address the points mentioned above in more detail and build the basis of this thesis:

CIR-associated particles

How stable are CIR-associated ion increases in solar longitude and which parameters can cause variations?

Solar energetic particles

- How wide do SEP events spread in heliographic longitude?
- Which processes are responsible for unexpectedly wide SEP spreads?
- Are there different types of such wide-spread SEP events and are they produced by different mechanisms or a combination of several processes?

An SEP increase as detected in interplanetary space is always determined by a mixture of acceleration, injection, and propagation conditions. Because different processes can lead to similar observations, it can be very complex to disentangle these, and very comprehensive measurements and detailed analyses are needed. With single-point measurements the possibilities are very limited even if remote-sensing observations of the Sun and in-situ measurements are available at the same time. The two STEREO spacecraft, however, in combination with close to Earth observations provide an excellent platform to investigate observations from well separated viewpoints. The STEREO mission and its instrumentation will be presented in the next section. The available observations from the Earth's viewpoint are discussed in Section 1.4.2. An observational and theoretical background will be given in Chapter 2 which describes the particle populations under study (CIR-associated and solar energetic particles, respectively) as well as the investigation methods. The important factors determining energetic charged particle transport and potential mechanisms which are able to spread solar energetic particles over wide longitudinal ranges are discussed in Sections 2.2.1 and 2.2.2, respectively.
The following three chapters present each an analysis which has been published or submitted to a peer-reviewed journal: Chapter 3 will summarize a study of spatial and temporal variations of CIRs. Chapters 4 and 5 build the main part of this thesis and concentrate on SEP events showing remarkably wide particle spreads in the inner heliosphere. Chapter 4 presents a case study of a wide-spread SEP event which occurred on 17 January 2010. Multi-spacecraft observations of this event were compared with modeling results of a 3D particle propagation code to estimate the role of perpendicular transport in the IP medium as a potential wide-spread agent. Chapter 5 displays a statistical analysis of 21 wide-spread events. Special attention is paid to the anisotropy observations at the different

view points which is an important information to disentangle source, injection, and transport processes, respectively.

1.4 SPACE-MISSIONS AND INSTRUMENTATION

1.4.1 *The STEREO Mission*

One key aspect of this thesis is the employment of measurements from multiple, well separated points. For this reason, the STEREO mission which will be introduced in the following was of particular importance. The Solar TErrestrial RElations Observatory (STEREO) is a NASA mission consisting of two nearly identical spacecraft. On 26 October 2006 these two STEREO spacecraft were launched into space to arrive one after another in an Earth-like orbit around the Sun. Figure 3 illustrates how one of the two satellites is situated *ahead* of the Earth (STEREO ahead / STEREO A) and the other one *behind* the Earth (STEREO behind / STEREO B) on its orbit around the Sun. Because STEREO A has a slightly smaller radial distance to the Sun compared to Earth (left hand image of Fig. 3), it orbits the Sun somewhat faster. For STEREO B it is the other way around. This leads to steadily increasing longitudinal separations of both STEREO spacecraft with respect to the Earth of about 22 degrees per year. The middle figure illustrates the stereoscopic view of the Sun provided by the longitudinal separation of the spacecraft with respect to the Earth. The nominal magnetic field spirals connecting the STEREO spacecraft and the Earth with the Sun are included in the right hand figure illustrating the reference frame of energetic particles which propagate along these magnetic field lines.
The most prominent science goal of the STEREO mission was to provide the

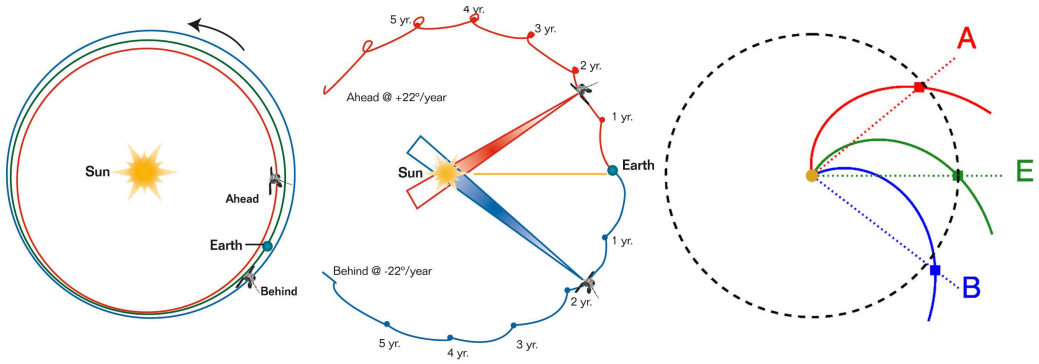

Figure 3: Illustration of the STEREO orbits. The left hand image illustrates the slightly different heliocentric distances of the STEREO spacecraft with respect to the Earth which causes an increasing longitudinal separation of each of the two spacecraft from Earth's longitude. This separation increases about 22 degrees per year and is sketched in the center figure. The right hand figure shows the same constellation including the nominal magnetic field spirals connecting each spacecraft and the Earth with the Sun. Figure adapted from http://stereo.jhuapl.edu/education/misGuide.php.

first-ever stereoscopic observations of the Sun and its CMEs to study the initiation and propagation of these structures. Further science objectives were improved

solar wind measurements, and to study the causes and acceleration sites of solar energetic particles close to the Sun and in the IP medium. To achieve these goals, both satellites are equipped with various instruments. A quick overview of the experiments important for this work will be given in the following.
As non-spinning spacecraft, both satellites have an unhindered and stable view onto the Sun which is important for the multiple remote-sensing instruments contained in the SECCHI (Sun Earth Connection Coronal and Heliospheric Investigation) instrument suite (*Howard et al.*, 2008), e.g. the extreme ultraviolet (EUV) telescopes EUVI, the coronagraphs COR1 and COR2, and the heliospheric imagers HI. These instruments deliver observations of the Sun with high cadence and resolution providing an excellent basis to study the dynamics of active and eruptive processes in the corona. The Sun's chromosphere and corona are imaged in EUV at four different emission lines (171, 195, 284, and 304 Å) but STEREO lacks remote-sensing X-ray observations and magnetic field measurements of the photosphere. Solar radio observations are performed with the STEREO/WAVES experiments (*Bougeret et al.*, 2008). Plenty of in-situ instruments provide further measurements, e.g. of the magnetic field and of energetic particles (contained in the IMPACT suite, *Luhmann et al.* (2007)), and of the solar wind parameters (PLASTIC, *Galvin et al.* (2008)). One of the energetic particle telescopes is the Solar Electron and Proton Telescope (SEPT, *Müller-Mellin et al.* (2008)) which was developed in at the University of Kiel. Figure 4 shows the sensor schematics of

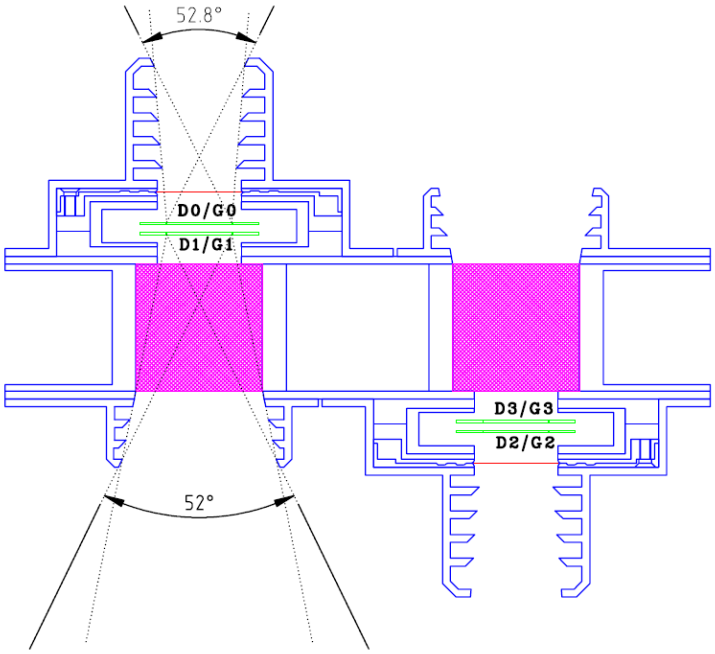

Figure 4: Schematic of the SEPT instrument. The silicon detectors (D0, ..., D3) with guard rings (G0, ..., G3) are marked in green. A Parylene foil (red line) prevents protons to enter the telescope from the one side, a magnetic field on the other side (perpendicular to the drawing plane, magenta square) defrectes the electrons to provide a clean proton measurement (*Müller-Mellin et al.*, 2008).

SEPT which consists of two double ended telescopes. Each of them has two solid

state detectors (marked by green bars) which are operated in anti-coincidence. To distinguish between electrons and protons a magnet-foil system is used: To reach the solid state detectors from the one side the particles have to pass a Parylene foil (red line in Fig. 4) which leaves the electron spectrum essentially unchanged but stops protons of energies up to ∼400 keV. Particles entering from the other end of the telescope have to pass a magnetic field (magenta square) which deflects electrons below 400 keV, but leaves ions unaffected. Because each side of the telescope is designed to only detect electrons or protons, two of these telescopes mounted in opposite directions are combined in one unit . Besides a measurement of protons and electrons from the same direction, such a SEPT unit provides already a forward and backward measurement of these particles. To cover four different viewing directions, two of these units are mounted on each of the STEREO spacecraft providing information on anisotropy. Therefore, one unit observes in the ecliptic along the nominal magnetic field line towards and away from the Sun, and the other one observes out of the ecliptic plane, looking towards north and south, respectively. A detailed instrument description of SEPT can be found in *Müller-Mellin et al.* (2008).

Because of their unique orbits, the STEREO spacecraft are perfectly suited to investigate CIRs and SEPs in terms of longitudinal variations. For this purpose, the negligible radial effects are one of the main advantages of the STEREO mission. From the beginning of the STEREO mission in 2007 up to 2010 the solar activity was very low in coincidence with an unusually prolonged and quiet solar minimum. Almost no SEP events occurred and only very few CMEs were measured so that a 'pristine' solar wind was observed. Such heliospheric conditions are perfect to study CIRs. Also the moderate longitudinal separation between the STEREO spacecraft was well suited to investigate CIRs in terms of stability or temporal and spatial variations. Chapter 3 will present results of a study of such variations. By February 2011, when both spacecraft were separated by 180 degrees from each other, the full Sun's surface was visible at once for the first time ever. This constellation, with the Earth located in between, formed an unprecedented platform to investigate the longitudinal variations of SEP events but, furthermore, provided a tool to detect and study wide-spread SEP events which are of great interest for this work (see Chapters 4 and 5).
The STEREO mission is described in detail in *Kaiser et al.* (2007) and references therein. Instruments which were used in our analysis are also described in Sections 4.1.2, 5.1.2, and Section 2 of Appendix C. See also Section 2.2.3 where the usage of the various measurements and investigation methods are described.

1.4.2 *Observations from Earth's viewpoint*

Ground-based observations as well as several operating spacecraft in the vicinity of Earth or situated at the first Lagrangian point L1 provide a third valuable observation point for multi-spacecraft investigations. This section will shortly summarize which observations from Earth's viewpoint added to the investigations

presented in this thesis.
The Electron, Proton, and Alpha Monitor (EPAM, *Gold et al.* (1998)) aboard the Advanced Composition Explorer (ACE) provides energetic electron measurements in the same energy range as provided by STEREO/SEPT. ACE is a spinning spacecraft. In contrast to the SEPT instrument, EPAM does not need several telescopes with different viewing directions to provide anisotropy measurements because directional particle measurements are directly determined through the different viewing directions which are scanned during each spin. A schematic of the EPAM instrument is shown in Fig. 2 of Appendix C. ACE also delivers further in-situ measurements, e.g. of the magnetic field (MAG, *Smith et al.* (1998)) and solar wind properties (SWEPAM, *McComas et al.* (1998)). Like ACE, the SOHO (SOlar and Heliospheric Observatory) satellite orbits L1. The energetic particle suite COSTEP (Comprehensive Suprathermal and Energetic Particle Analyzer) includes an energetic particle detector which was built in Kiel: The Electron Proton Helium Instrument (EPHIN, *Müller-Mellin et al.* (1995)). SOHO unfortunately lacks magnetic field measurements but provides another important instrument: The Large Angle and Spectrometric Coronagraph (LASCO, *Brueckner et al.* (1995)). The Extreme Ultraviolet Telescope (EIT) aboard SOHO was progressively replaced by the AIA (Atmospheric Imaging Assembly, *Lemen et al.* (2012)) instrument aboard the SDO spacecraft which was launched in 2010 and provides remote sensing observations in unprecedented high cadence and resolution. Solar radio bursts (see Section 2.2.3) are observed by several ground-based stations but are also provided by the WAVES instrument, covering lower frequencies than ground-based observatories, (*Bougeret et al.*, 1995) aboard WIND. X-ray observations of solar flares are provided by the Solar X-Ray Imager (SXI, *Hill et al.* (2005)) aboard the GOES spacecraft.

2

OBSERVATIONAL AND THEORETICAL BACKGROUND

2.1 COROTATING INTERACTION REGIONS

Figure 5 illustrates a stream interaction region which forms when a fast solar wind stream follows and interacts with a preceding slow solar wind stream. With increasing distance to the Sun the velocity components perpendicular to the interface between both streams increase until they reach super-magnetosonic values. Then, on both sides of the so-called Stream Interface (SI) that separates

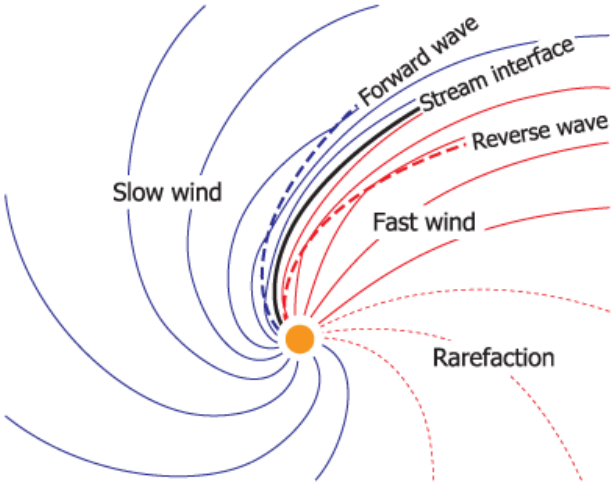

Figure 5: The formation of a CIR (Corotating Interaction Region): Fast solar wind causes a magnetic field pattern with less curvature (red lines) than slow solar wind (blue lines). Consequently, both solar wind streams interact and a CIR forms which is bounded by a reverse shock (wave) and a forward shock (wave). The stream interface which is the original separation plane between both streams, can still be found in the in-situ data of a CIR. The region of fast and less dense solar wind behind a CIR is called rarefaction region. Figure from *Owens and Forsyth* (2013).

the fast and slow streams, a shock wave forms: The reverse shock (RS) which runs back into the fast solar wind, and the forward shock (FS) which propagates into the slow solar wind ahead. Between both shock fronts a compression region is formed with increased temperature, density, and magnetic field strength. The shock fronts themselves serve as particle accelerators, predominantly accelerating ions up to a few MeV. Because the fast solar wind streams originate from the open magnetic field topology over coronal holes that can be stable over weeks or months (e.g. *Kunow et al.* (1999)), these stream interaction regions often reoccur with the periodicity of a solar rotation and are then called Corotating Interaction Regions (CIR). Figure 6 shows typical in-situ measurements of a CIR passing the

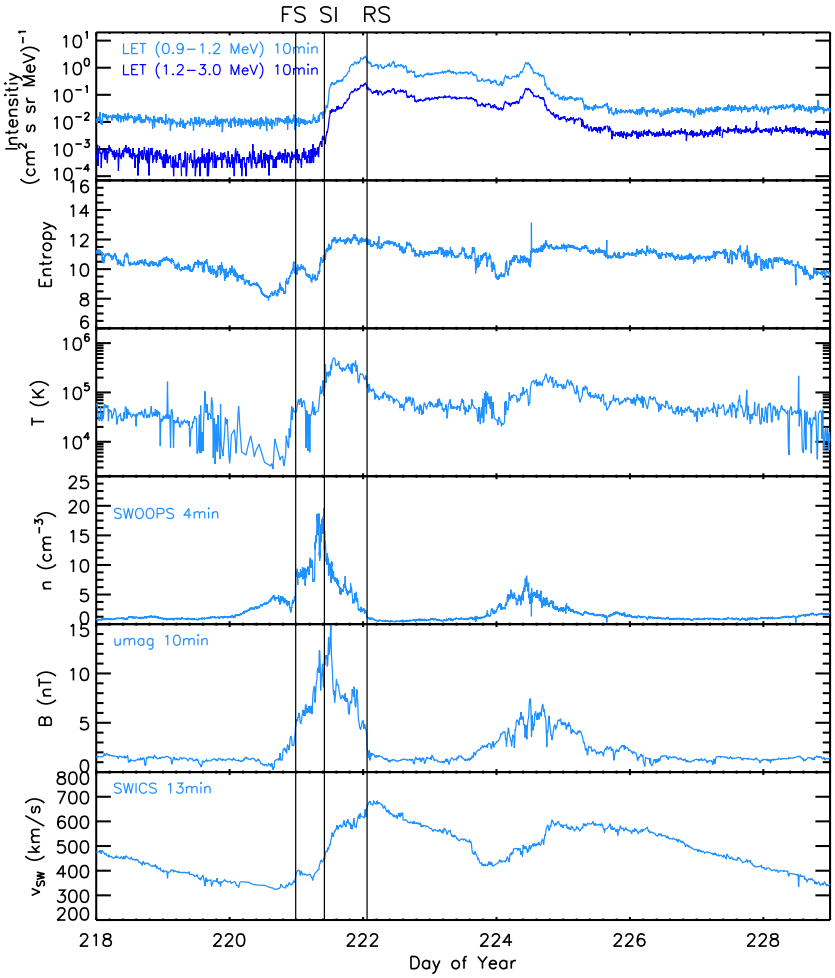

Figure 6: Typical in-situ data of a CIR, observed by Ulysses in 2007. From top to bottom: Intensities of MeV ions, entropy, temperature and densitiy of the solar wind, magnetic field magnitude, and solar wind speed. Forward shock, stream interface and reverse shock of the CIR are marked by vertical lines and 'FS', 'SI', and 'RS', respectively. Figure from (*Dresing et al.*, 2009).

Ulysses spacecraft which had a radial distance to the Sun of ∼1.4 AU and crossed the ecliptic plane during that time. While the shock waves can be identified by discontinuities in the plasma and magnetic field parameters (marked by vertical lines and FS/RS), the stream interface (marked by SI) has been identified by other plasma parameter characteristics like an increase in temperature and a drop in density. Usually, the reverse shock is most efficient in particle acceleration (e.g. *Desai et al.* (1999); *Mason et al.* (1999)) which is also true for Fig. 6. Note that, MeV ions do not show an increase associated with the forward shock but reach their maximum intensity correlated with the reverse shock passage. Pre-STEREO observations suggested that both shock fronts typically form at distances larger than one

AU (*Gosling et al.*, 1993) and not at exactly the same time. However, our example shows that the shocks can already be present at distances of ∼1 AU. This agrees with the findings by *Russell et al.* (2009) who presented STEREO measurements during the solar minimum between cycles 23/24 and reported that CIR-associated shocks often form already between Venus at 0.72 AU and 1 AU. Furthermore, if no shock has formed yet, steepening waves can be observed, and associated particle increases are already present (e.g. *Dresing et al.* (2009)). The acceleration of these particles is attributed to the turbulence inside the compression region and close to the steepening waves and is called *local acceleration* (*Giacalone et al.*, 2002). The presence of the STEREO spacecraft during the deep solar minimum in 2007 and 2008 provided the unprecedented opportunity to observe the same CIRs at different heliographic longitudes and times without significant radial effects. By comparing the observations from different spacecraft and correlating the observations with remote-sensing measurements, spatial and temporal variations could be resolved and linked to their parent sources. The study by *Gómez-Herrero et al.* (2011) will be discussed in Chapter 3.

2.1.1 *Ballistic Backmapping*

While the solar wind propagates outwards, the Sun rotates with a period of ∼25 days. As a result, the point of origin of a solar wind portion will not be in the line of sight of the spacecraft detecting it but be shifted to the west. To correlate in-situ solar wind measurements with structures at the Sun observed by remote-sensing instrumentation, the in-situ data can be mapped back to the solar origin. Following a radial propagation of the solar wind with constant speed allows to calculate the angle $\Delta\Phi$ the Sun rotated during the propagation time of the solar wind from the Sun to the spacecraft (e.g. (*Nolte* and *Roelof*, 1973)):

$$\Delta\Phi = \frac{\Omega_s(\vartheta) \cdot (r - r_0)}{V_{sw}}. \tag{1}$$

Here, Ω_s is the sidereal angular velocity of the Sun depends on the solar latitude ϑ due to the differential rotation of the corona (c.f. *Brajša et al.* (2001)). r and r_0 are the heliocentric distances of the spacecraft and the source surface (assumed to be at 2.5 solar radii), respectively, and V_{sw} is the measured solar wind speed. For spacecraft located close to the ecliptic plane like SOHO or STEREO, the differential rotation can be neglected for the backmapping technique. However, for Ulysses observations out of the ecliptic, this effect has to be taken into account.
A typical plot comparing backmapped data with coronal structures is illustrated in Fig. 7. Instead of time, the horizontal axis shows the Carrington rotation number which is a solar-fixed longitudinal coordinate (corotating with the Sun).

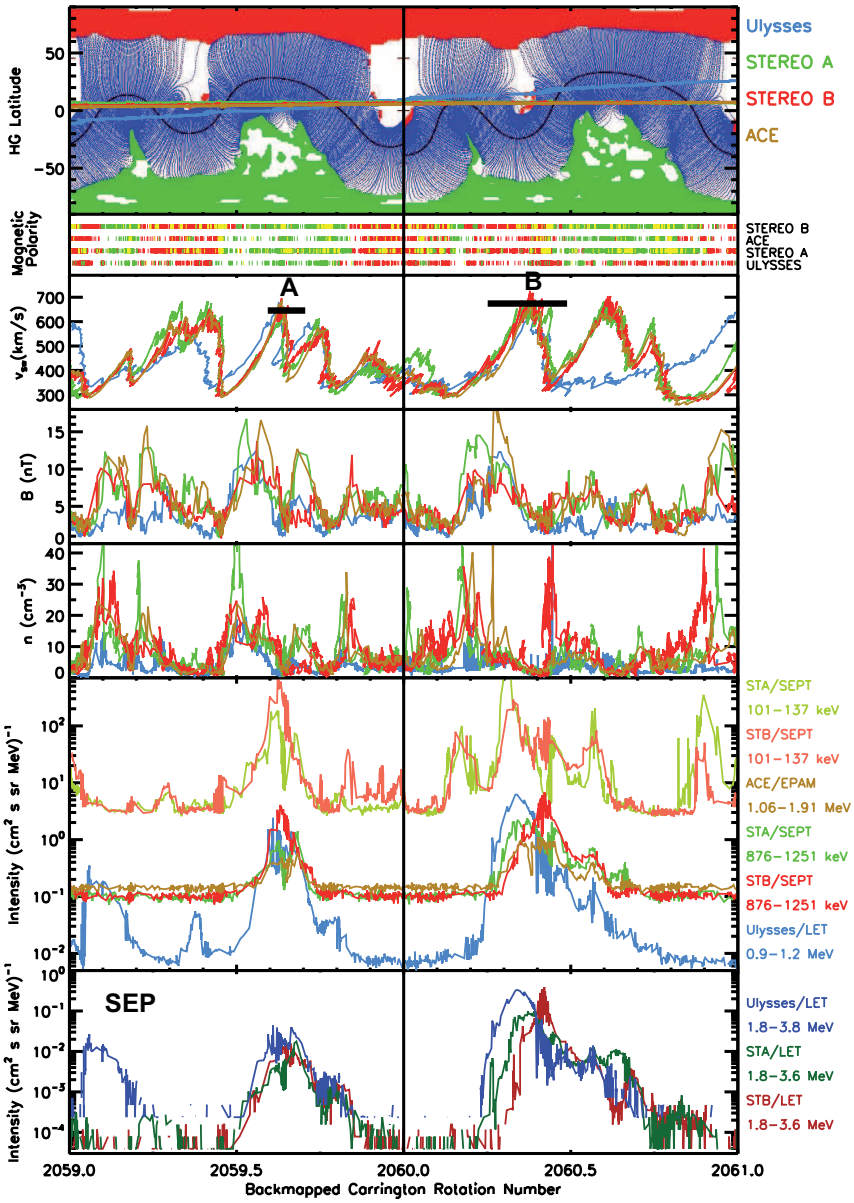

Figure 7: Backmapped in-situ data measured by Ulysses, ACE, STEREO A, and STEREO B in comparison with integral Carrington maps provided by the Global Oscillation Network Group (GONG, `http://gong.nso.edu/`) for Carrington rotations 2059 and 2060 (July to Sep 2007), respectively. The heliographic latitudes of the spacecraft are plotted on top of the GONG maps in the top panel, the colored bands below mark the in-situ magnetic field polarity detected at the spacecraft in colors corresponding to those of the GONG maps. Panel 1, 2, and 3 below show the solar wind speed, the magnetic field strength, and the solar wind density, respectively. The two bottom panels shows energetic ion intensities. The time axis below the plot marks the time corresponding to the backmapped Carrington rotation number as seen from Earth. Figure from *Dresing et al.* (2009). The high speed streams labeled **A** and **B** were periods of interest in *Dresing et al.* (2009).

As a result, the CIRs observed at different times and at different spacecraft which are well separated in space appear at the same Carrington rotation number corresponding to the source longitude of the parent solar wind stream. A comparison of the different in-situ observations as well as with structures of the solar corona (here presented through the GONG (Global Oscillation Network Group) maps in the top panel) is now straightforward. See e.g. *Dresing et al.* (2009) for details about employing GONG maps to link in-situ measurements to the coronal structure.

2.1.2 *Implications for SEP Investigations*

The main implication of CIR studies for those of SEPs is the ballistic backmapping which is a common tool used in both fields. Because of the frozen-in magnetic field, all solar wind portions which were launched from the same source region can be assumed to be connected by a magnetic field spiral. When a solar wind portion is detected in-situ, the spacecraft is magnetically connected to its source longitude although the solar wind portion may have left the Sun several days earlier. SEPs which are accelerated at the Sun propagate outwards along the magnetic field spirals within minutes to hours. If a good connection between acceleration region and spacecraft is present, the SEPs can directly stream to the spacecraft. The backmapped longitude of the solar wind source region follows the same longitude as that of the spacecraft's magnetic footpoint.
However, because several assumptions are made, the ballistic backmapping suffers some uncertainties. For instance, the assumption of a radially outwards propagating solar wind with constant speed is not completely true as an acceleration of the solar wind up to $\sim$10 solar radii is predicted by models (e.g. *Cranmer and van Ballegooijen* (2005)). Multi-point CIR studies like the one presented above are perfectly suited to estimate the uncertainties and limitations of the backmapping technique. It turned out that the method works very well when associating fast solar wind streams with their parent source regions at the Sun. When combining backmapped in-situ magnetic field and solar wind measurements with maps of the source surface, an unambiguous identification of the parent coronal holes can usually be made for the high speed streams. Finer structures and shorter time scales of e.g. hours, however, are hardly resolved in backmapped data (*Dresing et al.*, 2009) so that a 10 degree uncertainty can be assumed for the backmapping technique (c.f. *Nolte and Roelof* (1973)). Ten degrees in longitude correspond to the angle, the Sun rotates during 0.7 days (17 hours) which is in agreement with the findings of *Dresing et al.* (2009) and *Gómez-Herrero et al.* (2011). The study presented above also shows that the backmapping still works quite robustly even if interplanetary transient structures are embedded in the CIRs or located in its close vicinity. While the energetic particle increase was affected by these structures, the backmapped solar wind did not change significantly.
The effects investigated in the above study, which can cause variability in CIR observations only partly affect SEP events. Coronal hole evolutions, for example, are not important during the very small time scales of particle acceleration and injection at the Sun. The presence of CMEs or special magnetic structures in the

IP medium, however, may significantly change the overall magnetic field regime influencing the interplanetary particle propagation. However, as discussed above, this is probably not the case for slow and small-scale transients which are carried out by the solar wind. Nevertheless, CMEs as well as the stream interfaces of CIRs are known to be possible particle barriers (*Intriligator et al.*, 1995) so that the presence of these structures during an SEP event can potentially influence the SEP propagation.

The angular difference between the solar source region and the spacecraft magnetic footpoint (the separation angle) is an important factor in SEP studies, and here an uncertainty due to the backmapping procedure has to be kept in mind. While the ballistic backmapping just provides the magnetic connection between the spacecraft and the source surface at the Sun which is usually assumed to be at 2.5 solar radii, the sources of SEPs (solar flares) are located below in the low corona. Therefore, the uncertainty due to the magnetic field from the source surface to the location of particle acceleration and release is an important factor. Based on line of sight magnetic field measurements in the solar photosphere, this magnetic structure can be computed using Potential Field Source Surface (PFSS) models (c.f. *Altschuler* and *Newkirk* (1969)) such that maps of the solar source surface (like the GONG maps) can be produced. However, PFSS models assume the absence of any currents which is not fulfilled in the vicinity of Active Regions (AR) and especially not during solar flares (*Rayrole* and *Semel*, 1970). It turns out that the magnetic field below the source surface cannot be assumed to be radial and may provide connections to remote longitudes and latitudes. Figure 8 shows

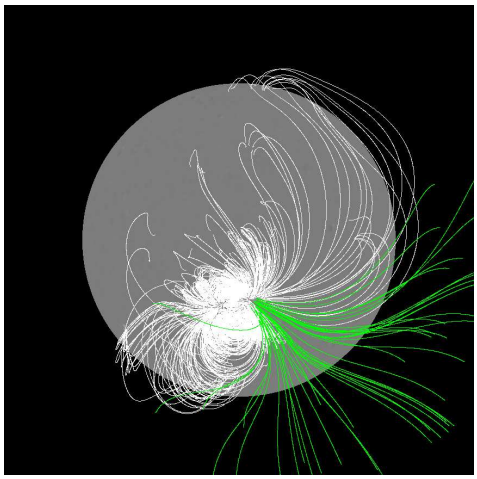

Figure 8: Magnetic field lines below the source surface originating in the vicinity of an AR. These lines were computed by a PFSS model, figure from *Dresing et al.* (2012)

a reconstruction of the magnetic field below the source surface computed by a PFSS model: Shown are the open (green) and closed (white) magnetic field lines emerging from a certain region in the vicinity of an AR. Field lines originating from other locations are not shown in this figure. The wide spread of the open field lines clearly illustrates that the rather confined AR can be broadened to several tens of degrees at the source surface (c.f. *Klein et al.* (2008)). This effect can cause an additional uncertainty for the separation angle between source location

and spacecraft magnetic footpoint. On the other hand, the effect may already cause a particle spread before the SEPs enter the IP magnetic field regime (see Section 2.2.2). Not only the magnetic field line spread causes an uncertainty but also the extent of the flaring AR itself which is identified by inspection of EUV images. These active regions sometimes appear as large as 10 to 20 degrees in diameter on the images. Furthermore, the latitude of the backmapped magnetic footpoint is assumed to be the same as the spacecraft position which may not be true especially when considering the magnetic field structure below the source surface. For this reason, *Lario et al.* (2013) assume an error of 20 degrees in latitude and longitude for the position of the spacecraft's magnetic footpoint determined with ballistic backmapping.

2.2 SOLAR ENERGETIC PARTICLE EVENTS

Solar energetic particles exist as many different particle species and with a wide range of energies and intensities. While the bulk consists of electrons and protons, helium and heavy ions can also be found. However, there are different source regions for SEPs. These sources differ not only in the acceleration process but also in their location. One possible SEP source are so-called solar flares which occur in the low corona in solar active regions. These strong magnetic reconnection processes accelerate particles to high energies up to hundreds of MeV or even up to the GeV-range. The majority of the particles does not escape from the rather confined magnetic field structure but streams back towards the denser plasma below. The resulting deceleration of these high energy particles causes the characteristic X-ray, synchrotron, EUV and sometimes even white light emissions, with typical durations of minutes to hours. A fraction of the accelerated particles, however, may escape along open magnetic field lines and propagate outwards into the IP magnetic field where they can be detected through their characteristic intensity increases. Flare-associated SEP events are usually electron-rich and impulsive, and are known for 1000-fold enhancements of the ^{3}He/^{4}He fraction. Because of the rather small acceleration region, the SEP spread in the IP medium is correspondingly narrow with typical values of $\sim$40 degrees (*Reames*, 1999).
Another known SEP source are CME-driven shocks. These shocks accelerate mainly protons and heavier ions, and varying elemental compositions and charge states are produced through different acceleration processes and seed populations (*Cane et al.*, 2003; *Tylka et al.*, 2005). In contrast to flares, CME-driven shocks have a much larger extent and consequently the SEP spread in the IP medium can be much broader, up to 180 degrees (*Cane*, 1996). Because CME shocks accelerate the particles over a long time while propagating outwards, the characteristic SEP increases are rather gradual. See e.g. *Reames* (1999) or *Kallenrode* (2003) for detailed reviews of CME- and flare-associated SEPs, respectively.
SEP events directed towards Earth can become an issue of space weather and very energetic events can cause a so-called Ground Level Enhancement (GLE). This means that the radiation level on the ground increases which can be seen in neutron monitor measurements.
As pointed out in Section 1.3, not only the different sources determine an SEP

event but also the particle injection and transport to the observer. The next section will introduce energetic charged particle propagation in interplanetary space and characterize the important factors influencing the transport.

2.2.1 *Solar Energetic Particle Transport*

The forces which determine the trajectories of energetic charged particles in space plasmas are provided by the electromagnetic fields. However, curvature and gradient drifts, respectively, can be neglected for solar energetic particles moving through the interplanetary magnetic field because their Larmor radii are small compared to the size of the magnetic field variations. To describe the propagation of energetic charged particles in the heliospheric (diverging) magnetic field, the model of focused transport has been introduced (*Roelof*, 1969) which is a qualitative model of the evolution of the gyro-averaged particles' phase-space density f:

$$\frac{\partial f}{\partial t} + \underbrace{\mu v \frac{\partial f}{\partial z}}_{\text{Advection}} + \underbrace{\frac{1-\mu^2}{2L} \cdot v \frac{\partial f}{\partial \mu}}_{\text{Focusing}} - \underbrace{\frac{\partial}{\partial \mu}\left(D_{\mu\mu}\frac{\partial f}{\partial \mu}\right)}_{\text{Diffusion}} = Q(z,\mu,t) \tag{2}$$

Instead of tracing the trajectory of a single particle, the model describes a full particle ensemble by its phase-space density which can be taken as a representative of the particle intensity measured during an event. The parallel propagation of particles with velocities v along the magnetic field line with distance z is described by the *advection* term; $\mu = \cos\theta$ is the particle's pitch angle cosine. When the energetic particles injected close to the Sun propagate into the weakening interplanetary magnetic field $B(z)$ their pitch angle is reduced. The resulting particle focusing is described by the *focusing* term in Eq. 2 with the focusing length $L = B(z)/(-\partial B/\partial z)$. The effect of pitch-angle scattering is introduced by the *diffusion* term with $D_{\mu\mu}$ being the pitch angle diffusion coefficient. Q, on the right hand side of Eq. 2, denotes a source term, e.g. a source of an SEP event which is located in the solar corona. Effects of convection and adiabatic deceleration in the expanding solar wind are neglected in this model so that it is only valid for particles with diffusion velocities much higher than the solar wind speed. A corotation with the Sun due to the corotation of the magnetic field spirals is only significant for particles with low energies: Protons of 30 keV, for example, need 20 hours to propagate along a nominal magnetic field line to 1 AU. With a solar rotation rate of ∼14 degrees per day these particles experience a significant transport in solar longitude. Energetic electrons of 100 keV, on the other hand, need less than 20 minutes to reach 1 AU. See e.g. *Kunow et al.* (1991); *Dröge* (2005) for comprehensive overviews of the transport models.

In summary, the two competing processes in the focused transport model are focusing and pitch-angle scattering. If the scattering is very low, the particles will arrive at a distance of 1 AU very beamed in a narrow cone of a few degrees. Their intensity-time profile is then very similar to the injection profile and only shifted by the propagation time along the magnetic field line. On the other hand, strong scattering leads to an effective longer path length which can be imagined

as a magnetic field spiral with superposed irregularities that significantly extend the length of the field line. As a consequence, the arrival time of the particles is delayed and the increase is less impulsive but more gradual until the maximum intensity is reached. However, note that during low scattering in the IP medium a gradual SEP increase can also be caused by an extended injection at the Sun. Because of that a very important observational parameter is the anisotropy which is a measure for the net streaming of the particles into a certain direction and, thus, a measure for the degree of scattering. The anisotropy is defined as

$$A = 3 \cdot \frac{\int_{-1}^{+1} \mathrm{I}(\mu) \cdot \mu \cdot d\mu}{\int_{-1}^{+1} \mathrm{I}(\mu) \cdot d\mu} \tag{3}$$

with $\mathrm{I}(\mu)$ being the pitch angle dependent intensity measured in the different viewing directions. Per definition, the anisotropy A ranges between -3 and 3 (depending on the magnetic field polarity). The absolute value of A, therefore, describes the degree of scattering with high absolute values pointing to nearly scatter-free transport and low values pointing to strong scattering.
Figure 9 shows measurements of a SEP event detected by STEREO B on 7 February 2010 (*Dröge et al.*, 2014). The event is rather impulsive and shows a significant anisotropy during the rising phase. Later, the anisotropy vanishes which is typical for SEP observations. Both the intensity-time profile (large middle panel) and the anisotropy-time profile (lower panel) have been fitted with a focused transport model (red lines, *Dröge et al.* (2014)). The fit computes the injection function (shown in the second panel from top) and allows to determine the pitch angle diffusion coefficient $D_{\mu\mu}$, and so the mean free path $\lambda_\parallel$ which relates the pitch-angle scattering to the spatial diffusion parallel to the ambient magnetic field (e.g. *Hasselmann* and *Wibberenz* (1968); *Agueda et al.* (2008)):

$$\lambda_\parallel = \frac{3v}{8} \int_{-1}^{+1} d\mu \frac{(1-\mu^2)^2}{D_{\mu\mu}(\mu)} \tag{4}$$

In space plasmas energetic particles can be assumed to be collisionless. Here, the mean free path describes the distance over which a particle changes its pitch angle by 90 degrees. The mean free path along a magnetic field line $\lambda_\parallel$ or the radial mean free path $\lambda_r = \lambda_\parallel cos^2\psi$, with ψ being the angle between the radial and the magnetic field spiral direction, are used as a parameter to describe the propagation conditions for an event. Low values for λ describe strong scattering and higher values less scattering.

An important fact to note about the focused transport model (Eq. 2) is that it assumes a direct magnetic connection between the source or injection region at the Sun and the observer. However, observations have shown that SEP events can be observed far from the nominal magnetic field line connecting the spacecraft and the AR (e.g. *Dalla et al.* (2003)). This may have different reasons (see next section). However, one important process may be the particle transport perpendicular to the average magnetic field (e.g. *McKibben et al.* (2001); *Cane* and *Erickson* (2003); *Dalla et al.* (2003); *Dröge et al.* (2010)). Different processes can provide a perpendicular transport: The random walk of the magnetic field lines, assumed to be caused by

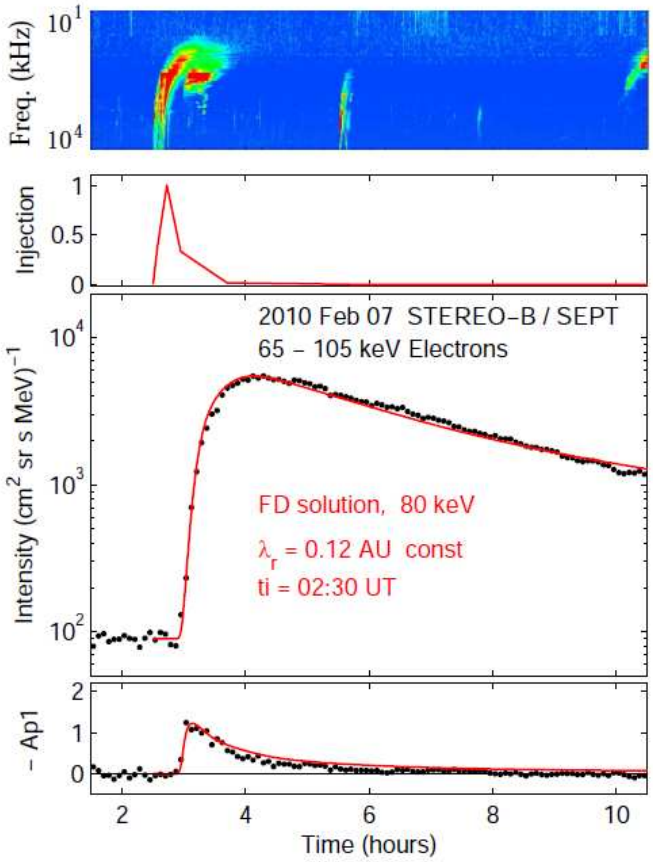

Figure 9: Intensity- and anisotropy-time profiles (bottom and middle panel) of an SEP event observed by STEREO B on 7 February 2010. The event has been fitted by a focused transport model (red solid lines). The resulting injection function is plotted in the second panel from top, and the corresponding radio observations showing the associated type III radio burst are shown in the top panel (*Dröge et al.*, 2014).

the motion of the photospheric footpoints of the magnetic field lines, or scattering in the turbulent magnetic field (the same as the pitch-angle scattering discussed above). While in the case of meandering magnetic field lines the particles' guiding center still follows one magnetic field line, the second process means that the guiding center of the particle moves from one field line to a neighboring one due to perpendicular irregularities in the field. For this reason, the latter process is also called perpendicular diffusion. Figure 10 sketches a wide SEP distribution caused by perpendicular diffusion. The small reddish range marks the region where a good connection to the source region is present and, therefore, an anisotropic event can be observed. The gray range marks the region which the particles just reach due to strong perpendicular transport in the IP medium. Because of the strong underlying scattering no significant anisotropy can be observed here. Modern three-dimensional (3D) particle propagation codes (e.g. *Zhang et al.* (2009); *Dröge et al.* (2010)) also include the effect of perpendicular diffusion and are able to

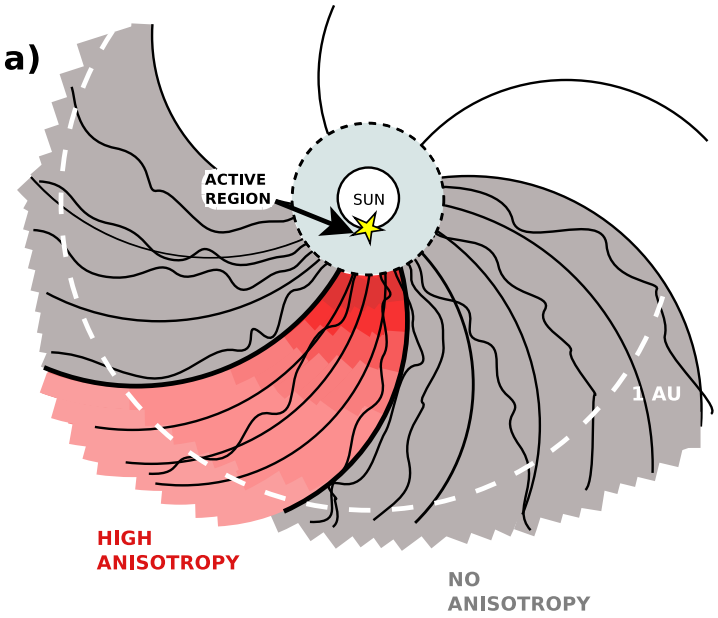

Figure 10: Cartoon illustrating a wide SEP distribution in the inner heliosphere (colored range). In the reddish region a good connection to the source location at the Sun is present and thus significant anisotropy is observed. In the gray region isotropic particle increases are observed. Figure from *Dresing et al.* (2014)

model the observations at a spacecraft which is not well connected to the flaring active region at the Sun.

2.2.2 *Wide-Spread Events and Potential Physical Processes*

The term 'wide-spread SEP event' has not yet been clearly defined by requesting a specific minimum particle spread at a certain heliocentric distance. A wide-spread SEP event can be understood as an event showing a larger particle distribution than expected. The longitudinal extent which is usually expected in the inner heliosphere was determined by pre-STEREO observations made with e.g. the two Helios spacecraft and is about 40 degrees for flare-associated events and up to 180 degrees for CME-associated events (c.f. *Reames* (1999); *Cane* (1996)). Although there were already multi-spacecraft observations before STEREO, the ability to detect and proof a wide SEP spread was very limited. The main problem was the lack of remote-sensing instrumentation on board spacecraft like Helios, IMP-8, or Ulysses so that an unambiguous solar association could not be made for many events. Furthermore, the different radial distances of the spacecraft mentioned above complicated a qualitative comparison of SEP intensities. A radial intensity gradient g_r had to be determined which is found in the literature with varying values from $g_r \sim R^{-2}$ to $g_r \sim R^{-4}$, where R is the radial distance to the Sun (see e.g. *Lario et al.* (2006) and references therein).
As discussed in Section 1.4.1 the STEREO spacecraft build an optimal and unprecedented platform to study SEP events. With increasing solar activity in 2010 as well as increasing longitudinal separation between the STEREO spacecraft

(∼150 degrees in mid 2010), the conditions were excellent to detect and study wide-spread SEP events.

There are several ideas and mechanisms which have been proposed to explain wide SEP spreads which are still subject to current research. This section will give a short overview.
While solar flares are often treated as point sources, there may be processes in the corona which spread the SEPs before these are injected into the open IP magnetic field, known as coronal transport (e.g. *Reinhard* and *Wibberenz* (1974); *Newkirk* and *Wentzel* (1978)). The divergence of the magnetic field lines below the source surface is just one mechanism which is supposed to produce a lateral particle spread of tens of degrees (*Klein et al.*, 2008). Figure 11 shows two magnetograms

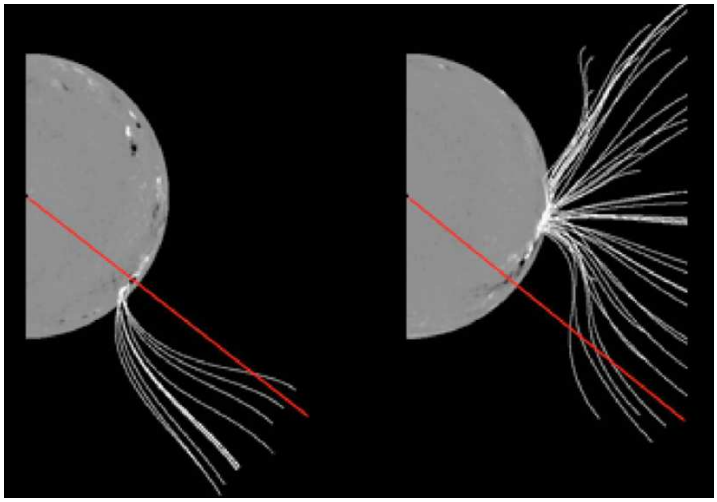

Figure 11: Magnetograms of the photosphere (by SOHO/MDI) and open magnetic field lines computed by a PFSS model (*Schrijver* and *De Rosa*, 2003) for two different events on 1 May 2001 (left) and 30 April 2001 (right). The red trajectories represent the longitudes where the nominal Parker field lines intersect the source surface (*Klein et al.*, 2008).

of the photosphere and open magnetic field lines computed by a PFSS model for two different events. In contrast to the left hand panel, the right hand figure shows a large spread of the open magnetic field lines below the source surface which is supposed to reach angles of up to ∼80 degrees (*Klein et al.*, 2008) and, therefore, could provide a pre-spreading of SEPs before these enter the IP magnetic field. Recently, the presence of so-called EUV waves, which appear as large scale disturbances in EUV images, has also been linked to the spread of SEP events (c.f. *Rouillard et al.* (2012); *Park et al.* (2013)). Figure 12 shows the propagation of an EUV wave front (yellow lines) observed on 17 January 2010 by STEREO B. One could imagine that an EUV wave intersecting the magnetic footpoint of a spacecraft may somehow contribute to the lateral SEP transport to that position. However, this theory is currently being investigated. The same is true for meandering magnetic field lines close to the Sun which are also supposed to have an important effect on the particle spread at 1 AU (*Laitinen et al.*, 2013).
Because of their size compared to flares, shock waves are good candidates to

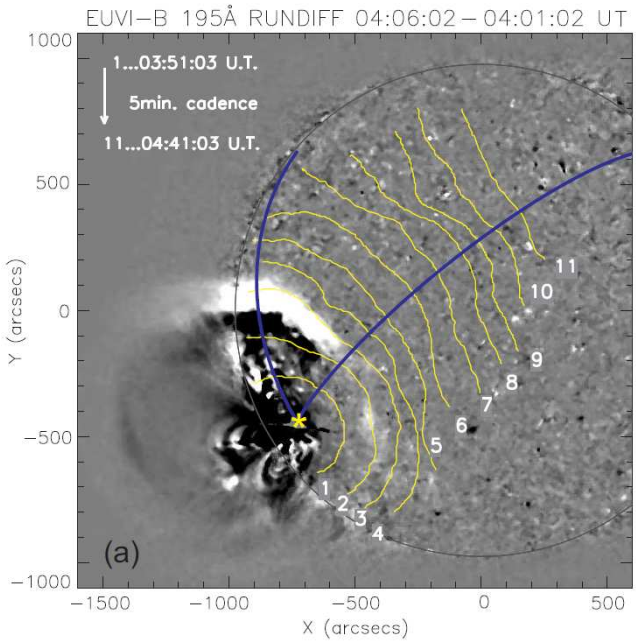

Figure 12: Running difference image of STEREO B EUVI 195 Å showing the propagation of an EUV wave indicated by the yellow lines (*Veronig et al.*, 2010).

produce wide particle spreads, as they build spatially extended source regions. Although electrons are accelerated much less efficiently at heliospheric shocks which are usually not discussed as the sources of solar electron events (*Lee*, 2006), coronal shocks may account for electron acceleration although this process is slower than the acceleration in solar flares (e.g. *Miteva* and *Mann* (2007); *Kahler* (2007)). These shock waves can be produced either as piston-driven shocks (i.e. a bow shock of a rising CME) or as blast waves due to a large pressure pulse produced by a flare.

A shock driven by a CME can propagate into the IP medium and build a moving source region in the inner heliosphere. It is generally accepted that these shocks produce wide-spread proton and ion events which show variable time series depending on which part of the shock the observer is connected to (*Reames*, 1999). Figure 13 shows such typical proton time series as observed from different longitudes with respect to the position of a CME-driven shock. An observer located at the eastern shock flank (left hand panel) will observe an impulsive increase because of the connection to the nose of the shock, which is the most efficient particle acceleration region, during the early phase of the event. When the shock reaches 1 AU, however, the observer is just connected to the weak outer part of the shock, yielding lower particle intensities. On the other hand, a centrally located observer (middle panel) will observe stronger particle flux while the shock approaches due to an improving connection to the shock nose. A spacecraft located west of the CME will detect very gradually rising intensities from the time on when the shock front extends up to the magnetic field lines connecting to the spacecraft. A shock peak can be observed when the shock front passes the spacecraft, however, a good connection to the shock nose may be provided

even later when the shock is already behind the spacecraft so that the highest intensities are observed after the shock passage. The compositional and elemental

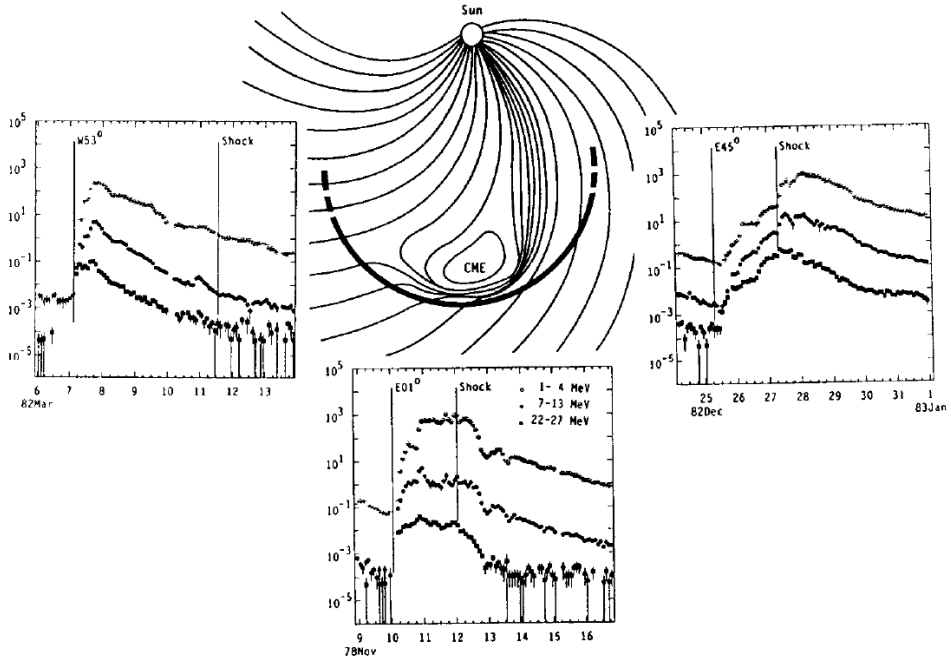

Figure 13: Intensity-time profiles of protons observed from different solar longitudes with respect to a CME-driven shock (*Reames*, 1999).

signatures of these SEP events clearly point to the shock as the source (c.f. *Cane et al.* (2003); *Tylka et al.* (2005)). The extent of the SEP distribution directly depends on the extent of the IP shock which may be as wide as 180 degrees (*Cliver* and *Cane*, 1996) in the inner heliosphere.

Apart from the nature of the source, the SEP transport may yield a large spread as well. The presence of large scale magnetic structures in the IP magnetic field itself can influence the SEP distribution by modifying the nominal magnetic connections, and consequently causing wider particle spreads. Strong and efficient perpendicular transport in the IP medium (see Section 2.2.1) may also spread the particles over wide ranges.

Extremely wide SEP spreads as reported in the two publications presented in Chapters 4 and 5, respectively, are not easily explained by each of the above processes. One has to either assume one process to be very strong and efficient in spreading the particles, for example very strong perpendicular transport in the IP medium, or several mechanisms acting together. Figure 14 illustrates such a complex scenario, where a large source distribution close to the Sun (red arc) provides a pre-spreading of the SEPs. Strong perpendicular diffusion in the IP magnetic field operates additionally distributing the particles even further so that the event can be observed over the whole colored range. The different colors mark regions of different anisotropy observations expected during such a scenario. Shedding some light on the important ingredients for wide-spread electron events

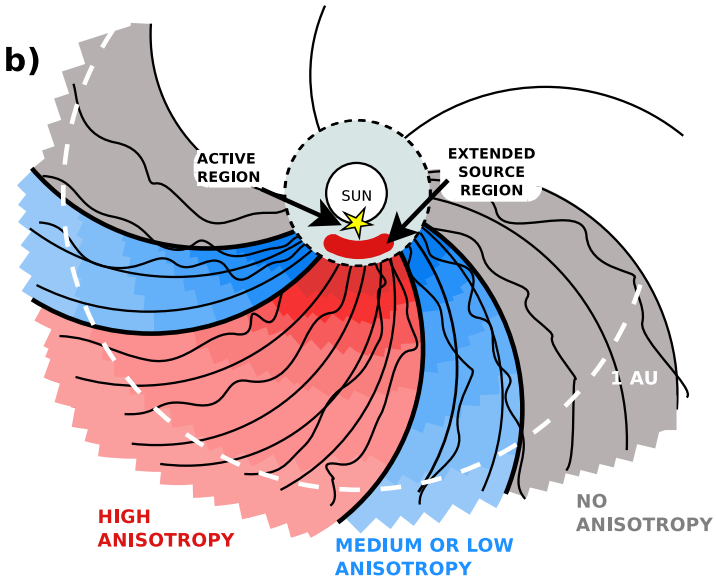

Figure 14: A complex scenario producing a wide-spread SEP event. Additional to the flare, a further extended source region is assumed to be present in the low corona. High anisotropy (reddish range) is measured if the observer is connected to this extended source region, no anisotropy (gray range) is observed at far separated positions if the particles reach the observer due to strong perpendicular diffusion. A region of medium anisotropy (blue range) forms in between because of the small magnetic separation to the edges of the extended source region at the Sun leaving some of the directional information. Figure from *Dresing et al.* (2014)

is the purpose of the studies presented in Sections 4.1 and 5.1. The next section will introduce the methods and important parameters for SEP studies.

2.2.3 *Investigation Methods for Solar Energetic Particle Events*

This section introduces the important parameters and investigation methods of SEP event studies. Concerning energetic particle measurements, an event is an intensity increase detected for example aboard a spacecraft. This increase already contains plenty of information like the maximum intensity depicting the magnitude of the event, the rise time, and the total duration of the increase. However, thanks to modern instrumentation and various operating spacecraft as well as ground-based observatories, there is much more information which can characterize the event in great detail and help to conclude about the nature of the source region, the particle injection, propagation conditions, spatial particle distributions and more. In the following paragraphs, we will discuss the different observations which are available and what can be extracted from these for the interpretation of an event.

In-Situ Observations

Besides energetic particle observations, the solar wind plasma parameters and magnetic field are measured by in-situ instruments. First of all, the measured solar wind speed is used for the backmapping to determine the magnetic footpoint of the spacecraft at the source surface of the Sun (see Section 2.1.1). Furthermore, we gain information on the solar wind stream (slow or fast) the spacecraft was embedded in and can determine if CIR-accelerated particles were present which could influence the SEP measurements. The magnetic field measurements can verify the potential presence of magnetic structures like ICMEs (Interplanetary Coronal Mass Ejections), loops, or magnetic clouds. This is important because strong deviations from the Parker magnetic field structure can strongly change the connectivity to the Sun and the particle propagation. If the magnetic field is for instance especially smooth, one is tempted to conclude that at least locally there might be only minor scattering and vice versa. Interplanetary shocks can also be clearly identified by discontinuities in magnetic field and plasma parameters (see for example Fig. 6 where the two shock waves of a CIR are marked by vertical lines and 'FS' and 'RS' for forward and reverse shock, respectively).
Figure 15 shows an example of an impulsive SEP increase observed by STEREO B

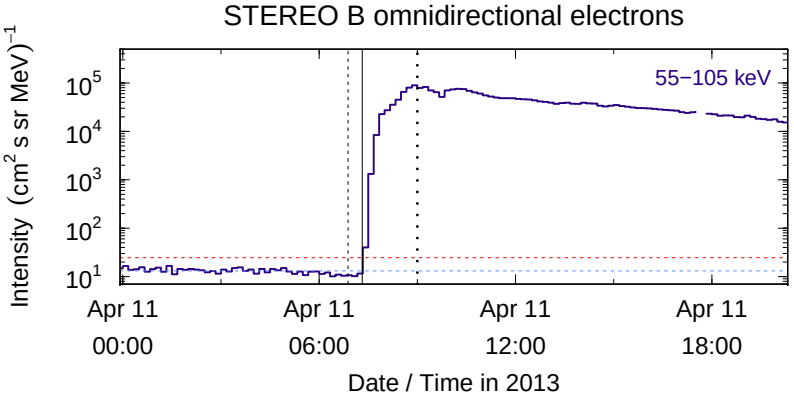

Figure 15: Intensity-time profile of the 11 April 2013 electron event observed by STEREO B / SEPT. The positions of the vertical lines represent the onset time of the associated type III radio burst (dashed), electron onset time at the spacecraft (solid), and the maximum time of the increase (dotted), respectively. The blue horizontal line represents the pre-event background level, while the red horizontal line lies at the background level plus four standard deviations.

on 11 April 2013. The vertical dashed line represents the time of the associated type III radio burst, the solid line marks the onset time of the event, and the dotted line represents the time of the maximum of the increase. The short rise time of the event (from onset to maximum) suggests that the particles were not scattered a lot during their propagation from the Sun to the spacecraft and that a good connection to the source region was present. More scattering would cause a longer rise time, that however, could also be produced by an extended injection. In the case of strong scattering, the SEP onset would be delayed because the actual path

the particles had to propagate would be significantly prolonged. Therefore, the determination of the event onset and comparison with the solar release time (see next section) is of major importance. In the above event, the relatively short onset delay of ∼30 minutes (from type III to electron onset) supports the assumption of a good connection and minor scattering. There are different techniques to identify the onset time of an SEP increase. The event onset marked by the solid vertical line in Fig. 15 was assigned by the sigma-method. This method determines the mean intensity I_0 (marked by the blue horizontal line) and standard deviation σ of the pre-event background. An onset is found if two consecutive points rise above $I_0 + 4\sigma$ (red horizontal line). If the event has a rather gradual increase, the onset determination is more complicated and data averaging is usually needed. Another technique, the CUSUM method (c.f. *Huttunen-Heikinmaa et al.* (2005)), turned out to work more robustly for gradual increases (*Thiel*, 2013). Figure 7 of Publication 1 (see Page 44) illustrates another method: The intensity-time profiles were fitted to exponential functions and the onsets were determined as the times where the fits meet the constant pre-event background.

If it is assumed that particles of all energies are released at the same time into the IP magnetic field during a solar flare event then particles with higher kinetic energies should arrive at the spacecraft earlier than particles with lower energies. If this so-called velocity dispersion is observed, one can extract two quantities by fitting the energy dependent onset times and extrapolating back to infinite velocities: The path length the particles have traveled and the injection time at the Sun. Figure 16 shows an ion spectrogram observed by STEREO B on 12 May 2012

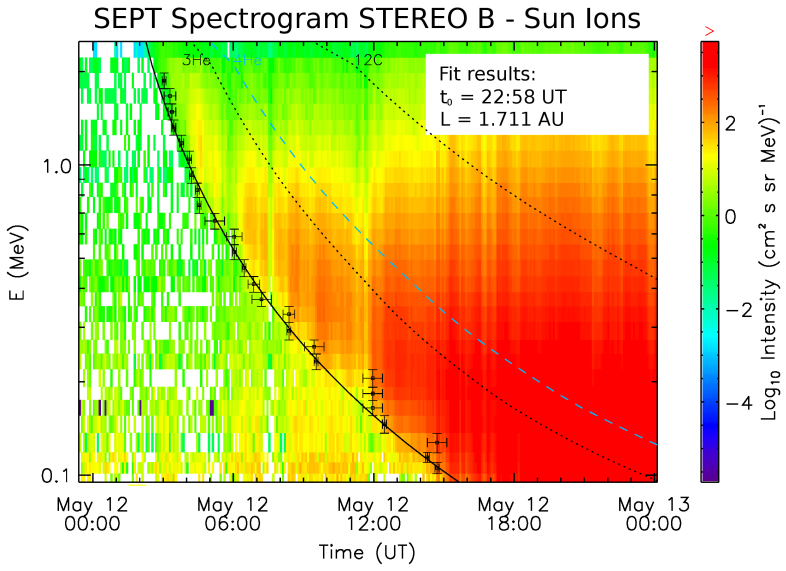

Figure 16: Ion spectrogram observed by STEREO B / SEPT-Sun on 12 May 2012 including a fit to the energy dependent ion onset times.

in the sunward telescope. The velocity dispersion appears as a curved feature, and a fit to the energy depended onset times yields a pathlength of L = 1.7 AU and a solar release time at t_0 =22:58 UT on the previous day. Unfortunately, a clear

velocity dispersion is often not observed for electron events. Due to the rather short onset differences in the energy range of the SEPT telescope of a few minutes, the velocity dispersion can be washed out quickly and cannot be resolved with the instrument resolution anymore.
A further very important parameter is the anisotropy which, in case of SEPs, measures the degree of scattering the particles have experienced (see Section 2.2.1 and Eq. 3). To determine the degree of the particle beaming when arriving at the spacecraft, measurements with different viewing directions must be available. For this purpose, the SEPT instrument provides four identical telescopes on each spacecraft with two of them viewing along the nominal magnetic field line towards and away from the Sun and two of them looking out of the ecliptic plane towards north and south. Because of the gyrotropic propagation of the SEPs, the spatial distribution is described through the pitch angle α of the particles which is the angle between the velocity vector of the particle and the magnetic field vector. An example of intensity- and anisotropy-time series during the 14 August 2010 SEP event is shown in Fig. 8 in Publication 2 (see Page 67) in the second and third panels from the top, respectively.
If all the above parameters are observed from multiple points during the same event, spatial and temporal variations can be analized which is impossible with single-point observations. Furthermore, the source region at the Sun producing the event may not be in the visible hemisphere as observed from a spacecraft detecting the event in-situ. Therefore, well separated spacecraft such as the STEREO satellites in combination with close to Earth observatories can monitor the Sun sufficiently to identify each SEP source region. The various remote-sensing observations which are presently available will be discussed in the next section.

Remote-Sensing Observations

The Sun is observed at many different wavelengths ranging from X-rays over ultraviolet down to the radio range. EUV images which display the chromosphere and corona in different EUV emission lines between $\sim$17 and 30 nm represent specific temperatures. Therefore, certain features and different layers of the chromosphere and corona are imaged. Coronal holes, the source regions of fast solar wind streams, are cold and less dense, and therefore appear as dark regions in EUV images while active regions which are hotter and denser are seen as bright spots. It is often useful to build difference images of two EUV pictures which show the changes from one to the next image. The visibility of certain structures as for example moving fronts disturbing the corona (EUV waves) is then enhanced (see Fig. 12). The electromagnetic radiation of solar flares spans a wide range of energies with some flares even being visible in white light. However, the classification of a flare depicting its strength is only based on its X-ray and H-α intensity. Unfortunately, the STEREO spacecraft lack X-ray telescopes so that a clear flare classification is still only possible if it appears on the visible disk as seen from Earth, where for example GOES can detect it. An attempt to relate the observed EUV intensity in the 195 Å channel of STEREO/EUVI to the X-ray intensity as observed by GOES has been made by *Nitta et al.* (2013).

The solar white-light corona is visible if the light of the solar disk is masked like during a solar eclipse. This is the measurement principle of the so-called coronagraphs which observe CMEs by their Thompson-scattered light up to distances of ∼15 solar radii. From these images its direction, angular width, and velocity can be determined. Page 41 (Fig. 2 to 4 of of Publication 1) illustrates direct as well as difference images of EUV and coronagraph detectors for the 17 January 2010 SEP event.
In association with solar activity radio bursts are observed. The most important types for SEP investigations are the type III and type II radio bursts. Figure 17

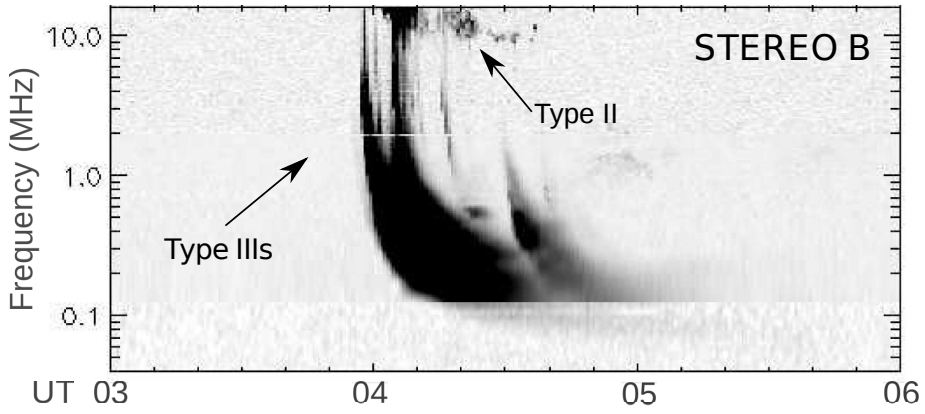

Figure 17: Radio spectrogram as observed by STEREO B / WAVES on 17 January 2010 between 03 and 06 UT. Type III radio bursts as well as a type II burst were observed. Figure adapted from *Dresing et al.* (2012).

shows a radio spectogram observed by STEREO B on 17 January 2010. The structures which quickly drift from high to low frequencies are type III radio bursts and are produced by electrons with energies of a few keV. When these electrons propagate through a plasma, they cause plasma instabilities, so that plasma oscillations are excited (Langmuir waves). These oscillations are transformed into electromagnetic waves which radiate at their characteristic frequency, the electron plasma frequency f_p (fundamental) or multiples of f_p (harmonics), which are detected as radio waves (e.g. *Suzuki* and *Dulk* (1985)). Higher frequencies are, therefore, produced in denser regions than lower frequencies so that the drifting from high to low frequencies can be understood as the electron beam propagating through the corona into the IP medium. The slower drifting structure in Fig. 17 is a so-called type II radio burst and is the signature of a moving shock wave. In this case the electrons which produce the radio signal are accelerated locally at the shock so that the drift velocity of the radio burst corresponds to the shock propagation which usually lies between 200 and 2000 km s^{-1} (*Nelson* and *Melrose*, 1985). However, it is not so straight forward to extract the exact heliocentric distance from the observed frequencies because density models have to be applied. It is plausible that if the type III associated electrons are released from the Sun into the open magnetic field regime, the same is true for the higher energy electrons which we detect as SEP event. Therefore, we assume the onset time of the type III burst at ∼10 MHz to be the solar release time of the SEPs. Often the onset or

maximum time of the solar flare is taken as the solar release time as well which can be up to tens of minutes apart from the type III onset.
To reconstruct the coronal magnetic field structure below the source surface using PFSS models (c.f. Section 2.1.2), line of sight observations of the solar photosphere (magnetograms) are needed as input. Unfortunately, the STEREO spacecraft also lack remote magnetic field measurements of the Sun so that such magnetic field reconstructions are only possible for regions on the visible disk as seen from Earth, where for example the SDO satellite provides high cadence measurements.

Different Approaches

To gain information on the underlying processes determining SEP events or especially wide-spread events, there are two different approaches: A case study or a statistical analysis. Both methods have their advantages. A case study offers the opportunity to perform a much more detailed analysis, and even to compare the observations with the output of a particle propagation model. Such propagation codes (e.g. *Agueda et al.* (2008); *Zhang et al.* (2009); *Dröge et al.* (2010)), however, are often very complex and not openly accessible, and therefore, a collaboration with an expert is needed. Such a case study has been performed in Publication 1. However, one may argue that the results of a case study are not representative for the physical processes of all events. If the event, which was chosen for the detailed analysis, is exceptional for some reasons, it will not represent the common processes determining other events. Although a statistical analysis cannot take into account very fine details, it is well suited to determine the usual ranges of the important parameters and its variations. It also provides the identification of different event types which could indicate the presence of different underlying processes. Publication 2 presents such a statistical investigation of 21 wide-spread events.

3

TEMPORAL AND SPATIAL VARIATIONS OF CIRS

As described in Section 2.1 the interaction between fast and slow solar wind can lead to the formation of shock waves and as a consequence to particle acceleration. While it is generally accepted that fast solar wind streams originate in coronal holes which appear as darker regions in EUV images of the solar corona, the exact source location of the slow solar wind remains unknown. The presence of solar wind streams of different speed and characteristics can build a useful tool. By comparison of in-situ measurements with the remote-sensing observations of the structure of the solar atmosphere, high speed streams can be unambiguously associated to their parent coronal holes when taking into account the solar rotation. If we imagine a solar wind showing always the same speed and characteristics, it would be very complicated to associate to specific source regions at the Sun. Furthermore, the conclusion that the solar wind propagates outward radially with nearly constant speed could not be made without many observational points at different heliocentric distances.

If the sources of fast and slow solar wind at the Sun remain stable, we expect that different observers at the same radial distance observe the same structures although they detect the same CIR at different times and longitudinal locations. But how stable are these structures in reality and which factors can produce variabilities? *Dresing et al.* (2009) show examples of very similar CIR observations at multiple viewpoints in 2007 when Ulysses, located at 1.4 AU, observed the same CIRs as the STEREO and SOHO spacecraft. The authors utilized these measurements to determine a radial gradient of CIR-accelerated ions. However, such stable structures are not always observed but large variabilities in the solar wind structure as detected at different locations have already been reported by *Schwenn* and *Marsch* (1990) who found that already small latitudinal differences of a few degrees in the spacecraft positions can be the cause. These latitudinal differences can have a large impact if a spacecraft is located close to the ecliptic plane where it is alternately connected to positive polarity magnetic fields or negative polarity fields, respectively. Depending on which side a spacecraft is connected to, it may detect a high-speed solar wind stream, a less pronounced high-speed stream, or even just slow solar wind. The influence of latitudinal and longitudinal separations on STEREO observations has been analyzed in *Gómez-Herrero et al.* (2011) (Appendix A). Figure 18 shows the correlation of the time-shifted solar wind speed as measured on STEREO A and STEREO B, respectively. Both time series (shown in the middle panel) have been time-shifted to the L1 position by applying a co-rotation time shift. The top panel shows the latitudinal separation angle in black and the longitudinal separation between the STEREO spacecraft in red, respectively. The bottom panel shows the correlation coefficient c, plotted as 1-c, so that zero means good correlation and larger values denote less correlation. The shape of this curve reflects nicely the spatial separations shown

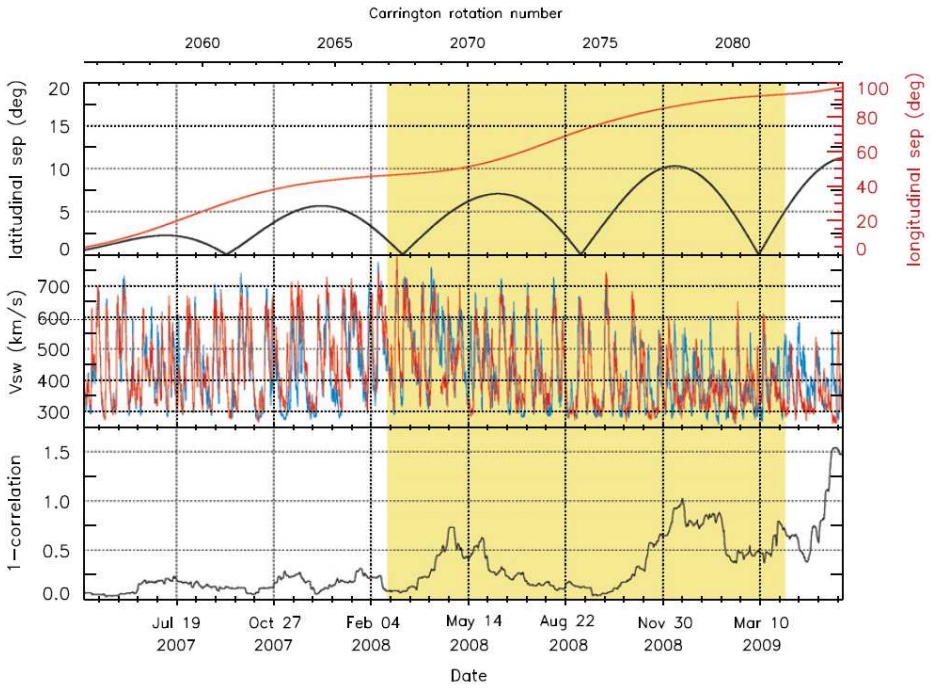

Figure 18: Top panel: Absolute longitudinal (red) and latitudinal (black) separation angles of the two STEREO spacecraft. Middle panel: Solar wind speed measured by STEREO A (red) and STEREO B (blue), both time shifted to the position of L1. Bottom panel: 1-correlation of the solar wind speeds measured by STEREO A and STEREO B (middle panel). This figure was published in *Gómez-Herrero et al.* (2011).

in the top panel: During periods of large latitudinal separations the correlation reduces. Furthermore, on top there is a trend of decreasing correlation during the whole period which agrees with the steadily increasing longitudinal separation of the STEREO spacecraft. The reason why large longitudinal separation yields a lower correlation between the STEREO A and B observations is the temporal change of the source regions at the Sun. The shapes and boundaries of the coronal holes evolve and so the CIRs observed from a single spacecraft may differ from rotation to rotation. The advantage of multiple spacecraft is that coronal hole changes of much shorter time scales can be investigated which is reported in Chapter 2.5 of *Gómez-Herrero et al.* (2011).

A third agent which can account for temporal variability of CIR observations is the presence and possible interaction with transient magnetic structures, e.g interplanetary coronal mass ejections (ICME). *Gómez-Herrero et al.* (2011) show several examples where a transient structure could be identified inside or following a CIR structure at a specific spacecraft while the other spacecraft observe an undisturbed CIR. The spacecraft detecting the transient always observes higher energetic ion fluxes associated with the CIR so that the authors conclude that the presence of the transient may support the acceleration of hundred-keV ions.

These CME-CIR interactions are another illustrative example for the importance

of a multi-spacecraft platform when investigating the longitudinal variation of energetic particles.

4

CASE STUDIES OF SEP EVENTS

Although the increase in solar activity was relatively late and weak in the current solar cycle 24, some interesting events have been detected by the STEREO spacecraft. The first of just two GLE events so far in this cycle occurred on 17 May 2012 and turned out to be a wide-spread SEP event, observed over a longitudinal range of ∼230 degrees (*Heber et al.*, 2013; *Gopalswamy et al.*, 2013). A surprising result was reported by *Wiedenbeck et al.* (2013), who found SEP observations with enhanced ^{3}He at all observing spacecraft which spanned a longitudinal angle of 136 degrees on 7 February 2010. As ^{3}He-rich events were thought to be only associated to solar flares, they were expected to show rather small angular extents. *Wiedenbeck et al.* (2013) propose that there must be processes which are capable of distributing these particles over wider ranges, as for example perpendicular diffusion in the IP magnetic field. *Rouillard et al.* (2012) studied an SEP event from 21 March 2011, and found a relation to the propagation of a so called EUV wave. The authors concluded that the EUV wave is linked to the spread of the SEPs close to the Sun, providing another agent which might be capable of spreading SEPs. Another event on 7 February 2010 was analyzed by *Dröge et al.* (2014) (see Appendix C). By applying two different particle propagation models and comparing with the in-situ observations, the authors conclude that the wide angular SEP spread in this event was most likely produced by a combination of perpendicular transport in the IP medium and a pre-spreading close to the Sun (e.g. coronal transport), respectively. The same analysis tools were applied to the 17 January 2010 event which is presented in the next section and showed an extremely wide SEP spread of ∼360 degrees (*Dresing et al.* (2012)). However, the situation was a different one here, with none of the observing spacecraft being located at a preferable well-connected position and no particle anisotropies being observed. Therefore, the argumentation favored perpendicular transport as the dominant spreading process in this event. The following section presents this publication which was published in the topical issue *The Sun 360* of Solar Physics in 2012. The next paragraph summarizes the key aspects of this publication.

DRESING *et al.* 2012: THE LARGE LONGITUDINAL SPREAD OF SOLAR ENERGETIC PARTICLES DURING THE 17 JANUARY 2010 SOLAR EVENT

Own contribution to the observational part: 80%
The modeling part of this paper was contributed by our collaborators in Würzburg: Wolfgang Dröge and Yulia Kartavykh

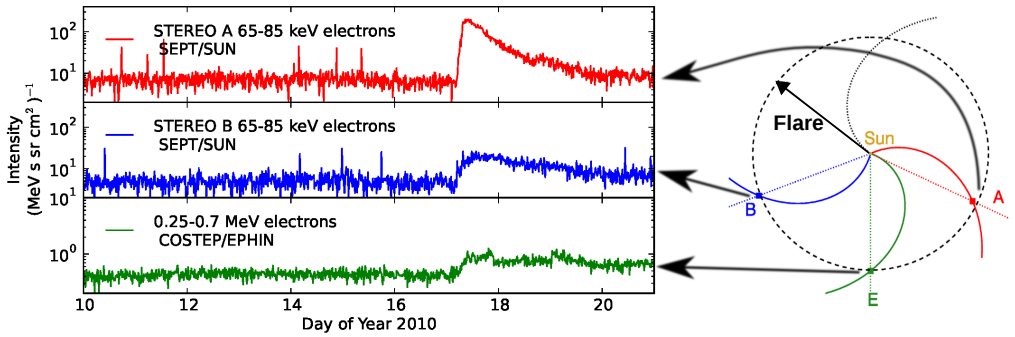

Figure 19: Near-relativistic electron measurements on board STEREO A (red), STEREO B (blue), and SOHO (green) during the 17 January 2010 SEP event. The sketch on the right hand side demonstrates the geometrical configuration of spacecraft positions, magnetic field lines connecting to the Sun and the position of the flaring AR (black arrow). Figure adapted from *Dresing et al.* (2012).

Short Summary of Publication 1

On 17 January 2010 an SEP event was detected on board STEREO A, STEREO B, and SOHO spanning a longitudinal range of 134 degrees. Each of the three spacecraft's magnetic footpoints was separated by more than 100 degrees in longitude from the parent active region. The flare was only on the visible hemisphere for STEREO B, but remained behind the solar limb for STEREO A and SOHO. A direct magnetic connection to the SEP source region could be excluded for each of the three observatories so that strong and efficient perpendicular diffusion is the most likely agent producing the observed wide SEP spread. A 3D propagation model (*Dröge et al.*, 2010) explains the observations well if a large ratio of perpendicular to parallel diffusion coefficients is applied. However, an extended particle spread close to the Sun of 20 degrees in latitude and longitude, respectively, was already assumed by the model and such an extended distribution close to the Sun may play an important role as well. Nevertheless, the final conclusion of the paper is that the efficiency of interplanetary perpendicular transport may vary from event to event, and in the case of the 17 January 2010 SEP event we may observe a case of rather strong lateral transport in the IP medium.

Solar Phys (2012) 281:281–300
DOI 10.1007/s11207-012-0049-y

THE SUN 360

The Large Longitudinal Spread of Solar Energetic Particles During the 17 January 2010 Solar Event

N. Dresing · R. Gómez-Herrero · A. Klassen · B. Heber · Y. Kartavykh · W. Dröge

Received: 10 October 2011 / Accepted: 6 June 2012 / Published online: 3 July 2012

Abstract We investigate multi-spacecraft observations of the 17 January 2010 solar energetic particle event. Energetic electrons and protons have been observed over a remarkable large longitudinal range at the two STEREO spacecraft and SOHO, suggesting a longitudinal spread of nearly 360 degrees at 1 AU. The flaring active region, which was on the backside of the Sun as seen from Earth, was separated by more than 100 degrees in longitude from the magnetic footpoints of each of the three spacecraft. The event is characterized by strongly delayed energetic particle onsets with respect to the flare and only small or no anisotropies in the intensity measurements at all three locations. The presence of a coronal shock is evidenced by the observation of a type II radio burst from the Earth and STEREO-B. In order to describe the observations in terms of particle transport in the interplanetary medium, including perpendicular diffusion, a 1D model describing the propagation along a magnetic field line (model 1) (Dröge, *Astrophys. J.* **589**, 1027 – 1039, 2003) and the 3D propagation model (model 2) by Dröge *et al.* (*Astrophys. J.* **709**, 912 – 919, 2010) including perpendicular diffusion in the interplanetary medium have been applied. While both models are capable of reproducing the observations, model 1 requires injection functions at the Sun of several hours. Model 2, which includes lateral transport in the solar wind, reveals high values for the ratio of perpendicular to parallel diffusion. Because we do not find evidence for unusual long injection functions at the Sun, we favor a scenario with strong perpendicular transport in the interplanetary medium as an explanation for the observations.

The Sun 360
Guest Editors: Bernhard Fleck, Bernd Heber, and Angelos Vourlidas

N. Dresing (✉) · R. Gómez-Herrero · A. Klassen · B. Heber
Institut für Experimentelle und Angewandte Physik, Christian-Albrechts-Universität zu Kiel, Kiel, Germany
e-mail: dresing@physik.uni-kiel.de

Y. Kartavykh · W. Dröge
Institut für Theoretische Physik und Astrophysik, Universität Würzburg, Würzburg, Germany

Y. Kartavykh
Ioffe Physical-Technical Institute, St-Petersburg, Russia

Keywords Solar energetic particles (SEPs) · Propagation · Perpendicular diffusion

1. Introduction

Energetic particle observations in the interplanetary medium provide fundamental information on acceleration processes and transport mechanisms. The well-known picture of impulsive and gradual events developed by Reames (1999) ordered solar energetic particle (SEP) events into two different types: impulsive SEP events were attributed to acceleration in a small-sized reconnection site yielding to narrow longitudinal distributions of SEPs at 1 AU around the nominal magnetic connection, and gradual events were attributed to acceleration in extended sources as coronal or interplanetary shocks. These were supposed to be capable of generating angular SEP distributions of more than 100 degrees from the flare site (Cane and Erickson, 2003; Cliver *et al.*, 2005; Kallenrode *et al.*, 1993). Using single spacecraft observations, Cliver *et al.* (1995) reported an 180 degree wide longitudinal spread of SEPs associated with a backside flare and attributed the observations to a coronal shock, which may have extended up to 300 degrees. Interplanetary shocks at 1 AU have been suggested to be as large as 180 degrees in longitude (Torsti *et al.*, 1999; Cliver and Cane, 1996), providing large acceleration regions as well. Multi-spacecraft investigations have been used for an improved characterization of SEP events. Simultaneous observations by *Helios* or *Ulysses* and the Earth caused a debate on the presence of efficient particle transport perpendicular to the magnetic field. Several authors (Wibberenz and Cane, 2006; Dalla *et al.*, 2003a, 2003b; Cane and Erickson, 2003; McKibben, Lopate, and Zhang, 2001) presented observational and modeling evidence supporting perpendicular transport in the interplanetary medium. However, Sanderson (2003) showed particle anisotropies observed at the onset of large SEP events, which were field-aligned with small or zero flow transverse to the magnetic field, and too small to account for perpendicular transport. Additional observational facts like particle dropout events (Mazur *et al.*, 2000) and nearly scatter-free propagating electron spikes (Klassen, Gómez-Herrero, and Heber, 2011) are difficult to explain in a global transport picture including efficient perpendicular diffusion and point to a complex structure of the interplanetary magnetic field (see, *e.g.*, Borovsky, 2008; Dunzlaff, Kopp, and Heber, 2010).

For an accurate determination of SEP properties as the angular spread, multi-point observations are invaluable, and the *Solar Terrestrial Relations Observatory* (STEREO) mission launched in 2006 has been optimized to perform such multi-point observations. Equipped with remote sensing and *in situ* instruments, it allows one to identify a possible source region of SEPs for nearly all events observed. This was not possible prior to this mission due to the lack of remote sensing instrumentation on board the *Helios* and *Ulysses* spacecraft. Another major advantage is that the radial distance for the STEREO spacecraft and the Earth is approximately the same, which minimizes the influence of varying radial distance on the analysis.

The twin spacecraft of the STEREO mission, equipped with identical instrumentation, perform heliocentric orbits following the motion of the Earth in the ecliptic plane. With one spacecraft moving ahead of the Earth (STEREO-A) and the other trailing behind (STEREO-B), the longitudinal separation between both spacecraft grows at 45 degrees per year while the radial distance to the Sun stays nearly the same at ~ 1 AU. The well-separated STEREO spacecraft offer an excellent platform for multi-point studies of widespread SEP events. On 17 January 2010 the spacecraft were separated by 134 degrees, with the Earth in between, when instruments at all three locations measured enhanced electron and proton fluxes. We identified the source region on the backside of the Sun as seen from Earth

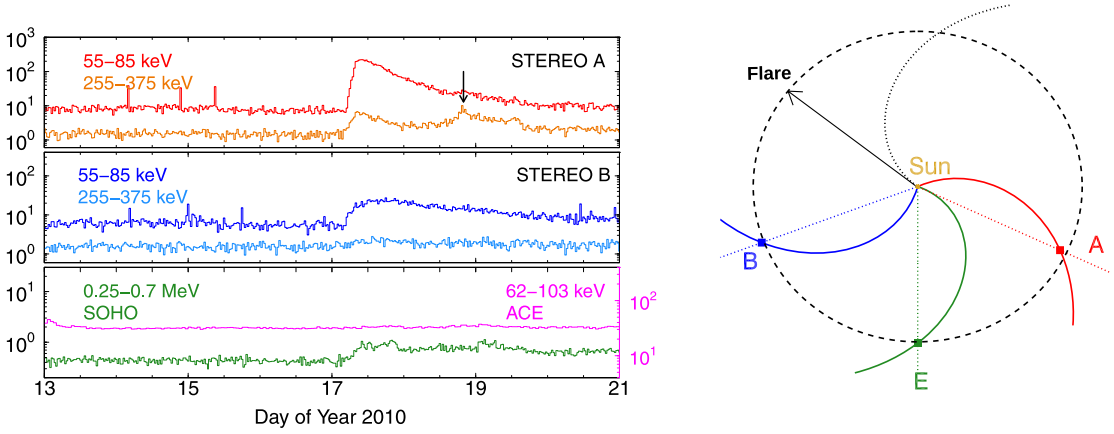

Figure 1 Left: Electron observations by the SEPT sunward pointing telescopes on board STEREO-A (top), and STEREO-B (center), and SOHO/EPHIN and ACE/EPAM (bottom) showing the SEP event on 17 January 2010. The second increase observed by STEREO-A, marked by the arrow, is due to strong ion contamination. Right: Sketch of the longitudinal configuration of the STEREO and SOHO spacecraft with respect to the flare longitude (represented by the black arrow). The spacecraft longitudinal positions are given by colored dotted lines intersecting the dashed 1 AU circle, where blue corresponds to STEREO-B, red to STEREO-A, and green to SOHO/ACE. The magnetic field lines connecting the Sun and the spacecraft are given by the colored spirals and correspond to the measured *in situ* solar wind speed. The black spiral represents the nominal magnetic field line originating from the flare position.

unambiguously at Carrington longitude 54 and −25 degrees latitude. Thus the longitudinal spread of the energetic particles at 1 AU during this event is expected to be larger than 300 degrees. Figure 1 (left) shows measurements at STEREO and ACE / SOHO in approximately the same energy range from ∼50 – 100 keV and ∼250 – 400 keV. The second increase observed by STEREO-A, marked by an arrow, is not real but due to ion contamination. The bottom panel also shows ACE/EPAM (LEFS 60) electron measurements in the range of 62 – 103 keV. Here the event is masked by the high background but appears with more than two sigma when background subtraction is applied (not shown), confirming the SOHO/EPHIN observations. Note, that for the DE channels the event is not seen even with background subtraction. On the right-hand side a sketch shows the longitudinal configuration of the spacecraft with respect to the flare position. In what follows, we discuss the instrumentation as well as the observations, and compare the observations with results of a solar energetic particle transport code (Dröge *et al.*, 2010).

2. Instrumentation

In this work, we use energetic particle measurements by the Low Energy Telescope (LET: Mewaldt *et al.*, 2007), the High Energy Telescope (HET: Von Rosenvinge *et al.*, 2007), and the Solar Electron and Proton Telescope (SEPT: Müller-Mellin *et al.*, 2007) contained in the *In situ* Measurements of Particles and Coronal mass ejection Transients (IMPACT) instrument suite (Luhmann *et al.*, 2007) on board the STEREO spacecraft. The SEPT instrument measures electrons in the range of 30 – 400 keV and nuclei from 60 – 7000 keV/n, each in four viewing directions: to the north (NORTH), to the south (SOUTH), along the Parker spiral to the Sun (SUN), and away from the Sun (ANTISUN). The Sun Earth Connection Coronal and Heliospheric Investigation (SECCHI: Howard *et al.*, 2008) provides remote sensing observations of the Sun with the Extreme Ultraviolet Imager (EUVI: Wuelser, 2004) as well

as coronagraphic observations (COR1 and COR2 instruments), which allow one to link *in situ* observations with the associated regions of solar activity.

In this work, the STEREO observations are complemented by *Solar and Heliospheric Observatory* (SOHO) and *Advanced Composition Explorer* (ACE) measurements. The *Electron, Proton, and Alpha Monitor* (EPAM) on board ACE measures the flux and direction of ions greater than 0.2 MeV to 93 MeV (Gold *et al.*, 1998). The *Electron Proton Helium Instrument* (EPHIN: Müller-Mellin *et al.*, 1995) on board SOHO measures energetic electrons and protons; remote sensing observations are performed by the *Extreme Ultraviolet Imaging Telescope* (EIT: Delaboudinière *et al.*, 1995) and the *Large Angle and Spectrometric Coronagraph* (LASCO: Brueckner *et al.*, 1995). Signatures of radio bursts are detected with the WAVES instrument on board *Wind* (Bougeret *et al.*, 1995) and the STEREO/WAVES instruments (Bougeret *et al.*, 2008). Solar wind plasma and interplanetary magnetic field data are provided by the STEREO/*Plasma and Suprathermal Ion Composition* (PLASTIC: Galvin *et al.*, 2008) and STEREO/MAG (Acuña *et al.*, 2007) instruments, respectively.

3. Observations

In this section, we first present the remote sensing observations (Section 3.1) followed by the *in situ* measurements (Section 3.2). We then describe the interplanetary (plasma and magnetic field) context in Section 3.3.

3.1. Remote Sensing Observations

On 17 January 2010 active region (AR) 11039, which recurred in the following rotation as AR 11041, produced a flare. The flare was first detected with the 171 Å band of the EUVI instrument on board STEREO-B at 3:49 UT. As shown in Figure 2 (left), the eruption site was located at E59 S25 as seen from STEREO-B, which corresponds to $\sim$37 degrees behind the east limb as seen from Earth. Only one other AR has been observed at this time from STEREO-A and the Earth (see AR2 in Figure 3) showing no significant activity during this period. Extreme ultraviolet (EUV) and coronograph observations by STEREO-B show a large-scale dome-shaped expanding coronal EUV wave with perfectly connected off-limb and on-disk signatures as reported by Veronig *et al.* (2010) and Grechnev *et al.* (2011). An EUV wave propagating toward the north-western direction is shown in the difference image in Figure 2 (right) adapted from Veronig *et al.* (2010). The yellow lines show the propagation of the front in five minute steps. The blue star slightly outside the figure represents the position of the STEREO-B magnetic footpoint. While the flare and EUV wave were observed only by STEREO-B, a coronal mass ejection (CME), directed slightly southward, was observed by all three viewpoints as displayed in Figure 4 (adapted from the COR1 CME catalog[1] and the SOHO/LASCO catalog).[2] As reported in the STEREO COR1 CME catalog, the CME was seen in the SE direction from STEREO-B and in the SSW direction from STEREO-A, respectively, with first appearance in the COR1 fields of view at 4:10 UT. The SOHO/LASCO CME catalog reports a partial halo CME appearing in the C2 field of view at 4:50 UT with a linear fit speed of 350 km s^{-1}, a central angle of 114 degrees, and an angular width of 126 degrees.

[1] http://cor1.gsfc.nasa.gov/catalog/.

[2] http://cdaw.gsfc.nasa.gov/CME_list/.

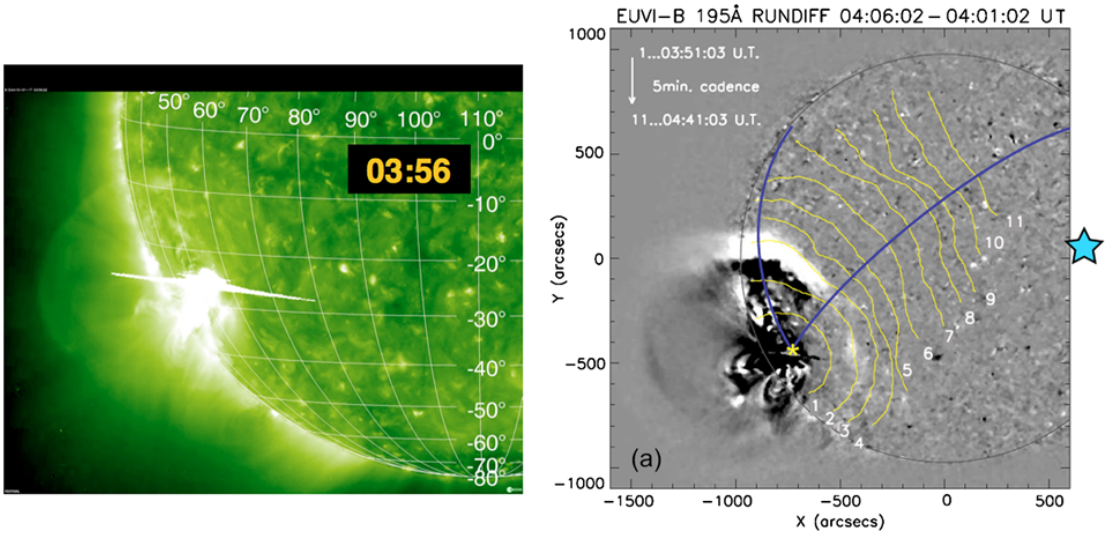

Figure 2 STEREO-B EUVI 195 Å observations. Left: The flare maximum on 17 January 2010 at 3:56 UT. Right: Five-minute running difference image showing the EUV wave (adapted from Veronig *et al.*, 2010, reproduced by permission of the AAS). The yellow lines mark the visually identified outer edges of the wavefronts. The blue star slightly outside the figure represents the position of the STEREO-B magnetic footpoint.

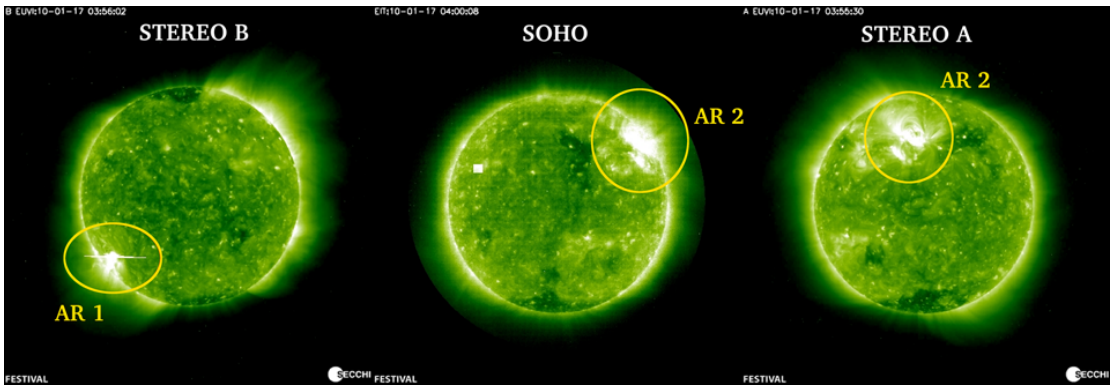

Figure 3 From left to right: EUV observations by STEREO-B, SOHO, and STEREO-A during the flare time on 17 January. Two different active regions were observed at the Sun, labeled "AR 1" (NOAA AR 11039) and "AR 2" (NOAA AR 11040), respectively. The flare was only seen in AR 1 by STEREO-B.

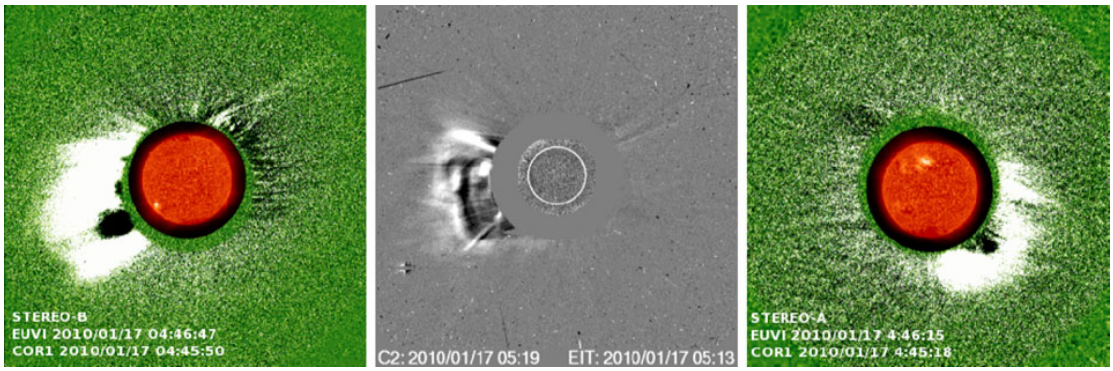

Figure 4 STEREO and SOHO observations of the CME on 17 January 2010 provided by the CME catalogs http://cor1.gsfc.nasa.gov/catalog/ and http://cdaw.gsfc.nasa.gov/CME_list/. Left: STEREO-B EUVI and COR1, center: SOHO/LASCO, right: STEREO-A EUVI and COR1. To increase the visibility of the CME, the coronograph observations are shown as difference images.

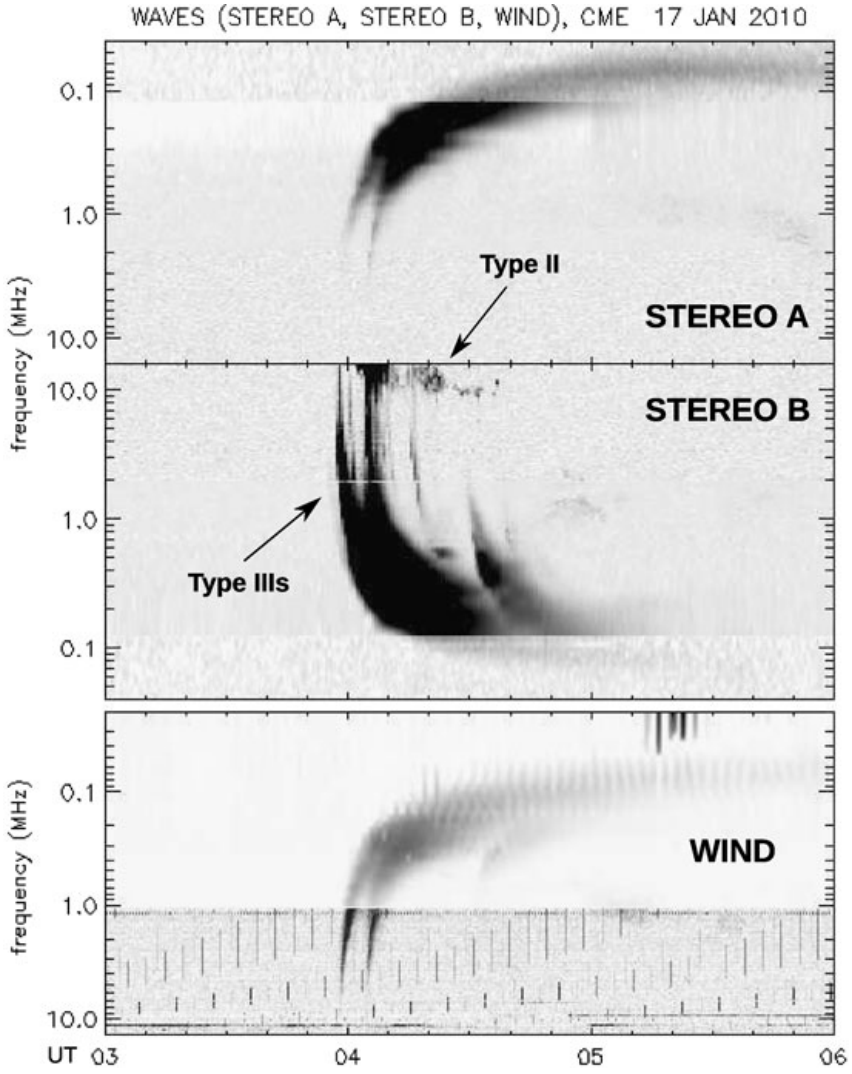

Figure 5 Radio spectrograms recorded by the SWAVES instruments on board STEREO-A (top), STEREO-B (middle), and *Wind*/WAVES (bottom) provided by the Meudon Radio Monitoring Survey (http://secchirh.obspm.fr/select.php).

Figure 5 shows dynamic spectra of radio waves detected on board STEREO-A (top), STEREO-B (center), and *Wind* (bottom), provided by the Meudon Radio Monitoring Survey.[3] Type III radio bursts were observed between 3:58 – 4:28 UT by all three spacecraft accordingly with the flare time at 3:49 UT. Their high frequency part in the STEREO-A and *Wind* spectrograms show a clear attenuation. This is also in agreement with the relative positions of the AR 11039 and presumably of the type III sources) of about 77 degrees behind the west limb for STEREO-A, and 37 degrees behind the east limb for *Wind*. A type II radio burst indicating the presence of a coronal/IP shock was detected at STEREO-B from 4:02 to 4:37 UT, visible in Figure 5, second panel, and has also been reported by the ground-based radio observatory HiRAS from 3:51 to 3:58 UT in the range of 310 – 80 MHz. Grechnev *et al.* (2011) concluded that "the EUV wave most likely was a near-surface trail of a large-scale coronal MHD wave" and that "the shock was weak to moderate." The figure shows no

[3] http://secchirh.obspm.fr/select.php.

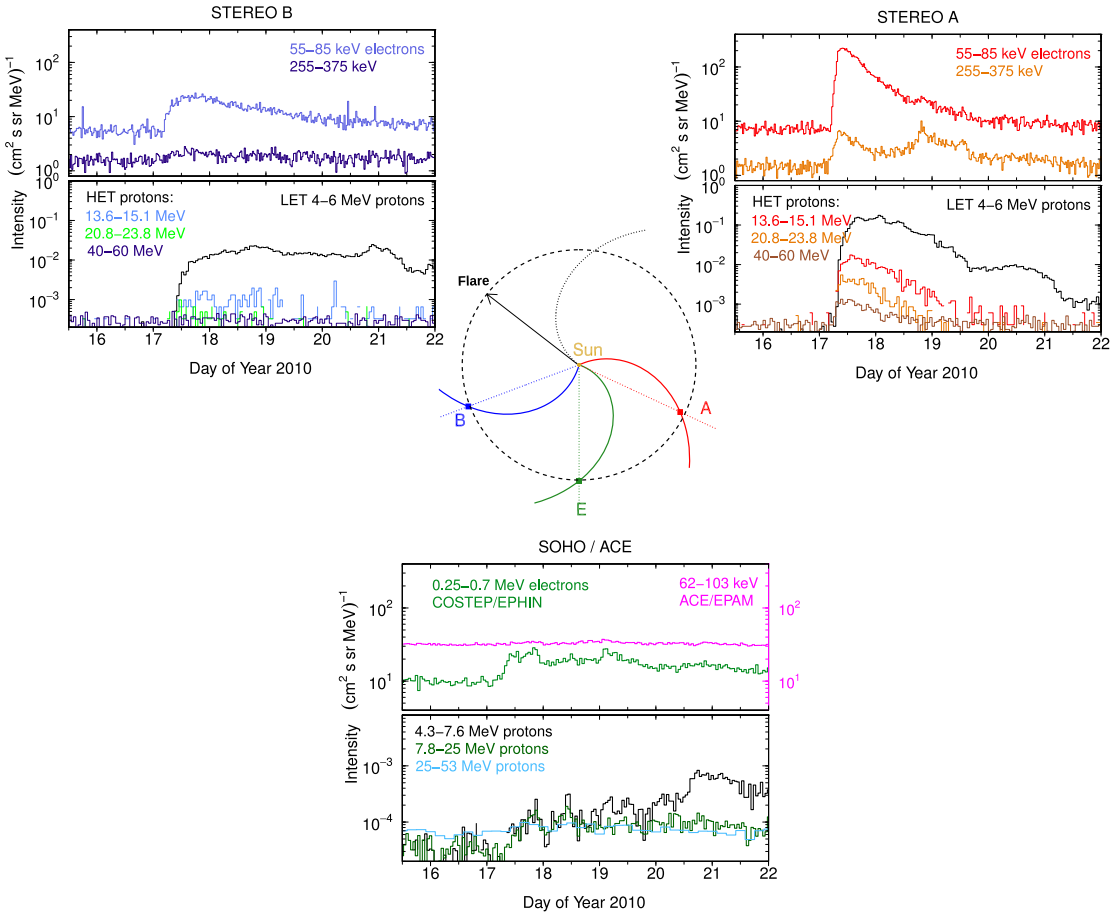

Figure 6 Sketch of the longitudinal configuration of the STEREO and SOHO spacecraft with respect to the flare longitude as in Figure 1. The sketch is surrounded by electron (top panels) and proton (bottom panels) measurements by the SEPT, LET, and HET instruments on board STEREO-B (left), STEREO-A (right), and SOHO/EPHIN and ACE/EPAM (bottom).

further radio activity detected hours before and after the event. Consequently, the combination of radio and EUV observations by the three viewpoints discards the presence of another source region apart from the one (AR 11039) clearly seen on the visible disk for STEREO-B. Other eruptive events from the same AR can be excluded by the absence of further type III bursts for more than seven hours around the investigated event.

3.2. *In Situ* Observations

On 17 January 2010 STEREO-B was located 69.2 degrees behind the Earth and SOHO longitude, and STEREO-A was 64.7 degrees ahead of it. The configuration of the three spacecraft and the flare position is sketched in Figure 6 (center). Dashed colored lines and the black arrow mark the longitudinal positions of the spacecraft and the flare, respectively. The spiral lines represent the connecting magnetic field lines between the spacecraft and the Sun using the measured solar wind speed, and the black spiral is the nominal magnetic field line connecting to the AR. The dashed black circle indicates a 1 AU distance to the Sun. The longitudinal separation between the spacecraft magnetic footpoint, consistent with the solar wind speed measured *in situ*, and the flare position is about 113 degrees for STEREO-B, 117 degrees for STEREO-A, and 161 degrees for SOHO. The top panels of the three plots surrounding the sketch in Figure 6 show electron time profiles by the sunward pointing SEPT

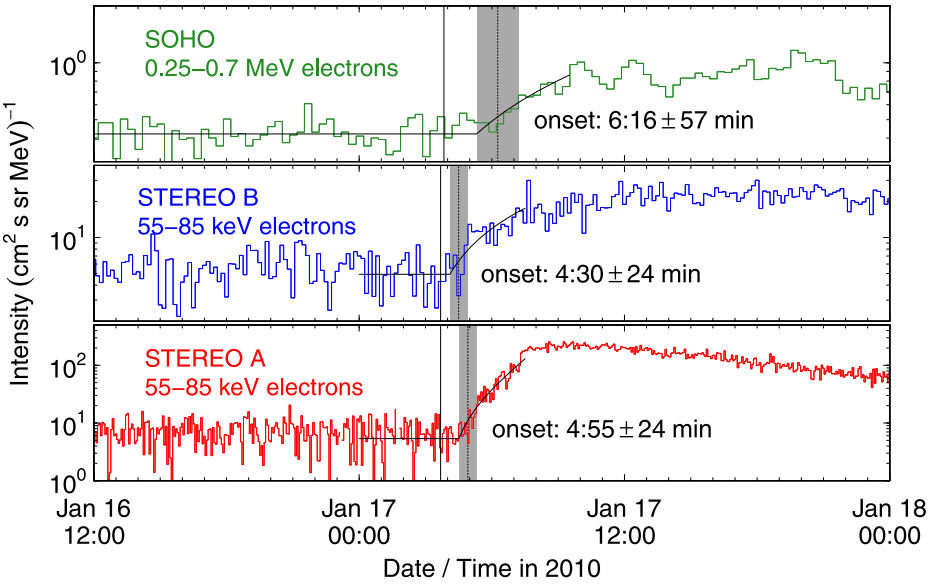

Figure 7 Electron measurements and onset times (vertical dashed lines) at STEREO-A (bottom), STEREO-B (center), and SOHO (top). The gray shadow represents the range of uncertainty, and the solid black line marks the flare onset time (shifted by 8 minutes light travel time). Due to poor statistics, the data had to be averaged before determining the onset times by 4 minutes for STEREO-A, 10 minutes for STEREO-B, and 20 minutes for SOHO.

telescopes on board STEREO-B (left) and STEREO-A (right) in the energy range from 65 to 85 keV, and by the SOHO/EPHIN instrument in the lowest available energy channel ranging from 250 to 700 keV, as well as the ACE/EPAM instrument (bottom). Energetic proton measurements in the range from 4 to 60 MeV taken by the LET and HET instruments on board the two STEREO spacecraft and protons in the range from 4 to 25 MeV measured by the SOHO/EPHIN instrument are displayed in the bottom panels.

The particles arrive at all three spacecraft delayed with respect to the flare onset (which is taken as the first optical (EUV) flare observation at 3:41 UT) with at least 49 minutes (STEREO-B) delay for < 100 keV electrons. Figure 7 shows electron measurements at the three spacecraft. The electron onset times of the event are indicated by dashed lines in the center of the gray shadow. The onset time of the flare at 3:41 UT is presented by the solid black line and has been corrected by eight minutes light travel time. The gray shadow illustrates the range of uncertainty for the specific onset time defined as the range between a lower and an upper limit for the onset time. The upper limit is the first time when the electron flux exceeds the pre-event mean flux by at least three standard deviations and continues above that value for at least two consecutive intervals. The lower limit was determined by fitting the data with the function

$$I(t) = I_0 + A \cdot \mathrm{e}^{B(t-t_0)} \tag{1}$$

with free parameters I_0, A, B and onset time t_0. While the fit retained relatively stable for the STEREO-A data, it was very sensitive to the fitting window for STEREO-B and SOHO data due to the poor statistics. Therefore, an additional inspection by eye was needed to verify the specific fit parameters. The fits are also included in the figure. While the electron onset times at both STEREO spacecraft are nearly simultaneous within the range of uncertainty, there is a larger delay for the SOHO electrons. An onset analysis has also been applied to the 4 – 6 MeV protons as measured by the LET instruments on board STEREO. In contrast to the

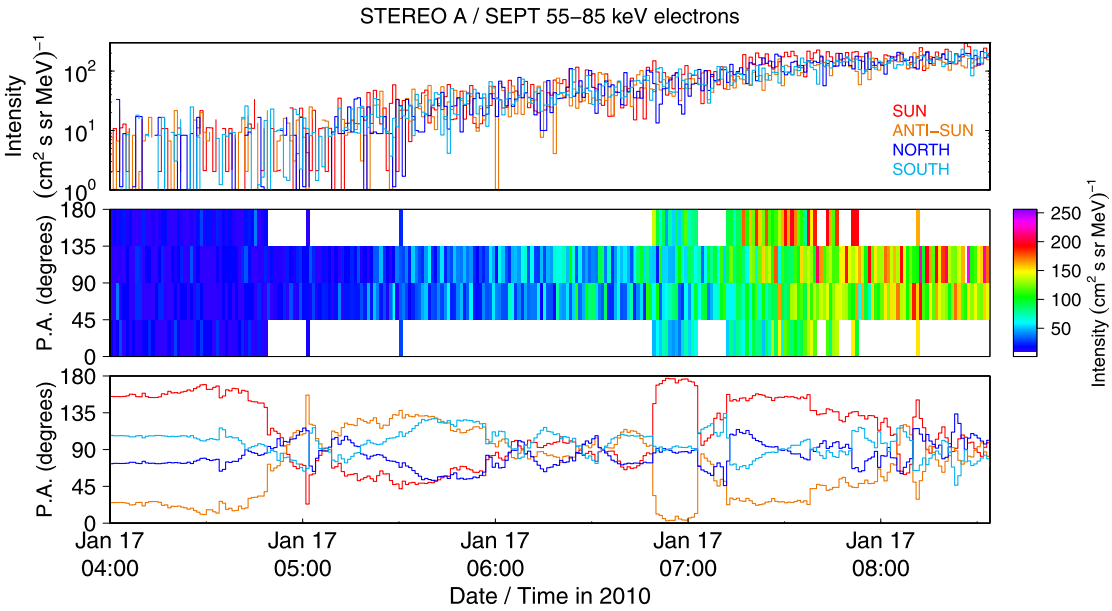

Figure 8 From top to bottom: STEREO-A 55 – 85 keV electrons in all four viewing directions of the SEPT instrument, 3D pitch angle distribution, and pitch angles of each of the four SEPT sensors. Note that white spaces in the center panel denote sectors with no pitch angle coverage.

nearly simultaneous electron onset, the protons arrive at least one hour later at STEREO-B compared to STEREO-A (not shown). Figure 8 (top) shows 65 – 75 keV electrons measured by SEPT A in all four viewing directions. The center and bottom panels of Figure 8 show the three-dimensional (3D) pitch angle distribution and pitch angles of each SEPT sensor, respectively. Clearly, the pitch angle coverage, especially during the onset of the event, is poor. During these periods no clear statement on the anisotropy can be made. Later phases of the event, when the pitch angle coverage is better, show only a small anisotropy. A velocity dispersion analysis for STEREO-A gave no clear results, while the STEREO-B and SOHO statistics did not allow this analysis.

Table 1 summarizes the observations made by the STEREO spacecraft and observers at Earth, SOHO, or *Wind*, respectively as presented so far. Onset times of flare, radio bursts, and energetic electrons (T_o) at the spacecraft as well as longitudinal separations between flare site and spacecraft or spacecraft magnetic footpoints ($\Delta\theta$ and $\Delta\varphi$, respectively) are listed. The time delays between flare and electron onset times Δt as well as the travel times of the electrons along a nominal Parker spiral t_{travel} are included. Information on SEP anisotropies and velocity dispersion is listed, and the spectral indices γ for electrons in the range of 65 to 195 keV for a period of 30 minutes during the maximum time of the event are listed as well. With $\gamma = -2.0 \pm 0.1$ STEREO-B shows a harder spectrum compared to STEREO-A with $\gamma = -2.20 \pm 0.03$.

3.3. Interplanetary Context

Figure 9 shows *in situ* measurements by STEREO-B (left) and STEREO-A (right) from 1 January to 23 January 2010. The two top panels, presenting < 100 keV electrons and 4 – 60 MeV protons, respectively, clearly show the 17 January 2010 SEP event. Below, the azimuthal and latitudinal magnetic field angles, the magnetic field magnitude, and the solar wind speed are displayed. The red/green colored band at the bottom of each plot indicates the *in situ* magnetic field polarity where red is negative and green is positive polarity. During

Table 1 Summary of the observations. Onset times of flare, radio bursts, and first appearance of CMEs have been shifted by −8.3 minutes to correct from light travel time. If a column is empty, the feature has not been observed by the spacecraft. $\Delta\theta$ and $\Delta\varphi$ represent the longitudinal separations between flare and spacecraft longitude as well as between flare and spacecraft magnetic footpoint (taking into account the measured solar wind speed), respectively. A minus indicates that the flare is located eastward of the spacecraft. The heliographic (HG) latitude of the spacecraft is displayed as well. Electron onset times in the energy range from 55 – 85 keV for STEREO and 0.25 – 0.7 MeV for SOHO are indicated by T_o, and Δt is the time delay between these onset times and the flare onset. t_{travel} is the expected electron travel time along a nominal Parker spiral of 1.2 AU length. Anisotropy and velocity dispersion information regarding electron and proton measurements and the spectral index γ during the maximum of the event (for electrons only) are also listed.

	STEREO-B	STEREO-A	Earth(E)/SOHO(S)/*Wind*(W)
Flare onset	3:41 UT	–	–
Type II onset	< 3:54 UT	–	< 3:43 UT (E)
Type III onset	< 3:50 UT	< 3:51 UT	< 3:50 UT (W)
CME	4:02 UT	4:02 UT	4:42 UT (S)
$\Delta\theta$	−59°	173°	−128°
$\Delta\varphi$	−113°	117°	−161°
HG latitude	3.740	−7.060	−4.753
T_o (UT)	$4:30 \pm 24$ min	$4:55 \pm 24$ min	$6:16 \pm 57$ min (S)
Δt	49 min	74 min	∼ 2.5 h
t_{travel}	∼ 20 min	∼ 20 min	∼ 11 min
SEP anisotropy	unclear	small	too poor statistics
Velocity dispersion	too poor statistics	unclear	too poor statistics
Spectral index γ	-2.0 ± 0.2	-2.20 ± 0.03	no overlap with STEREO range

the SEP event, STEREO-B stands in a positive polarity magnetic sector, while STEREO-A and the Earth (not shown) are in a negative magnetic sector. Figure 10 shows a potential field source surface (PFSS) Carrington map overlying a magnetogram map of Carrington rotation 2092 provided by the Global Oscillation Network Group (GONG).[4] The blue wavy line represents the neutral sheet separating the negative polarity sector, with the uppermost closed magnetic field lines marked in red, from the positive polarity sector marked in green. The projected positions of the spacecraft have been added as open circles while the positions of the magnetic footpoints of the spacecraft (always to the right) are represented by the filled circles. The AR producing the 17 January event is seen in the bottom left part of the map in a positive polarity magnetic sector. The STEREO *in situ* measurements in Figure 9 show some minor compression regions caused by stream interactions but no completely evolved corotating interaction regions (CIRs) with shocks. The small gray bar on 20 January in the STEREO-B plot in Figure 9 indicates a magnetic cloud possibly associated with the CME from the 17 January event. According to the STEREO COR1[5] and LASCO[6] CME catalogs, at least five CMEs were present in the interplanetary medium between the Sun and 1 AU when the 17 January SEP event occurred. These CMEs had mostly small angular widths and low velocities. According to Jian *et al.*[7] no shocks were observed *in situ* by the STEREO spacecraft during January 2010.

[4] http://gong.nso.edu/.

[5] http://cor1.gsfc.nasa.gov/catalog/.

[6] http://cdaw.gsfc.nasa.gov/CME_list/.

[7] http://www-ssc.igpp.ucla.edu/forms/stereo/stereo_level_3.html.

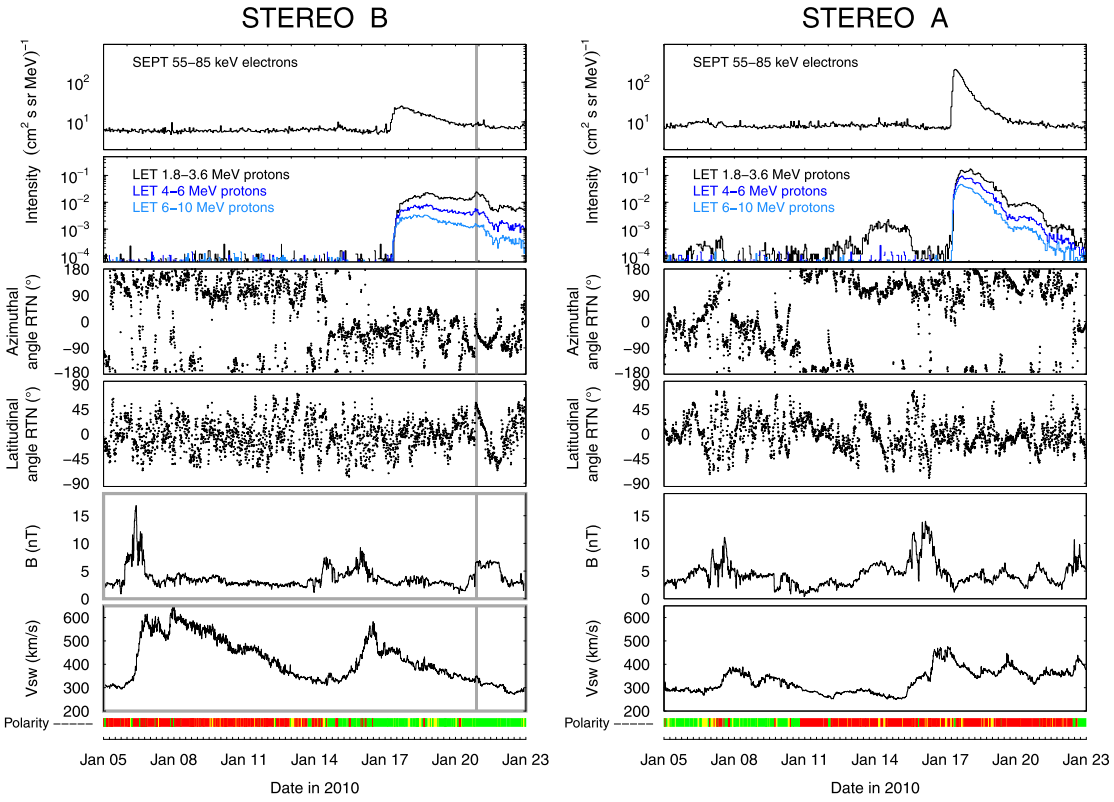

Figure 9 *In situ* measurements by STEREO-B (left) and STEREO-A (right). From top to bottom: Electron intensities, proton intensities, magnetic field azimuthal and latitudinal angles, magnetic field magnitude, and solar wind speed. The gray-shaded bar indicates a magnetic cloud measured by STEREO-B on 20 January at 20:20 UT. The colored bar at the bottom of each plot represents the measured magnetic field polarity with negative polarity in red and positive polarity in green.

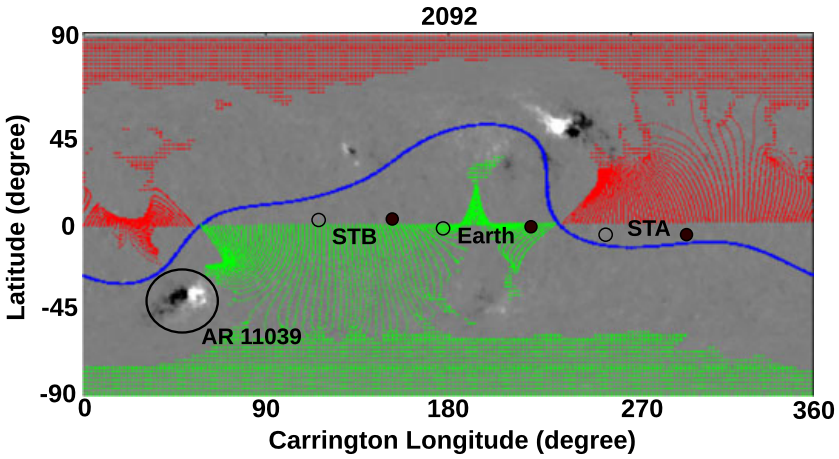

Figure 10 Synoptic ecliptic-plane field plot overlying a GONG-provided magnetogram map for Carrington rotation 2092. The projected positions of STEREO-B (STB), STEREO-A (STA), and the Earth have been added as open circles, while the positions of the magnetic footpoints of the spacecraft are given by filled circles always to the right.

4. Simulations

4.1. The 3D Transport Model

The appearance of solar particle events observed in the near-Earth environment reflects the combination of a number of physical processes. For particles originating from solar flares these processes include acceleration in the flaring region, some kind of lateral transport in the solar corona to a magnetic field line connected with the observer, and transport in the solar wind. In the undisturbed solar wind, *i.e.*, in the absence of CMEs and shocks, the latter can usually be described as adiabatic motion along the average interplanetary magnetic field represented by an Archimedean spiral, and pitch angle scattering off the fluctuations superimposed on the field. Diffusion perpendicular to the magnetic field is caused by interactions with fluctuations which scatter the particles' gyrocenter from one field line to another and by the combined effects of parallel transport and field line mixing (*cf.* Jokipii, 1966; Jokipii and Parker, 1969; Ragot, 1999). Transport perpendicular to the average field (called corotation) also arises due to the action of an induced electric field, $\boldsymbol{E} = \boldsymbol{V}_{\mathrm{sw}} \times \boldsymbol{B}$, where $\boldsymbol{V}_{\mathrm{sw}}$ is the solar wind velocity and $\boldsymbol{B}$ denotes the magnetic field. Depending on the particle species and energy, convection and energy losses in the interplanetary medium can also be important for the transport process. In the most general case the quantitative treatment of the evolution of the particle's gyro-averaged phase space density $f(\boldsymbol{r}, \mu, p, t)$ (which is proportional to the observed particle flux) at the location $\boldsymbol{r}$ can be cast into the form (*cf.* Dröge *et al.*, 2010 for details):

$$\frac{\partial f}{\partial t} = -\mu v \boldsymbol{b} \cdot \nabla f - \frac{1-\mu^2}{2L} v \frac{\partial f}{\partial \mu} + \frac{\partial}{\partial \mu}\left(D_{\mu\mu}(\mu) \frac{\partial f}{\partial \mu} \right) + q(\boldsymbol{r}, \mu, p, t) \tag{2a}$$

$$- (\boldsymbol{V}_{\mathrm{sw}} + \boldsymbol{V}_{\mathrm{d}}) \cdot \nabla f - \left[\frac{\mu(1-\mu^2)}{2} (\nabla \cdot \boldsymbol{V}_{\mathrm{sw}} - 3\boldsymbol{bb} : \nabla \boldsymbol{V}_{\mathrm{sw}}) \right] \frac{\partial f}{\partial \mu} \tag{2b}$$

$$+ \left[\frac{1-\mu^2}{2} (\nabla \cdot \boldsymbol{V}_{\mathrm{sw}} - \boldsymbol{bb} : \nabla \boldsymbol{V}_{\mathrm{sw}}) + \mu^2 \boldsymbol{bb} : \nabla \boldsymbol{V}_{\mathrm{sw}} \right] p \frac{\partial f}{\partial p} \tag{2c}$$

$$+ \nabla \cdot (\boldsymbol{K}_{\perp} \nabla f). \tag{2d}$$

Here v is the particle speed, $\mu = \cos\vartheta$ the particle pitch angle cosine, t the time, and $\boldsymbol{b} = \boldsymbol{B}/B$ a unit vector in the direction of the average magnetic field $\boldsymbol{B}$. The focusing of particles due to the divergence of the magnetic field is described by $L(\boldsymbol{r}) = -(\boldsymbol{b} \cdot \nabla \ln B(\boldsymbol{r}))^{-1}$, and the stochastic forces are taken into account through the pitch angle diffusion coefficient $D_{\mu\mu}(\mu)$ and the tensor $\boldsymbol{K}_{\perp}$ which describes the diffusion of particles in the two dimensions perpendicular to the average magnetic field direction. The injection of particles close to the Sun is given by $q(\boldsymbol{r}, \mu, p, t)$.

As analytical solutions of transport equations for the pitch angle-dependent phase space density are not known, numerical methods must be applied. Finite difference (FD) schemes have been used for this purpose since the 1980s, and more recently Monte Carlo (MC) simulations have been employed to solve the corresponding stochastic differential equations (SDEs).

In this work we use two different techniques to model the particle transport (they will be called model 1 and model 2, respectively). Both approaches assume an Archimedean spiral magnetic flux tube connecting the Sun and the spacecraft, consistent with the solar wind speed measured *in situ*. Also, they assume that the effects of energy losses and of convection are small for the near-relativistic electrons considered here, and can be neglected.

4.2. Model 1 – No Perpendicular Diffusion in the Solar Wind

The first model is based on an FD scheme (see, *e.g.*, Dröge, 2003). This model also neglects the effects of diffusion perpendicular to the average magnetic field and instead assumes that there is no variation across the magnetic field, and that the respective solutions are identical in neighboring flux tubes. In this case all relevant effects are contained in Equation (2a), which is solved for a fixed energy, corresponding to the midpoint of the energy interval under consideration. The lateral spread of the electrons is assumed to occur in the corona, and the injection on the field line connected to the observing spacecraft at a distance of $r = 0.05$ AU is described by $q(\boldsymbol{r}, \mu, p, t)$.

When modeling time profiles of solar particle events with solutions of the transport equation in order to derive transport parameters, it is important not only to fit the isotropic part of the distribution function, but also to make use of the information contained in its angular dependence. A first-order anisotropy parallel to the magnetic field can be defined as

$$A_{\mathrm{p1}} = \frac{3\int_{-1}^{+1} \mathrm{d}\mu\, \mu f(\mu)}{\int_{-1}^{+1} \mathrm{d}\mu\, f(\mu)}. \tag{3}$$

If the scattering is sufficiently strong, $f(\boldsymbol{r}, \mu, t)$ adjusts rapidly to a nearly isotropic distribution, and the solutions of Equations (2a), (2b) become similar to those of a spatial diffusion model. The mean free path $\lambda_{\parallel}$, which relates the pitch angle scattering rate to the spatial diffusion parallel to the ambient magnetic field, is given by

$$\lambda_{\parallel} = \frac{3v}{8} \int_{-1}^{+1} \mathrm{d}\mu \frac{(1-\mu^2)^2}{D_{\mu\mu}(\mu)}. \tag{4}$$

The parallel mean free path, related to the parallel diffusion coefficient by $K_{\parallel} = v/3 \cdot \lambda_{\parallel}$, is often used as a convenient parameter to characterize the varying degrees of scattering from one solar particle event to another, even when it adopts values close to or larger than the observer's distance from the Sun and the transport process cannot be considered as spatial diffusion.

Figure 11 (left) shows a fit obtained from the FD model to the 65 – 105 keV electron observations on STEREO-A. Unfortunately, at the onset of the event, when the anisotropy usually reaches a maximum, the pitch angle coverage of the instrument was not favorable (see Figure 8). No clear anisotropy profile suitable for the modeling could be derived. The data indicate that the anisotropy was small throughout the event, not exceeding a value of 0.4 or so. Under this restriction, a reasonably good fit was achieved assuming a radially constant mean free path of $\lambda_{\mathrm{r}} = 0.07$ AU and the injection profile shown in the upper panel.

Similarly, a fit to the electron observations on STEREO-B was obtained assuming a radially constant mean free path of $\lambda_{\mathrm{r}} = 0.1$ AU. The injection profiles derived for the STEREO-A and STEREO-B observations are much longer than what is usually observed for electrons in this energy range. But because of the large angular distance the particles have to propagate in the 17 January 2010 event, which is, according to this model, in the solar corona, these findings might not be unrealistic.

4.3. Model 2 – Perpendicular Diffusion in the Interplanetary Medium

For an alternative interpretation, we consider a second model which assumes that the particles are released from a source region with a width of 20 degrees in longitude and latitude,

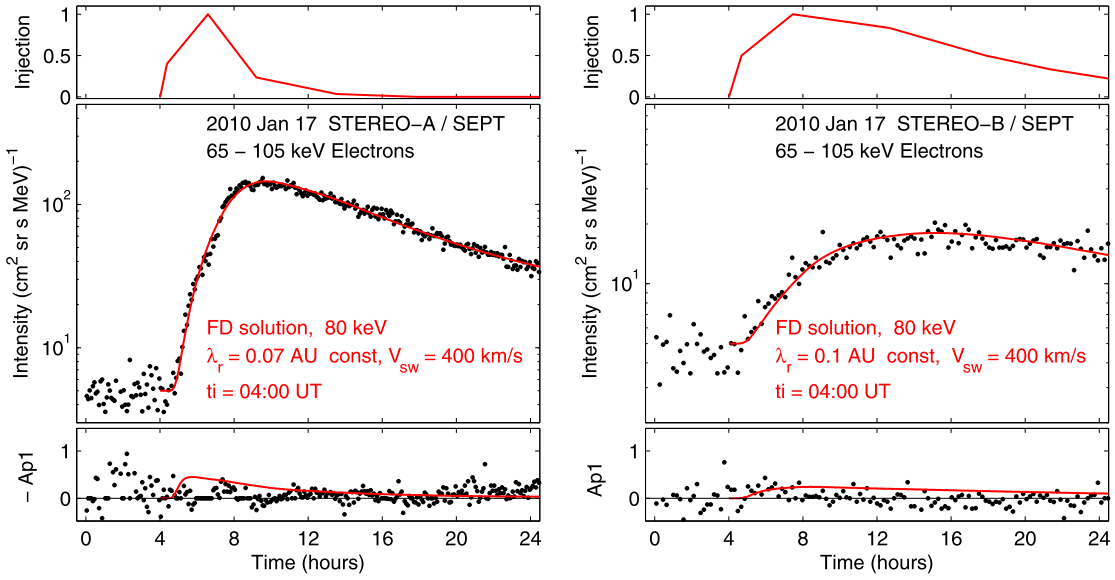

Figure 11 Fits obtained from the FD model to the omnidirectional intensity-time and anisotropy-time profiles of 65 – 105 keV electrons observed by STEREO-A (left) and STEREO-B (right). The top panel shows the derived injection functions.

centered at the location of the optical flare. No coronal propagation is assumed; instead any lateral transport occurs due to diffusion of the electrons in the interplanetary medium perpendicular to the ambient magnetic field. The model is based on a Monte Carlo solution of the stochastic differential equations corresponding to Equations (2a), (2b) (*cf.* Dröge *et al.*, 2010). We still neglect energy losses and convection of the electrons with the solar wind, but now take into account perpendicular diffusion and corotation. Accordingly, the SDE for the momentum transport is omitted, and only the following two SDEs are left:

$$\mathrm{d}\boldsymbol{r}(t) = \mu v \boldsymbol{b}\,\mathrm{d}t + \sqrt{2\boldsymbol{K}_\perp}\,\mathrm{d}\boldsymbol{W}_\perp(t) + \nabla \boldsymbol{K}_\perp\,\mathrm{d}t, \tag{5}$$

$$\mathrm{d}\mu(t) = \sqrt{2D_{\mu\mu}}\,\mathrm{d}W_\mu(t) + \left[\frac{v}{2L}\left(1-\mu^2\right) + \frac{\partial D_{\mu\mu}}{\partial \mu}\right]\mathrm{d}t, \tag{6}$$

where $W_\mu(t)$ and $\boldsymbol{W}_\perp(t)$ denote 1D and 2D Wiener processes, respectively.

Following our previous work, we consider that the perpendicular mean free path scales with the gyroradius of the particle, *i.e.*, with the magnetic field strength and with the particle's pitch angle (Dröge *et al.*, 2010):

$$\lambda_\perp(\mu, r) = \alpha \cdot \lambda_\parallel(r) \cdot \left(\frac{r}{1\ \mathrm{AU}}\right)^2 \cdot \cos\left(\psi(r)\right) \cdot \sqrt{1-\mu^2}, \tag{7}$$

where ψ is the angle between the radial direction and the magnetic field, and α gives approximately the ratio $\lambda_\perp/\lambda_\parallel$ at 1 AU in the case where the electron distribution function is nearly isotropic at that location. We note that for smaller radial distances and anisotropic distribution functions $\lambda_\perp/\lambda_\parallel$ can be considerably smaller than α.

Figure 12 (left) shows the electron intensities observed on STEREO-A and B as well as ACE/EPAM electron observations in the same energy range. It is evident from the figure that the ACE/EPAM background is considerably higher than those on both STEREO spacecraft, and that a possible electron flux resulting from the flare stays below that background (*cf.* Figure 1). However, the background flux was used as a constraint for the modeling, the

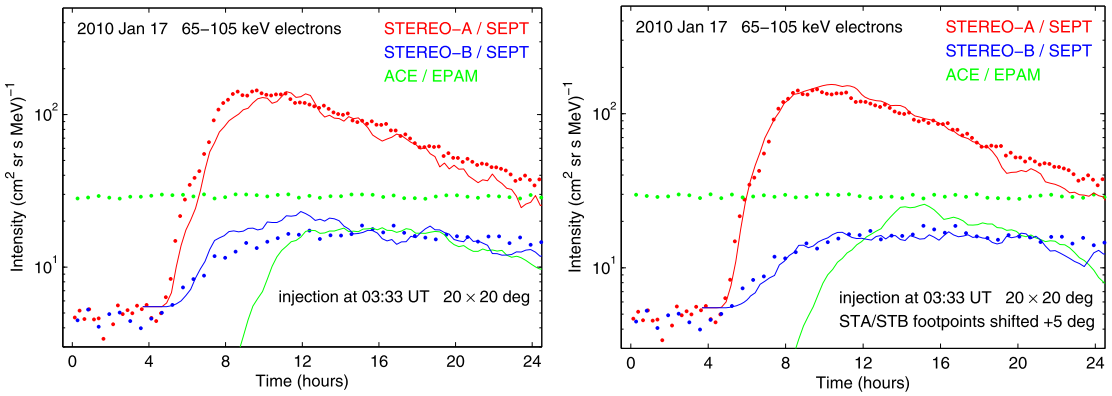

Figure 12 Left: Fits obtained from the MC model to the omnidirectional intensity-time profile of 65 – 105 keV electrons observed by STEREO-A and STEREO-B assuming azimuthal distances of the footpoints from the flare region derived from the observed solar wind speeds. Right: Fits obtained assuming that the footpoints are shifted in the western direction by 5 degrees.

results of which are shown as solid lines in the figure. It was assumed that electrons are injected at a radial distance 0.05 AU, with an energy distribution according to a power law with a spectral index $\gamma = 3$. Note that the model assumes an impulsive injection of the particles. The injection height of 0.05 AU has been chosen to save computation time. However, a lower injection height of 0.02 AU as suggested by the highest frequency of the type III bursts would not change the model results at the existing resolution of the observations. In accordance with the first model, a constant $\lambda_r = 0.1$ AU was assumed, and a value of $\alpha = 0.3$. The parallel anisotropy in this event was not quantifiable but probably very low and was not used for the modeling. The figure shows that the resulting intensities, which were normalized by a single factor, reproduce basic features of the electron observations. Both the shapes of the intensity profiles observed on STEREO-A and B and the ratio of the maximum intensities are matched well. The intensity predicted for the near-Earth environment stays well below the observed background for ACE/EPAM. Note that the SOHO/EPHIN electron observations, which show the SEP event, have not been modeled. Because of the much higher energy range (250 – 700 keV) this would require too many additional assumptions, *e.g.*, on the spectral shape, and an energy dependence of the mean free path.

One of the uncertainties in the modeling is the exact structure of the interplanetary magnetic field and of the resulting extrapolation of the location of the origin of the field line connecting to the spacecraft. The right side of Figure 12 shows the result of a modeling where the origins of the field lines have been shifted counterclockwise (to the west) by 5 degrees, and the other parameters have been left unchanged. This moderate shift, which is well within the limits of the uncertainties regarding the distance between the source region and the connecting field lines, leads to a nearly perfect fit of the intensity profiles.

5. Discussion of Model Results and Conclusions

Although the source of flare-related energetic particles is commonly treated as a point source, we applied an extended source in model 2. This is suggested by the remote observation of a shock through the type II radio burst (*cf.* Grechnev *et al.*, 2011). On the other hand, PFSS models describing the coronal magnetic field also support an extension of the source region, which is due to diverging magnetic field lines as described by Klein *et al.* (2008). Figure 13 shows three different views to the flaring active region of the presented

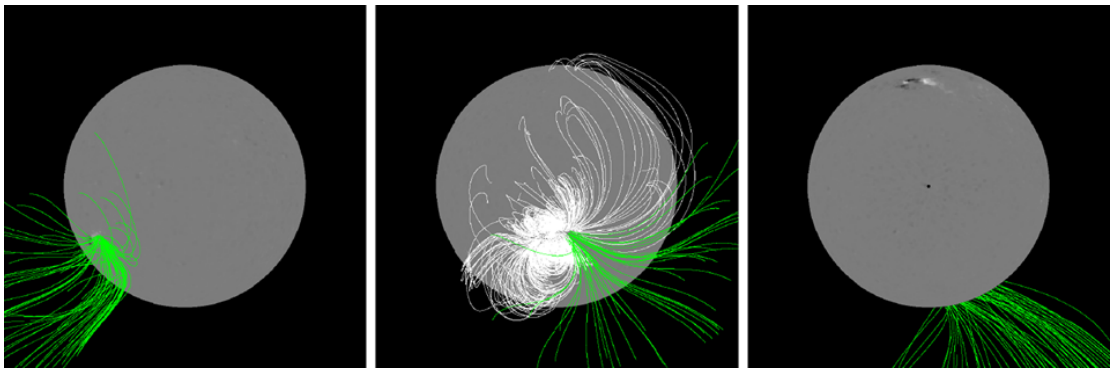

Figure 13 PFSS plots produced with the SolarSoft package pfss_viewer. The figures show open field lines (green) of positive polarity and closed field lines (white, only center figure) emerging from the AR, which produced the flare on 17 January. The left figure shows the 17 January STEREO-B perspective, the center figure presents a frontal view onto the AR, and the right figure shows a view from the north.

event. The green lines show open magnetic field lines of positive polarity emerging from the positive part of the active region. The white lines represent closed field lines and are only shown in the center panel of the figure. The central viewing angle for the left figure is 120 degrees, the center figure shows the AR more frontal with an angle of 70 degrees, and the right figure presents a view from the north. The starting height was set to 1.0159 solar radii and the upper height is 2.5 solar radii. The model shows that the open magnetic field lines are located to the west, and a divergence of open magnetic field lines of several tens of degrees can be seen. This agrees with the second model run of model 2 (see Figure 13 (right)), where the source region was shifted by 5 degrees to the west. Note that the AR is behind the limb for the Earth on 17 January 2010, so the magnetogram observations taken for this PFSS model are not up to date and could have changed.

We conclude that both models considered here for the lateral transport can explain the electron observations on STEREO-A and B following the flare on 17 January 2010. However, because we do not find evidence for unusually long injection functions at the Sun, as proposed by model 1, we tend to believe more in a scenario with strong perpendicular diffusion in the interplanetary medium as described by model 2. Of course, a combination of both processes, coronal transport and perpendicular diffusion in the interplanetary medium, is likely a more realistic description of the problem. Furthermore, the EUV wave directed toward the magnetic footpoint of STEREO-B (see Figure 2 right) may also influence the coronal particle propagation, as suggested by Rouillard *et al.* (2012). More information about the nature of the lateral transport of solar energetic particles can be expected if more simultaneous two- or three-spacecraft observations of particle events with a measurable anisotropy become available.

6. Summary

We present multi-spacecraft observations of the 17 January 2010 solar energetic particle event, which was detected from three viewpoints provided by the two STEREO spacecraft and the near-Earth spacecraft SOHO. Although it is a backside event as seen from Earth and all magnetic footpoints of the three spacecraft are separated by more than 100 degrees from the flaring active region, energetic electrons and protons are observed at all these positions. The longitudinal spread of energetic particles in this event is consequently suggested to be nearly 360 degrees at 1 AU. Remote observations of the flare and of an EUV wave have been

obtained by STEREO-B only, while a CME and type III radio bursts were also observed by STEREO-A, SOHO, and *Wind*. A type II radio burst, indicating the presence of a coronal shock, was recorded by STEREO-B and the Earth-based radio observatory HiRAS, while no associated interplanetary shock has been detected *in situ*. Energetic particles arrive at the spacecraft strongly delayed with respect to the flare onset. Because the pitch angle coverage for STEREO-A, which measures the most significant event, is rather poor, it is difficult to obtain the anisotropy of the event. However, later phases during the event with better pitch angle coverage show only very small anisotropy. The long time delay, the large angular spread, and small anisotropy point to the fact that the particles are not directly streaming away from an extended region but undergo strong scattering in the interplanetary medium. In order to characterize the event in terms of particle transport in the interplanetary medium including perpendicular diffusion, two model approaches have been considered. While the first model describes the parallel particle propagation along the magnetic field lines and neglects perpendicular motion to the average magnetic field (Dröge, 2003), the second model is a 3D propagation code including perpendicular diffusion in the interplanetary medium (Dröge *et al.*, 2010), where an extended source of 20 degrees in latitude and longitude has been applied. We find both models capable of describing the observed time-intensity profiles observed at the STEREO spacecraft. The first model assumes all lateral transport to be performed in the corona and requires injection functions at the Sun with durations of several hours, while the second model yields a large ratio of perpendicular to parallel diffusion of 0.3. Because we do not find evidence for extremely prolonged particle injections at the Sun, we favor the second model results for explaining the observations, although we cannot exclude a combination of both processes, perpendicular diffusion in the interplanetary medium and coronal transport. Nevertheless, the results suggest that the ratio of perpendicular to parallel diffusion may vary among different solar events and large values of the ratio have to be considered.

Acknowledgements We acknowledge the STEREO PLASTIC, IMPACT, SECCHI, EIT, and *Wind* teams for providing the data used in this paper. The STEREO/SEPT and SOHO/EPHIN projects are supported under Grant 50 OC 0902 by the German Bundesministerium für Wirtschaft through the Deutsches Zentrum für Luft- und Raumfahrt (DLR). We thank the Geophysical Institute, University of Alaska, Fairbanks for providing the ecliptic plane IMF maps. The radio monitoring survey is generated and maintained at the Observatoire de Paris by the LESIA UMR CNRS 8109 in cooperation with the Artemis team, the Universities of Athens and Ioanina, and the Naval Research Laboratory. This work utilizes data obtained by the Global Oscillation Network Group (GONG) program, managed by the National Solar Observatory, which is operated by AURA, Inc. under a cooperative agreement with the National Science Foundation. The data were acquired by instruments operated by the Big Bear Solar Observatory, High Altitude Observatory, Learmonth Solar Observatory, Udaipur Solar Observatory, Instituto de Astrofísica de Canarias, and Cerro Tololo Inter-American Observatory. Y.K. was partially supported by the Russian Foundation for Basic Research (project No. 09-02-00019-a).

References

Acuña, M.H., Curtis, D., Scheifele, J.L., Russell, C.T., Schroeder, P., Szabo, A., Luhmann, J.G.: 2007, The STEREO/IMPACT magnetic field experiment. *Space Sci. Rev.* **136**, 203 – 226. doi:10.1007/s11214-007-9259-2. http://adsabs.harvard.edu/abs/2008SSRv..136..203A.

Borovsky, J.E.: 2008, Flux tube texture of the solar wind: Strands of the magnetic carpet at 1 AU? *J. Geophys. Res.* **113**, A08110. doi:10.1029/2007JA012684. http://adsabs.harvard.edu/abs/2008JGRA..11308110B.

Bougeret, J.L., Kaiser, M.L., Kellogg, P.J., Manning, R., Goetz, K., Monson, S.J., Monge, N., Friel, L., Meetre, C.A., Perche, C., Sitruk, L., Hoang, S.: 1995, WAVES: The radio and plasma wave investigation on the WIND spacecraft. *Space Sci. Rev.* **71**, 231 – 263. doi:10.1007/BF00751331. http://adsabs.harvard.edu/abs/1995SSRv...71..231B.

Bougeret, J.L., Goetz, K., Kaiser, M.L., Bale, S.D., Kellogg, P.J., Maksimovic, M., Monge, N., Monson, S.J., Astier, P.L., Davy, S., Dekkali, M., Hinze, J.J., Manning, R.E., Aguilar-Rodriguez, E., Bonnin, X., Briand, C., Cairns, I.H., Cattell, C.A., Cecconi, B., Eastwood, J., Ergun, R.E., Fainberg, J., Hoang, S., Huttunen, K.E.J., Krucker, S., Lecacheux, A., MacDowall, R.J., Macher, W., Mangeney, A., Meetre, C.A., Moussas, X., Nguyen, Q.N., Oswald, T.H., Pulupa, M., Reiner, M.J., Robinson, P.A., Rucker, H., Salem, C., Santolik, O., Silvis, J.M., Ullrich, R., Zarka, P., Zouganelis, I.: 2008, S/WAVES: The radio and plasma wave investigation on the STEREO mission. *Space Sci. Rev.* **136**, 487 – 528. doi:10.1007/s11214-007-9298-8. http://adsabs.harvard.edu/abs/2008SSRv..136..487B.

Brueckner, G.E., Howard, R.A., Koomen, M.J., Korendyke, C.M., Michels, D.J., Moses, J.D., Socker, D.G., Dere, K.P., Lamy, P.L., Llebaria, A., Bout, M.V., Schwenn, R., Simnett, G.M., Bedford, D.K., Eyles, C.J.: 1995, The Large Angle Spectroscopic Coronagraph (LASCO). *Solar Phys.* **162**, 357 – 402. doi:10.1007/BF00733434. http://adsabs.harvard.edu/abs/1995SoPh..162..357B.

Cane, H.V., Erickson, W.C.: 2003, Energetic particle propagation in the inner heliosphere as deduced from low-frequency (<100 kHz) observations of type III radio bursts. *J. Geophys. Res.* **108**, 1203. http://adsabs.harvard.edu/abs/2003JGRA..108.1203C.

Cliver, E.W., Cane, H.V.: 1996, The angular extents of solar/interplanetary disturbances and modulation of galactic cosmic rays. *J. Geophys. Res.* **101**, 15533 – 15546. doi:10.1029/96JA00492. http://adsabs.harvard.edu/abs/1996JGR...10115533C.

Cliver, E.W., Kahler, S.W., Neidig, D.F., Cane, H.V., Richardson, I.G., Kallenrode, M.B., Wibberenz, G.: 1995, Extreme "propagation" of solar energetic particles. In: *24th International Cosmic Ray Conference* **4**, 257 – 260. http://adsabs.harvard.edu/abs/1995ICRC....4..257C.

Cliver, E.W., Laurenza, M., Storini, M., Thompson, B.J.: 2005, On the origins of solar EIT waves. *Astrophys. J.* **631**, 604 – 611. http://adsabs.harvard.edu/abs/2005ApJ...631..604C.

Dalla, S., Balogh, A., Krucker, S., Posner, A., Müller-Mellin, R., Anglin, J.D., Hofer, M.Y., Marsden, R.G., Sanderson, T.R., Traquille, C., Heber, B., Zhang, M., McKibben, R.B.: 2003a, Properties of high heliolatitude solar energetic particle events and constraints on models of acceleration and propagation. *Geophys. Res. Lett.* **30**, 8035. doi:10.1029/2003GL017139. http://adsabs.harvard.edu/abs/2003GeoRL..30sULY9D.

Dalla, S., Balogh, A., Krucker, S., Posner, A., Müller-Mellin, R., Anglin, J.D., Hofer, M.Y., Marsden, R.G., Sanderson, T.R., Heber, B., Zhang, M., McKibben, R.B.: 2003b, Delay in solar energetic particle onsets at high heliographic latitudes. *Ann. Geophys.* **21**, 1367 – 1375. doi:10.5194/angeo-21-1367-2003. http://adsabs.harvard.edu/abs/2003AnGeo..21.1367D.

Delaboudinière, J.P., Artzner, G.E., Brunaud, J., Gabriel, A.H., Hochedez, J.F., Millier, F., Song, X.Y., Au, B., Dere, K.P., Howard, R.A., Kreplin, R., Michels, D.J., Moses, J.D., Defise, J.M., Jamar, C., Rochus, P., Chauvineau, J.P., Marioge, J.P., Catura, R.C., Lemen, J.R., Shing, L., Stern, R.A., Gurman, J.B., Neupert, W.M., Maucherat, A., Clette, F., Cugnon, P., Dessel, E.L.: 1995, EIT: Extreme-ultraviolet imaging telescope for the SOHO mission. *Solar Phys.* **162**, 291 – 312. doi:10.1007/BF00733432. http://adsabs.harvard.edu/abs/1995SoPh..162..291D.

Dröge, W.: 2003, Solar particle transport in a dynamical quasi-linear theory. *Astrophys. J.* **589**, 1027 – 1039. doi:10.1086/374812.

Dröge, W., Kartavykh, Y.Y., Klecker, B., Kovaltsov, G.A.: 2010, Anisotropic three-dimensional focused transport of solar energetic particles in the inner heliosphere. *Astrophys. J.* **709**, 912 – 919. http://adsabs.harvard.edu/abs/2010ApJ...709..912D.

Dunzlaff, P., Kopp, A., Heber, B.: 2010, Propagation of Jovian electron jets in heliospheric flux tube structures. *J. Geophys. Res.* **115**. doi:10.1029/2009JA015142. http://adsabs.harvard.edu/abs/2010JGRA..11510106D.

Galvin, A.B., Kistler, L.M., Popecki, M.A., Farrugia, C.J., Simunac, K.D.C., Ellis, L., Möbius, E., Lee, M.A., Boehm, M., Carroll, J., Crawshaw, A., Conti, M., Demaine, P., Ellis, S., Gaidos, J.A., Googins, J., Granoff, M., Gustafson, A., Heirtzler, D., King, B., Knauss, U., Levasseur, J., Longworth, S., Singer, K., Turco, S., Vachon, P., Vosbury, M., Widholm, M., Blush, L.M., Karrer, R., Bochsler, P., Daoudi, H., Etter, A., Fischer, J., Jost, J., Opitz, A., Sigrist, M., Wurz, P., Klecker, B., Ertl, M., Seidenschwang, E., Wimmer-Schweingruber, R.F., Koeten, M., Thompson, B., Steinfeld, D.: 2008, The plasma and suprathermal ion composition (PLASTIC) investigation on the STEREO observatories. *Space Sci. Rev.* **136**, 437 – 486. doi:10.1007/s11214-007-9296-x. http://adsabs.harvard.edu/abs/2008SSRv..136..437G.

Gold, R.E., Krimigis, S.M., Hawkins, S.E., III, Haggerty, D.K., Lohr, D.A., Fiore, E., Armstrong, T.P., Holland, G., Lanzerotti, L.J.: 1998, Electron, proton, and alpha monitor on the advanced composition explorer spacecraft. *Space Sci. Rev.* **86**, 541 – 562.

Grechnev, V.V., Afanasyev, A.N., Uralov, A.M., Chertok, I.M., Eselevich, M.V., Eselevich, V.G., Rudenko, G.V., Kubo, Y.: 2011, Coronal shock waves, EUV waves, and their relation to CMEs. III. Shock-associated CME/EUV wave in an event with a two-component EUV transient. *Solar Phys.* **273**, 461 – 477. doi:10.1007/s11207-011-9871-y. http://adsabs.harvard.edu/abs/2011arXiv1104.3375G.

Howard, R.A., Moses, J.D., Vourlidas, A., Newmark, J.S., Socker, D.G., Plunkett, S.P., Korendyke, C.M., Cook, J.W., Hurley, A., Davila, J.M., Thompson, W.T., St Cyr, O.C., Mentzell, E., Mehalick, K., Lemen, J.R., Wuelser, J.P., Duncan, D.W., Tarbell, T.D., Wolfson, C.J., Moore, A., Harrison, R.A., Waltham, N.R., Lang, J., Davis, C.J., Eyles, C.J., Mapson-Menard, H., Simnett, G.M., Halain, J.P., Defise, J.M., Mazy, E., Rochus, P., Mercier, R., Ravet, M.F., Delmotte, F., Auchere, F., Delaboudiniere, J.P., Bothmer, V., Deutsch, W., Wang, D., Rich, N., Cooper, S., Stephens, V., Maahs, G., Baugh, R., McMullin, D., Carter, T.: 2008, Sun Earth Connection Coronal and Heliospheric Investigation (SECCHI). *Space Sci. Rev.* **136**, 67 – 115. doi:10.1007/s11214-008-9341-4. http://adsabs.harvard.edu/abs/2008SSRv..136...67H.

Jokipii, J.R.: 1966, Cosmic-ray propagation. I. Charged particles in a random magnetic field. *Astrophys. J.* **146**, 480 – 487. doi:10.1086/148912. http://adsabs.harvard.edu/abs/1966ApJ...146..480J.

Jokipii, J.R., Parker, E.N.: 1969, Stochastic aspects of magnetic lines of force with application to cosmic-ray propagation. *Astrophys. J.* **155**, 777 – 798. doi:10.1086/149909. http://adsabs.harvard.edu/abs/1969ApJ...155..777J.

Kallenrode, M.B., Wibberenz, G., Kunow, H., Müller-Mellin, R., Stolpovskii, V., Kontor, N.: 1993, Multi-spacecraft observations of particle events and interplanetary shocks during November/December 1982. *Solar Phys.* **147**, 377 – 410. doi:10.1007/BF00690726. http://adsabs.harvard.edu/abs/1993SoPh..147..377K.

Klassen, A., Gómez-Herrero, R., Heber, B.: 2011, Electron spikes, type III radio bursts and EUV jets on 22 February 2010. *Solar Phys.* **273**, 413 – 419. doi:10.1007/s11207-011-9735-4. http://adsabs.harvard.edu/abs/2011SoPh..tmp..154K.

Klein, K.L., Krucker, S., Lointier, G., Kerdraon, A.: 2008, Open magnetic flux tubes in the corona and the transport of solar energetic particles. *Astron. Astrophys.* **486**, 589 – 596. http://adsabs.harvard.edu/abs/2008A%26A...486..589K.

Luhmann, J.G., Curtis, D.W., Schroeder, P., McCauley, J., Lin, R.P., Larson, D.E., Bale, S.D., Sauvaud, J.A., Aoustin, C., Mewaldt, R.A., Cummings, A.C., Stone, E.C., Davis, A.J., Cook, W.R., Kecman, B., Wiedenbeck, M.E., Rosenvinge, T., Acuna, M.H., Reichenthal, L.S., Shuman, S., Wortman, K.A., Reames, D.V., Mueller-Mellin, R., Kunow, H., Mason, G.M., Walpole, P., Korth, A., Sanderson, T.R., Russell, C.T., Gosling, J.T.: 2007, STEREO IMPACT investigation goals, measurements, and data products overview. *Space Sci. Rev.* **136**, 117 – 184. doi:10.1007/s11214-007-9170-x. http://adsabs.harvard.edu/abs/2008SSRv..136..117L.

Mazur, J.E., Mason, G.M., Dwyer, J.R., Giacalone, J., Jokipii, J.R., Stone, E.C.: 2000, Interplanetary magnetic field line mixing deduced from impulsive solar flare particles. *Astrophys. J. Lett.* **532**, L79 – L82. doi:10.1086/312561. http://adsabs.harvard.edu/abs/2000ApJ...532L..79M.

McKibben, R.B., Lopate, C., Zhang, M.: 2001, Simultaneous observations of solar energetic particle events by IMP 8 and the Ulysses cospin high energy telescope at high solar latitudes. *Space Sci. Rev.* **97**, 257 – 262. doi:10.1023/A:1011816715390. http://adsabs.harvard.edu/abs/2001SSRv...97..257M.

Mewaldt, R.A., Cohen, C.M.S., Cook, W.R., Cummings, A.C., Davis, A.J., Geier, S., Kecman, B., Klemic, J., Labrador, A.W., Leske, R.A., Miyasaka, H., Nguyen, V., Ogliore, R.C., Stone, E.C., Radocinski, R.G., Wiedenbeck, M.E., Hawk, J., Shuman, S., Von Rosenvinge, T.T., Wortman, K.: 2007, The low-energy telescope (LET) and SEP central electronics for the STEREO mission. *Space Sci. Rev.* **136**, 285 – 362. doi:10.1007/s11214-007-9288-x. http://adsabs.harvard.edu/abs/2008SSRv..136..285M.

Müller-Mellin, R., Kunow, H., Fleissner, V., Pehlke, E., Rode, E., Röschmann, N., Scharmberg, C., Sierks, H., Rusznyak, P., Mckenna-Lawlor, S., Elendt, I., Sequeiros, J., Meziat, D., Sanchez, S., Medina, J., Peral, L., Witte, M., Marsden, R., Henrion, J.: 1995, COSTEP – comprehensive suprathermal and energetic particle analyser. *Solar Phys.* **162**, 483 – 504. doi:10.1007/BF00733437. http://adsabs.harvard.edu/abs/1995SoPh..162..483M.

Müller-Mellin, R., Böttcher, S., Falenski, J., Rode, E., Duvet, L., Sanderson, T., Butler, B., Johlander, B., Smit, H.: 2007, The solar electron and proton telescope for the STEREO mission. *Space Sci. Rev.* **136**, 363 – 389. doi:10.1007/s11214-007-9204-4. http://adsabs.harvard.edu/abs/2008SSRv..136..363M.

Ragot, B.R.: 1999, On the quasilinear transport of magnetic field lines. *Astrophys. J.* **525**, 524 – 532. doi:10.1086/307875. http://adsabs.harvard.edu/abs/1999ApJ...525..524R.

Reames, D.V.: 1999, Particle acceleration at the Sun and in the heliosphere. *Space Sci. Rev.* **90**, 413 – 491. http://adsabs.harvard.edu/abs/1999SSRv...90..413R.

Rouillard, A.P., Sheeley, N.R., Tylka, A., Vourlidas, A., Ng, C.K., Rakowski, C., Cohen, C.M.S., Mewaldt, R.A., Mason, G.M., Reames, D., Savani, N.P., StCyr, O.C., Szabo, A.: 2012, The longitudinal properties of a solar energetic particle event investigated using modern solar imaging. *Astrophys. J.* **752**, 44. doi:10.1088/0004-637X/752/1/44. http://stacks.iop.org/0004-637X/752/i=1/a=44?key=crossref.b124f469ff775ee8f148c7eb986c1ce1.

Sanderson, T.R.: 2003, Propagation of energetic particles in the high-latitude high-speed solar wind. *Geophys. Res. Lett.* **30**, 8036. doi:10.1029/2003GL017306. http://adsabs.harvard.edu/abs/2003GeoRL..30ULY10S.

Torsti, J., Kocharov, L., Teittinen, M., Anttila, A., Laitinen, T., Mäkelä, P., Riihonen, E., Vainio, R., Valtonen, E.: 1999, Energetic (10 – 65 MeV) protons observed by ERNE on August 13 – 14, 1996: Eruption on the solar back side as a possible source of the event. *J. Geophys. Res.* **104**, 9903 – 9909. doi:10.1029/1998JA900017. http://adsabs.harvard.edu/abs/1999JGR...104.9903T.

Veronig, A.M., Muhr, N., Kienreich, I.W., Temmer, M., Vršnak, B.: 2010, First observations of a dome-shaped large-scale coronal extreme-ultraviolet wave. *Astrophys. J. Lett.* **716**, L57 – L62. http://adsabs.harvard.edu/abs/2010ApJ...716L..57V.

Von Rosenvinge, T., Cummings, A., Cohen, C., Leske, R., Mewaldt, R., Stone, E., Wiedenbeck, M.: 2007, The high energy telescope for STEREO. *Space Sci. Rev.* **136**, 391 – 435. doi:10.1007/s11214-007-9300-5.

Wibberenz, G., Cane, H.V.: 2006, Multi-spacecraft observations of solar flare particles in the inner heliosphere. *Astrophys. J.* **650**, 1199 – 1207. http://adsabs.harvard.edu/abs/2006ApJ...650.1199W.

Wuelser, J.P.: 2004, EUVI: The STEREO-SECCHI extreme ultraviolet imager. *Proc. SPIE* **5171**, 111 – 122. doi:10.1117/12.506877. http://adsabs.harvard.edu/abs/2004SPIE.5171..111W.

5 STATISTICAL INVESTIGATIONS OF SEP EVENTS

In many statistical studies of SEP events, even previous to the STEREO mission, the longitudinal separation angle to the source active region was presented and longitudinal variations of event properties were analyzed (*Schellert et al.*, 1985; *Kallenrode*, 1993; *Wibberenz* and *Cane*, 2006). The longitudinal separation angle between the spacecraft's magnetic footpoint and the parent active region has been found to be the dominant parameter which determines the peak intensities (*Lario et al.*, 2006) at the different spacecraft. Furthermore, the observer who is best connected usually detects the earliest event onset, meaning that the onset delay increases with increasing longitudinal separation angle (c.f. *Kallenrode* (1993); *Wibberenz* and *Cane* (2006)). In the case of a small source region at the Sun, this is not surprising because a larger longitudinal separation angle implies a longer path length which the particles have to propagate before reaching the spacecraft. This is especially the case if perpendicular diffusion is present in the IP medium where the particles undergo strong scattering which strongly enlarges the propagation path. Relatively small onset delays at separation angles of up to ∼60 degrees were often interpreted to be caused by the presence of a so-called *fast propagation region* (*Wibberenz et al.*, 1976; *Kallenrode*, 1993) where the particles were distributed over this range by a fast and efficient process like a coronal shock or coronal transport. While *Lario et al.* (2006) had to deal with the radial differences when investigating Helios observations in terms of peak intensities, *Lario et al.* (2013) (see Appendix B) analyzed a set of 35 SEP events detected with STEREO and ACE without this disadvantage. The standard deviation resulting from a Gaussian fitting of $\sigma = 45 \pm 1$ degrees for 25-53 MeV protons (*Lario et al.*, 2013) is slightly wider than the one found with Helios and IMP-8 of $\sigma = 36 \pm 2$ degrees for 27-37 MeV protons (*Lario et al.*, 2006) which could be due to the fact that the Helios spacecraft were located closer to the Sun or that a different sample of events was used (*Lario et al.*, 2013).

While previous to STEREO often the anisotropy was incorporated in SEP studies, there are only few STEREO investigations paying attention to the SEP anisotropies especially not in a statistical SEP analysis. The publication which is presented in the next section therefore utilizes the anisotropy as a key information to disentangle different source and transport mechanisms. A summary of the main aspects is given in the next paragraph.

DRESING *et al.* SUBMITTED MARCH 2014: A STATISTICAL SURVEY OF WIDE-SPREAD SOLAR ELECTRON EVENTS OBSERVED WITH STEREO AND ACE WITH SPECIAL ATTENTION ON ANISOTROPIES

Own contribution: 85%

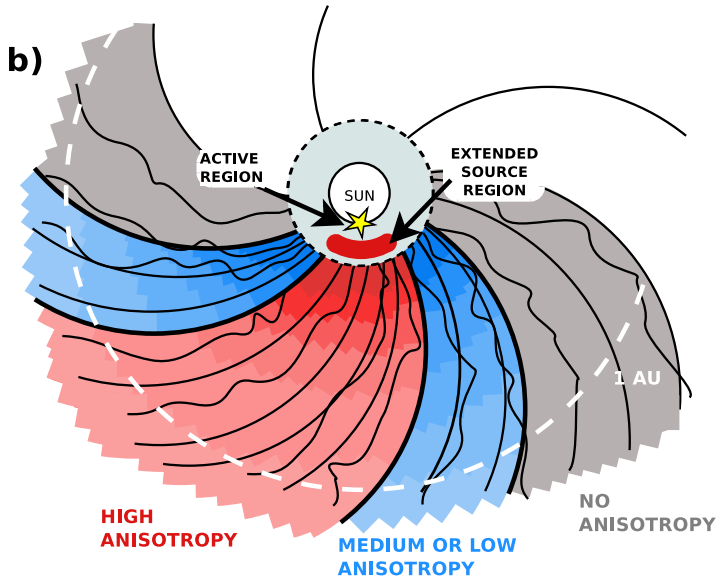

Figure 20: Regions of varying anisotropy during a rising solar energetic particle event: A spacecraft located in the reddish area is directly connected to the source AR (yellow star) and will observe an impulsive and strongly anisotropic event. Far separated from the flare longitude (gray area) a spacecraft may still detect SEPs, however, these reach the spacecraft just due to perpendicular diffusion which will wash out the anisotropy. If an extended SEP distribution close to the Sun is present (red arc), an extended region of anisotropic observations is present in the IP medium (blue region). At the outer borders of this region a connection through field line random walk may still provide some anisotropy. Note that the anisotropy closer to the Sun is always larger which is indicated by darker coloring. Figure from *Dresing et al.* (2014).

Short Summary of Publication 2

A sample of 21 wide-spread solar near-relativistic electron events has been collected and is investigated in a statistical manner. We require a minimum longitudinal separation angle of 80 degrees between the associated flare location and the magnetic footpoint of the widest separated spacecraft observing the event to be counted as a wide-spread event.
Beside determining the longitudinal variation of peak intensities and onset delays, we introduce a new parameter, the event broadness. This parameter characterizes the SEP extent in the inner heliosphere by incorporating not only the standard deviation of a Gaussian fitting to the peak intensities but also the injected intensity. As a key parameter the maximum observed anisotropy at the different spacecraft is investigated. By means of the anisotropy distribution the events have been divided into three classes which are in agreement with different source and transport scenarios. While class-(1) events agree with strong perpendicular diffusion providing the large electron spread (no anisotropies observed at far-separated locations), events of class (2) show significant anisotropies over large angular ranges suggesting a wide SEP distribution close to the Sun. This wide distribution may be caused by some coronal transport process, however, the presence of a shock, a

CME or even an EUV wave could contribute. Events of class (3) show unexpected anisotropy distributions in the way that not the best connected spacecraft observes the largest anisotropy but a further-separated spacecraft does. These events are more challenging to explain and the role of magnetic flux-rope structures as well as strongly varying spatial diffusion conditions are discussed.
For the majority of the events in our study (class-(1) and class-(2) events) we conclude that both perpendicular diffusion in the IP medium as well as a large coronal SEP spread must be present to produce wide-spread electron events while the importance of each of the processes may vary from event to event. Such a scenario is sketched in Fig. 20 which includes an extended source region in the corona as well as perpendicular diffusion in the IP medium producing a wide-spread event at 1 AU with regions of varying anisotropies.

Astronomy & Astrophysics manuscript no. paper_statistics_ani_aa
March 6, 2014

A statistical survey of wide-spread solar electron events observed with STEREO and ACE with special attention on anisotropies

N. Dresing[1], R. Gómez-Herrero[2], B. Heber[1], A. Klassen[1], O. Malandraki[3], W. Dröge[4], and Y. Kartavykh[4,5]

[1] Institut für Experimentelle und Angewandte Physik, Christian-Albrechts-Universität zu Kiel, Germany
e-mail: dresing@physik.uni-kiel.de
[2] Space Research Group, University of Alcalá, Spain

[3] IAASARS, National Observatory of Athens, Greece

[4] Institut für Theoretische Physik und Astrophysik, Universität Würzburg, Germany

[5] Ioffe Physical-Technical Institute, St-Petersburg, Russia

ABSTRACT

Context. In February 2011 the two STEREO spacecraft reached a separation of 180 degrees in longitude, offering a complete view of the Sun for the first time ever. Since the full Sun's surface is visible, source active regions of solar energetic particle (SEP) events can be identified unambiguously. STEREO, in combination with near-Earth observatories like ACE or SOHO provide three well separated viewpoints, building an unprecedented platform to investigate SEP events with respect to their longitudinal variations.
Aims. In this study we show an ensemble of SEP events, which were observed in the period between 2009 and mid 2013 by at least two spacecraft and show a remarkable wide particle spread. The main selection criterion for these events is that the longitudinal separation between active region and spacecraft magnetic footpoint is at least 80 degrees for the widest separated spacecraft. We investigate the events in a statistical manner in terms of maximum intensities, onset delays, and rise times and determine their longitudinal event broadnesses, which is the range filled by SEPs during the events. Energetic electron anisotropies are investigated to disentangle source and transport mechanisms leading to the observed wide particle spreads.
Methods. According to the anisotropy distributions we divide the events into three classes which point to different source and transport scenarios. One potential mechanism for wide-spread events is efficient perpendicular transport in the interplanetary medium that competes with another scenario which is a large particle spread performed close to the Sun. In the latter case, the observations at 1 AU during the early phase of the events are expected to show significant anisotropies due to the wide injection range at the Sun and particle focusing during the outwards propagation while in the first case only low anisotropies are anticipated.
Results. For both of the above scenarios we find events in our sample, which suit the expected observations and even further events, which do not agree with these. Finally we conclude that it is likely that both an extended source region at the Sun and perpendicular transport in the interplanetary medium are involved for the majority of these wide-spread events.

Key words. Wide Spread Events – Solar Energetic Particles (SEPs) – Propagation – Anisotropy – CME – Shock

1. Introduction

Solar energetic particle (SEP) events are of great interest because they allow unique insights on particle acceleration, injection and transport mechanisms in the inner heliosphere. Energy spectra, time series of intensity and anisotropy, as well as ionic charge states are signatures of acceleration, injection, and transport. Multi-spacecraft observations from well-separated points do not only proof an event at a certain angular distance but provide information on the actual angular spread of the event at a certain distance to the Sun. Helios observations revealed that the angular spread in the inner heliosphere can be very different ranging from tens of degrees up to more than 180 degrees (Kallenrode (1993); Reames (1999); Torsti et al. (1999); Cliver et al. (2005); Wibberenz & Cane (2006).
Flaring active regions at the Sun are believed to be strong particle accelerators producing impulsive, electron- and ^{3}He-rich events, respectively (Lin & Hudson (1976); Hsieh & Simpson (1970)). As rather confined regions these sources are expected to lead to narrow longitudinal spreads inside the inner heliosphere if the SEPs simply propagate outwards along the magnetic field spirals which are connected to the source active region (e.g. Klassen et al. (2012)). Recent observations from the STEREO mission reported by Wiedenbeck et al. (2013), however, question the constraint of a narrow spread of ^{3}He-rich events. Wider angular particle distributions and especially extremely wide spreads of SEPs which indicate distributions all around the Sun (i.e. Dresing et al. (2012)), are even more challenging and several ideas and processes have been put forth to explain such observations. These processes may be separated into two categories operating predominantly close to the Sun (in the corona) or in the interplanetary (IP) medium. The former includes coronal shocks accelerating particles in a large spatial region or efficient transport processes in the corona. Several mechanisms have been proposed as coronal transport, i.e. diverging magnetic field lines below the source surface (Klein et al. 2008) or different coronal diffusion (Reinhard & Wibberenz (1974); Newkirk & Wentzel (1978)), which provide a "pre-spreading" of tens of degrees before the

particles enter the open magnetic field lines and escape into the IP medium. The presence of EUV waves has also been introduced to be responsible for the spread of SEP events (Krucker et al. (1999); Rouillard et al. (2012); Park et al. (2013)).
By the end of the 1990's, events with wider spreads were classified as gradual, not flare-associated events. These proton-rich events were associated to CME-driven shocks building an extended source region in the IP medium (Mason et al. (1984); Cane et al. (1986); Kallenrode (1993); Reames (1999)). Another mechanism operating in the IP medium, which is capable of providing a large SEP spread, might be strong and efficient transport perpendicular to the mean magnetic field (Dalla (2003); Dröge et al. (2010); Laitinen et al. (2013); Marsh et al. (2013)). In this sense, both the random walk of magnetic field lines as well as perpendicular diffusion due to scattering may contribute to the lateral transport. Furthermore, pre-event ICMEs, large magnetic loops and transient structures may perturb and deform the IP magnetic field structure and modify the nominal connectivity (c.f. Richardson et al. (1991); Gómez-Herrero et al. (2006); Leske et al. (2012); Lario et al. (2013)).
To disentangle the processes mentioned above, very specific and comprehensive observations are required. Besides in-situ measurements, remote-sensing observations are indispensable to make a clear identification of the source region at the Sun. Of great importance also is the presence of multiple viewpoints well-separated in space to study angular variations and the angular spread of the event. To exclude radial gradient effects these viewpoints should be situated at the same radial distance. The above requirements are all fulfilled by the twin STEREO spacecraft (s/c) which constitute an excellent and unique platform to study SEP events especially when complemented with close to Earth spacecraft (like SOHO, ACE, and SDO) and ground-based observations.
In this work we investigate a set of near relativistic solar energetic electron events showing a remarkable longitudinal distribution. We chose a statistical approach and investigate the longitudinal variation of event properties like maximum intensities, onset delays, and rise times of these extreme events. As a key information we investigate the anisotropies observed at different viewpoints. With this information we will discuss the role and importance of the different transport and injection mechanisms that can lead to large longitudinal spread observed.

2. Instrumentation

The electron observations used in this work are provided by the Solar Electron and Proton Telescope (SEPT, Müller-Mellin et al. (2008)) aboard the STEREO spacecraft and the Electron Proton and Alpha Monitor (EPAM) on board ACE (Gold et al. 1998). The SEPT instrument measures electrons in the range of 45-400 keV. It consists of four identical telescopes mounted to cover four viewing directions, which are to the north, to the south, along the nominal Parker spiral to the Sun, and away from the Sun, respectively. ACE/EPAM measures the flux and direction of electrons and protons. The LEFS60 telescope provides 40 keV to about 350 keV electron measurements and by the spinning of the spacecraft the measurements are divided into eight different directional sectors. Complementary information on plasma properties are provided by the STEREO/PLASTIC (Galvin et al. 2008) and ACE/SWEPAM (McComas et al. 1998) instruments. The interplanetary magnetic field measurements by STEREO/MAG (Acuña et al. 2007) and ACE/MAG (Smith et al. 1998) are investigated to determine the pitch angle distributions and particle anisotropies. To link in-situ observations with the associated active regions (AR) at the Sun we evaluate images taken by the SECCHI investigation (Howard et al. 2008) in extreme ultra violet (EUVI) and coronographic observations (COR1 and COR2 instruments) provided by the STEREO spacecraft. EUV observations by SDO/AIA (Lemen et al. 2012) and the coronograph LASCO (Brueckner et al. 1995) aboard the SOHO spacecraft complete these observations. The occurrence of CMEs and its key parameters like CME speed and width can be found in the SOHO LASCO CME CATALOG (http://cdaw.gsfc.nasa.gov/CME_list/) or in the CACTus CME lists (http://sidc.oma.be/cactus/), which also provides lists for STEREO A and STEREO B observations. Radio (type II and type III) bursts are detected with the WAVES instrument aboard WIND (Bougeret et al. 1995) and the STEREO/WAVES instruments (Bougeret et al. 2008) at frequencies $\leq 16\,MHz$.

3. Event selection and overview

The increasing longitudinal separation of the two STEREO spacecraft from Earth provided progressively wider imaging coverage of the solar atmosphere until February 2011 when the STEREOs reached a 180 degrees separation from each other making the full Sun visible at once for the first time ever. In contrast to the Helios era, backside events as seen from one spacecraft can now be unambiguously linked to the parent active region when employing another spacecraft observing the event from the front side. With this 360° view one can not only study the longitudinal variation of event parameters but also identify and investigate wide-spread SEP events. Multi-spacecraft STEREO observations of the same event also allow to estimate the actual longitudinal spread of the SEPs at 1 AU, which we call the longitudinal event broadness (see Dresing et al. (2013)).
To collect a list of wide-spread events, we scanned the whole STEREO dataset since the beginning of the nominal mission in January 2007 up to mid 2013. The events have been selected by the following criteria:
(1) An electron increase in the energy range of 55-105 keV above background has to be detected by at least two of the three spacecraft, and
(2) The widest separated spacecraft must have a flare to s/c footpoint longitudinal separation of at least 80 degrees.
Several event candidates had to be excluded from the list because of strong ion contamination masking the electron event or if an unambiguous identification of the source AR was not possible due to additional type III and flare candidates.
The longitudinal coordinates of the spacecraft magnetic footpoints at the Sun were calculated according to a Parker spiral taking into account the measured solar wind speed during the event onset. The latitude of the s/c footpoint is simply equal to be the s/c latitude. The coordinates of the flare were determined using EUV images and movies taken by STEREO/EUVI and SDO/AIA.

Table 1 presents the event numbers, dates and associated type III radio burst onset times in columns 1 to 3. We consider the type III onset (at ~ 14 MHz measured by STEREO/WAVES and WIND/WAVES) as the expected solar injection time instead of the flare start time. The source Carrington longitude of the associated flare and the longitudinal separation angles of the magnetic footpoints of the spacecraft to the flare longitude are listed in columns 4 to 7, respectively. While positive values denote source regions situated to the west of the spacecraft magnetic footpoints, negative values represent a source to the east. The last four columns show CME speed and width and presence of

Table 1: Event number, event date, type III radio burst onset time, flare Carrington longitude (CL), longitudinal separation angles between the s/c footpoint and the flaring AR. CME speed and width if accompanied by a CME, and presence of associated type II radio bursts and EUV waves. CME speed and width have been taken from the SOHO LASCO CME catalog (marked with (S)), or the CACTus catalogs (see section 2), where (B) means STEREO B, (A) means STEREO A, and (cS) stands for SOHO. The type II radio burst marked by * was only observed at high frequencies > 200 MHz by a ground-based station (BLEN).)

No.	Date	Type III	Flare	Longitudinal			Associated Phenomena			
		Onset	CL	Separation Angle (°)			CME	CME	Type II	EUV
		(UT)		STB	ACE	STA	speed	width	burst	wave
1	2009-11-03	03:31	215	105	62	3	0	0	0	1
2	2010-01-17	03:54	54	-112	165	118	532 (B)	90	1	1
3	2010-02-07	02:29	255	7	-78	-121	421 (S)	142	0	1
4	2010-02-12	11:24	180	-32	-87	-129	568 (B)	92	1*	1
5	2010-08-07	18:11	350	-40	-96	-160	871 (S)	142	1	1
6	2010-08-14	10:01	350	45	-5	-92	1205 (S)	148	1	1
7	2010-08-18	05:32	350	92	36	-42	1471 (S)	184	1	1
8	2010-08-31	20:48	213	133	72	17	892 (A)	100	1	1
9	2010-09-09	23:22	52	90	25	-50	818 (S)	147	1	1
10	2011-02-24	07:30	177	-27	-154	115	1186 (S)	158	1	1
11	2011-11-03	22:14	10	-133	137	13	781 (A)	216	1	1
12	2011-11-26	07:14	275	87	-12	-115	933 (S)	190	1	1
13	2012-01-23	03:40	208	61	-32	-152	1136 (A)	120	1	1
14	2012-03-07	00:17	300	18	-94	163	961 (B)	352	1	1
15	2012-04-15	02:10	73	-27	-151	89	1644 (cS)	160	1	DG
16	2012-04-16	17:25	73	1	-150	111	822 (cS)	80	0	1
17	2012-05-17	01:31	190	141	16	-89	1302 (cS)	200	1	1
18	2012-08-31	19:50	90	-11	-111	128	651 (cS)	210	1	1
19	2013-03-05	03:16	73	-98	156	18	1316 (S)	360	1	1
20	2013-04-11	06:58	71	64	-77	153	694 (B)	348	1	1
21	2013-06-21	02:48	160	9	-132	91	1249 (cS)	160	1	1

DG: Data Gap

a type II radio burst or an EUV wave. Actually all but one of the events were accompanied by a CME, 18 events (86 %) were associated with a type II radio burst, indicating the presence of a shock, and all events were accompanied by an EUV wave (with one event being unclear due to a data gap (DG) in SDO/AIA).
In Fig. 1 the longitudinal configurations of flare and spacecraft positions are sketched for each of the events listed in Table 1. The longitude of the flaring active region is marked by the arrow, the dotted black spiral is the nominal Parker field line connecting to the active region. The colored spirals and dotted lines mark the field lines which connect the spacecraft to the Sun and their longitudinal positions, respectively.
Columns 1 to 3 of Table 2 are the same as in Table 1. The next three columns show the 55-105 keV electron onset times at the spacecraft and columns 7 to 9 list the maximum times of the events at the three spacecraft, respectively. The maxima of the events have been identified using 10 min averages and local phenomena like shock spikes or pitch angle changes due to magnetic field variations were excluded when determining the maximum time. For some events affected by shocks we used different viewing sectors to identify the onset and maximum times. The maximum intensity has been corrected by a pre-event background subtraction. With an energy bin of 53-103 keV, the ACE/EPAM data are well comparable to the STEREO/SEPT measurements of 55-105 keV electrons. However, an intercalibration factor of 1/1.3 (c.f. Lario et al. (2013)) has been applied to the ACE data to incorporate the different instrument responses. Fig. 2 illustrates the procedure how we determined onset and time to maximum for the example of the 7 March 2012 event observed by STEREO A. The first vertical line labeled with t_{inj} marks the onset time of the type III radio burst, the second line (t_{ons}) marks the onset time of the electron increase and the last line (t_{max}) represents the maximum time determined for this event. Note, that the maximum has been identified as the first maximum although the later maximum around day of year 67.3 is slightly higher. The delay between t_{ons} and t_{max} is the rise time of the event Δt.
To make sure that all the spacecraft observations are associated with the same event, all events have been checked carefully for further possible source regions as flares or type III radio bursts close in time. In unclear cases the events have been excluded.
Table 3 lists the event numbers, dates, maximum intensities detected at each of the spacecraft, and the anisotropy class defined in Sec. 4.3.

4. Data Analysis

4.1. Longitudinal Variation of Maximum Intensities and Event Broadness

Fig. 3 shows the maximum intensities (as listed in Table 3) of each event detected by each s/c as a function of the longitudinal separation angle. A separation angle of 0 denotes a perfect connection meaning that the s/c and the source active region are directly connected by a Parker magnetic field line according to the measured solar wind speed. Different symbols mark the different spacecraft and each color stands for a specific event. If a spacecraft did not observe an intensity increase the point has been put onto the horizontal axis to indicate the longitudinal separation angle of this spacecraft. The same has been done for ambiguous events which were excluded (c.f. table 2 and 3).
For those of the 21 wide-spread events providing three points,

A&A proofs: manuscript no. paper_statistics_ani_aa

Table 2: Event number, and date, type III radio burst onset times, onset and maximum times of 55-105 kev electrons at the three spacecraft. Times marked by a * occur on the next day.

No.	Date	Type III Onset (UT)	Electron Onset Time (UT)			Electron Maximum Time (UT)		
			STB	ACE	STA	STB	ACE	STA
1	2009-11-03	03:31	06:44	03:54	03:57	09:55	05:50	04:25
2	2010-01-17	03:54	04:30	NE	04:55	13:35	NE	09:35
3	2010-02-07	02:29	03:04	03:00	05:32	03:45	06:35	12:35
4	2010-02-12	11:24	12:14	12:20	13:04	13:15	13:15	15:45
5	2010-08-07	18:11	19:07	19:32	NE	22:35	20:55	NE
6	2010-08-14	10:01	10:30	10:18	10:52	11:35	11:05	12:25
7	2010-08-18	05:32	06:53	06:16	06:10	07:35	08:25	07:05
8	2010-08-31	20:48	22:07	21:29	21:21	22:15	02:15*	23:05
9	2010-09-08	23:22	AM	00:10*	NA	06:15*	01:15*	NA
10	2011-02-24	07:30	08:19	NE	12:12	12:45	NE	13:55
11	2011-11-03	22:14	23:24	23:08	22:42	12:15*	01:05*	01:15*
12	2011-11-26	07:14	08:15	07:27	IC	12:25	09:45	IC
13	2012-01-23	03:40	NA	04:00	07:45	NA	06:05	AM
14	2012-03-07	00:17	00:59	01:45	01:38	01:55	14:35	04:15
15	2012-04-15	02:10	02:38	NE	03:03	06:45	NE	06:25
16	2012-04-16	17:25	17:58	NE	18:35	19:05	NE	20:35
17	2012-05-17	01:31	04:35	01:48	07:15	13:45	02:45	IC
18	2012-08-31	19:50	20:11	21:08	03:50*	21:55	01:05*	19:15*
19	2013-03-05	03:16	05:15	09:50	03:40	23:05	10:35*	04:45
20	2013-04-11	06:58	07:24	07:52	14:15	09:05	10:25	AM
21	2013-06-21	02:48	03:14	07:55	05:50	03:55	AM	08:05

AM: Ambiguous, no maximum, if rise takes too long and other type III bursts follow; or no onset because of too poor increase
IC: Ion contamination saturates the electron measurement
NE: No event detected
NA: There is an increase but likely not associated to the event.

we approximate the longitudinal distribution of peak intensities with Gaussian functions:

$$I(\phi) = I_0 \exp[-(\phi - \phi_0)^2/2\sigma^2]. \quad (1)$$

Here, I_0 represents the maximum intensity at 1 AU and zero degrees separation angle ϕ, and σ is the standard deviation. ϕ_0 is the center of the Gaussian. The colored curves in Fig. 3 are approximations of Eq. 1 to each of the three-spacecraft events. Since for most of the events Eq. 1 approximates the data points well, the σ-distribution shown in Fig. 4 can be understood as a representation of possible values. Note, that we excluded fits revealing a $|\phi_0| > 90°$ as poor fits here. We find a large variety in the standard deviation σ between 32° and 48° degrees with a mean of 37.3° degrees (not taking into account two spacecraft events and the events with $|\phi_0| > 90°$, leaving 7 events).
In a similar investigation Lario et al. (2013) studied 35 STEREO multi-spacecraft SEP events and found a standard deviation σ of 49±2° and an asymmetry of $\phi_0 = -16°$ to the east for 71-112 keV electron events. Although we investigate wide-spread events in this paper, our value of $\sigma = 37.3°$ is significantly smaller than the one found by Lario et al. (2013). Note, if we apply the same fitting method like Lario et al. (2013), we obtain $\sigma = 39.1°$ and $\phi_0 = 11°$. A symmetric Gaussian fit centered around $\phi_0 = 0°$ results in a mean standard deviation of $\sigma = 35.5°$. The longitudinal distribution of the SEP events, however, is not completely characterized by a standard deviation. Moreover, several factors play an important role, namely the strength of the event and the instrumental background of the detectors. To characterize the actual longitudinal SEP extent at 1 AU, we introduce the longitudinal broadness of the events, which is described by the range, the fitted curves (Fig. 3) span above a background value (represented by the black horizontal line which represents a detection limit of 2σ above background). Different to the angular range spanned by the spacecraft observing the event, the broadness describes the longitudinal range over which a significant SEP increase could be detected during the event. Fig. 5 shows the fitted parameters I_0 vs. σ of the wide-spread three-spacecraft events, again excluding fits yielding $|\phi_0| > 90°$. The dashed lines mark longitudinal broadnesses of 180 degrees (black), 300 degrees (red), and 360 degrees (blue). The shaded area cannot be filled by definition of the selection criterion. The broadnesses of our events all lie above 180 degrees with some of them even exceeding 300 degrees. Fig. 6 right shows the same but these points are the outcome of Gaussian fits which were forced to be centered around $\phi_0 = 0°$, assuming a symmetric distribution around the best connection angle. The results of both methods are comparable but the broadnesses of the symmetric Gaussians tend to be larger even reaching 360°.

4.2. Longitudinal Variation of Onset Delays

Fig. 7 displays the SEP onset delay, which is the time between the injection at the Sun (assumed to be the type III burst onset, c.f. Fig. 2) and the electron onset at the spacecraft, as a function of the longitudinal separation angle. A correction of ~8 minutes for the light travel time has been applied to the type III burst onset time, so that the onset delay can be seen as the propaga-

Table 3: Event number, and date, maximum intensities of 55-105 keV electrons at the three spacecraft, and anisotropy class of the event (see Sec. 4.3). The maximum intensities at ACE have been corrected by an intercalibration factor of 1/1.3 (see text).

No.	Date	Maximum Intensity $(cm^2\ s\ sr\ MeV)^{-1}$			Anisotropy class
		STB	ACE	STA	
1	2009-11-03	2.21E+01	4.65E+02	2.14E+03	1
2	2010-01-17	2.12E+01	NE	1.91E+002	1
3	2010-02-07	6.90E+03	6.16E+02	6.28E+01	2
4	2010-02-12	1.20E+04	1.23E+03	3.34E+02	2
5	2010-08-07	2.41E+03	2.32E+02	NE	1
6	2010-08-14	2.18E+03	6.21E+03	4.88E+01	3
7	2010-08-18	6.91E+02	1.03E+04	4.55E+03	3
8	2010-08-31	2.23E+01	8.73E+03	8.84E+04	2
9	2010-09-08	1.67E+01	3.18E+02	NA	1
10	2011-02-24	2.35E+03	NE	6.04E+01	3
11	2011-11-03	3.25E+03	9.80E+02	7.80E+04	3
12	2011-11-26	4.29E+02	9.81E+03	IC	1
13	2012-01-23	NA	1.74E+05	AM	1
14	2012-03-07	2.32E+04	7.45E+05	1.85E+03	2
15	2012-04-15	1.02E+03	NE	5.72E+02	1
16	2012-04-16	1.22E+03	NE	1.54E+02	2
17	2012-05-17	5.79E+01	2.66E+04	IC	1
18	2012-08-31	1.87E+05	1.44E+03	7.04E+01	1
19	2013-03-05	7.81E+003	2.54E+002	3.33E+005	1
20	2013-04-11	1.09E+005	1.30E+004	AM	2
21	2013-06-21	7.61E+004	AM	7.45E+001	2

AM: Ambiguous, no maximum, if rise takes too long and other type III bursts follow; or no onset because of too poor increase
IC: Ion contamination saturates the electron measurement
NE: No event detected
NA: There is an increase but likely not associated to the event.

tion time of the electrons. Like in Fig. 3, each color represents an individual event and each symbol marks a specific spacecraft. The numbers on the right hand vertical axis illustrate the path lengths traveled by 55-105 keV electrons according to the delays shown on the left hand vertical axes (assuming these particles were injected at the type III burst onset time). The black horizontal solid line marks the travel time of 55-105 keV electrons along a nominal Parker spiral of 1.18 AU length from the Sun to 1 AU which is ~20 minutes (using a geometric mean energy of 76 keV and assuming scatter-free propagation). It is evident that most of the points in Fig. 7 lie above that line meaning that the particles arrive delayed at the spacecraft. While such a delay may be expected for growing longitudinal separations thinking in terms of perpendicular transport in the IP medium, it is remarkable that several well-connected events show delays of up to ~30 minutes, indicating either a delayed injection or a short mean free path along the IP magnetic field. Furthermore, strong event to event variations can be seen with extreme delays which would give the electrons time to diffusively propagate a distance of up to ~30 AU. However, these delays could also be caused by other mechanisms like a shock which takes some time to expand and intersect the magnetic field lines connecting to the s/c.
To gain more information on the involved processes we will analyze the anisotropy observed at each of the spacecraft during the same events in Section 4.3.

4.3. Longitudinal variation of event anisotropies

The transport of solar energetic particles in the inner heliosphere is determined by a number of physical processes (e.g., Zhang et al. 2009; Dröge et al. 2010). For fast particles, as the electrons considered in the present study, these include advection along the interplanetary magnetic field lines, adiabatic focusing in a diverging magnetic field which tends to drive the particles to the opposite of the parallel gradient in the magnetic field strength, interaction with magnetic field fluctuations which lead to a randomization of the particle's pitch angles, diffusion across the average magnetic field, and drift motions due to gradients and curvature in the interplanetary magnetic fields, as well as due to induced electric fields (the latter leading to co-rotation of solar particle events). For slower particles (e.g., ions with energies of a few MeV/n and below) also the effects of convection with the solar wind and of adiabatic energy losses are important, but for the electrons studied here we can safely neglect them. Besides processes governing the injection into the interplanetary medium, the onset of a solar electron event observed on a spacecraft which is magnetically well connected to the acceleration region is then basically determined by the effects of advection, focusing and pitch-angle diffusion, for events not magnetically well connected also perpendicular diffusion and co-rotation can be of importance. In large solar particle events frequently CMEs and interplanetary shock waves lead to distortions in the geometry of the interplanetary magnetic field, which in some cases can heavily influence the transport of energetic electrons.
The anisotropy of solar particles observed during an event is a

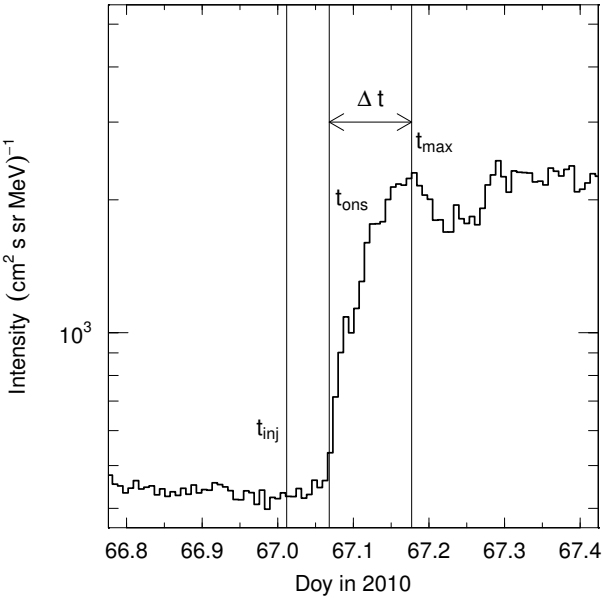

Fig. 2: Onset and maximum time determination for STEREO A observations of the Mar 7, 2012 event. The increase in 55-105 keV electrons has been detected by the SEPT instrument in the Sun sector. The three horizontal lines mark (from left to right) the type III radio burst onset time (t_{inj}), the electron onset time (t_{ons}), and the electron maximum time (t_{max}), respectively (c.f. Table 2). The rise time of the event is the time from electron onset to electron maximum (Δt).

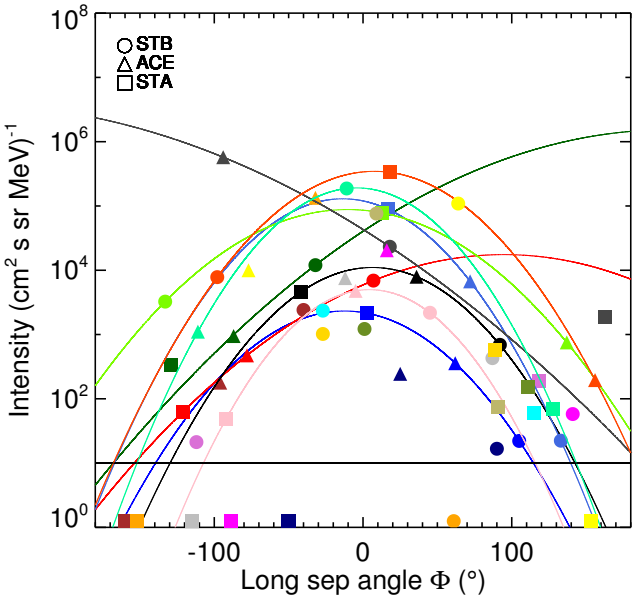

Fig. 3: Maximum intensities as function of longitudinal separation angle. Positive separation angles denotes a source to the west, negative angles mark a source to the east of the spacecraft magnetic footpoint. Observations of the same event are marked by the same color. Points lying on the horizontal axis denote no observations due to different reasons (c.f. Tables 2 and 3). The curves represent Gaussian fits (Eq. 1) for the three-spacecraft events.

crucial parameter in characterizing the properties of their transport. For energetic electrons the anisotropy is mainly determined by the balance between the effect of focusing and the degree of scattering at magnetic fluctuations. If the measurement reveals a strong anisotropy the particles are assumed to have propagated relatively scatter-free and a good magnetic connection to the source region must have been present. The more scattering the particles experience during their travel, the more isotropic the flux becomes and the directionality is washed out. Usually the anisotropy is strongest during the onset of an event while the flux isotropizes during the decay phase. Sometimes a long-lasting injection at the Sun can lead to a persisting anisotropy also in the decay phase.

To obtain the anisotropy we employ sectored intensity measurements taken by the STEREO/SEPT and ACE/EPAM instruments which provide four and eight different viewing sectors, respectively. For details see Section 2. The anisotropy A is defined as

$$A = \frac{3 \int_{-1}^{+1} I(\mu) \cdot \mu \cdot d\mu}{\int_{-1}^{+1} I(\mu) \cdot d\mu} \quad (2)$$

where $I(\mu)$ is the pitch angle dependent intensity measured in a given viewing direction and μ is the average pitch angle cosine for that direction. Omni-directional intensities were calculated by integrating second-order polynomial fits to the pitch angle dependent intensities $I(\mu)$ using five minute averages of the data. To stabilize the fit during periods of poor pitch angle coverage an artificial point was added to the pitch angle distribution to fill the uncovered range (cf., Dröge et al. 2014). Fig. 8 shows STEREO B measurements during the August 14, 2010 SEP event which serves as a good example of an anisotropic event. The upper panel shows the time series of the intensity in color coding as a function of pitch angle. Below the 55-105 keV electron intensity measured by the four SEPT telescopes SUN, ANTI-SUN, NORTH, and SOUTH are shown. The third panel shows the anisotropy as deduced from the pitch angle dependent intensity measurements. The anisotropy reaches a maximum of 1.93 during the onset of this event. The four panels below show the magnetic field latitudinal and azimuthal angles, the magnetic field magnitude, and the solar wind speed.

The maximum anisotropies were now determined for each of the observations of the listed events. Therefor, just the rising phases of the events were considered. If a later contribution by a shock was present, this was not taken into account. Although the anisotropies show an overall dependence on the longitudinal separation angle, the dependence is not as clear as for peak intensities or onset delays. We see different kind of distributions and, therefore, separate the events into three classes of comparable observations:

(1) Significant anisotropy is observed at a well-connected spacecraft ($\phi < 50°$) but almost no anisotropy at a far separated spacecraft (A < 0.6 at $\phi > 60°$, with ϕ being the longitudinal separation angle). The 17 May 2012 event is an example for this class (see Fig. 9 and discussion below).

(2) The highest anisotropy is observed by the best connected spacecraft but significant anisotropy (A > 0.6) is still observed at far separated positions ($\phi > 60°$). Fig. 11 shows the 7 March 2012 event, serving as an example for class (2).

(3) The highest anisotropy is not observed by the best-connected

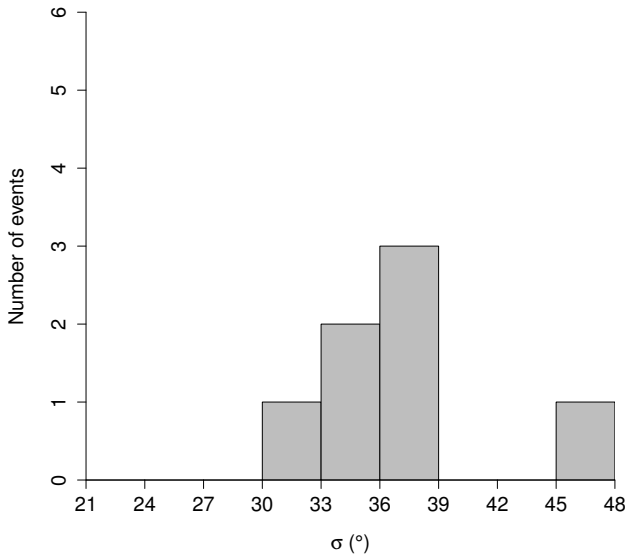

Fig. 4: Distribution of σ-values of the fits shown in Fig. 3, where fits yielding a $|\phi_0| > 90°$ were excluded.

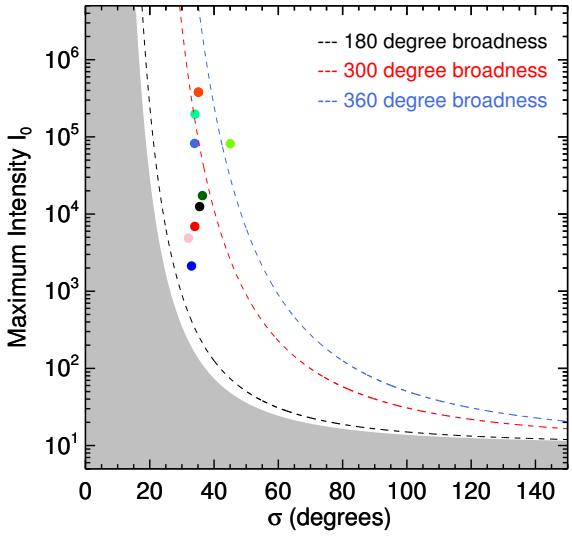

Fig. 6: The same as Fig. 5 but the points were determined using a symmetric Gaussian fit, which was forced to be centered around $\phi_0 = 0°$.

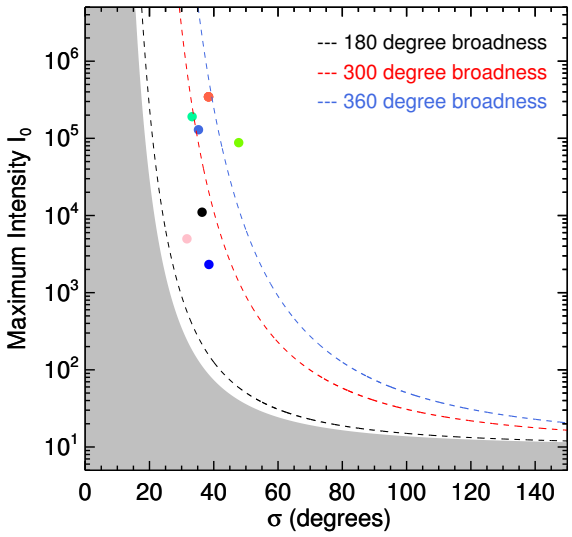

Fig. 5: Parameters I_0 as function of σ of the fitted curves of Fig. 3 representing the longitudinal broadnesses of the events. Broadnesses of 180 degrees, 300 and 360 degrees are indicated by dashed lines. The gray shaded area cannot be filled by definition through the event selection criteria.

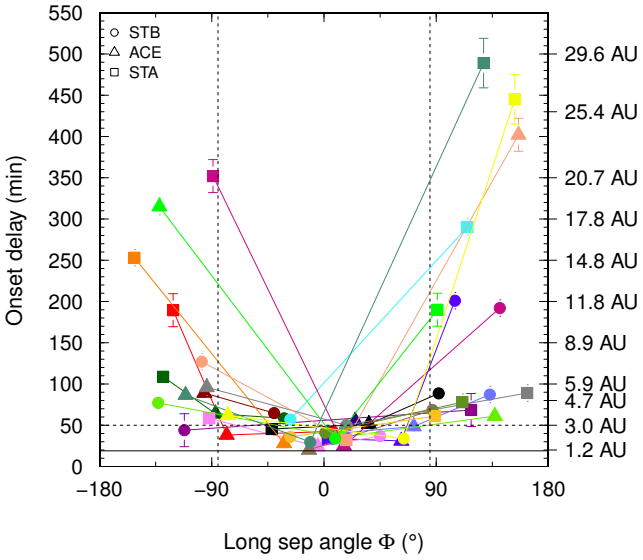

Fig. 7: Onset delay (delay between type III onset and electron onset time at the spacecraft) of the events as function of longitudinal separation angle. A correction of 8.3 minutes for light travel time has been applied. The numbers on the right hand vertical axis correspond to distances, the 55-105 keV electrons would travel during the corresponding delay (displayed on the left hand vertical axis).

spacecraft but by a further-separated one. This is the case in the 14 Aug 2010 event, presented in Fig. 12.

Each of the Figures 9 to 12 shows from top to bottom the time series of the intensity in color coding as a function of pitch angle, the pitch angle of each of the four telescopes, the 55-105 keV electron intensity as measured in the four telescopes, and the anisotropy, respectively. Fig. 9 presents observations of the event on May 17, 2012 which was the first Ground Level Enhancement (GLE) of solar cycle 24 (Heber et al. (2013); Gopalswamy et al. (2013); Papaioannou et al. (2013)). While ACE (shown in the middle figure) is well-connected to the source flaring AR ($\Phi = 16$) and observes a clear anisotropic event, STEREO A and B are separated by 89 and 141 degrees, respectively. Although both STEREO spacecraft detect a significant intensity increase, both increases are rather isotropic.

Fig. 11 shows the event on March 7, 2012, which is an example of class (2) where both of the angular far separated spacecraft

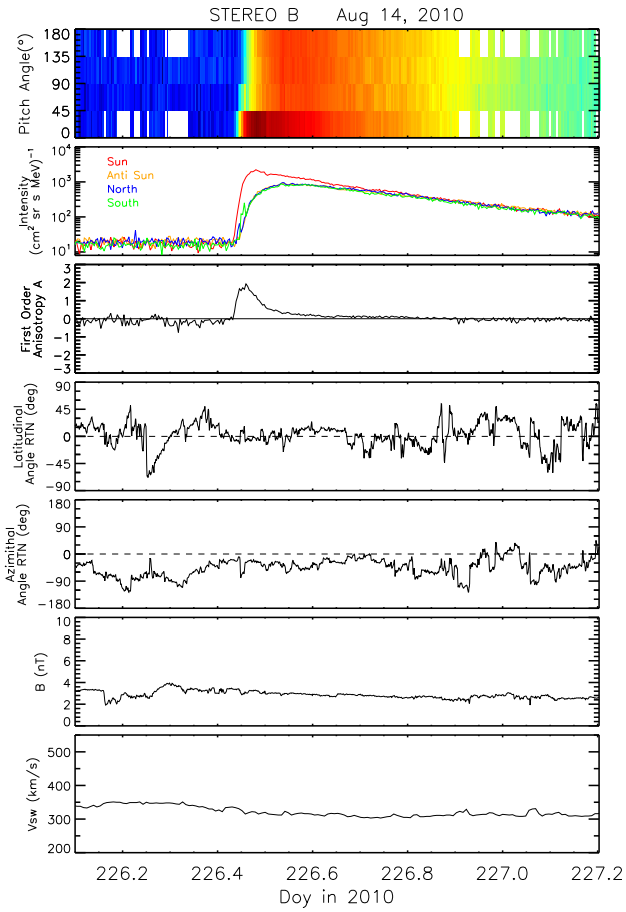

Fig. 8: In-situ observations during the Aug 14, 2010 SEP event observed by STEREO B. From top to bottom: Pitch angle dependent intensity distribution in color coding, intensity measured in each of the above telescopes (Sun (red), Anti Sun (orange), North (blue), and South (green)), anisotropy, magnetic field latitudinal and azimuthal angles, magnetic field magnitude, and solar wind speed.

still observes significant anisotropy. Here, STEREO B (middle figure) is the best connected spacecraft (Φ = 64) and ACE and STEREO A are separated by 77 and 153 degrees, respectively.
Fig. 11 shows an event of class (3) which occurred on August 14, 2010. Although ACE (middle figure) is the best connected (Φ=-5°) spacecraft, and observes the highest intensity, and although the footpoint of STEREO B was 15° away from the flare longitude, STEREO B observes stronger anisotropy. The absolute maximum value is 1.93 which is twice the value observed by ACE (1.05). Interestingly enough STEREO A, separated by 92 degrees, observes no significant anisotropy during this event.
Fig. 12 illustrates the statistics of the absolute anisotropy maxima for the events under study observed by the three spacecraft as a function of longitudinal separation angle. The left panel of Fig. 12 shows the anisotropies of events in class (1), the middle panel events of class (2), and events of class (3) are shown in the right panel, respectively.
Black and red symbol fillings denote good or poor pitch angle coverage, respectively. In cases of poor pitch angle coverage (<90 degrees) the anisotropy rather serves as lower limit.
Wibberenz & Cane (2006) argue that the onset delays and times to maximum are correlated due to the propagation conditions. Thus Fig. 13 shows the onset delay as a function of the rise time of each event. The events have been again separated into the three classes as derived from the anisotropy distribution. The Pearson correlation coefficient of each set of points is displayed at the top right of each panel. The points in class (1) show a correlation of c=0.76. Class (2) shows an even larger correlation of c=0.85. Only the points of class (3) do not correlate (c=0.05). Even if we exclude the point, which is far from the rest of the points (onset delay ~290 min), the correlation coefficient stays low at c=0.34.

5. Discussion and conclusion

Varying anisotropy distributions could serve as one of the key informations to disentangle source and transport processes. Fig. 14, therefore, sketches three different source and transport scenarios which are in agreement with such variable anisotropy distributions as presented above. While in Fig. 14a) just a small source region at the Sun (flare) is present (yellow star), the scenarios in Fig. 14b), and c) comprise an extended source region at the Sun (red arc). Such an extended source region may be created by coronal transport (c.f. Reinhard & Wibberenz (1974); Newkirk & Wentzel (1978); Klein et al. (2008)) and may be supported by a large (coronal) shock (Cliver et al. 1995) and/or an EUV wave (Rouillard et al. (2012); Park et al. (2013)). However, none of the suggested lateral transport mechanisms can be favored due to our analysis. In all three diagrams red areas mark regions of strong anisotropy, because here a good connection to the source is present. This region is rather narrow in scenario a). Scenario a) is in agreement with the observations of anisotropy class (1) (Fig. 12 left). Here, just a good-connected observer detects an anisotropic increase but far-separated spacecraft observe an isotropic event. Thus SEPs reach far-separated positions just due to strong perpendicular diffusion, with vanishing anisotropies (represented by the gray areas). The intensity increase at the spacecraft is consequently more gradual here and starts later. The presence of perpendicular transport in the IP medium is represented by the wavy magnetic field lines in the sketches. Note, that these stand for wandering magnetic field lines as well as perpendicular diffusion through scattering.
In scenario b) the SEPs are injected over a much wider angular range at the Sun and under normal conditions particles will arrive at Earth having a noticeable anisotropy. The result is therefore a significant anisotropy over a larger longitudinal extent correlated with the extent of this source region which is in agreement with observations in class (2) (Fig. 12 center). Here, the best-connected observer detects the largest anisotropy but further-separated spacecraft still observe significant anisotropies during the rising phase of the event. Note that the anisotropy is always higher close to the Sun which is indicated by darker colors in the red and blue areas.
Because the angular distribution of the particles close to the Sun may take some time, we expect a larger onset delay in the outer regions (shaded in red and blue in Fig. 12b)). If no strong scattering is present, however, a rather short rise time is expected. However note, that a prolonged injection time can also cause a more gradual increase of the event. Due to field line random walk or due to an outwards weakening source region at the Sun, a region of medium anisotropy is formed (blue areas). Further out, the situation is again as in scenario a). In the gray region no anisotropy is present any more because the particles reached these positions due to strong scattering.

The anisotropy class (3) comprises all events which are left (Fig. 12 right). These events are more challenging to explain because the best-connected spacecraft does not observe the highest anisotropy but a further-separated spacecraft does. Scenario c) (Fig. 14c)) illustrates one possible situation leading to such situation. Here, an extended source region is also present but the propagation conditions in the IP medium strongly vary so that a nominally best-connected spacecraft may not observe the highest anisotropy because of a smaller parallel mean free path in this region. A neighboring spacecraft, however, may detect the highest anisotropy because of a rather scatter-free transport to its position. To investigate such varying propagation conditions, detailed modeling would be required.
However, also pre-event CMEs or large IP flux rope structures could produce class-(3) observations when a better connection to a further-separated spacecraft is provided than to the nominally best-connected one (c.f. Richardson et al. (1991); Gómez-Herrero et al. (2006); Leske et al. (2012); Lario et al. (2013)). One of our class-(3) events is the Aug 18, 2010 event, which has been analyzed by Leske et al. (2012), who found a pre-event CME to play a major role for the STEREO A observations. Note, that if a specific structure would play a major role, we would also expect the peak intensities to follow this changed ordering. But just one event of the studied sample does not follow the expected ordering in peak intensities, which is the Mar 7, 2012 event, and this event appears in class (1). Another possibility is the presence of sympathetic activity, so that the observations at the different spacecraft were not necessarily associated to the same solar event. However, a careful inspection of all available data from optical (EUV) and radio observations suggests that any additional and sympathetic activity can be excluded here. Furthermore, noisy data, local intensity spikes and limited pitch angle coverage can cause varying uncertainties in the anisotropy.

Perpendicular diffusion is known to be a rather slow process (Jokipii (1966); Dröge et al. (2010)) due to the much smaller perpendicular diffusion coefficient. If strong perpendicular transport is present, the events tend to be more gradual (larger rise times) and start later (larger onset delays). Especially with increasing longitudinal separation angle these numbers increase even more due to the increasing path length of the particles. Thus, we expect the events showing the largest onset delays and rise times to appear in class (1). Furthermore, a correlation between onset times and rise times should be present in class (1). Figure 13 plots these values against each other for the different anisotropy classes. Figure 13 a) shows only observations of class (1), 13 b) of class (2), 13 d) of class (3), and 13 c) combines class-(1) and class-(2) events, respectively. The largest onset delays and rise times indeed tend to appear in class (1), however, also class (2) shows some strongly delayed events. In agreement with our expectations there is no correlation between onset delays and rise times for class-(3) events, probably supporting the idea of large-scale structures in the magnetic field changing the overall geometry. However, although there is some correlation for class-(1) events (c=0.76), the same is true for class-(2) events, where the correlation coefficient is c=0.85. If a large SEP distribution close to the Sun is the dominant process for the wide spread of class-(2) events, we might expect an increasing onset delay with increasing separation angle because the coronal transport to far points may also take some time, however, this does not account for an increasing rise time of the events. However, we do not find a significant difference in the linear fits to class-(1) and class-(2) events. Nevertheless, the correlations for class (1) and class (2) as well as any combination of the events in these classes do not change significantly. Therefore, we conclude that both, an extended distribution close to the Sun as well as perpendicular transport in the IP medium exist at the same time (c.f. Fig. 14b)) for both classes. We therefore expect the limit between class (1) and class (2) to be a smooth one. If an event appears in one or the other class depends just upon the individual importance of an extended source vs. perpendicular diffusion but is also influenced by the specific magnetic connection of the spacecraft and the flaring AR during the event. In order to investigate the event to event variations and the specific dominance of the different mechanisms, detailed modeling of the events would be required (e.g. Dröge et al. (2010); Kallenrode et al. (1992); Dröge et al. (2014)).

All but one event of our sample are accompanied by a CME. 18 out of the 21 events (86 %) show an associated type II radio burst, marking the presence of a shock. Interestingly, two of the three events lacking a type II radio burst are class-(2) events, suggesting that a shock may not be the key ingredient for the wide SEP distribution close to the Sun. This is also the conclusion by Dröge et al. (2014), who studied one of these events, the 7 February 2010 event, in detail and suggest that the lateral transport of the SEPs in this event occurs partially close to the Sun and partially in the IP medium. Furthermore, all of the events in our sample are accompanied by EUV waves (see Table 1). Recently, Rouillard et al. (2012) and Park et al. (2013) have pointed out that the propagation of an EUV front may be spatially and temporally linked to the SEP release and, therefore, to the observed onset delays. Other authors, however, question such a correlation (Miteva et al. 2014) and lots of EUV waves are observed at well-connected positions without any associated SEP increase.

6. Summary

We present a sample of wide-spread solar (55-105 keV) electron events observed by the two STEREO spacecraft, and ACE. As a wide-spread event we request a longitudinal separation angle of flare to spacecraft magnetic footpoint of at least 80 degrees for one spacecraft. The sample contains 21 events from November 2009 up to August 2013. The observations have been investigated in a statistical manner in terms of peak intensities (Fig. 3), onset delays (Fig. 7) and maximum anisotropies (Fig. 12). We approximate the longitudinal variation of peak intensities with Gaussian distributions and find a mean standard deviation of $\sigma = 37.3°$. From the fitted maximum intensities and standard deviations we derive the actual longitudinal event broadnesses at 1 AU as the longitudinal ranges spanned by the fitted Gaussians until these reach a characteristic background value. In contrast to the longitudinal range spanned by the spacecraft observing the event, the longitudinal broadness represents the longitudinal range over which the event is detectable. The broadnesses of the analyzed events all lie above 180 degrees with several events turning out to be ∼300 degree wide events at 1 AU.
While all events but one show the expected peak intensity distribution of highest intensity at the best-connected spacecraft and decreasing intensity with increasing separation angle (Fig. 3), the dependence is not so obvious for the onset delays. Although a clear overall dependence on the separation angle is observed in the whole sample, several events show deviations from that and a strong event to event variation is present. Some onsets are even delayed by 300 to 500 minutes, which corresponds to the time these electrons would need to travel a distance of ∼ 20 AU. This

corresponds to an effective path length from the Sun to Jupiter.

As a key characteristic we also investigate the longitudinal variation of maximum anisotropies observed at the individual spacecraft during the rising phases of the events. The overall dependence on the longitudinal separation angle is even less clear. To describe the different anisotropy distributions we define three classes: Class (1) comprises events showing high anisotropy at small longitudinal separations ($\phi < 50°$) and no anisotropy at far longitudinal separations ($\phi > 60°$). The observations of this class (Fig. 12 left) are in agreement with what we expect if perpendicular diffusion in the IP medium plays the main role for the particle spread. Events of class (2) also show the highest anisotropy at the best and well-connected spacecraft but significant anisotropy is still observed at a far separated point ($\phi > 60°$, Fig. 12 center). To obtain such observations a wide SEP distribution close to the Sun is required. Class (3) contains the rest of the events, which always show higher anisotropy at a further-separated spacecraft than at the best-connected spacecraft. These events cannot be explained by either just perpendicular diffusion in the IP medium or an extended SEP distribution close to the Sun but rather suggest to be produced by special IP magnetic configurations or by strong spatial variations in the propagation conditions.

For the same classes as defined for the anisotropy distributions we determined the correlation between onset delay and rise time of the events. A correlation of these two parameters is expected if perpendicular diffusion is present. However, although the class-(3) events show no correlation, both class-(1) and class-(2) events show some correlation. This may suggest that even if an extended SEP distribution close to the Sun is needed to explain the observed anisotropies of class-(2) events, perpendicular transport is also present. In the same sense it is conceivable that a pre-spreading for the class-(1) events happens already close to the Sun before perpendicular transport in the IP medium begins to operate. Which mechanisms in detail are responsible for a widening of the SEP distribution close to the Sun is not clear. It may be any coronal transport process as proposed by e.g. Reinhard & Wibberenz (1974); Newkirk & Wentzel (1978); Klein et al. (2008). Recently EUV waves, which accompany all of our events, get in favor to be associated to the SEP spreads (Rouillard et al. (2012); Park et al. (2013)). Furthermore, the presence of type II radio bursts as indication for a shock in 87% of our events and CMEs, which are almost always present may be important ingredients.

From our analysis we conclude that wide-spread SEP events are not always produced by the same and only one mechanism but rather different processes are capable of spreading the SEPs over large longitudinal ranges. We find three different classes of events with respect to their anisotropy distributions which suggest, that perpendicular transport in the IP medium on the one hand and a wide particle spread close to the Sun on the other hand play the major roles for the majority of the events studied here. It is likely that a combination of these (and probably other) mechanisms is present for the investigated events, however, the importance of the different processes may vary from event to event.

Acknowledgements. We acknowledge the STEREO PLASTIC, IMPACT, SECCHI, EIT and Wind teams for providing the data used in this paper. The STEREO/SEPT Chandra/EPHIN and SOHO/EPHIN project is supported under grant 50OC1302 by the Federal Ministry of Economics and Technology on the basis of a decision by the German Bundestag. We acknowledge the SEPserver project under grant agreement no. 262773. R. Gómez-Herrero acknowledges the financial support from the Spanish Ministerio de Ciencia e Innovación under project AYA2011-29727-C02-01. Y.K. was also partially supported by program No.22 of the Russian Academy of sciences

References

Acuña, M. H., Curtis, D., Scheifele, J. L., et al. 2007, Space Sci. Rev., 136, 203
Bougeret, J. L., Goetz, K., Kaiser, M. L., et al. 2008, Space Sci. Rev., 136, 487
Bougeret, J. L., Kaiser, M. L., Kellogg, P. J., et al. 1995, Space Sci. Rev., 71, 231
Brueckner, G. E., Howard, R. A., Koomen, M. J., et al. 1995, Sol. Phys., 162, 357
Cane, H. V., McGuire, R. E., & von Rosenvinge, T. T. 1986, ApJ, 301, 448
Cliver, E. W., Kahler, S. W., Neidig, D. F., et al. 1995, 24th International Cosmic Ray Conference (Rome), 257
Cliver, E. W., Thompson, B. J., Lawrence, G. R., et al. 2005, 29th International Cosmic Ray Conference (Pune), 121
Dalla, S. 2003, Geophys. Res. Lett., 30
Dresing, N., Gómez-Herrero, R., Klassen, A., et al. 2012, Sol. Phys., 281, 281
Dresing, N., Gómez-Herrero, R., Klassen, A., et al. 2013, Proc. 33rd Internat. Cosmic Ray Conf. (Rio de Janeiro), paper 0611
Dröge, W., Kartavykh, Y. Y., Dresing, N., Heber, B., & Klassen, A. 2014, J. Geophys. Res., submitted
Dröge, W., Kartavykh, Y. Y., Klecker, B., & Kovaltsov, G. A. 2010, ApJ, 709, 912
Galvin, A. B., Kistler, L. M., Popecki, M. A., et al. 2008, Space Sci. Rev., 136, 437
Gold, R. E., Krimigis, S. M., Hawkins, I. I. I. . S. E., et al. 1998, Space Sci. Rev., 86, 541
Gómez-Herrero, R., Klassen, A., Müller-Mellin, R., Heber, B., & Wimmer-Schweingruber, R. F. 2006, in ESA Special Publication, Vol. 617, SOHO-17. 10 Years of SOHO and Beyond
Gopalswamy, N., Xie, H., Akiyama, S., et al. 2013, ApJ, 765, L30
Heber, B., Dresing, N., Dröge, W., et al. 2013, Proc. 33rd Internat. Cosmic Ray Conf. (Rio de Janeiro), paper 0746
Howard, R. A., Moses, J. D., Vourlidas, A., et al. 2008, Space Sci. Rev., 136, 67
Hsieh, K. C. & Simpson, J. A. 1970, ApJ, 162, L191
Jokipii, J. R. 1966, ApJ, 146, 480
Kallenrode, M.-B. 1993, J. Geophys. Res., 98, 5573
Kallenrode, M.-B., Wibberenz, G., & Hucke, S. 1992, ApJ, 394, 351
Klassen, A., Gómez-Herrero, R., Heber, B., et al. 2012, A&A, 542, A28
Klein, K.-L., Krucker, S., Lointier, G., & Kerdraon, A. 2008, A&A, 486, 589
Krucker, S., Larson, D. E., Lin, R. P., & Thompson, B. J. 1999, ApJ, 519, 864
Laitinen, T., Dalla, S., & Marsh, M. S. 2013, ApJ, 773, L29
Lario, D., Aran, A., Gómez-Herrero, R., et al. 2013, ApJ, 767, 41
Lemen, J. R., Title, A. M., Akin, D. J., et al. 2012, Sol. Phys., 275, 17
Leske, R. A., Cohen, C. M. S., Mewaldt, R. A., et al. 2012, Sol. Phys., 281, 301
Lin, R. P. & Hudson, H. S. 1976, Sol. Phys., 50, 153
Marsh, M. S., Dalla, S., Kelly, J., & Laitinen, T. 2013, ApJ, 774, 4
Mason, G. M., Gloeckler, G., & Hovestadt, D. 1984, ApJ, 280, 902
McComas, D. J., Bame, S. J., Barker, P., et al. 1998, Space Science Reviews, 86, 563
Miteva, R., Klein, K.-L., Kienreich, I., et al. 2014, Sol. Phys., accepted
Müller-Mellin, R., Böttcher, S., Falenski, J., et al. 2008, Space Sci. Rev., 136, 363
Newkirk, Jr., G. & Wentzel, D. G. 1978, J. Geophys. Res., 83, 2009
Papaioannou, A., Souvatzoglou, G., Paschalis, P., Gerontidou, M., & Mavromichalaki, H. 2013, Sol. Phys.
Park, J., Innes, D. E., Bucik, R., & Moon, Y.-J. 2013, ApJ, 779, 184
Reames, D. V. 1999, Space Sci. Rev., 90, 413
Reinhard, R. & Wibberenz, G. 1974, Sol. Phys., 36, 473
Richardson, I. G., Cane, H. V., & von Rosenvinge, T. T. 1991, J. Geophys. Res., 96, 7853
Rouillard, A. P., Sheeley, N. R., Tylka, A., et al. 2012, ApJ, 752, 44
Smith, C. W., L'Heureux, J., Ness, N. F., et al. 1998, Space Science Reviews, 86, 613
Torsti, J., Kocharov, L., Teittinen, M., et al. 1999, J. Geophys. Res., 104, 9903
Wibberenz, G. & Cane, H. V. 2006, ApJ, 650, 1199
Wiedenbeck, M. E., Mason, G. M., Cohen, C. M. S., et al. 2013, ApJ, 762, 54
Zhang, M., Qin, G., & Rassoul, H. 2009, ApJ, 692, 109

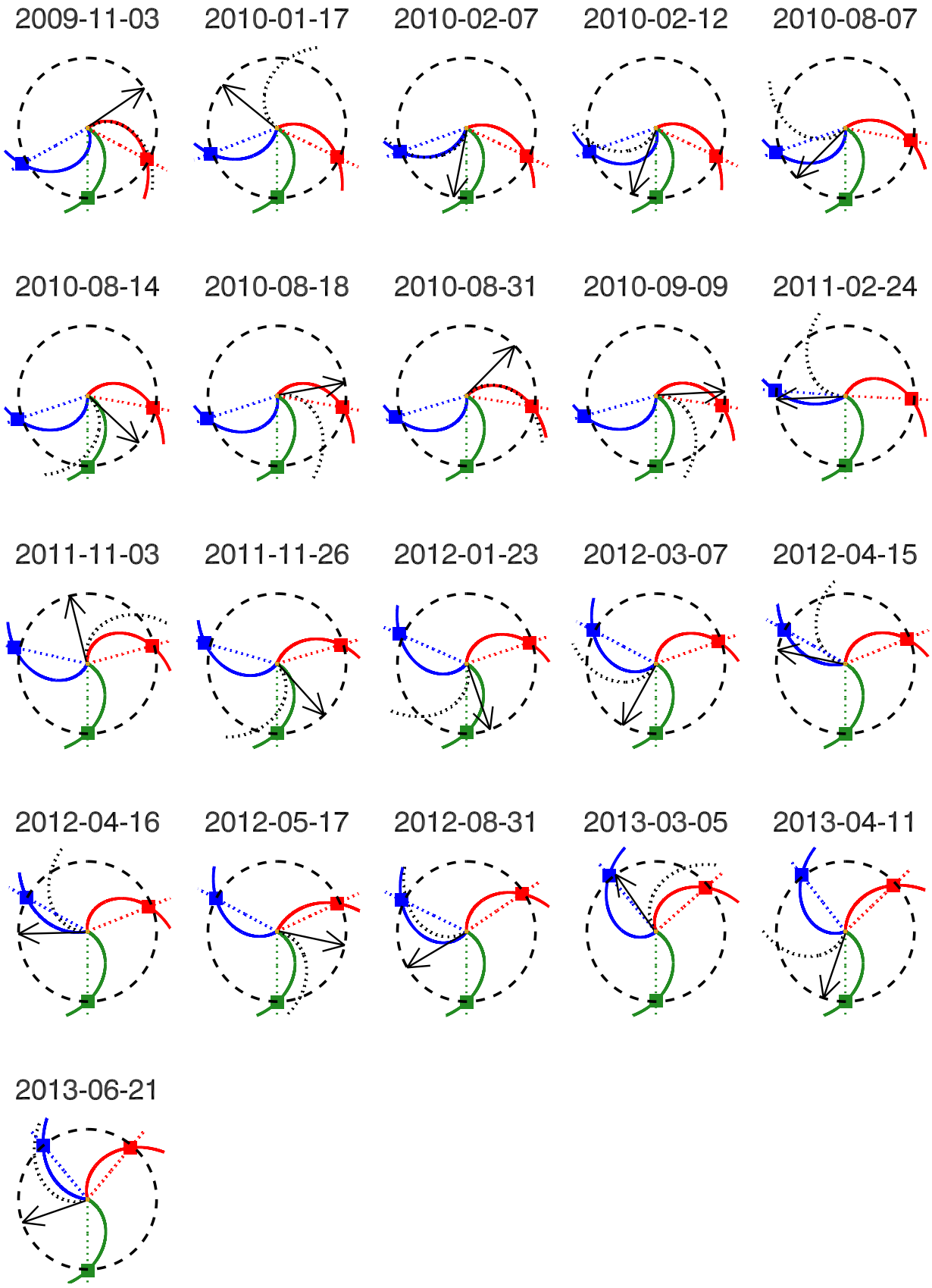

Fig. 1: Longitudinal configurations of spacecraft and source active regions for each of the analyzed events. The arrow marks the longitude of the flaring source active region, the dotted black spiral is the nominal Parker field line originating from the source region. The colored spirals represent the magnetic field lines connecting the spacecraft to the Sun correspondent to the measured solar wind speed. The dotted colored lines mark the longitudinal positions of each spacecraft where blue marks STEREO B, red STEREO A, and green ACE, respectively.

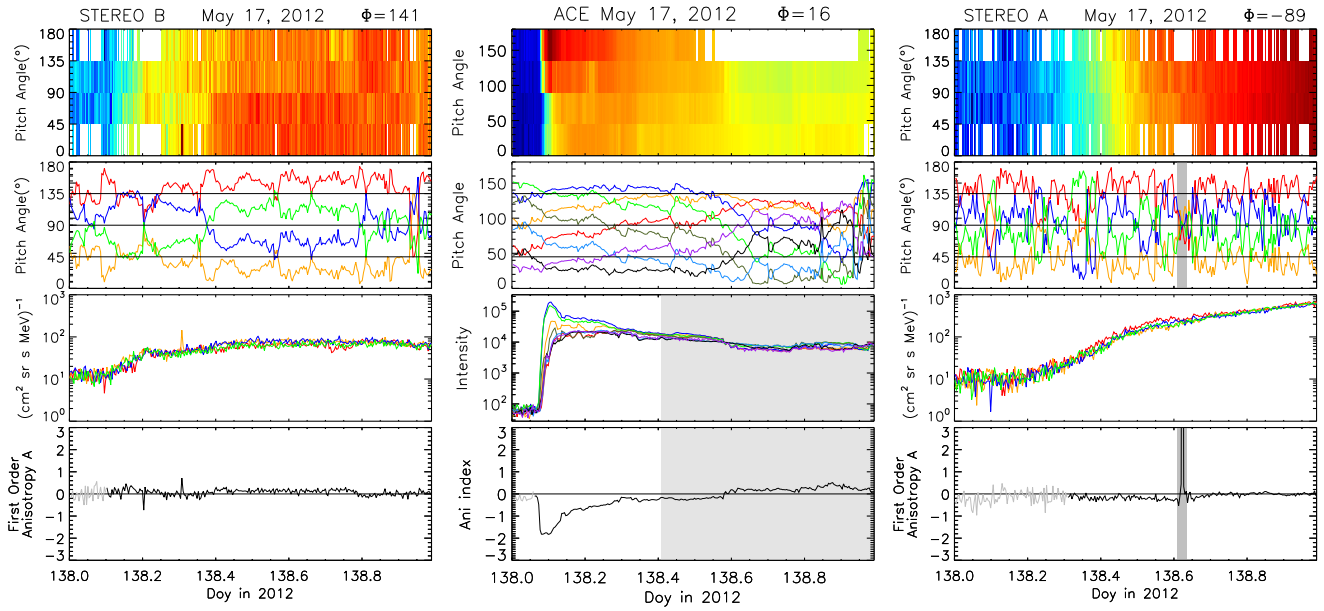

Fig. 9: Anisotropy and intensity time profiles of the SEP event on May 17, 2012 observed by STEREO B (left), ACE (middle), and STEREO A (right). Anisotropy plotted in lighter color denotes periods of background intensity for which the anisotropy calculation is very uncertain. Gray shading in ACE observations marks a period where the electron measurements (and following the anisotropy) are contaminated by ions. The small shaded area in STEREO A measurements denotes a period of very poor pitch angle coverage leading to an incorrect anisotropy determination.

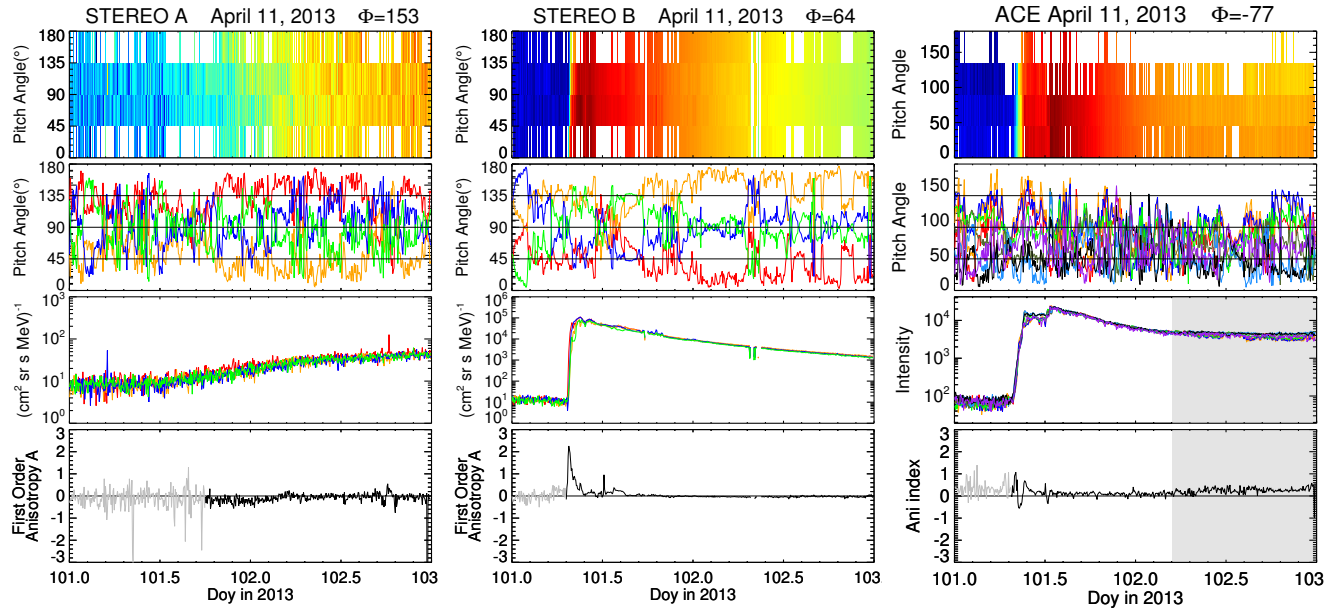

Fig. 10: Anisotropy and intensity time profiles of the April 11, 2013 SEP event observed by STEREO A (left), STEREO B (middle), and ACE (right). Anisotropy plotted in lighter color denotes periods of background intensity for which the anisotropy calculation is very uncertain. The gray shaded area in the ACE plot marks a period of ion contamination.

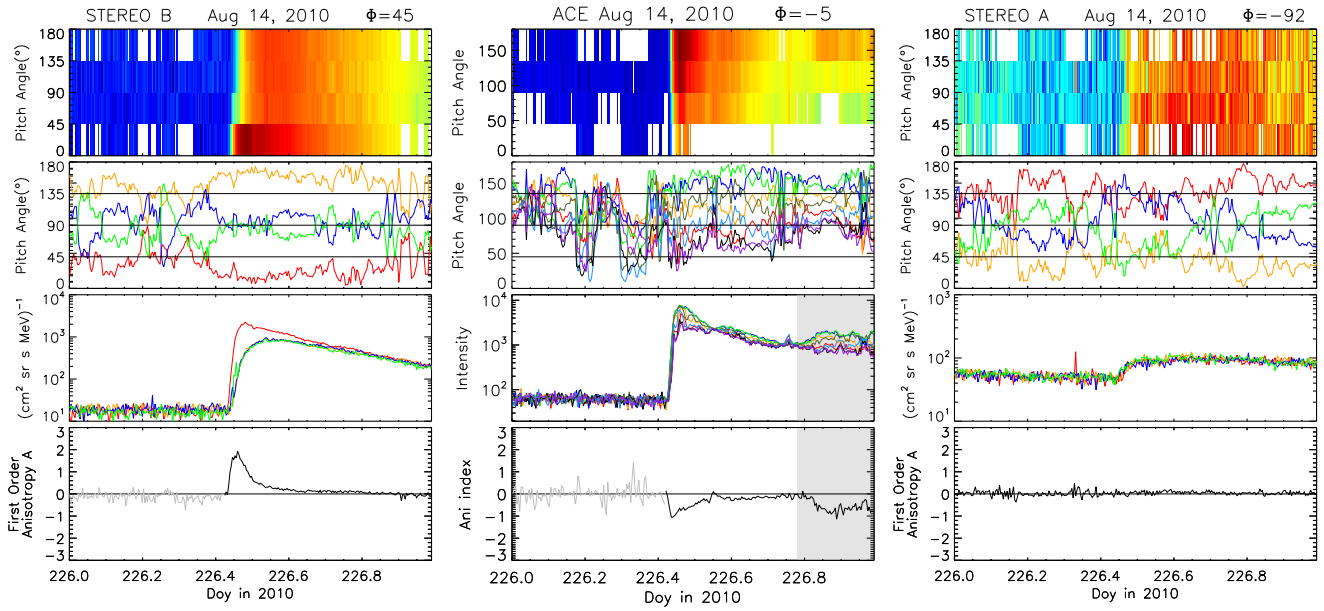

Fig. 11: Anisotropy and intensity time profiles of the SEP event on Aug 14, 2010 observed by STEREO B (left), ACE (middle), and STEREO A (right). Anisotropy plotted in lighter color denotes periods of background intensity for which the anisotropy calculation is very uncertain. The gray shaded area in ACE anisotropy and intensity marks a period of ion contamination which saturates the electron measurements and leads to an incorrect anisotropy determination.

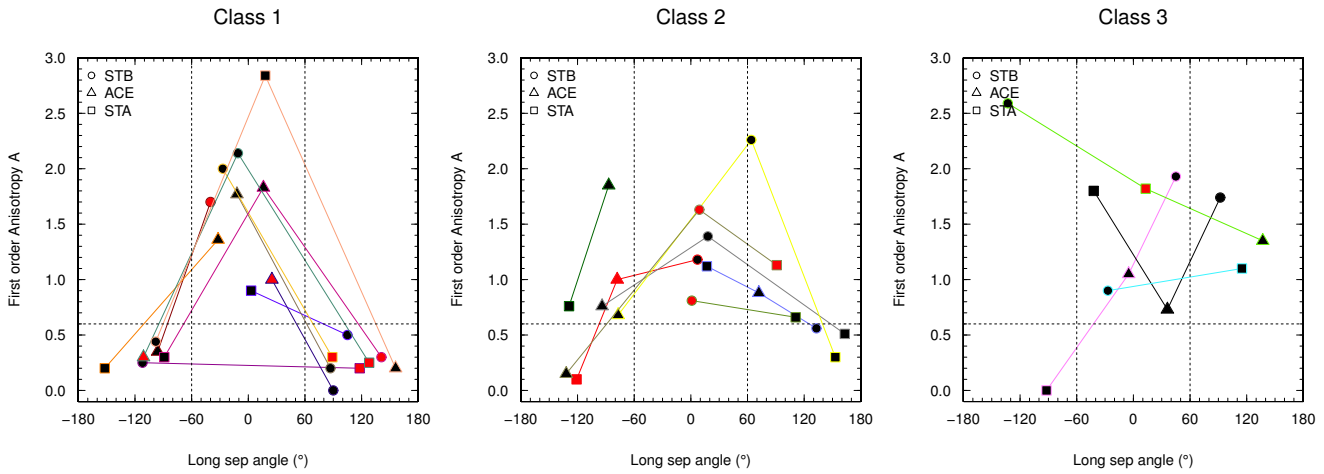

Fig. 12: Maxima of absolute anisotropies observed during the early phases of the events. The observations have been ordered into three different classes (see text) which appear in the left, middle, and right part of this figure. Red symbol fillings denote that the anisotropy may be underestimated due to poor pitch angle coverage, black fillings means, that the pitch angle coverage was sufficient. The dashed lines mark the boarders defining the different anisotropy classes (see text).

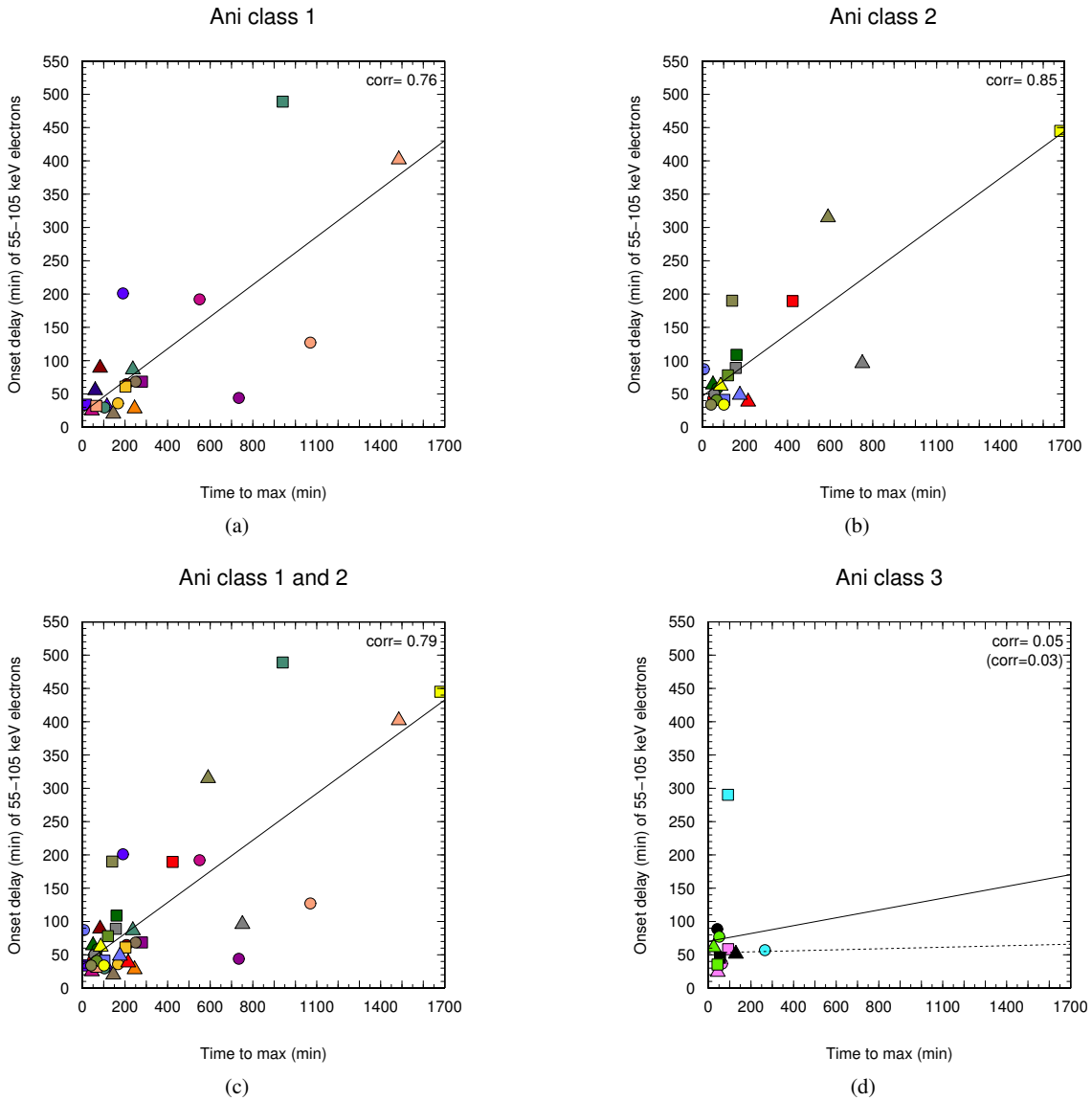

Fig. 13: Onset delay (type III to electron onset) as function of the rise time of the events. Panel (a) comprises only measurement of class (1), (b) of class (2) and (d) of class (3), respectively. Panel (c) combines class-(1) and class-(2) events. The Pearson correlation coefficient of each group is presented at the top right of each panel, the solid line represents the corresponding fit. The value in brackets of panel (b) describes the correlation if the yellow point to the right is excluded, the value in brackets in panel (d) is the correlation when excluding the top cyan point. The dashed lines correspond to these correlations.

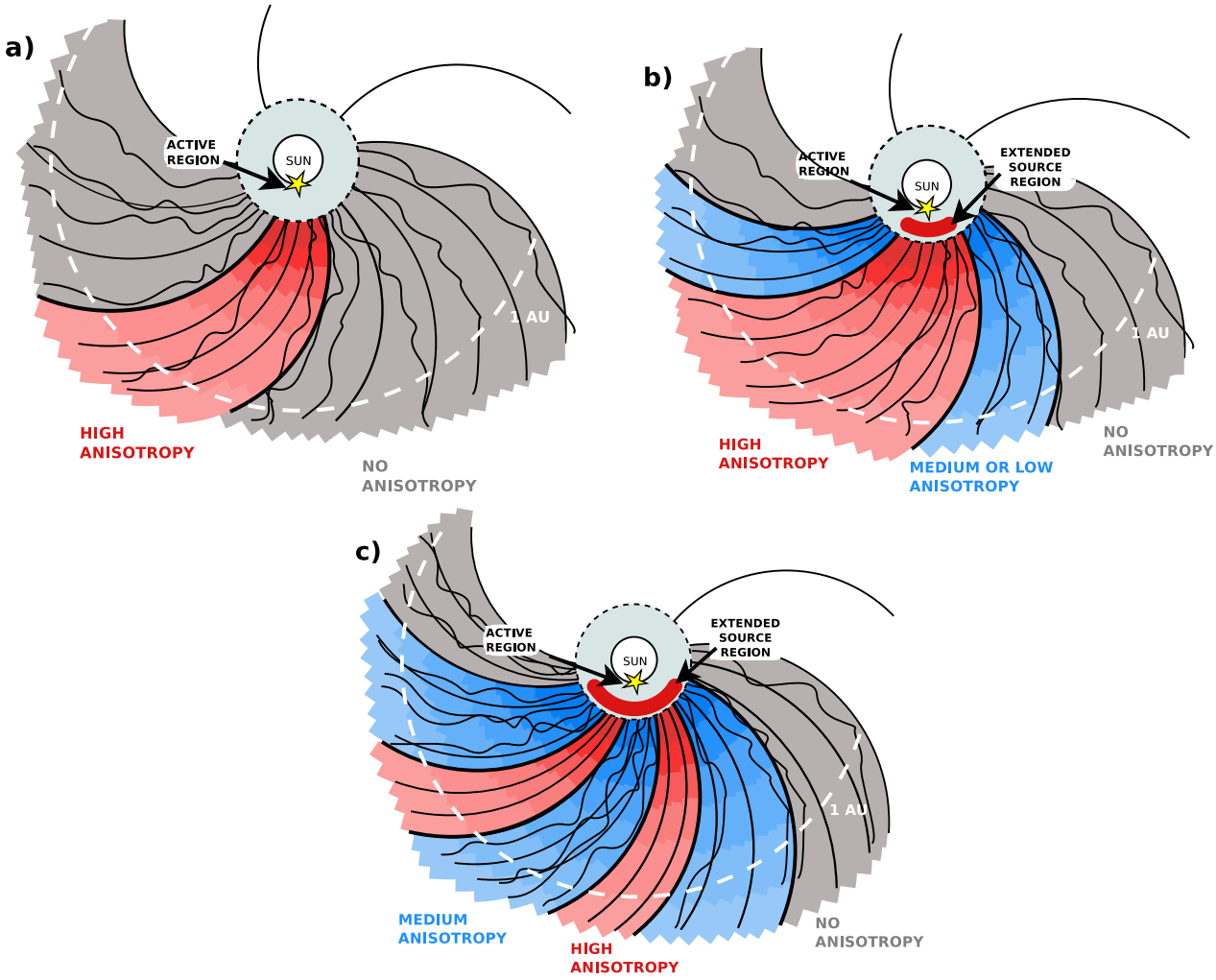

Fig. 14: Regions of varying anisotropy for different source and transport processes. Each diagram describes a wide-spread event extending over all the colored range. While scenario a) represents a small source region at the Sun (yellow star), an additional extended source region is present in scenario b) and c), represented by the red arc. Reddish areas mark regions where strong anisotropy is observed, blue regions mark medium anisotropy while gray areas are regions where no anisotropy can be measured any more. Wavy magnetic field lines represent regions where perpendicular transport in the IP medium is present.

6 SUMMARY AND CONCLUSIONS

Energetic particle increases observed in the heliosphere are always determined by a combination of their underlying acceleration, injection, and propagation mechanisms. A full description of the observed particle event can only be made once all these aspects are completely understood. While each of the above aspects is still subject to intensive research, the purpose of this thesis was to contribute to the full picture by employing multi-spacecraft measurements. The two STEREO spacecraft which were launched into Earth-like orbits around the Sun provide an unprecedented platform to analyze the longitudinal nature of energetic particle distributions in the inner heliosphere. Therefore, two particle populations, CIR-associated and solar energetic particles lend themselves for detailed investigations.

Temporal and Spatial Variations of CIRs

While it is known that the structures of CIRs and their associated energetic particle increases can be very stable over large longitudinal ranges and even over several solar rotations, the study presented in Chapter 3 focuses on the agents which can cause variations. Owing to the beneficial orbit of the STEREO spacecraft, dissimilar CIR measurements could be directly associated with latitudinal and longitudinal separations between the spacecraft.

- STEREO could confirm that multiple spacecraft situated at slightly different latitudes can observe completely different solar wind structures leading to unequal CIRs because they are connected to different solar wind source regions changing with latitude.
- Additionally, dissimilar CIR observations which correlate with an increasing longitudinal separation between the spacecraft were observed. This effect could be explained by the presence of temporal coronal hole evolutions. If these solar wind source regions change, the arising CIR also changes.
- A third agent which was found to cause temporal and spatial CIR variations was the presence of a transient structure as an ICME, embedded or in the vicinity of the CIR. While the solar wind structure remained relatively unchanged, the spacecraft observing such interactions always observed stronger 100 keV-ion increases suggesting that the presence of such transient structures amplified the particle acceleration.

The Longitudinal Distribution of SEPs

In contrast to CIR-associated particle increases, the source regions of SEPs at the Sun are far away from the observer increasing the role of the particle transport to

the observer. While it is known that the longitudinal separation of the solar source region to the spacecraft's magnetic footpoint is the main parameter determining the SEP observations (*Lario et al.*, 2006), different mechanisms can lead to similar observations at 1 AU, making it hard to disentangle acceleration, injection, and transport effects. In order to investigate SEP events in terms of their longitudinal distribution, multi-spacecraft observations were employed. After three years since the start of the STEREO mission, the two spacecraft had separated about 150 degrees from each other. When combined with close to Earth spacecraft, these well separated viewpoints provided the opportunity to observe, identify, and study wide-spread SEP events which build the main topic of this thesis. Chapters 4 and 5 discuss two studies which pay special attention to these events showing an unexpectedly wide particle distribution in the inner heliosphere.

- Several events were found which suggest a longitudinal particle spread of up to 360 degrees at a distance of 1 AU to the Sun.

After a detailed study of an individual event (see Section 4.1), a statistical analysis was performed with a sample of 21 wide-spread events (Section 5.1) to shed some light on the physical processes which are involved in creating these remarkably wide particle distributions.

- For the event on 17 January 2010 (Publication 1), very strong and efficient perpendicular transport in the IP medium was found suitable to explain the observations. This is supported by the 3D propagation model which has been applied to the observations. Unfortunately, none of the three spacecraft observing this event was closer connected than ∼100 degrees in longitude, giving us no chance to conclude about an extended particle distribution close to the Sun which would produce anisotropic measurements over a broader longitudinal range than ∼60 degrees. The modeling, however, required an extended source region of 20 degrees in longitude and latitude to fit the observations.

In our statistical study of 21 wide-spread events (Publication 2), we pay special attention to the observed anisotropies.

- While we find events like the 17 January 2010 with no anisotropy observations at longitudinal separations >60 degrees (class (1)), supporting perpendicular transport to be the important process, there are also several events showing anisotropies over large longitudinal ranges (class (2)) which points to a large particle distribution close to the Sun.

- The most accepted candidates producing such a wide particle distribution close to the Sun are coronal transport processes or a coronal shock. However, further mechanisms as large scale disturbances in the solar corona (EUV waves) are under discussion to play a role as well (*Rouillard et al.*, 2012; *Park et al.*, 2013).

- A third type of events we find in our statistical study reminds us that the scenarios creating wide-spread events may be rather complex and may

have different agents. The presence of interplanetary magnetic structures, therefore, could produce these class-(3) events which show larger particle anisotropies at a further separated spacecraft than at the best-connected one. Strongly varying propagation conditions in the IP medium in combination with a large source distribution close to the Sun, however, could also produce these observations.

- An inspection of onset delays and rise times for the three classes of events suggests that there may be no major difference between class-(1) and class-(2) events because a correlation of both parameters is found for both classes, suggesting that perpendicular diffusion plays a role in all these events.

We, therefore, conclude that both perpendicular transport in the IP medium as well as a lateral spread in the corona must be present for the majority of our wide-spread events. The importance of the different processes may vary from event to event, however, the specific positions of the spacecraft with respect to the solar source region can also influence the observations and consequently the classification of the events.

Outlook

Our conclusions agree with recent findings by *Dröge et al.* (2014) who suggest that the wide-spread event on 7 February 2010 was produced by lateral transport partly in the corona and partly in the IP medium. From our analyses we cannot conclude on the nature of the extended source regions at the Sun and on which processes produce these. However, almost all events are accompanied by a CME and an EUV wave. 87% of the events show a type II radio burst as an indication of a propagating shock wave close to the Sun. Which of these agents are important for wide-spread SEP events needs to be investigated in future studies. Furthermore, an extremely large variety of events is observed, ranging from very narrow spike events (c.f. *Klassen et al.* (2011)) up to nearly 360-degree wide SEP events presented here. Certainly different conditions and mechanisms must be present to form these very diverging observations. A qualitative comparison of such different events could contribute to identify the important mechanisms of wide- or narrow-spread events.
In the beginning of 2015 the two STEREO spacecraft will pass each other behind the Sun as seen from Earth. The period around this conjunction will provide STEREO observations of SEP events close to each other. Such observations provide the investigation of small angular variations and possible asymmetries. Together with transport modeling the role of spatially varying propagation conditions will be investigated in more detail. Another important subject is the source distribution of the particles at the Sun: Is there only one source providing the observations at different points? Or are there several varying parts of one source or even different sources? In order to address these questions, a first step will be to compare the injection functions as determined by propagation models for multiple observations of the same events. For this purpose, we hope that the STEREO spacecraft will

observe much more interesting events, and we are looking forward to future missions like the Solar Orbiter to provide new measurements.

BIBLIOGRAPHY

Agueda, N., R. Vainio, D. Lario, and B. Sanahuja: "Injection and Interplanetary Transport of Near-Relativistic Electrons: Modeling the Impulsive Event on 2000 May 1". *Astrophys. J.*, **675**, (2008), 1601–1613.

Altschuler, M. D. and G. Newkirk: "Magnetic Fields and the Structure of the Solar Corona. I: Methods of Calculating Coronal Fields". *Solar Phys.*, **9**, (1969), 131–149.

Bougeret, J. L., K. Goetz, M. L. Kaiser, S. D. Bale, P. J. Kellogg, M. Maksimovic, N. Monge, S. J. Monson, P. L. Astier, S. Davy, *et al.*: "S/WAVES: The Radio and Plasma Wave Investigation on the STEREO Mission". *Space Sci. Rev.*, **136**, (2008), 487–528.

Bougeret, J. L., M. L. Kaiser, P. J. Kellogg, R. Manning, K. Goetz, S. J. Monson, N. Monge, L. Friel, C. A. Meetre, C. Perche, *et al.*: "WAVES: The radio and plasma wave investigation on the wind spacecraft". *Space Sci. Rev.*, **71**, (1995), 231–263.

Brajša, R., H. Wöhl, B. Vršnak, V. Ruždjak, F. Clette, and J.-F. Hochedez: "Solar differential rotation determined by tracing coronal bright points in SOHO-EIT images. I. Interactive and automatic methods of data reduction". *Astron. Astrophys.*, **374**, (2001), 309–315.

Brueckner, G. E., R. A. Howard, M. J. Koomen, C. M. Korendyke, D. J. Michels, J. D. Moses, D. G. Socker, K. P. Dere, P. L. Lamy, A. Llebaria, *et al.*: "The Large Angle Spectroscopic Coronagraph (LASCO)". *Solar Phys.*, **162**, (1995), 357–402.

Cane, H. V.: "Longitudinal extents of coronal/interplanetary shocks". In "AIP Conference Proceedings", volume 374. AIP (1996). 124–130.

Cane, H. V. and W. C. Erickson: "Energetic particle propagation in the inner heliosphere as deduced from low-frequency (<100 kHz) observations of type III radio bursts". *J. Geophys. Res.*, **108**, (2003), 1203.

Cane, H. V., T. T. von Rosenvinge, C. M. S. Cohen, and R. A. Mewaldt: "Two components in major solar particle events". *Geophys. Res. Lett.*, **30**, (2003), 8017.

Cliver, E. W. and H. V. Cane: "The angular extents of solar/interplanetary disturbances and modulation of galactic cosmic rays". *J. Geophys. Res.*, **101**, (1996), 15533–15546.

Cranmer, S. R. and A. A. van Ballegooijen: "On the Generation, Propagation, and Reflection of Alfvén Waves from the Solar Photosphere to the Distant Heliosphere". *Astrophys. J., Supplement*, **156**, (2005), 265–293.

Cummings, A. C., J. R. Cummings, R. A. Mewaldt, E. C. Stone, B. Blake, M. Fraenz, B. Klecker, D. Hovestadt, and W. R. Webber: "Observations of anomalous cosmic rays in the heliosphere from the SAMPEX, Ulysses, Voyager, and Pioneer spacecraft". *Advances in Space Research*, **16**, (1995), 337.

Dalla, S., A. Balogh, S. Krucker, A. Posner, R. Müller-Mellin, J. D. Anglin, M. Y. Hofer, R. G. Marsden, T. R. Sanderson, B. Heber, *et al.*: "Delay in solar energetic particle onsets at high heliographic latitudes". *Annales Geophysicae*, **21**, (2003), 1367–1375.

Dalla, S., A. Balogh, S. Krucker, A. Posner, R. Müller-Mellin, J. D. Anglin, M. Y. Hofer, R. G. Marsden, T. R. Sanderson, C. Tranquille, *et al.*: "Properties of high heliolatitude solar energetic particle events and constraints on models of acceleration and propagation". *Geophys. Res. Lett.*, **30**, (2003), 8035.

Desai, M. I., R. G. Marsden, T. R. Sanderson, D. Lario, E. C. Roelof, G. M. Simnett, J. T. Gosling, A. Balogh, and R. J. Forsyth: "Energy spectra of 50-keV to 20-MeV protons accelerated at corotating interaction regions at Ulysses". *J. Geophys. Res.*, **104**, (1999), 6705–6720.

Dresing, N., R. Gómez-Herrero, B. Heber, A. Klassen, O. Malandraki, Y. Kartavykh, and W. Dröge: "A statistical survey of wide-spread solar electron events observed with STEREO and ACE with special attention on anisotropies". *Astron. Astrophys.*, **submitted**.

Dresing, N., R. Gómez-Herrero, B. Heber, R. Müller-Mellin, R. Wimmer-Schweingruber, and A. Klassen: "Multi-spacecraft Observations of CIR-Associated Ion Increases During the Ulysses 2007 Ecliptic Crossing". *Solar Phys.*, **256**, (2009), 409–425.

Dresing, N., R. Gómez-Herrero, A. Klassen, B. Heber, Y. Kartavykh, and W. Dröge: "The Large Longitudinal Spread of Solar Energetic Particles During the 17 January 2010 Solar Event". *Solar Phys.*, **281**, (2012), 281–300.

Dröge, W.: "Probing heliospheric diffusion coefficients with solar energetic particles". *Advances in Space Research*, **35**, (2005), 532–542.

Dröge, W., Y. Kartavykh, N. Dresing, B. Heber, and A. Klassen: "Wide longitudinal distribution of interplanetary electrons following the 7 February 2010 solar event: observations and transport modeling". *J. Geophys. Res.*, **submitted**.

Dröge, W., Y. Kartavykh, B. Klecker, and G. A. Kovaltsov: "Anisotropic Three-Dimensional Focused Transport of Solar Energetic Particles in the Inner Heliosphere". *Astrophys. J.*, **709**, (2010), 912–919.

Fichtner, H.: "Anomalous Cosmic Rays: Messengers from the Outer Heliosphere". *Space Sci. Rev.*, **95**, (2001), 639–754.

Galvin, A. B., L. M. Kistler, M. A. Popecki, C. J. Farrugia, K. D. C. Simunac, L. Ellis, E. Möbius, M. A. Lee, M. Boehm, J. Carroll, *et al.*: "The Plasma and Suprathermal Ion Composition (PLASTIC) Investigation on the STEREO Observatories". *Space Sci. Rev.*, **136**, (2008), 437–486.

Garcia-Munoz, M., G. M. Mason, and J. A. Simpson: "The relative abundances of the elements silicon through nickel in the low energy galactic cosmic rays". *International Cosmic Ray Conference*, **1**, (1977), 224–229.

Giacalone, J., J. R. Jokipii, and J. Kóta: "Particle Acceleration in Solar Wind Compression Regions". *Astrophys. J.*, **573**, (2002), 845–850.

Gold, R. E., S. M. Krimigis, I. I. I. . S. E. Hawkins, D. K. Haggerty, D. A. Lohr, E. Fiore, T. P. Armstrong, G. Holland, and L. J. Lanzerotti: "Electron, Proton, and Alpha Monitor on the Advanced Composition Explorer spacecraft". *Space Sci. Rev.*, **86**, (1998), 541–562.

Gómez-Herrero, R., O. Malandraki, N. Dresing, E. Kilpua, B. Heber, A. Klassen, R. Müller-Mellin, and R. Wimmer-Schweingruber: "Spatial and temporal variations of CIRs: Multi-point observations by STEREO". *J. Atmos. Solar Terr. Phys.*, **73**, (2011), 551–565.

Gopalswamy, N., H. Xie, S. Akiyama, S. Yashiro, I. G. Usoskin, and J. M. Davila: "The First Ground Level Enhancement Event of Solar Cycle 24: Direct Observation of Shock Formation and Particle Release Heights". *Astrophys. J. Lett.*, **765**, (2013), L30.

Gosling, J. T., S. J. Bame, W. C. Feldman, D. J. McComas, J. L. Phillips, and B. E. Goldstein: "Counterstreaming suprathermal electron events upstream of corotating shocks in the solar wind beyond approximately 2 AU: ULYSSES". *Journal of Geophysical Research*, **20**, (1993), 2335–2338.

Hasselmann, K. and G. Wibberenz: *Z. Geophys.*, **34**, (1968), 353.

Heber, B., N. Dresing, W. Dröge, R. Gómez-Herrero, K. Herbst, Y. Kartavykh, A. Klassen, J. Labrenz, O. Malandraki, and R. Müller-Mellin: "The First Ground Level Event of Solar Cycle 24 and its longitudinal distribution in the inner heliosphere". *Proc. 33rd Internat. Cosmic Ray Conf. (Rio de Janeiro)*, paper 0746.

Heber, B. and M. S. Potgieter: "Cosmic Rays at High Heliolatitudes". *Space Sci. Rev.*, **127**, (2006), 117–194.

Hill, S. M., V. J. Pizzo, C. C. Balch, D. A. Biesecker, P. Bornmann, E. Hildner, L. D. Lewis, R. N. Grubb, M. P. Husler, K. Prendergast, *et al.*: "The NOAA Goes-12 Solar X-Ray Imager (SXI) 1. Instrument, Operations, and Data". *Solar Phys.*, **226**, (2005), 255–281.

Howard, R. A., J. D. Moses, A. Vourlidas, J. S. Newmark, D. G. Socker, S. P. Plunkett, C. M. Korendyke, J. W. Cook, A. Hurley, J. M. Davila, *et al.*: "Sun Earth Connection Coronal and Heliospheric Investigation (SECCHI)". *Space Sci. Rev.*, **136**, (2008), 67–115.

Huttunen-Heikinmaa, K., E. Valtonen, and T. Laitinen: "Proton and helium release times in SEP events observed with SOHO/ERNE". *Astron. Astrophys.*, **442**, (2005), 673–685.

Intriligator, D. S., G. L. Siscoe, G. Wibberenz, H. Kunow, and J. T. Gosling: "Stream interfaces and energetic ions II: ULYSSES test of Pioneer results". *Geophys. Res. Lett.*, **22**, (1995), 1173–1176.

Kahler, S. W.: "Evidence for solar shock production of heliospheric near-relativistic and relativistic electron events". *Highlights of Astronomy*, **14**, (2007), 86–86.

Kaiser, M. L., T. A. Kucera, J. M. Davila, O. C. Cyr, M. Guhathakurta, and E. Christian: "The STEREO Mission: An Introduction". *Space Sci. Rev.*, **136**, (2007), 5–16.

Kallenrode, M.-B.: "Neutral lines and azimuthal 'transport' of solar energetic particles". *J. Geophys. Res.*, **98**, (1993), 5573–5591.

Kallenrode, M.-B.: "Current views on impulsive and gradual solar energetic particle events". *Journal of Physics G Nuclear Physics*, **29**, (2003), 965–981.

Klassen, A., R. Gómez-Herrero, and B. Heber: "Electron Spikes, Type III Radio Bursts and EUV Jets on 22 February 2010". *Solar Phys.*, **273**, (2011), 413–419.

Klein, K.-L., S. Krucker, G. Lointier, and A. Kerdraon: "Open magnetic flux tubes in the corona and the transport of solar energetic particles". *Astron. Astrophys.*, **486**, (2008), 589–596.

Kunow, H., M. A. Lee, L. A. Fisk, R. J. Forsyth, B. Heber, T. S. Horbury, E. Keppler, J. Kóta, Y.-Q. Lou, R. B. McKibben, *et al.*: "Corotating Interaction Regions at High Latitudes". *Space Sci. Rev.*, **89**, (1999), 221–268.

Kunow, H., G. Wibberenz, G. Green, R. Müller-Mellin, and M.-B. Kallenrode: "Energetic Particles in the Inner Solar System" (1991). 243–342.

Laitinen, T., S. Dalla, and M. S. Marsh: "Energetic Particle Cross-field Propagation Early in a Solar Event". *Astrophys. J. Lett.*, **773**, (2013), L29.

Lario, D., A. Aran, R. Gómez-Herrero, N. Dresing, B. Heber, G. C. Ho, R. B. Decker, and E. C. Roelof: "Longitudinal and Radial Dependence of Solar Energetic Particle Peak Intensities: STEREO, ACE, SOHO, GOES, and MESSENGER Observations". *Astrophys. J.*, **767**, (2013), 41.

Lario, D., M.-B. Kallenrode, R. B. Decker, E. C. Roelof, S. M. Krimigis, A. Aran, and B. Sanahuja: "Radial and Longitudinal Dependence of Solar 4-13 MeV and 27-37 MeV Proton Peak Intensities and Fluences: Helios and IMP 8 Observations". *Astrophys. J.*, **653**, (2006), 1531–1544.

Lee, M. A.: "Diffusive Ion Acceleration by CME-Driven Shocks". *Washington DC American Geophysical Union Geophysical Monograph Series*, **165**, (2006), 245.

Lemen, J. R., A. M. Title, D. J. Akin, P. F. Boerner, C. Chou, J. F. Drake, D. W. Duncan, C. G. Edwards, F. M. Friedlaender, G. F. Heyman, *et al.*: "The Atmospheric Imaging Assembly (AIA) on the Solar Dynamics Observatory (SDO)". *Solar Phys.*, **275**, (2012), 17–40.

Luhmann, J. G., D. W. Curtis, P. Schroeder, J. McCauley, R. P. Lin, D. E. Larson, S. D. Bale, J.-A. Sauvaud, C. Aoustin, R. A. Mewaldt, *et al.*: "STEREO IMPACT Investigation Goals, Measurements, and Data Products Overview". *Space Sci. Rev.*, **136**, (2007), 117–184.

Mason, G. M., R. von Steiger, R. B. Decker, M. I. Desai, J. R. Dwyer, L. A. Fisk, G. Gloeckler, J. T. Gosling, M. Hilchenbach, R. Kallenbach, *et al.*: "Origin, Injection, and Acceleration of CIR Particles: Observations Report of Working Group 6". *Space Sci. Rev.*, **89**, (1999), 327–367.

McComas, D. J., S. J. Bame, P. Barker, W. C. Feldman, J. L. Phillips, P. Riley, and J. W. Griffee: "Solar wind electron proton alpha monitor (swepam) for the advanced composition explorer". *Space Science Reviews*, **86**, (1998), 563–612.

McComas, D. J., R. W. Ebert, H. A. Elliott, B. E. Goldstein, J. T. Gosling, N. A. Schwadron, and R. M. Skoug: "Weaker solar wind from the polar coronal holes and the whole Sun". *Geophys. Res. Lett.*, **35**, (2008), 18103.

McKibben, R. B., C. Lopate, and M. Zhang: "Simultaneous Observations of Solar Energetic Particle Events by imp 8 and the Ulysses Cospin High Energy Telescope at High Solar Latitudes". *Space Sci. Rev.*, **97**, (2001), 257–262.

Miteva, R. and G. Mann: "The electron acceleration at shock waves in the solar corona". *Astron. Astrophys.*, **474**, (2007), 617–625.

Müller-Mellin, R., S. Böttcher, J. Falenski, E. Rode, L. Duvet, T. Sanderson, B. Butler, B. Johlander, and H. Smit: "The Solar Electron and Proton Telescope for the STEREO Mission". *Space Sci. Rev.*, **136**, (2008), 363–389.

Müller-Mellin, R., H. Kunow, V. Fleissner, E. Pehlke, E. Rode, N. Röschmann, C. Scharmberg, H. Sierks, P. Rusznyak, S. Mckenna-Lawlor, *et al.*: "COSTEP - Comprehensive Suprathermal and Energetic Particle Analyser". *Solar Phys.*, **162**, (1995), 483–504.

Nelson, G. J. and D. B. Melrose: *Type II Bursts*. SOLAR RADIOPHYSICS, Cambridge University Press (1985) .

Newkirk, G., Jr. and D. G. Wentzel: "Rigidity-independent propagation of cosmic rays in the solar corona". *J. Geophys. Res.*, **83**, (1978), 2009–2015.

Nitta, N. V., M. J. Aschwanden, P. F. Boerner, S. L. Freeland, J. R. Lemen, and J.-P. Wuelser: "Soft X-ray Fluxes of Major Flares Far Behind the Limb as Estimated Using STEREO EUV Images". *Solar Phys.*, **288**, (2013), 241–254.

Nolte, J. T. and E. C. Roelof: "Large-Scale Structure of the Interplanetary Medium, I: High Coronal Source Longitude of the Quiet-Time Solar Wind". *Solar Phys.*, **33**, (1973), 241–257.

Owens, M. J. and R. J. Forsyth: "The Heliospheric Magnetic Field". *Living Reviews in Solar Physics*, **10**, (2013), 5.

Park, J., D. E. Innes, R. Bucik, and Y.-J. Moon: "The Source Regions of Solar Energetic Particles Detected by Widely Separated Spacecraft". *Astrophys. J.*, **779**, (2013), 184.

Rayrole, J. and M. Semel: "Evaluation of the Electric Current in a Sunspot by the Study of the Observed Transverse Component of the Magnetic Field". *Astron. Astrophys.*, **6**, (1970), 288.

Reames, D. V.: "Particle acceleration at the Sun and in the heliosphere". *Space Sci. Rev.*, **90**, (1999), 413–491.

Reinhard, R. and G. Wibberenz: "Propagation of Flare Protons in the Solar Atmosphere". *Solar Phys.*, **36**, (1974), 473–494.

Richardson, I. G.: "Energetic Particles and Corotating Interaction Regions in the Solar Wind". *Space Sci. Rev.*, **111**, (2004), 267–376.

Roelof, E. C.: "Propagation of Solar Cosmic Rays in the Interplanetary Magnetic Field". In "Lectures in High-Energy Astrophysics", edited by H. Ögelman and J. R. Wayland (1969). 111.

Rouillard, A. P., N. R. Sheeley, A. Tylka, A. Vourlidas, C. K. Ng, C. Rakowski, C. M. S. Cohen, R. A. Mewaldt, G. M. Mason, D. Reames, *et al.*: "The Longitudinal Properties of a Solar Energetic Particle Event Investigated Using Modern Solar Imaging". *Astrophys. J.*, **752**, (2012), 44.

Russell, C. T., L. K. Jian, X. Blanco Cano, J. G. Luhmann, and T. L. Zhang: "STEREO observations of shock formation in the solar wind". *Geophys. Res. Lett.*, **36**, (2009), 2103.

Schellert, G., G. Wibberenz, and H. Kunow: "Coronal propagation of flare associated electrons and protons". *International Cosmic Ray Conference*, **4**, (1985), 305–308.

Schrijver, C. J. and M. L. De Rosa: "Photospheric and heliospheric magnetic fields". *Solar Phys.*, **212**, (2003), 165–200.

Schwenn, R. and E. Marsch: *Physics of the inner heliosphere. 1. Large-scale phenomena.*, volume 20. Physics and Chemistry in Space (1990).

Smith, C. W., J. L'Heureux, N. F. Ness, M. H. Acuña, L. F. Burlaga, and J. Scheifele: "The ace magnetic fields experiment". *Space Science Reviews*, **86**, (1998), 613–632.

Suzuki, S. and G. A. Dulk: *Bursts of Type II and Type V*. SOLAR RADIOPHYSICS, Cambridge University Press (1985) .

Thiel, B.: *Bestimmung der Einsatzzeit von Teilchenereignissen mit Hilfe der Methode der kumulativen Summen*. Master's thesis, CAU Kiel (2013).

Tylka, A. J., C. M. S. Cohen, W. F. Dietrich, M. A. Lee, C. G. Maclennan, R. A. Mewaldt, C. K. Ng, and D. V. Reames: "Shock Geometry, Seed Populations, and the Origin of Variable Elemental Composition at High Energies in Large Gradual Solar Particle Events". *Astrophys. J.*, **625**, (2005), 474–495.

Veronig, A. M., N. Muhr, I. W. Kienreich, M. Temmer, and B. Vršnak: "First Observations of a Dome-shaped Large-scale Coronal Extreme-ultraviolet Wave". *Astrophys. J.*, **716**, (2010), L57–L62.

Wibberenz, G. and H. V. Cane: "Multi-Spacecraft Observations of Solar Flare Particles in the Inner Heliosphere". *Astrophys. J.*, **650**, (2006), 1199–1207.

Wibberenz, G., L. J. Lanzerotti, and D. Venkatesan: "Solar particle propagation in the interplanetary environment - A study of the November 18, 1968, event". *J. Geophys. Res.*, **81**, (1976), 5807–5821.

Wiedenbeck, M. E., G. M. Mason, C. M. S. Cohen, N. V. Nitta, R. Gómez-Herrero, and D. K. Haggerty: "Observations of Solar Energetic Particles from ^{3}He-rich Events over a Wide Range of Heliographic Longitude". *Astrophys. J.*, **762**, (2013), 54.

Zhang, M., G. Qin, and H. Rassoul: "Propagation of Solar Energetic Particles in Three-Dimensional Interplanetary Magnetic Fields". *Astrophys. J.*, **692**, (2009), 109–132.

APPENDIX

Within the framework of this thesis some contributions have been made to studies by our collaborators. The appendix presents the three most important publications which are in close context with our own investigations and therefore have been discussed above.

Appendix A

Gómez-Herrero *et al.*, 2010

Multi-spacecraft Observations of CIR-Associated Ion Increases During the Ulysses 2007 Ecliptic Crossing

Own contribution: 30 %

Appendix B

Lario *et al.*, 2013

LONGITUDINAL AND RADIAL DEPENDENCE OF SOLAR ENERGETIC PARTICLE PEAK INTENSITIES: STEREO, ACE, SOHO, GOES, AND MESSENGER OBSERVATIONS

Own contribution: 10 %

Appendix C

Dröge *et al.*, submitted 2014

Wide longitudinal distribution of interplanetary electrons following the 7 February 2010 solar event: observations and transport modeling

Own contribution to observational part: 45%

Journal of Atmospheric and Solar-Terrestrial Physics 73 (2011) 551–565

Contents lists available at ScienceDirect

Journal of Atmospheric and Solar-Terrestrial Physics

journal homepage: www.elsevier.com/locate/jastp

Spatial and temporal variations of CIRs: Multi-point observations by STEREO

R. Gómez-Herrero [a,*], O. Malandraki [b,a], N. Dresing [a], E. Kilpua [c], B. Heber [a], A. Klassen [a], R. Müller-Mellin [a], R.F. Wimmer-Schweingruber [a]

[a] Institut für Experimentelle und Angewandte Physik, Christian-Albrechts University, Kiel, Germany
[b] Institute of Astronomy and Astrophysics, National Observatory of Athens, Greece
[c] Department of Physical Sciences, Theoretical Physics Division, University of Helsinki, Finland

ARTICLE INFO

Article history:
Received 12 August 2010
Received in revised form
8 November 2010
Accepted 11 November 2010
Available online 23 November 2010

Keywords:
Energetic particles
Interplanetary Coronal Mass Ejections (ICMEs)
Co-rotating Interaction Regions (CIRs)
Multi-spacecraft observations

ABSTRACT

In the absence of solar activity, Co-rotating Interaction Regions (CIRs) are a prevailing source of energetic ions observed near 1 AU. The combination of observations by near-Earth space observatories and the twin STEREO spacecraft offers an excellent platform for multi-point studies of CIRs. The analysis of CIR events during Carrington rotations 2067–2082 provides evidence that CIR-associated energetic ions frequently show significant differences, particularly at sub-MeV energies. We found discrepancies in the structures observed by different spacecraft which cannot always be attributed to the latitudinal separation or to changes in the coronal hole which generates the high-speed stream. We present several cases where these differences are linked to the presence of Interplanetary Coronal Mass Ejections (ICMEs) or small-scale interplanetary transients in the vicinity of or embedded within the CIR. Evidence of the possible role of ICME-CIR interactions as sources of temporal variations in the CIR-associated ion increases are presented and discussed.

1. Introduction

The major features of the interaction between fast and slow solar wind streams were discussed already in the early 70's (Belcher and Davis, 1971). The fast solar wind originating from coronal holes interacts with the preceding low-speed solar wind forming so-called Co-rotating Interaction Regions (CIRs) (Pizzo, 1978). Since coronal holes are often long-lived structures, the same CIR reappears often for several consecutive solar rotations. Forward and reverse shocks bounding the CIRs are commonly formed beyond ~2 AU (Smith and Wolfe, 1976, 1977, 1979; Gosling et al., 1993). These shocks are known to accelerate ions up to several MeV per nucleon. Thus, ion increases are frequently observed in association with CIRs (Barnes and Simpson, 1976; McDonald et al., 1976). For a review of the effects of CIRs on energetic particles, see Richardson (2004) and references therein. Consistent with this model of shock acceleration is the net particle flow towards the Sun (Marshall and Stone, 1978) and the strong positive outward radial gradients (Kunow et al., 1977; van Hollebeke et al., 1978; Christon and Simpson, 1979; Dresing et al., 2009) observed during CIR-associated ion events. It has been suggested that apart from the main contribution from the CIR shocks, statistical acceleration in the vicinity of CIRs could also contribute to particle acceleration (see, e.g. Scholer et al., 1999).

The recent extended solar minimum in coincidence with the beginning of the STEREO mission has provided optimal conditions for multi-spacecraft in situ and remote-sensing observations of CIRs, which have been the focus of several recent papers (e.g. Bučík et al., 2009a; Rouillard et al., 2008; Jian et al., 2009; Gómez-Herrero et al., 2009; Dresing et al., 2009; Bučík et al., 2009b; Mason et al., 2009; Simunac et al., 2009; Tappin and Howard, 2009; Leske et al., 2010; Wood et al., 2010).

In this work we present multi-spacecraft observations of CIRs from February 2008 to April 2009, during the solar minimum between solar cycles 23 and 24. We compare multi-point observations of the same CIR events and correlate them with remote-sensing observations of the solar corona with the aim of identifying the structures observed by different spacecraft. In particular, we will present and discuss several cases where the presence of Interplanetary Coronal Mass Ejections (ICMEs) in the vicinity of or embedded within the CIR is accompanied by significant changes in the CIR structure and in the associated energetic ions.

2. Observations and data analysis

2.1. Instrumentation

The STEREO mission consists of two nearly identical space-based observatories launched on October 25, 2006 (Kaiser et al., 2008). STEREO A (STA) moves ahead of the Earth and STEREO B

* Corresponding author. Tel.: +49 431 8802486.
E-mail address: gomez@physik.uni-kiel.de (R. Gómez-Herrero).

1364-6826/$ - see front matter © 2010 Elsevier Ltd. All rights reserved.
doi:10.1016/j.jastp.2010.11.017

(STB) trails behind. We analyze energetic ion observations carried out with the Solar Electron and Proton Telescope (SEPT, Müller-Mellin et al., 2008) and Low Energy Telescope (LET, Mewaldt et al., 2008), parts of the IMPACT investigation (Luhmann et al., 2008). Magnetic field data were obtained from IMPACT-MAG (Acuña et al., 2008) and solar wind plasma data from the PLASTIC (Galvin et al., 2008) instrument. STEREO in situ observations were complemented by plasma and magnetic field observations from the MAG (Smith et al., 1998) and SWEPAM (McComas et al., 1998) instruments onboard the Advanced Composition Explorer (ACE), orbiting the first Lagrange point L1. Extreme ultraviolet images of the solar disk from SOHO/EIT (Delaboudinière et al., 1995) and STEREO/SECCHI-EUVI (Howard et al., 2008) were also used to identify and track the evolution of coronal holes.

2.2. Observation period

We selected for this study the time interval from February 21, 2008 to April 5, 2009, which corresponds to Carrington Rotations (CR) 2067.0–2082.0. This period was characterized by very low solar activity, indeed 265 and 262 sunspotless days were registered during 2008 and 2009, respectively, making them the quietest years since 1913 (SIDC, Royal Observatory of Belgium, International Sunspot Number: http://www.sidc.be/sunspot-data/). During this period the angular separation between the two STEREO spacecraft grew from 46° to 93°. The Earth is always located very close to the central axis of the STA-Sun-STB angle, meaning that during this period the separation angle between each STEREO and the Earth grew from $\sim 22^{\circ}$ to $\sim 47^{\circ}$. Assuming a solar wind speed of 450 km/s, this corresponds to nominal co-rotation times between 3.1 and 6.4 days and offers an excellent opportunity for multi-spacecraft studies of CIR-associated particle increases during an extended period of low solar activity.

2.3. Comparing remote sensing and multi-spacecraft in situ observations

Assuming that the solar wind propagates radially outward with constant speed from the solar source surface to the observer, the co-rotation time between two points located at heliolongitudes ϕ_B and ϕ_A and heliocentric distances r_B and r_A can be estimated by (e.g. van Hollebeke et al., 1978; Richardson et al., 1998)

$$t_A - t_B = \frac{\phi_A - \phi_B}{\Omega_S} + \frac{r_A - r_B}{V_{SW}} \quad (1)$$

where Ω_S is the sidereal angular velocity of the Sun, and V_{SW} is the solar wind speed (assumed to be radial). Since the two STEREO spacecraft are always close to the ecliptic plane, the separation with respect to the solar equator is always below 7.4°. Thus, the effect of the differential solar rotation can be neglected and Ω_S is assumed to be independent of the heliographic latitude.

Eq. (1) provides the time delay between two spacecraft A and B, which can be used to apply a temporal shift to the in situ observations of co-rotating structures from one spacecraft to another one. This method can be improved taking into account the small effect of the orbital motion of the spacecraft during the co-rotation time.

An alternative method to compare the in situ observations of co-rotating features in the solar wind is to map the in situ observations back to the solar corona. The angle $\Delta\phi$ through which the Sun rotates during the solar wind travel time from the source surface to the spacecraft is given by (see, e.g. Nolte and Roelof, 1973; Schwenn and Marsch, 1990)

$$\Delta\phi = \frac{\Omega_S (r - r_0)}{V_{SW}} \quad (2)$$

where r and r_0 are the heliocentric distances of the spacecraft and the solar source surface (that is assumed at 2.5 solar radii), respectively. Using Eq. (2) the in situ data can be displayed as a function of the Carrington longitude of the spacecraft magnetic footpoint (i.e. the source longitude of the solar wind observed by the spacecraft) and directly compared with the coronal structures. The backmapping technique has been routinely used in the past to correlate in situ observations of solar wind streams and remote observations of coronal holes (e.g. Nolte et al., 1976; Schwenn and Marsch, 1990; Posner et al., 1999, 2000; Neugebauer et al., 2004).

Fig. 1 shows a summary of backmapped in situ observations during CR 2067.0–2082.0 compared with remote-sensing observations of the corona. The in situ data have been mapped back using Eq. (2) and the source decimal Carrington rotation number has been used as the abscissa in the plots. The top panel shows the heliocentric distances for STA, STB and the Lagrange point L1. The second panel shows synoptic coronal hole maps from the Global Oscillation Network Group (GONG). These maps are obtained using magnetogram data and a potential-field source-surface (PFSS) model of the coronal field. The green and red areas in these maps are the photospheric footprints of coronal holes with positive and negative polarity, respectively. The gray areas correspond to the highest closed field lines, with vanishing radial component just below 2.5 R_{SUN}. The wavy black line corresponds to the neutral line, while the blue, red and green lines are the heliographic latitudes of STB, STA and L1. The synoptic maps were obtained at the GONG webpage (http://gong.nso.edu/data/magmap/archive.html). Each CR map has been mirrored in order to have the time running from left to right (increasing CR number). The third panel in Fig. 1 shows backmapped measurements of the solar wind speed by STEREO/PLASTIC and ACE/SWEPAM. The colored bands on the top part of this panel represent the Interplanetary Magnetic Field (IMF) polarity measured in situ by STEREO and ACE magnetometers, with red denoting negative (inward) polarity and green positive (outward) polarity. The bottom panel in Fig. 1 shows backmapped measurements of 101–137 keV ions and 4–6 MeV protons from STEREO/SEPT and STEREO/LET, respectively. These ion intensities are averages of all the looking directions.

The period represented in Fig. 1 started with a well defined two-sector/two-stream structure in the interplanetary (IP) medium associated with large northern (negative) and southern (positive) coronal holes extending to near-equatorial latitudes. The matching magnetic polarity is shown by the corresponding colors in the GONG coronal hole maps (panel 2) and the in situ magnetic field polarity (top colored bands in panel 3). The fast solar wind streams are accompanied by energetic ion increases associated with CIRs (bottom panel). After CR 2071, the equatorial extension of the southern coronal hole and the corresponding stream was significantly reduced. The northern coronal hole and its associated high-speed stream were remarkably long-lived, but started to diminish after CR 2077. The later part of the period (CR 2077.0–2082.0) is characterized by smaller extensions of the coronal holes near the equator, leading to 2–3 narrower and slower high-speed streams per rotation. Lee et al. (2010) already reported an overall weakening of the high-speed streams and recurrent particle increases observed near the Earth after CR 2080.

From the point of view of the energetic ions, the period under study was dominated by CIR-related increases and only a few small solar energetic particle (SEP) events were observed (marked by inverted triangles in the x-axis of the bottom panel in Fig. 1). These events were identified using the 30–400 keV electron intensities measured by SEPT (not shown) as well as checking the ion fluxes for observational signatures indicative of solar origin (velocity dispersion, correlation with solar flares, etc.). While recurrent 101–137 keV ion increases were regularly observed throughout

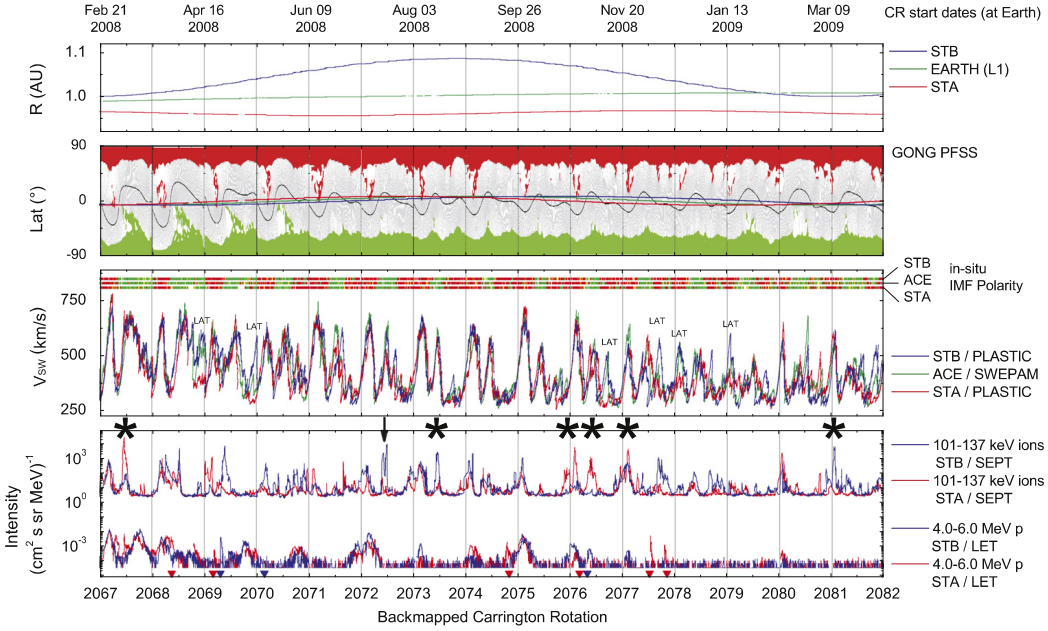

Fig. 1. Summary of backmapped observations compared with coronal maps and orbital data during CR 2067.0–2082.0. From top to bottom: (1) heliocentric distance, (2) Synoptic coronal hole maps from GONG showing the photospheric footpoints of coronal holes as colored areas. Red and green colors denote negative and positive polarity, respectively. (3) Backmapped solar wind speed measured by ACE and the two STEREO spacecraft, (4) 101–137 keV omnidirectional ion intensities measured by STEREO/SEPT and 4–6 MeV omnidirectional proton intensities measured by STEREO/LET. Periods dominated by latitudinal separation effects are marked with the label 'LAT'. The asterisks mark ICME periods analysed in Section 2.7. Solar energetic particle events are marked with inverted triangles in the *x*-axis of the bottom panel (see text). (For interpretation of the references to color in this figure legend, the reader is referred to the web version of this article.)

the period, after rotation 2077 the reduction in both maximum speed and width of the high-speed streams, was accompanied by a dramatic reduction of the 4–6 MeV ion increases. When the ion enhancements at 4–6 MeV are present, they tend to occur inside the high-speed streams, as expected if they are streaming Sunward from CIR reverse shocks beyond 1 AU.

2.4. Importance of heliographic latitude

Sheeley and Harvey (1981) pointed out that the most important factor influencing the correlation between the central-meridian passage times of coronal holes and the occurrence of high-speed streams at Earth seems to be the latitude of the holes relative to the heliographic latitude of the Earth. The observations with the Helios missions (1974–1985) (Schwenn and Marsch, 1990) highlighted the effect of latitudinal separation for multi-spacecraft observations of high-speed streams and CIRs. Two spacecraft located at different heliographic latitudes scan the solar wind from different latitudinal sections of the same coronal hole and small latitudinal separations of a few degrees can lead to significant differences in the structures observed in situ. A tendency to find better agreement in the backmapped solar wind speed profiles during periods of minimum latitudinal separation is evident in Fig. 1 (see for instance CR 2067, 2073 and 2074 in panel 5). On the contrary, the periods labelled 'LAT' in the figure are examples of intervals where the latitudinal separation plays a major role. This is the case for instance for the narrow high-speed stream recurring at the end of CR 2076, 2077 and 2078, originating in an extension of the northern coronal hole. During all the period STB was located closer to the coronal hole and observed a more prominent solar wind stream than STA, located between 5° and 10° south from STB. Indeed, for CR 2076, the stream was totally missed by STA. Though the parent coronal hole showed some evolution, the sustained dependence of solar wind speed and particle fluxes with the heliographic latitudinal separation is likely the main parameter organizing the observations. For rotations 2077 and 2078, increases in the ~120 keV ion fluxes were observed by STB, while the increases for STA were much lower. A detail of the latitudinal effect observed during CR 2076 and 2077 is shown in Fig. 2. The top panel shows synoptic ecliptic-plane field plots from GONG. These plots show model field lines that are open to the heliosphere at the ecliptic plane, and coronal holes, which are represented by dots. The second panels show the in situ solar wind speed and magnetic field polarity measured by the two STEREO spacecraft. The black arrows in the bottom panel mark the solar wind stream which was observed by STB in both rotations but missed by STA, very likely due to the latitudinal separation. Another period when the latitudinal separation plays a major role can be observed at the end of CR 2068 and 2069, when STB and ACE observed a stream originating in the southern polar coronal hole, which is missed by STA, likely located above the northern latitudinal boundary of the stream at 1 AU.

In order to study the degree of coincidence in the solar wind structures observed by the two STEREO spacecraft as the longitudinal and latitudinal separations vary, we have investigated the correlation between STB and STA measurements of the solar wind speed. A co-rotating time shift (Eq. (1)) to the Lagrange point L1 was applied to both measurements, and then Pearson's correlation coefficient (see, e.g. Rodgers and Nicewander, 1988) over a running 27-day-long time window was calculated. This approach is similar to the technique described by Opitz et al. (2009) to track the temporal changes in the solar wind bulk velocity measured by STEREO in 2007. Fig. 3 shows the temporal behavior of the correlation coefficient subtracted from unity from April 15, 2007 to June 3, 2009. We used this parameter because its variation follows the temporal behaviour of the latitude, simplifying the comparison. The shaded area corresponds to the time period previously presented in Fig. 1. The latitudinal and longitudinal separations between both spacecraft are shown in the top panel as black and red lines, respectively. A tendency to find better correlation during periods of small latitudinal separation can be observed. The final part of the period plotted in Fig. 3 is more disturbed as a consequence of the higher variability of the stream structure commencing at the end of 2008. The values greater than unity at the end of the period (meaning anticorrelation) are due to the stream configuration: while STA is in the decay phase of a high-speed stream, STB separated more than 10° in latitude is observing the rising phase of a different stream.

Fig. 3 illustrates how STB and STA measurements of the solar wind speed are better correlated when the latitudinal separation approaches zero. This tendency is present even at the final part of the period. The actual importance of the latitudinal separation for one particular time interval is affected by several factors such as the relative positions of the spacecraft with respect to the coronal hole

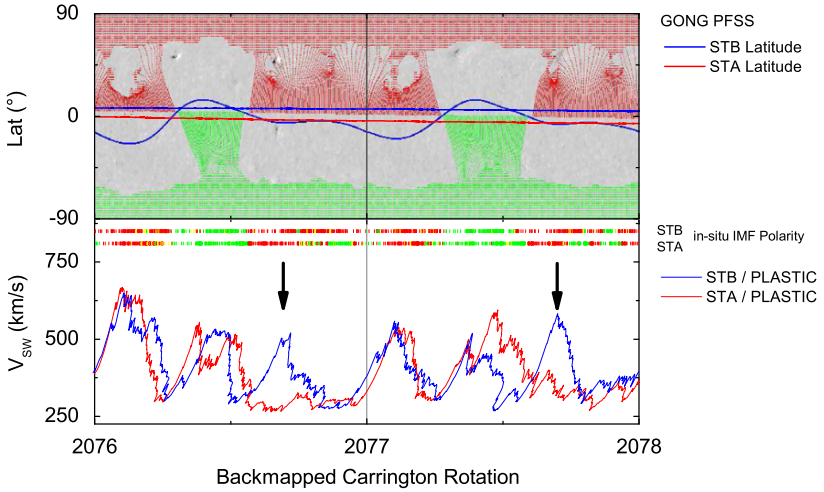

Fig. 2. Detail of Carrington rotations 2076 and 2077. Top panel: synoptic map from GONG showing the PFSS model field lines that are open to the heliosphere at the ecliptic plane. Bottom panel: solar wind speed measured by the two STEREO. The colored bands on the top part of this panel represent the in situ magnetic field polarity. The arrows mark a solar wind stream observed two consecutive times by STB but missed by STA due to the latitudinal separation. (For interpretation of the references to color in this figure legend, the reader is referred to the web version of this article.)

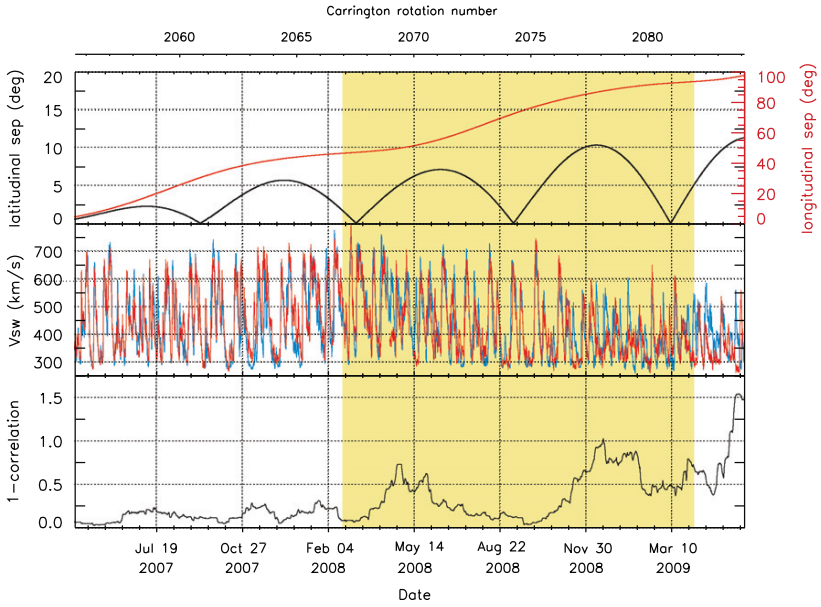

Fig. 3. Top: absolute values of the heliographic latitudinal (black) and longitudinal (red) separation between the two STEREO spacecraft as a function of time. Middle: STB (blue) and STA (red) solar wind speed measurement time-shifted to L1 (1 h resolution). Bottom: 1 minus the correlation coefficient between the time-shifted solar wind speed measured by both spacecraft, calculated using a running time window of 27 days. The shaded interval corresponds to the period shown in Fig. 1. (For interpretation of the references to color in this figure legend, the reader is referred to the web version of this article.)

boundaries or the shape of the coronal hole contours. For this reason, highly correlated structures can occasionally be found during periods of relatively large latitudinal separation, for instance in December 2007 (see also Gómez-Herrero et al., 2009, Figure 6). The correlation also shows a slowly decreasing trend as the longitudinal separation increases.

2.5. Effects of coronal hole variations

The evolution of the large-scale solar magnetic fields and their associated coronal holes produces long-term variations of the high-speed solar wind streams at the Earth (Broussard et al., 1978). For this reason, changes in the shape or magnetic topology of coronal holes give rise to changes in the corresponding CIR structure observed at 1 AU. The effect of long-term variations, such as the progressive reduction of the southern coronal hole after CR 2070 which led to a contraction of the associated fast solar wind stream, is easily visible in Fig. 1. If the evolution of the coronal hole occurs sufficiently fast and takes place in the visible hemisphere, the effect can be measured using multi-point observations within the same Carrington rotation. Fig. 4 shows one of these rare events observed during the center of CR 2072 (July 2008). The event was associated with a near-equatorial coronal hole extension with positive polarity which produced a high-speed stream observed in situ by ACE and the two STEREO spacecraft. The six top panels show remote-sensing observations of the corona in the wavelength of 171 Å by STEREO/EUVI and SOHO/EIT. The coronal hole appears as a dark region extending between -10° and $+10^{\circ}$ of heliographic latitude and 180° and 210° of Carrington longitude. The spacecraft projections are shown by color asterisks. The three top images correspond to the time when STB, SOHO and STA crossed Carrington longitude 200° (leading section of the hole, above the solar equator), while the three bottom images correspond to Carrington longitude 190° (trailing section of the hole, below the solar equator). Note how the hole area expanded between July 17–19 and contracted again by July 21–22. The bottom panel shows backmapped observations of the solar wind speed. In this plot, the yellow and magenta lines mark the source longitudes 200° and 190°, respectively. Despite the uncertainty inherent to the backmapping technique and the potential deviations due to the super-radial expansion of the coronal holes above the source surface (e.g. Bromage et al., 2000) and the effects of the compression in the leading edge of the fast stream, this simple representation still provides a satisfactory link between interplanetary solar wind measurements and the source coronal structures. The coronal hole showed time variations which correlate with the in situ observations. The slower speed measured by STA is due to the smaller area of the hole combined with the northern location of the spacecraft. ACE measured a slightly faster and broader stream than STB, due to the expansion of the two sections of the hole during the co-rotation time from STB to ACE. The event was accompanied by ions of several hundred keV, which showed much more prominent increase at STB than at STA (see bottom panel in Fig. 1, where the event is marked by a vertical arrow).

2.6. Transient structures in the slow wind

The slow solar wind is characterized by large variations of the plama and fields parameters (e.g. McComas et al., 2000; Song et al., 2009). Since CIRs are the consequence of the interaction between a fast solar wind stream and the preceding slow wind, transient changes in the slow wind are also a potential source of temporal variations in the CIR structure. In particular, slow ICMEs or small scale transients (Kilpua et al., 2009b; Rouillard et al., 2009, 2010a, 2010b) are frequently found near the heliospheric current sheet, embedded in the slow solar wind preceding high-speed streams at 1 AU. ICMEs can influence the Earth's magnetosphere and may give rise to geomagnetic storms (e.g. Antoniadou et al., 2008). Previous studies (Fenrich and Luhmann, 1998; Dal Lago et al., 2006) showed that when a high-speed stream compresses a preceding ICME, the interaction results in an enhanced plasma density at the end of the ICME and often an increase in magnetic field strength as well. In some particular cases this situation leads to an enhanced geo-effectiveness. Previous papers (Burlaga and Ogilvie, 1973; Burlaga and Scudder, 1975; Burlaga et al., 1987, 1991; Malandraki et al., 2008, 2007)

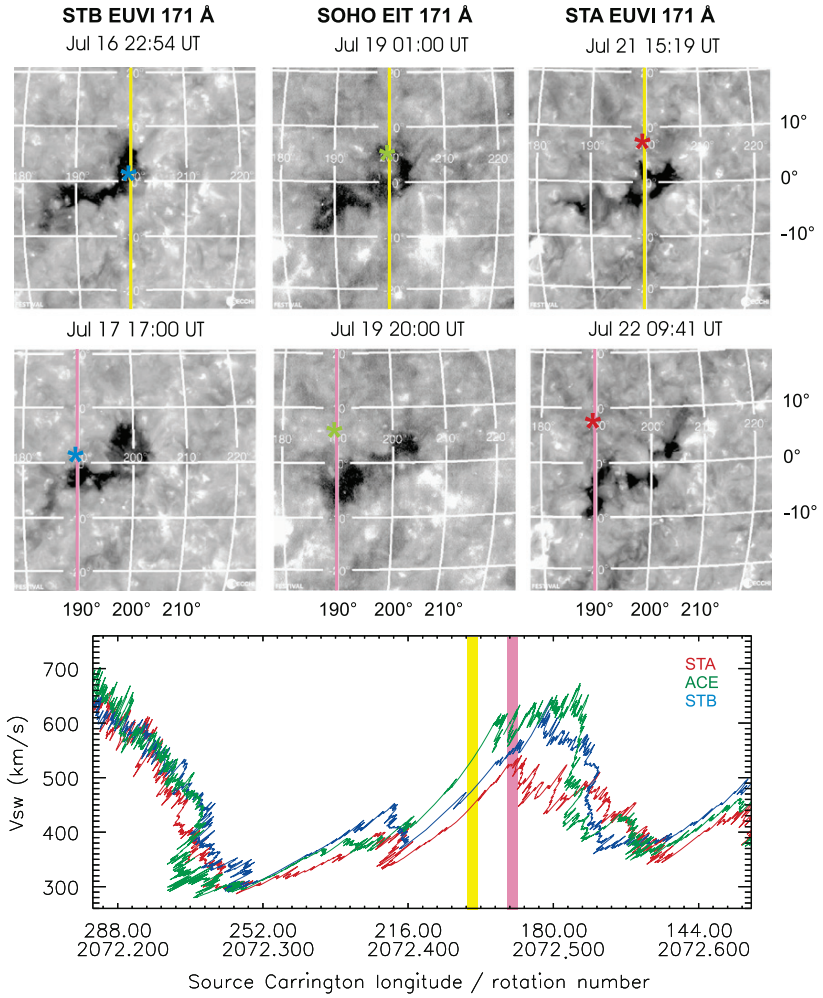

Fig. 4. Multi-spacecraft observations of an evolving coronal hole near the center of CR 2072 and the corresponding variations in the in situ high-speed stream (see text for details).

studied the interaction and merging of ICMEs with pre-existing CIRs to produce a *compound stream*.

Fig. 5 shows STB in situ observations of a high-speed stream and the associated CIR and energetic ion increase during three consecutive rotations. The positions of the stream interfaces, labelled 'SI' and marked by vertical solid lines in the figure, are based on the UCLA-IGPP level 3 Results of STEREO IMPACT/PLASTIC (http://www-ssc.igpp.ucla.edu/forms/stereo/stereo_level_3.html). The careful inspection of the plasma and magnetic field data for the last panel (January 2009) suggests that the stream interface in this case is likely located some hours before the time provided by the IMPACT level 3 list, in coincidence with a density decrease and the sudden increase of the energetic ions. The improved identification of this stream interface has been marked by a dotted vertical line in the right panel. The compression and the energetic ion enhancement were more prominent during CR 2077 (December 2008, central panel). For that particular rotation, ICME signatures were observed on December 8 by STB (Kilpua et al., 2009a). This ICME corresponds to the area shaded in blue between 17:00 and 20:30, which is embedded within the CIR observed by PLASTIC and only 2.25 h before the corresponding stream interface. The shaded area between December 7 15:45 UT and December 8 10:10 UT following an IP shock ('FS' in the figure) corresponds to a previous ICME. The interplanetary signatures of both ICMEs are summarized in Appendix A (see Fig. 10). The 119–137 keV ion intensity peaked on December 9 about 5–6 UT. There is no shock listed in the level 3 IMPACT shock list during this period; however, the inspection of the plasma and the high time resolution magnetic field data shows a possible developing reverse shock at 05:23:45 UT, consistent with the ion intensity peak. No ICME signatures were observed near the CIR for rotations 2076 and 2078. The comparison of the three bottom panels shows that the duration and the intensity of the 119–137 keV ion increase reached the highest values for the December 2008 event. This event was also characterized by higher density and magnetic field peaks which reveal an enhanced compression.

The recurrent high-speed stream shown in Fig. 5 was faster and broader during CR 2077, making it difficult to discern whether the ICME plays some role in the enhanced compression and particle acceleration observed for that rotation. Multi-spacecraft observations are required in order to compare the properties of CIRs during time scales shorter than one solar rotation and identify the possible role of ICME-CIR interaction. STA observations during the period shown in the center panel of Fig. 5 are inconclusive because of the strong latitudinal effect: as can be seen in Fig. 1, the stream at the final part of CR 2077 originated in a northern coronal hole and was very weak at STA, located more than 10° south from STB.

Another event more suitable for multi-spacecraft studies is shown in Fig. 6 which corresponds to a CIR observed by both

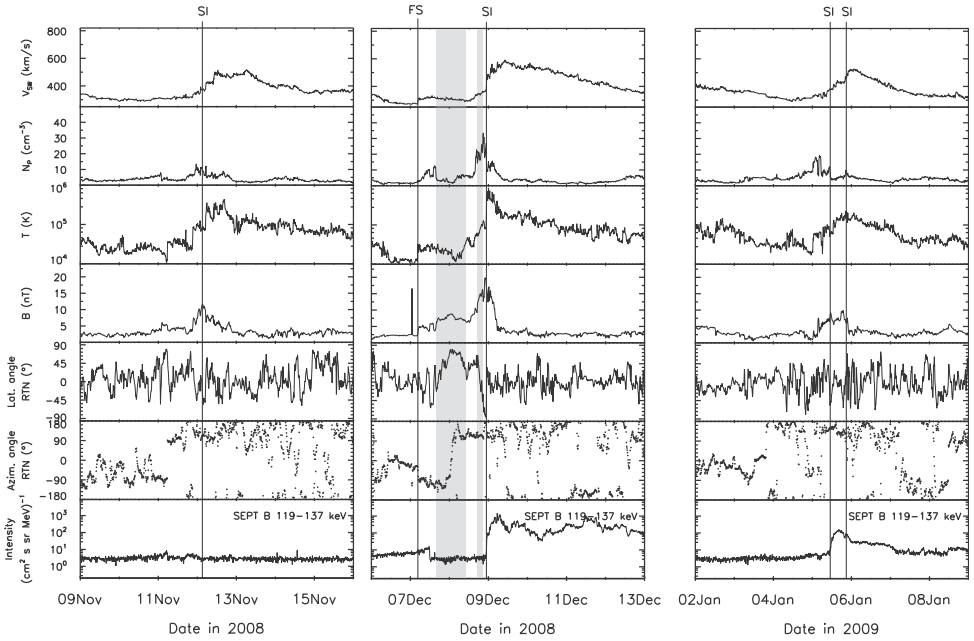

Fig. 5. STB observations of a CIR during three consecutive Carrington rotations (2076, 2077 and 2078). From top to bottom: solar wind speed, proton density, proton temperature, magnetic field magnitude, magnetic field latitudinal and azimuthal angles and 119–137 keV omnidirectional ion intensities. The central panel corresponds to the end of December 2008, when STB observed an ICME embedded within the CIR. The comparison of the three bottom panels shows that the highest 119–137 keV ion acceleration occurred during the December 2008 event.

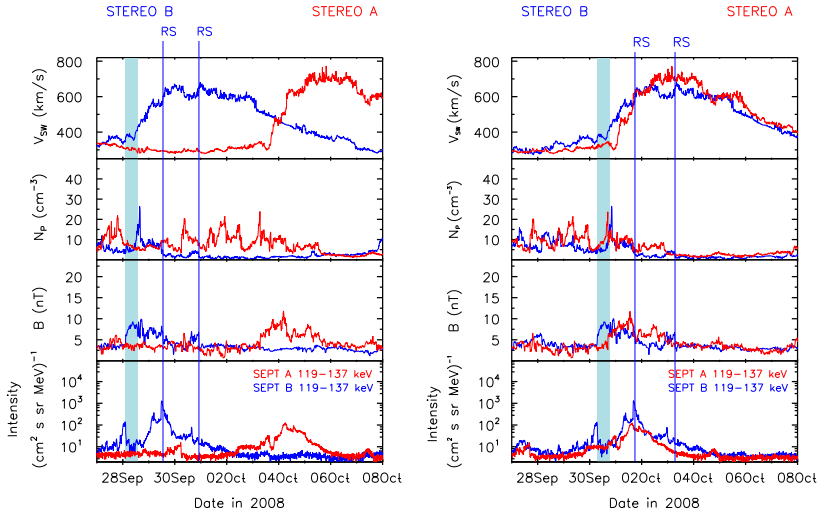

Fig. 6. Plasma and particle observations during a CIR-associated ion event observed at the beginning of CR 2075. In the right panel, a co-rotating time shift to L1 has been applied to STB and STA measurements in order to compare the observations (see text for details).

STEREO at the beginning of CR 2075 (this corresponds to the end of September 2008, a period of good correlation in Fig. 3). The left panel shows from top to bottom: solar wind speed, proton density, magnetic field magnitude and low energy ions measured by the two STEREO spacecraft. The right panel shows the same observations after the application of a co-rotating time shift of both STEREO to the Lagrange point L1, which simplifies the direct comparison of the measurements carried out by different spacecraft. An ICME was observed by STB in front of the high-speed stream on September 28 between 02:30 UT and 14:00 UT (Kilpua et al., 2009a). The stream interface was located at 15:42 UT (UCLA-IGPP level 3 Results of STEREO IMPACT/PLASTIC, http://www-ssc.igpp.ucla.edu/forms/stereo/stereo_level_3.html), less than 2 h after the trailing boundary of the ICME. In spite of the nominal co-rotation time of ~5 days and the latitudinal separation of 3.8°, both spacecraft observed very similar structures for both, plasma and energetic ions (see also the good correlation during this period shown in Fig. 3). The good agreement of the solar wind speed measurements proves that the high-speed stream showed very similar characteristics during the co-rotation time period. None of the spacecraft observed especially enhanced compression and the STB magnetic field did not show a great intensification in association with the ICME. Nevertheless, the CIR-associated 119–137 keV ions were more intense at STB, particularly in the interval preceding the ICME and during the absolute intensity maximum. The particle maximum at STB occurred in coincidence with an in situ reverse shock

(first label 'RS' in the left panel of the figure). A second reverse shock was observed by STB at the end of September 30, when the particle intensity was returning to pre-event levels. STA did not observe any shock signatures during the CIR, and the absolute maximum ion intensity at STA is factor 10 below the prominent local spike observed by STB during the first reverse shock.

2.7. *A search for the effect of solar wind transients on CIR particle events*

Figs. 5 and 6 are an indication of time variability in CIRs, which sometimes show in situ shocks only at one spacecraft. In these two cases, the presence of ICMEs preceding or within the CIR suggests that interplanetary transients could play some role changing the plasma conditions of the CIR, which eventually could affect the acceleration of energetic ions. In order to investigate for further evidence, we studied additional CIR events potentially affected by the presence of ICMEs or small interplanetary transients in at least one spacecraft. In situ observations of the events are presented in chronological order in Figs. 7 and 8. The top three panels in each figure (1a,2a,3a) show solar wind speed, proton density, magnetic field magnitude and omnidirectional energetic ions measured by the two STEREO spacecraft at 119–137 KeV and 4–6 MeV energies (solar wind speed measured by ACE is also included in the top plots for comparison). The bottom three panels (1b,2b,3b) present the same observations after a co-rotating time shift to L1 has been applied to the measurements by the two STEREO spacecraft. In order to simplify the comparison with remote-sensing observations, the events are marked with asterisks at the bottom panel of Fig. 1. The recent compilation by Kilpua et al. (2009a) and the level 3 event list compiled by UCLA-IGPP (http://www-ssc.igpp.ucla.edu/forms/stereo/stereo_level_3.html) were used for the identification of the transient or ICME intervals shown in the figures as shaded areas (light blue for STB and pink for STA). The in situ signatures for those events not included in these ICME lists are presented in Appendix A. Vertical solid lines mark the location of in situ shocks according to the IMPACT/PLASTIC level 3 list. This list uses the time of maximum total perpendicular pressure to identify the possible stream interfaces (see Jian et al., 2006); however, the plasma signatures do not always permit an unambiguous confirmation of these locations. For this reason, we marked with dotted vertical lines only those stream interfaces showing clear plasma signatures

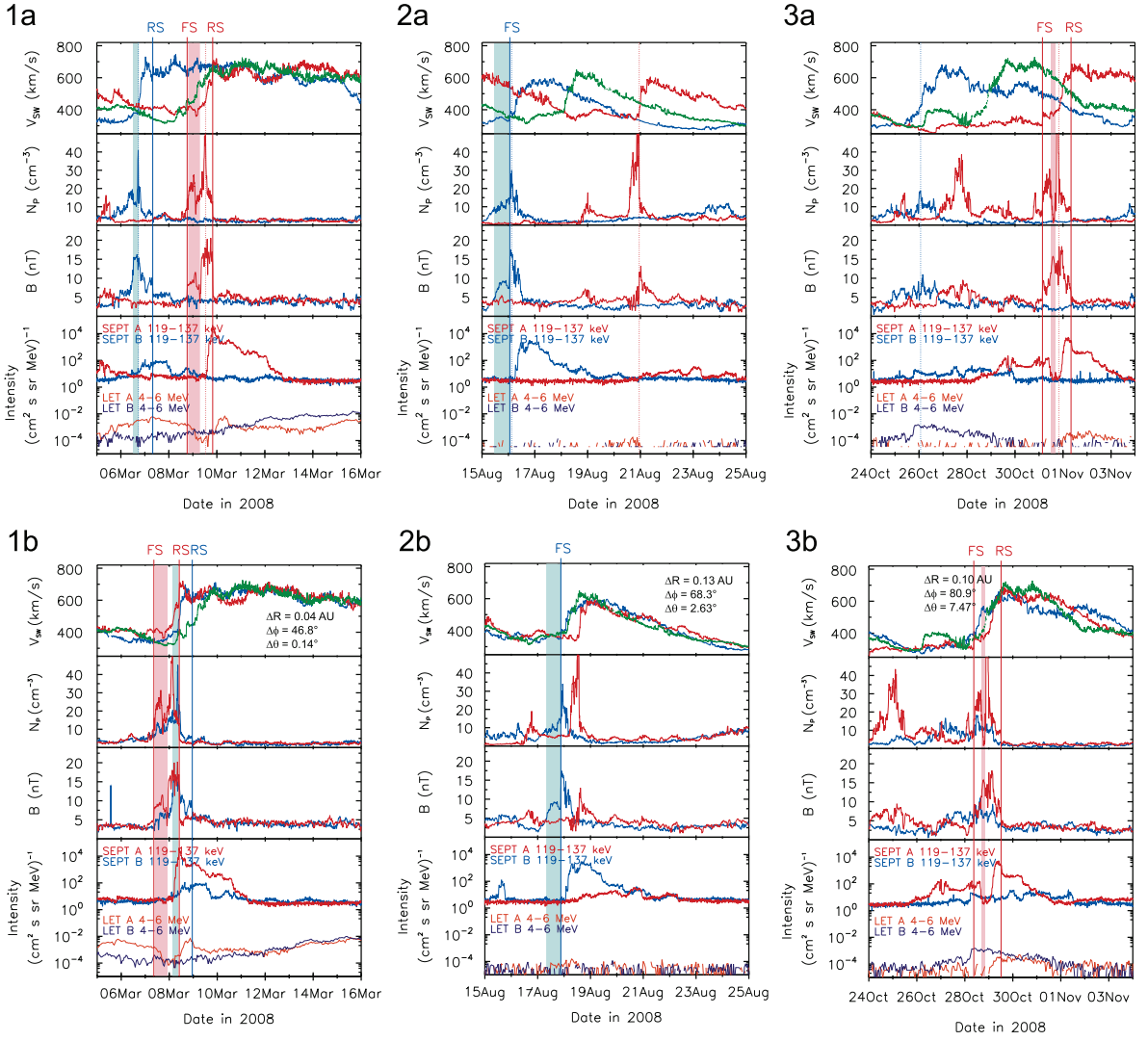

Fig. 7. Plasma and particle observations during events showing ICMEs in the vicinity of CIRs. From top to bottom: solar wind speed from ACE and the two STEREO spacecraft, proton density, magnetic field magnitude and omnidirectional ion intensities from STEREO. The three lower panels show the same data after application of a co-rotating time shift.

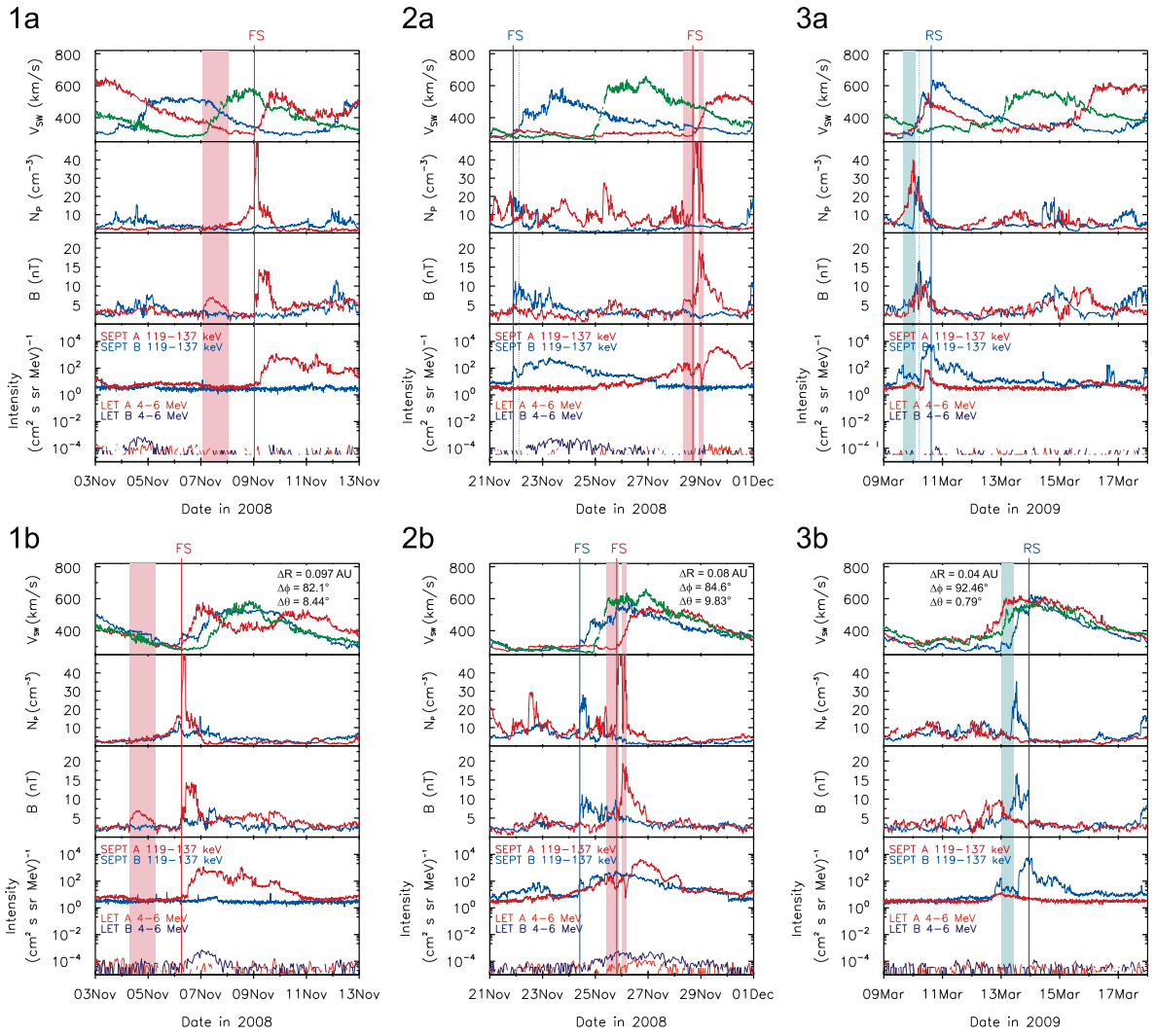

Fig. 8. Plasma and particle observations during events showing ICMEs in the vicinity of CIRs. From top to bottom: solar wind speed from ACE and the two STEREO spacecraft, proton density, magnetic field magnitude and omnidirectional ion intensities from STEREO. The three lower panels show the same data after application of a co-rotating time shift.

(see Gosling et al., 1978). The radial, latitudinal and azimuthal separation of the two STEREO spacecraft for the center of the period are shown in the bottom panels (solar wind speed plot).

Panels 1a and b in Fig. 7 show a complex case of different ICMEs observed by different spacecraft before the same high-speed stream during CR 2067. STB observed ICME signatures on March 6, 2008 from 12:35 UT to 17:03 UT. Two days later, near-Earth observatories (Wind and ACE) observed another interval with ICME signatures. A careful inspection of the plasma parameters and magnetic field reveals that another ICME was also observed by STA. We refer the reader to Appendix A for a deeper analysis of the ICME intervals observed in situ by Wind and STA, which are presented in Fig. 9. For STB the magnetic field was more intense during the ICME than during the CIR, for STA the higher magnetic field intensity was observed during the CIR. Both spacecraft observed in situ reverse shocks (RS in the figure), but STA measured a much higher 119–137 keV ion increase. The ratio of the maximum intensities measured by both spacecraft at the event maximum exceeds two orders of magnitude. At 4–6 MeV, the increase is also higher for STA during the CIR interval (see also Leske et al., 2010), but later, LET measured a long-duration gradual increase which peaks several days after the CIR. This delayed increase which is presumably due to a late connection to the distant part of the CIR reverse shock, was observed by both spacecraft (with the expected co-rotating delay).

Panels 2a and b in Fig. 7 correspond to a clear example of ICME-CIR interaction observed by STB during CR 2073. During August 15, 12-22 UT, an ICME with distinct flux-rope signatures crossed the STB location. After the ICME passage the magnetic field magnitude reached a maximum due to the interaction with the high-speed stream originating from a coronal hole with positive polarity. This interaction was not present for STA, which observed a much less intense CIR-associated 119–137 keV ion increase. The latitudinal separation on August 19 was 2.6° and the time-shifted solar wind speed profiles are remarkably similar except for the delayed leading edge for STA. STB observed an in situ forward shock (FS) at the front part of the CIR, not observed later by STA, but the particle increase started later, reaching maximum values when the spacecraft was inside the fast solar wind stream. These particles were absent during the ICME interval and increased abruptly after the stream interface, meaning that both structures act as barriers for the energetic ions. The LET instrument onboard both STEREO did not observe significant 4–6 MeV increases during this CIR.

Panels 3a and b in Fig. 7 show a CIR observed at the beginning of CR 2076, in connection with a negative polarity coronal hole. STB,

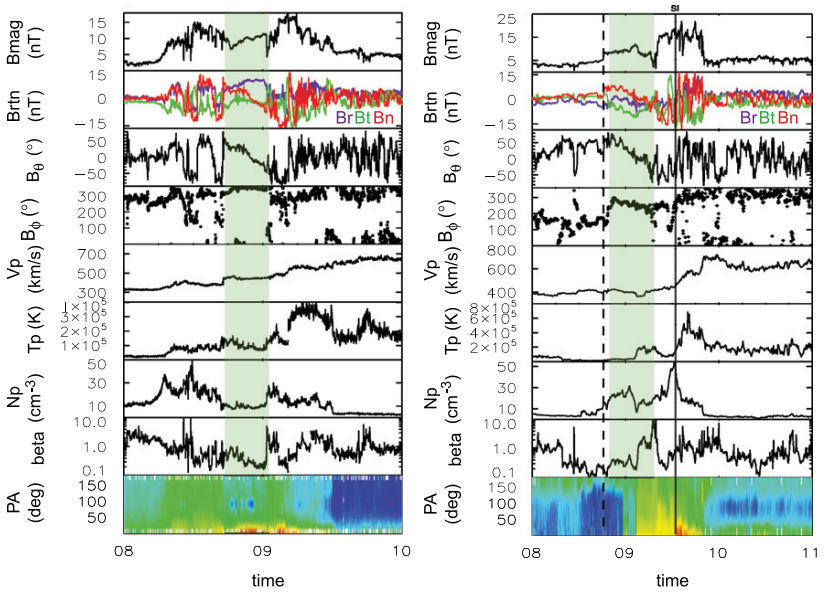

Fig. 9. Details of ICME signatures observed by ACE (left) and STA (right) during March 8–9, 2008. From top to bottom: magnetic field magnitude, magnetic field RTN Cartesian components, magnetic field RTN angular coordinates θ and ϕ, solar wind proton speed, proton temperature, proton density, plasma beta and electron pitch-angle distribution.

located 1.07 AU from the Sun, observed only a broad and weak compression region during October 24–26. STA, located at a heliocentric distance of 0.97 AU observed a well defined CIR from October 31 to November 1. This CIR was fully developed, showing forward and reverse shocks, which generated significant 119–137 keV ion increases. In this case the ICME was embedded within the CIR structure, preceding the stream interface. The particles showed a deep local minimum during the ICME interval. The flux increased again after the stream interface (not shown in the figure) and reached the absolute maximum shortly before the reverse shock passage. STB did not observe any in situ shocks and the energetic ion increase was much smaller. The heliographic latitudinal separation between the two STEREO spacecraft was more than 7°, but the stream was clearly observed by both spacecraft and the backmapped solar wind speed profiles show a reasonable agreement. It is also remarkable that at several MeV energies the situation is reversed and the proton fluxes observed by LET were higher at STB than at STA.

Panels 1a and b in Fig. 8 correspond to a CIR observed in early November 2008, during CR 2076. The event was related to a positive polarity coronal hole extending near the equator. STA and STB observed significant differences in the time-shifted solar wind profiles, probably due to the large latitudinal separation of 8.4°. An ICME was observed by STA between November 7, 02:00 UT and November 8, 01:15 UT. The CIR started one day later. However, the density and the magnetic field showed more prominent enhancements for STA compared to STB. Moreover, 119–137 keV ion fluxes show a two order of magnitude increase 2 h after the density peak for STA while they stay almost at background levels for STB. The 4–6 MeV ions observed by LET remained at background levels for STA, while a small increase observed by STB on November 4 is an SEP event and unrelated to the CIR (see Wiedenbeck et al., 2010). STA observed an in situ forward shock on November 9, 00:39 UT, before the particle increase while a careful examination of the plasma and magnetic field data showed the presence of a possible developing reverse shock at November 9, 14:02 UT, near the ion maximum. No in situ shocks were observed by STB.

Panels 2a and b in Fig. 8 correspond to a CIR observed in November 2008, at the beginning of CR 2077, associated with a negative polarity coronal hole. The time-shifted profiles reveal that the leading edge of the stream was significantly delayed at STA. This delay could be related to the 9.8° latitudinal separation, but also to the presence of two ICMEs between November 28, 07:45–18:25 UT and from November 28, 21:49 UT to November 29, 02:00 UT (Kilpua et al., 2009a). These ICME obstacles could account for the strong compression observed by STA during the CIR which is much more intense than for STB as a result of the interaction with the ICME. Both spacecraft observed forward shocks, which in the case of STA was located between both ICMEs. Both spacecraft measured large and broad increases of the 119–137 keV ion fluxes. The time-shifted profiles of these increases are in relatively good agreement for the rising and decay phase, but STA exceeded by nearly a factor 10 the maximum flux observed by STB. This maximum was reached after the stream interface, during the fast wind region. In contrast, the 4–6 MeV protons observed by LET show higher fluxes and a broader increase for STB compared to STA. The radial separation was 0.08 AU.

Panels 3a and b in Fig. 8 show a CIR event observed in March 2009, at the beginning of CR 2081, associated with a negative polarity coronal hole. The apparent agreement observed by STB and STA during March 9–10 (panel 3a) is related to a time-coincident but totally unrelated stream observed by STA at the same time. The CIR of interest was observed by STA six days later. The latitudinal separation between the two STEREO spacecraft was only 0.8° and the time-shifted profiles observed by both spacecraft showed a quite similar structure, but with a remarkable delay at the leading edge observed by STB. Just before the stream, STB observed an interval of smooth magnetic field which we identified as an ICME (see green area in Fig. 11 in Appendix A). After this ICME, the density and the magnetic field reached a maximum during the compression region, which was significantly enhanced in comparison with STA. The 119–137 keV ion fluxes were also greatly enhanced for STB in comparison to STA. The maximum particle flux for STB was reached after the stream interface, in coincidence with the reverse shock, observed in situ on March 10, 14:47 UT, but not present later when the same CIR passed through the STA location. The STB maximum exceeded the STA maximum by more than two orders of magnitude. The LET instrument observed no significant ion increases in the few-MeV range for any of the spacecraft.

3. Discussion and conclusions

The privileged location of the twin STEREO spacecraft, carrying onboard nearly identical instrumentation, and the extremely quiet conditions observed during the recent solar minimum offered a unique opportunity for multi-point observations of CIRs. We have presented multi-spacecraft near-ecliptic observations of high-speed streams and CIR-associated ion increases during a period of very low solar activity from Carrington rotation 2067.0 to 2082.0. Recurrent CIR-associated ion increases in the energy interval from some hundreds of keV to a few MeV were regularly observed by the SEPT and LET instruments onboard the twin STEREO spacecraft. The majority of high-speed streams and the associated CIRs observed by STB were later observed by STA; however, the structure of the high-speed streams observed at 1 AU is generally highly dependent on the heliographic latitude of the spacecraft. For this reason, two spacecraft separated by few degrees in latitude often observe a different structure during the passage of the same high-speed stream. In extreme cases, the stream can be totally missed by one of the spacecraft. Recent works using STEREO data (Mason et al., 2009; Gómez-Herrero et al., 2009, 2010; Leske et al., 2010) have pointed out the deviations from the ideal rigid rotation in the CIR structures and the importance of the latitudinal separation, confirming previous results found by the Helios mission (Schwenn and Marsch, 1990). Mason et al. (2009) suggested that while there is some temporal evolution of the CIRs over periods of days, the bulk of the changes are due to the small and irregular coronal hole source sizes together with the different heliolatitude connections.

Apart from the important effect of the latitudinal separation, Fig. 3 shows how as the co-rotation time between the two STEREO spacecraft increases, the correlation between the in situ structures observed by both spacecraft decrease. This effect, independent of the latitudinal separation, is an indication of pure temporal evolution. One cause of such temporal evolution is the changes in the extension and the location of the source coronal holes. These changes are obvious when observations are compared for several successive solar rotations. Occasionally significant changes in the coronal holes occur over short time scales of a few days. Two spacecraft properly located can track these changes and correlate them with the variations observed in the in situ structure of the associated high-speed stream. We found that another source of temporal evolution during CIRs is the presence of transient structures in the solar wind preceding the high-speed streams. We presented several cases, where the presence of an ICME in the vicinity of or embedded in the CIR for one spacecraft is accompanied by enhanced ion acceleration in the hundred-keV energy range. Normally the 4–6 MeV ion fluxes are not largely affected in a similar way. In some cases the ion increases are associated to shocks observed in situ by only one of the spacecraft.

The October 24–November 4, 2008 interval shown in panels 3a and b of Fig. 7 is a remarkable case illustrating the high degree of temporal variability during a CIR in the course of a few days. STA observed a well-formed CIR, bounded by forward and reverse shocks at 0.97 AU, while STB, at 1.07 AU did not observe any in situ shocks. This strong variation occurred in coincidence with the presence of an ICME embedded inside the CIR for STA, which observed enhanced acceleration of ions in the range of hundreds of keV.

The main conclusions of this study can be summarized as follows:

- Heliographic latitudinal separation is a common source of discrepancies in the CIR properties measured by different spacecraft. This effect can be significant even for separations of a few degrees but its importance varies from case to case depending on the proximity to the latitudinal boundaries and also on the topology of the coronal hole.
- Excluding pure spatial effects (like the latitudinal effect or the radial gradients), we conclude that CIRs are not ideal stationary structures showing identical characteristics at two spacecraft separated by co-rotation times of several days. The sources of temporal variations can be found at the Sun or in the interplanetary medium. In some cases the same CIR is accompanied by in situ shocks only at one spacecraft, with the consequent enhanced particle acceleration.
- The evolution of the coronal structure (particularly the changes in coronal hole contours) gives rise to variations of the high-speed streams observed in the interplanetary medium. This kind of variation is easy to track in the long term, comparing in situ and remote-sensing observations for successive Carrington rotations, but occasionally quick changes are found during the co-rotation time from STB to STA. These changes have a direct counterpart in the in situ particle and plasma data observed at 1 AU.
- Another source of temporal evolution is the presence of transient structures in the solar wind preceding the high-speed streams. We presented several cases, where the presence of an ICME in the vicinity of or embedded in the CIR for one spacecraft apparently favored the formation of forward and reverse shocks at 1 AU, resulting in enhanced local ion acceleration in the hundred-keV energy range. During the ICME transient intervals, normally local minima or particle decreases in the ion fluxes are found. This can be explained by the closed magnetic topology of the ICMEs (see Richardson, 1997; Malandraki et al., 2005) or by a lack of connection to the CIR shocks.
- During the ICME-CIR events showing enhanced hundred-keV ion acceleration by the CIR, the several MeV ion fluxes are less affected and the higher intensities are normally measured by the outer spacecraft (STB). This suggests that MeV protons come mainly from CIR-shocks located beyond the spacecraft, while at energies of hundreds of keV, the particles are accelerated in the vicinity of the spacecraft. In most cases of our study, the low energy ion maxima are associated with shocks or developing shocks observed locally at 1 AU, in some other cases no shocks were observed. This illustrates the general importance of local phenomena for the acceleration of $\sim$100 keV ions during CIRs (see, e.g. Richardson and Zwickl, 1984; Richardson, 1985; Schwadron et al., 1996; Mason et al., 1997; Chotoo et al., 2000; Giacalone et al., 2002). A theoretical modelling approach and the systematic comparison of STEREO measurements with near-Earth observations would allow further progress to clarify the physical processes involved in these complex interaction regions.

Acknowledgments

We thank two anonymous referees for their valuable comments and suggestions. We acknowledge PLASTIC, IMPACT, SECCHI, EIT and Wind teams and the ACE Science Center for providing the data used in this paper. We are also grateful to Richard Leske and the LET team for the discussion about LET data interpretation. The STEREO/SEPT project is supported under Grant 50 OC 0902 by the German Bundesministerium für Wirtschaft through the Deutsches Zentrum für Luft- und Raumfahrt (DLR). E. Kilpua acknowledges Academy of Finland Project 130298. This work utilizes data obtained by the Global Oscillation Network Group (GONG) program, managed by the National Solar Observatory, which is operated by AURA, Inc. under a cooperative agreement with the National Science Foundation. The data were acquired by instruments operated by the Big Bear Solar Observatory, High Altitude Observatory, Learmonth Solar Observatory, Udaipur Solar Observatory,

Instituto de Astrofísica de Canarias, and Cerro Tololo Interamerican Observatory.

Appendix A. ICME identification

In this section we describe in detail some ICMEs that were identified at the leading edges of CIRs discussed in this paper. As a reference we have used the ICME list published in Kilpua et al. (2009a) and the IMPACT/MAG level 3 ICME list (http://www-ssc.igpp.ucla.edu/forms/stereo/stereo_level_3.html). The ICME identification is not unambiguous as there is no signature that is present in all ICMEs and as the various signatures do not always occur simultaneously. In particular, ICMEs that are merged at the leading edges of CIRs can be difficult to identify as they can get significantly distorted by the interaction with ambient solar wind (e.g. Richardson and Cane, 2004; Riley et al., 2006). Crooker et al. (1996) have reported small transient flux ropes embedded within the heliospheric plasma sheet. However, the durations of these structures (less than an hour) are very small when compared to ICMEs (from several hours to days). We have also searched associated CMEs by determining the extrapolated CME onset time for each event using the average speed within the ICME and assuming radial propagation at the constant speed to the spacecraft. We have searched possible CME candidates within a time window of two days centered at the extrapolated time.

March 2008 ICMEs. The ICME signatures observed by ACE and STA are presented in Fig. 9, where the green areas correspond to the region of magnetic field rotation. At ACE the ICME was bracketed by high magnetic field regions associated with the CIR. The level of magnetic field fluctuations are clearly depressed and the latitude angle of the magnetic field B_θ rotates smoothly from north to south. At the center of the ICME the field points to the east indicating that the magnetic field rotation is right-handed (i.e. anticlockwise). Plasma beta is also depressed during the ICME. The magnetic field changes during the ICME at STA are more irregular than at ACE, but as demonstrated by Fig. 9 B_θ exhibits a north-to-south rotation. At STA the magnetic field rotation is also right-handed. Note that at STA the region of depressed temperature and plasma beta starts already 11.5 h before the marked green area. However, the magnetic field changes during this extended region are not well-organized. The pitch-angle spectrogram of suprathermal heat flux electrons in the bottom of Fig. 9 shows that during the ICME at ACE the heat flux flow is unidirectional and flowing parallel to the magnetic field (i.e. pitch angle (PA) 0°. The magnetic field is primarily in the away sector, consistent with the electron heat flux direction along open field lines. Considering the observations at STEREO A, the dashed vertical line marks the passage of a very weak forward shock (IMPACT/PLASTIC level 3 list), but it is unclear whether it is CME driven or CIR related. The solar wind sector structure is quite different at the location of STA. Within the ICME the magnetic field changes from the toward to the away sector and heat flux correspondingly from antiparallel to parallel flow. The angular separation between STA and ACE at the time of this event was 22.7°.

At such large separations it is not straightforward to relate observations between the spacecraft and one cannot be confident that the spacecraft traversed through the same ICME (Mulligan et al., 1999; Kilpua et al., in revision). Although magnetic field directional changes were rather similar between the spacecraft it is not clear that they present the same extended flux rope. As discussed above the large-scale solar wind structure had discrepancies between ACE and STA. Furthermore, both ICMEs had distinct CME association. On mid-day March 4 and early March 5 the coronagraphs on STB observed clear CME eruptions, consistent with the estimated launch times of the ICMEs at STA (March 4 at 15:17 UT) and ACE (March 4 at 23:18 UT), respectively. The plasma signatures of ICME detected at ACE are not clear, and as discussed above the identification of ICMEs is particularly difficult when they are interacting with CIRs. However, due to distinct magnetic field signatures and a clear CME association we conclude that this event is very likely an ICME embedded within a CIR.

December 2008 ICMEs. Two ICMEs observed by STB on 7–9 December 2008 are presented in Fig. 10, where the green areas correspond to the ICME intervals. The latter, very narrow ICME that is compressed at the leading edge of the overtaking CIR is included both in Kilpua et al. (2009a) and IMPACT/PLASTIC level 3 lists. The ICME was indentified from the clear magnetic field rotation from north to south, depressed temperature and plasma beta. The preceding ICME drives an interplanetary shock that is indicated by a dashed line. The ICME is identified from the coherent magnetic field rotation, smooth magnetic field profile and counterstreaming heat flux electrons. The boundaries of this ICME are difficult to determine accurately, possibly due to distortion by the following CME/CIR structure. The extrapolated CME onset times are 2 December at 5 UT and 3 December at 21 UT, respectively. STEREO COR1 CME catalogue lists two CMEs that were detected within a suitable time window. The first CME was detected at 01:35 UT on 2 December and the latter one 04:35 UT on 3 December. Both CMEs left from the east limb in the STA field of view indicating that they were propagating towards STB. STEREO beacon 304 Å movie shows that the first CME was associated with an impressive eruption of a high-latitude large prominence. The CME quickly deflected to the equator within the STA/COR2 field of view. A similar event

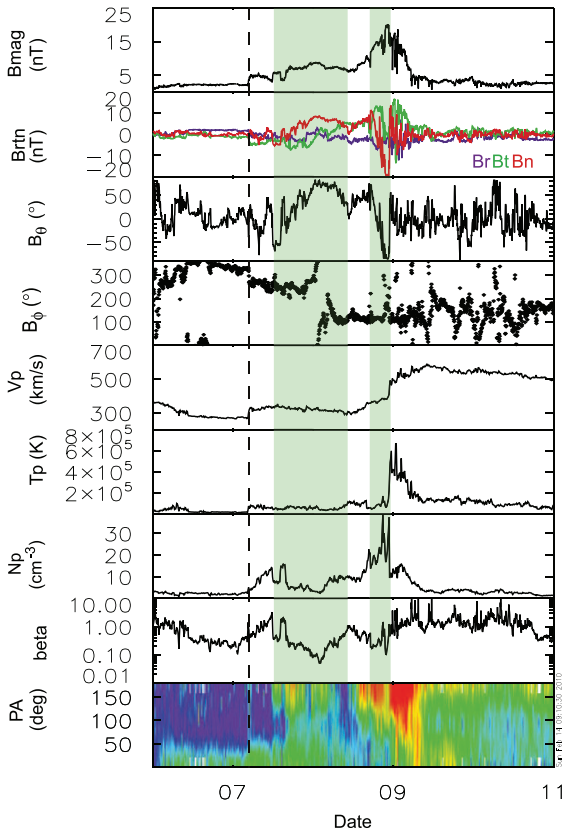

Fig. 10. Details of ICME signatures observed by STB during the December 7–9, 2008. From top to bottom: magnetic field magnitude, magnetic field RTN Cartesian components, magnetic field RTN angular coordinates θ and ϕ, solar wind proton speed, proton temperature, proton density, plasma beta and electron pitch-angle distribution.

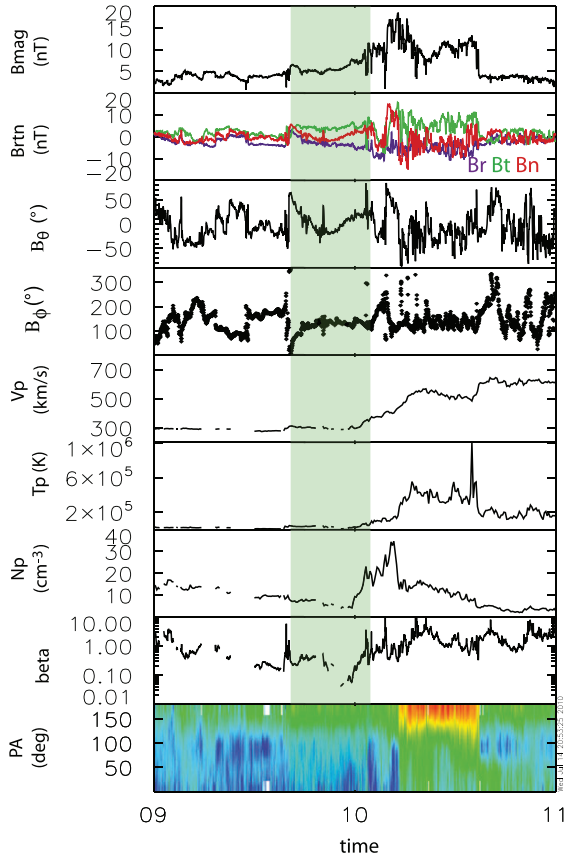

Fig. 11. Details of ICME signatures observed by STB during the March 8–9, 2009. From top to bottom: magnetic field magnitude, magnetic field RTN Cartesian components, magnetic field RTN angular coordinates θ and ϕ, solar wind proton speed, proton temperature, proton density, plasma beta and electron pitch-angle distribution.

where a CME associated with a high-latitude prominence eruption deflected towards the equator and was later observed near the ecliptic plane is discussed in detail in Kilpua et al. (2009a).

March 2009 ICMEs. The observations during the ICME identified at STA on 9–10 March 2009 are shown in Fig. 11. Within the green area in the figure the magnetic field exhibits organized behaviour. The magnetic field latitude angle rotates from north to south at the middle of the ICME and then back to the north at the trailing portion of the ICME. In addition, plasma beta is also clearly depressed. Even though no bidirectional electrons were observed, based on the clear magnetic field signatures and the depressed plasma beta associated with this structure we can conclude that it presents an ICME. The extrapolated CME onset time is 3 March at 13 UT. The COR1 catalogue indicates that STA observed a CME leaving from the east limb starting on 2 March 22:05 UT. This CME was also associated with a high-latitude prominence eruption in STA 304 Å movie and in STA/COR2 field of view the CME was seen to propagate close to the solar equator.

References

Acuña, M.H., Curtis, D., Scheifele, J.L., Russell, C.T., Schroeder, P., Szabo, A., Luhmann, J.G., 2008. The STEREO/IMPACT magnetic field experiment. Space Sci. Rev. 136, 203–226.

Antoniadou, I., Geranios, A., Vandas, M., Panagopoulou, M., Zacharopoulou, O., Malandraki, O., 2008. Elliptical magnetic clouds and geomagnetic storms. Planet. Space Sci. 56, 492–500.

Barnes, C.W., Simpson, J.A., 1976. Evidence for interplanetary acceleration of nucleons in corotating interaction regions. Astrophys. J. Lett. 210, L91–L96.

Belcher, J.W., Davis Jr., L., 1971. Large-amplitude Alfvén waves in the interplanetary medium, 2. J. Geophys. Res. 76, 3534–3563.

Bromage, B.J.J., Alexander, D., Breen, A., Clegg, J.R., Del Zanna, G., DeForest, C., Dobrzycka, D., Gopalswamy, N., Thompson, B., Browning, P.K., 2000. Structure of a large low-latitude coronal hole. Solar Phys. 193, 181–193.

Broussard, R.M., Tousey, R., Underwood, J.H., Sheeley Jr., N.R., 1978. A survey of coronal holes and their solar wind associations throughout sunspot cycle 20. Solar Phys. 56, 161–183.

Burlaga, L.F., Behannon, K.W., Klein, L.W., 1987. Compound streams, magnetic clouds, and major geomagnetic storms. J. Geophys. Res. 92, 5725–5734.

Burlaga, L.F., Hewish, A., Behannon, K.W., 1991. Structure and evolution of compound streams at not greater than 1 AU. J. Geophys. Res. 96, 21213.

Burlaga, L.F., Ogilvie, K.W., 1973. Solar wind temperature and speed. J. Geophys. Res. 78, 2028–2034.

Burlaga, L.F., Scudder, J.D., 1975. Motion of shocks through interplanetary streams. J. Geophys. Res. 80, 4004–4010.

Bučík, R., Mall, U., Gómez-Herrero, R., Korth, A., Mason, G.M., 2009a. STEREO observations of energetic ions in corotating interaction regions during the May 2007 solar events. Solar Phys. 259, 361–380.

Bučík, R., Mall, U., Korth, A., Mason, G.M., 2009b. On acceleration of <1 MeV/n He ions in the corotating compression regions near 1 AU: STEREO observations. Ann. Geophys. 27, 3677–3690.

Chotoo, K., Schwadron, N.A., Mason, G.M., Zurbuchen, T.H., Gloeckler, G., Posner, A., Fisk, L.A., Galvin, A.B., Hamilton, D.C., Collier, M.R., 2000. The suprathermal seed population for corotating interaction region ions at 1 AU deduced from composition and spectra of H^+, He^{++}, and He^+ observed on Wind. J. Geophys. Res. 105, 23107–23122.

Christon, S.P., Simpson, J.A., 1979. Separation of corotating nucleon fluxes from solar flare fluxes by radial gradients and nuclear composition. Astrophys. J. Lett. 227, L49–L53.

Crooker, N.U., Burton, M.E., Phillips, J.L., Smith, E.J., Balogh, A., 1996. Heliospheric plasma sheets as small-scale transients. J. Geophys. Res. 101, 2467–2474.

Dal Lago, A., Gonzalez, W.D., Balmaceda, L.A., Vieira, L.E.A., Echer, E., Guarnieri, F.L., Santos, J., da Silva, M.R., de Lucas, A., Clua de Gonzalez, A.L., Schwenn, R., Schuch, N.J., 2006. The 17–22 October (1999) solar-interplanetary-geomagnetic event: very intense geomagnetic storm associated with a pressure balance between interplanetary coronal mass ejection and a high-speed stream. J. Geophys. Res. (Space Phys.) 111, A07S14.

Delaboudinière, J., Artzner, G.E., Brunaud, J., Gabriel, A.H., Hochedez, J.F., Millier, F., Song, X.Y., Au, B., Dere, K.P., Howard, R.A., Kreplin, R., Michels, D.J., Moses, J.D., Defise, J.M., Jamar, C., Rochus, P., Chauvineau, J.P., Marioge, J.P., Catura, R.C., Lemen, J.R., Shing, L., Stern, R.A., Gurman, J.B., Neupert, W.M., Maucherat, A., Clette, F., Cugnon, P., van Dessel, E.L., 1995. EIT: extreme-ultraviolet imaging telescope for the SOHO mission. Solar Phys. 162, 291–312.

Dresing, N., Gómez-Herrero, R., Heber, B., Müller-Mellin, R., Wimmer-Schweingruber, R., Klassen, A., 2009. Multi-spacecraft observations of CIR-associated ion increases during the Ulysses 2007 ecliptic crossing. Solar Phys. 256, 409–425.

Fenrich, F.R., Luhmann, J.G., 1998. Geomagnetic response to magnetic clouds of different polarity. Geophys. Res. Lett. 25, 2999–3002.

Galvin, A.B., Kistler, L.M., Popecki, M.A., Farrugia, C.J., Simunac, K.D.C., Ellis, L., Möbius, E., Lee, M.A., Boehm, M., Carroll, J., Crawshaw, A., Conti, M., Demaine, P., Ellis, S., Gaidos, J.A., Googins, J., Granoff, M., Gustafson, A., Heirtzler, D., King, B., Knauss, U., Levasseur, J., Longworth, S., Singer, K., Turco, S., Vachon, P., Vosbury, M., Widholm, M., Blush, L.M., Karrer, R., Bochsler, P., Daoudi, H., Etter, A., Fischer, J., Jost, J., Opitz, A., Sigrist, M., Wurz, P., Klecker, B., Ertl, M., Seidenschwang, E., Wimmer-Schweingruber, R.F., Koeten, M., Thompson, B., Steinfeld, D., 2008. The plasma and suprathermal ion composition (PLASTIC) investigation on the STEREO observatories. Space Sci. Rev. 136, 437–486.

Giacalone, J., Jokipii, J.R., Kóta, J., 2002. Particle acceleration in solar wind compression regions. Astrophys. J. 573, 845–850.

Gómez-Herrero, R., Klassen, A., Müller-Mellin, R., Heber, B., Wimmer-Schweingruber, R., Böttcher, S., 2009. Recurrent CIR-accelerated ions observed by STEREO SEPT. J. Geophys. Res. (Space Phys.) 114, A05101.

Gómez-Herrero, R., Malandraki, O., Dresing, N., Kilpua, E., Heber, B., Klassen, A., Müller-Mellin, R., Wimmer-Schweingruber, R.F., 2010. Multi-point observations of CIR-associated energetic particles during the 2008 solar minimum. In: Twelfth International Solar Wind Conference, vol. 1216, pp. 608–612.

Gosling, J.T., Asbridge, J.R., Bame, S.J., Feldman, W.C., 1978. Solar wind stream interfaces. J. Geophys. Res. 83, 1401–1412.

Gosling, J.T., Bame, S.J., Feldman, W.C., McComas, D.J., Phillips, J.L., Goldstein, B.E., 1993. Counterstreaming suprathermal electron events upstream of corotating shocks in the solar wind beyond approximately 2 AU: ULYSSES. Geophys. Res. Lett. 20, 2335–2338.

Howard, R.A., Moses, J.D., Vourlidas, A., Newmark, J.S., Socker, D.G., Plunkett, S.P., Korendyke, C.M., Cook, J.W., Hurley, A., Davila, J.M., Thompson, W.T., St Cyr, O.C., Mentzell, E., Mehalick, K., Lemen, J.R., Wuelser, J.P., Duncan, D.W., Tarbell, T.D., Wolfson, C.J., Moore, A., Harrison, R.A., Waltham, N.R., Lang, J., Davis, C.J., Eyles, C.J., Mapson-Menard, H., Simnett, G.M., Halain, J.P., Defise, J.M., Mazy, E., Rochus, P., Mercier, R., Ravet, M.F., Delmotte, F., Auchere, F., Delaboudiniere, J.P., Bothmer, V., Deutsch, W., Wang, D., Rich, N., Cooper, S., Stephens, V., Maahs, G., Baugh, R., McMullin, D., Carter, T., 2008. Sun Earth connection coronal and heliospheric investigation (SECCHI). Space Sci. Rev. 136, 67–115.

Jian, L., Russell, C.T., Luhmann, J.G., Skoug, R.M., 2006. Properties of stream interactions at one AU during 1995–2004. Solar Phys. 239, 337–392.

Jian, L.K., Russell, C.T., Luhmann, J.G., Galvin, A.B., MacNeice, P.J., 2009. Multi-spacecraft observations: stream interactions and associated structures. Solar Phys. 259, 345–360.
Kaiser, M.L., Kucera, T.A., Davila, J.M., St. Cyr, O.C., Guhathakurta, M., Christian, E., 2008. The STEREO mission: an introduction. Space Sci. Rev. 136, 5–16.
Kilpua, E.K.J., Jian, L., Li, Y., Luhmann, J., Russell, C. Multipoint ICME encounters: pre-STEREO and STEREO observations. Journal of Atmospheric and Solar Terrestrial Physics, in press, doi:10.1016/j.jastp.2010.10.012.
Kilpua, E.K.J., Pomoell, J., Vourlidas, A., Vainio, R., Luhmann, J., Li, Y., Schroeder, P., Galvin, A.B., Simunac, K., 2009a. STEREO observations of interplanetary coronal mass ejections and prominence deflection during solar minimum period. Ann. Geophys. 27, 4491–4503.
Kilpua, E.K.J., Pomoell, J., Vourlidas, A., Vainio, R., Luhmann, J., Li, Y., Schroeder, P., Galvin, A., Simunac, K., 2009b. Small solar wind transients and their connection to the large-scale coronal structure. Solar Phys. 256, 327.
Kunow, H., Witte, M., Wibberenz, G., Hempe, H., Mueller-Mellin, R., Green, G., Iwers, B., Fuckner, J., 1977. Cosmic ray measurements on board HELIOS 1 from December 1974 to September 1975 Quiet time spectra, radial gradients, and solar events. J. Geophys. Z. Geophys. 42, 615–631.
Lee, C.O., Luhmann, J.G., de Pater, I., Mason, G.M., Haggerty, D., Richardson, I.G., Cane, H.V., Jian, L.K., Russell, C.T., Desai, M.I., 2010. Organization of energetic particles by the solar wind structure during the declining to minimum phase of solar cycle 23. Solar Phys. 73.
Leske, R.A., Mewaldt, R.A., Mason, G.M., Cohen, C.M.S., Cummings, A.C., Labrador, A.W., Stone, E.C., Wiedenbeck, M.E., von Rosenvinge, T.T., 2010. STEREO and ACE observations of energetic particles from corotating interaction regions. In: Twelfth International Solar Wind Conference, vol. 1216, pp. 379–382.
Luhmann, J.G., Curtis, D.W., Schroeder, P., McCauley, J., Lin, R.P., Larson, D.E., Bale, S.D., Sauvaud, J.-A., Aoustin, C., Mewaldt, R.A., Cummings, A.C., Stone, E.C., Davis, A.J., Cook, W.R., Kecman, B., Wiedenbeck, M.E., von Rosenvinge, T., Acuna, M.H., Reichenthal, L.S., Shuman, S., Wortman, K.A., Reames, D.V., Mueller-Mellin, R., Kunow, H., Mason, G.M., Walpole, P., Korth, A., Sanderson, T.R., Russell, C.T., Gosling, J.T., 2008. STEREO IMPACT investigation goals, measurements, and data products overview. Space Sci. Rev. 136, 117–184.
Malandraki, O.E., Lario, D., Lanzerotti, L.J., Sarris, E.T., Geranios, A., Tsiropoula, G., 2005. October/November 2003 interplanetary coronal mass ejections: ACE/EPAM solar energetic particle observations. J. Geophys. Res. (Space Phys.) 110, A09S06.
Malandraki, O.E., Marsden, R.G., Tranquille, C., Forsyth, R.J., Elliott, H.A., Geranios, A., 2008. Energetic particle measurements from the Ulysses/COSPIN/LET instrument obtained during the August/September 2005 events. Ann. Geophys. 26, 1029–1037.
Malandraki, O.E., Marsden, R.G., Tranquille, C., Forsyth, R.J., Elliott, H.A., Lanzerotti, L.J., Geranios, A., 2007. Energetic particle observations by Ulysses during the declining phase of solar cycle 23. J. Geophys. Res. (Space Phys.) 112, A06111.
Marshall, F.E., Stone, E.C., 1978. Characteristics of sunward flowing proton and alpha particle fluxes of moderate intensity. J. Geophys. Res. 83, 3289–3298.
Mason, G.M., Desai, M.I., Mall, U., Korth, A., Bucik, R., von Rosenvinge, T.T., Simunac, K.D., 2009. In situ observations of CIRs on STEREO, Wind, and ACE during 2007–2008. Solar Phys. 256, 393–408.
Mason, G.M., Mazur, J.E., Dwyer, J.R., Reames, D.V., von Rosenvinge, T.T., 1997. New spectral and abundance features of interplanetary heavy ions in corotating interaction regions. Astrophys. J. Lett. 486, L149–L152.
McComas, D.J., Bame, S.J., Barker, P., Feldman, W.C., Phillips, J.L., Riley, P., Griffee, J.W., 1998. Solar wind electron proton alpha monitor (SWEPAM) for the advanced composition explorer. Space Sci. Rev. 86, 563–612.
McComas, D.J., Barraclough, B.L., Funsten, H.O., Gosling, J.T., Santiago-Muñoz, E., Skoug, R.M., Goldstein, B.E., Neugebauer, M., Riley, P., Balogh, A., 2000. Solar wind observations over Ulysses first full polar orbit. J. Geophys. Res. 105, 10419–10434.
McDonald, F.B., Teegarden, B.J., Trainor, J.H., von Rosenvinge, T.T., Webber, W.R., 1976. The interplanetary acceleration of energetic nucleons. Astrophys. J. Lett. 203, L149–L154.
Mewaldt, R.A., Cohen, C.M.S., Cook, W.R., Cummings, A.C., Davis, A.J., Geier, S., Kecman, B., Klemic, J., Labrador, A.W., Leske, R.A., Miyasaka, H., Nguyen, V., Ogliore, R.C., Stone, E.C., Radocinski, R.G., Wiedenbeck, M.E., Hawk, J., Shuman, S., von Rosenvinge, T.T., Wortman, K., 2008. The low-energy telescope (LET) and SEP central electronics for the STEREO mission. Space Sci. Rev. 136, 285–362.
Müller-Mellin, R., Böttcher, S., Falenski, J., Rode, E., Duvet, L., Sanderson, T., Butler, B., Johlander, B., Smit, H., 2008. The solar electron and proton telescope for the STEREO mission. Space Sci. Rev. 136, 363–389.
Mulligan, T., Russell, C.T., Anderson, B.J., Lohr, D.A., Rust, D., Toth, B.A., Zanetti, L.J., Acuna, M.H., Lepping, R.P., Gosling, J.T., 1999. Intercomparison of NEAR and wind interplanetary coronal mass ejection observations. J. Geophys. Res. 104, 28217–28224.
Neugebauer, M., Liewer, P.C., Goldstein, B.E., Zhou, X., Steinberg, J.T., 2004. Solar wind stream interaction regions without sector boundaries. J. Geophys. Res. 109 (A18), 10102.
Nolte, J.T., Krieger, A.S., Timothy, A.F., Gold, R.E., Roelof, E.C., Vaiana, G., Lazarus, A.J., Sullivan, J.D., McIntosh, P.S., 1976. Coronal holes as sources of solar wind. Solar Phys. 46, 303–322.
Nolte, J.T., Roelof, E.C., 1973. Large-scale structure of the interplanetary medium, I: high coronal source longitude of the quiet-time solar wind. Solar Phys. 33, 241–257.
Opitz, A., Karrer, R., Wurz, P., Galvin, A.B., Bochsler, P., Blush, L.M., Daoudi, H., Ellis, L., Farrugia, C.J., Giammanco, C., Kistler, L.M., Klecker, B., Kucharek, H., Lee, M.A., Möbius, R.F., Popecki, M., Sigrist, M., Simunac, K., Singer, K., Thompson, B., Wimmer-Schweingruber, R.F., 2009. Temporal evolution of the solar wind bulk velocity at solar minimum by correlating the STEREO A and B PLASTIC measurements. Solar Phys. 256, 365–377.
Pizzo, V., 1978. A three-dimensional model of corotating streams in the solar wind. I—theoretical foundations. J. Geophys. Res. 83, 5563–5572.
Posner, A., Bothmer, V., Kunow, H., Gosling, J.T., Heber, B., Lazarus, A.J., Linker, J.A., Marsden, R.G., Mikić, Z., Müller-Mellin, R., Sanderson, T.R., Szabo, A., Thompson, B.J., 2000. Energetic particle signatures of a corotating interaction region from a high latitude coronal hole: SOHO, Wind and Ulysses observations. Advances in Space Research 26, 865–870.
Posner, A., Bothmer, V., Thompson, B.J., Kunow, H., Heber, B., Müller-Mellin, R., Lazarus, A.J., Szabo, A., Mikić, Z., Linker, J.A., 1999. In-ecliptic CIR-associated energetic particle events and polar coronal hole structures: SOHO/COSTEP observations for the Whole Sun Month Campaign. J. Geophys. Res. 104, 9881–9890.
Richardson, I.G., 1985. Low energy ions in co-rotating interaction regions at 1 AU evidence for statistical ion acceleration. Planet. Space Sci. 33, 557–569.
Richardson, I.G., 1997. Using energetic particles to probe the magnetic topology of ejecta. In: Crooker, N., Joselyn, J.A., Feynman, J. (Eds.), Coronal Mass Ejections. Geophysical Monograph Series, vol. 99. AGU, pp. 189–196.
Richardson, I.G., 2004. Energetic particles and corotating interaction regions in the solar wind. Space Sci. Rev. 111, 267–376.
Richardson, I.G., Cane, H.V., 2004. Identification of interplanetary coronal mass ejections at 1 AU using multiple solar wind plasma composition anomalies. J. Geophys. Res. (Space Phys.) 109, A09104.
Richardson, I.G., Mazur, J.E., Mason, G.M., 1998. A comparison of recurrent energetic ion enhancements observed at ULYSSES and at 1 AU by IMP 8 and SAMPEX–ULYSSES launch until following the first north polar passage. J. Geophys. Res. 103, 2115–2129.
Richardson, I.G., Zwickl, R.D., 1984. Low energy ions in corotating interaction regions at 1 AU observations. Planet. Space Sci. 32, 1179–1193.
Riley, P., Schatzman, C., Cane, H.V., Richardson, I.G., Gopalswamy, N., 2006. On the rates of coronal mass ejections: remote solar and in situ observations. Astrophys. J. 647, 648–653.
Rodgers, J.L., Nicewander, W.A., 1988. Thirteen ways to look at the correlation coefficient. The American Statistician 42, 59–66.
Rouillard, A.P., Davies, J.A., Forsyth, R.J., Rees, A., Davis, C.J., Harrison, R.A., Lockwood, M., Bewsher, D., Crothers, S.R., Eyles, C.J., Hapgood, M., Perry, C.H., 2008. First imaging of corotating interaction regions using the STEREO spacecraft. Geophys. Res. Lett. 35, 10110.
Rouillard, A.P., Davies, J.A., Lavraud, B., Forsyth, R.J., Savani, N.P., Bewsher, D., Brown, D.S., Sheeley, N.R., Davis, C.J., Harrison, R.A., Howard, R.A., Vourlidas, A., Lockwood, M., Crothers, S.R., Eyles, C.J., 2010a. Intermittent release of transients in the slow solar wind: 1. Remote sensing observations. J. Geophys. Res. (Space Phys.) 115 (April), A04103.
Rouillard, A.P., Lavraud, B., Davies, J.A., Savani, N.P., Burlaga, L.F., Forsyth, R.J., Sauvaud, J., Opitz, A., Lockwood, M., Luhmann, J.G., Simunac, K.D.C., Galvin, A.B., Davis, C.J., Harrison, R.A., 2010b. Intermittent release of transients in the slow solar wind: 2. In situ evidence. J. Geophys. Res. (Space Phys.) 115, A04104.
Rouillard, A.P., Savani, N.P., Davies, J.A., Lavraud, B., Forsyth, R.J., Morley, S.K., Opitz, A., Sheeley, N.R., Burlaga, L.F., Sauvaud, J., Simunac, K.D.C., Luhmann, J.G., Galvin, A.B., Crothers, S.R., Davis, C.J., Harrison, R.A., Lockwood, M., Eyles, C.J., Bewsher, D., Brown, D.S., 2009. A multispacecraft analysis of a small-scale transient entrained by solar wind streams. Solar Phys. 256, 307–326.
Scholer, M., Mann, G., Chalov, S., Desai, M.I., Fisk, L.A., Jokipii, J.R., Kallenbach, R., Keppler, E., Kóta, J., Kunow, H., Lee, M.A., Sanderson, T.R., Simnett, G.M., 1999. Origin, injection, and acceleration of CIR particles: theory report of working group 7. Space Sci. Rev. 89, 369–399.
Schwadron, N.A., Fisk, L.A., Gloeckler, G., 1996. Statistical acceleration of interstellar pick-up ions in co-rotating interaction regions. Geophys. Res. Lett. 23, 2871–2874.
Schwenn, R., Marsch, E.E., 1990. Physics of the Inner Heliosphere I. Large-Scale Phenomena. Springer-Verlag, Heidelberg.
Sheeley Jr., N.R., Harvey, J.W., 1981. Coronal holes, solar wind streams, and geomagnetic disturbances during 1978 and 1979. Solar Phys. 70, 237–249.
Simunac, K.D.C., Kistler, L.M., Galvin, A.B., Popecki, M.A., Farrugia, C.J., 2009. In situ observations from STEREO/PLASTIC: a test for L5 space weather monitors. Ann. Geophys. 27, 3805–3809.
Smith, C.W., L'Heureux, J., Ness, N.F., Acuña, M.H., Burlaga, L.F., Scheifele, J., 1998. The ACE magnetic fields experiment. Space Sci. Rev. 86, 613–632.
Smith, E.J., Wolfe, J.H., 1976. Observations of interaction regions and corotating shocks between one and five AU: Pioneers 10 and 11. Geophys. Res. Lett. 2, 137–140.
Smith, E.J., Wolfe, J.H., 1977. Pioneer 10, 11 observations of evolving solar wind streams and shocks beyond 1 AU. In: Shea, M.A., Smart, D.F., Wu, S.T. (Ed.), Study of Travelling Interplanetary Phenomena, Astrophysics and Space Science Library, vol. 71, pp. 227–257.
Smith, E.J., Wolfe, J.H., 1979. Fields and plasmas in the outer solar system. Space Sci. Rev. 23, 217–252.
Song, H.Q., Chen, Y., Liu, K., Feng, S.W., Xia, L.D., 2009. Quasi-periodic releases of streamer blobs and velocity variability of the slow solar wind near the Sun. Solar Phys. 258, 129–140.
Tappin, S.J., Howard, T.A., 2009. Direct observation of a corotating interaction region by three spacecraft. Astrophys. J. 702 (September), 862–870.

van Hollebeke, M.A.I., McDonald, F.B., Trainor, J.H., von Rosenvinge, T.T., 1978. The radial variation of corotating energetic particle streams in the inner and outer solar system. J. Geophys. Res. 83, 4723–4731.

Wiedenbeck, M.E., Mason, G.M., Gómez-Herrero, R., Haggerty, D., Nitta, N.V., Cohen, C.M.S., Chollet, E.E., Cummings, A.C., Leske, R.A., Mewaldt, R.A., Stone, E.C., von Rosenvinge, T.T., Müller-Mellin, R., Desai, M., Mall, U., 2010. Observations of a ^{3}He-rich SEP event over a broad range of heliographic longitudes: results from STEREO and ACE. In: Twelfth International Soar Wind Conference, vol. 1216, pp. 621–624.

Wood, B.E., Howard, R.A., Thernisien, A., Socker, D.G., 2010. The three-dimensional morphology of a corotating interaction region in the inner heliosphere. Astrophys. J. Lett. 708, L89–L94.

The Astrophysical Journal, 767:41 (18pp), 2013 April 10 doi:10.1088/0004-637X/767/1/41

LONGITUDINAL AND RADIAL DEPENDENCE OF SOLAR ENERGETIC PARTICLE PEAK INTENSITIES: *STEREO*, *ACE*, *SOHO*, *GOES*, AND *MESSENGER* OBSERVATIONS

D. Lario[1], A. Aran[2], R. Gómez-Herrero[3,4], N. Dresing[3], B. Heber[3], G. C. Ho[1], R. B. Decker[1], and E. C. Roelof[1]
[1] The Johns Hopkins University, Applied Physics Laboratory, Laurel, MD 20723, USA; david.lario@jhuapl.edu
[2] Departament d'Astronomia i Meteorologia, Institut de Ciències del Cosmos, Universitat de Barcelona, Barcelona, Spain
[3] Institute of Experimental and Applied Physics, Christian-Albrechts University of Kiel, Kiel, Germany
Received 2012 October 2; accepted 2013 February 16; published 2013 March 22

ABSTRACT

Simultaneous measurements of solar energetic particle (SEP) events by two or more of the spacecraft located near 1 AU during the rising phase of solar cycle 24 (i.e., *STEREO-A*, *STEREO-B*, and near-Earth spacecraft such as *ACE*, *SOHO*, and *GOES*) are used to determine the longitudinal dependence of 71–112 keV electron, 0.7–3 MeV electron, 15–40 MeV proton, and 25–53 MeV proton peak intensities measured in the prompt component of SEP events. Distributions of the peak intensities for the selected 35 events with identifiable solar origin are approximated by the form $\exp[-(\phi-\phi_0)^2/2\sigma^2]$, where ϕ is the longitudinal separation between the parent active region and the footpoint of the nominal interplanetary magnetic field (IMF) line connecting each spacecraft with the Sun, ϕ_0 is the distribution centroid, and σ determines the longitudinal gradient. The *MESSENGER* spacecraft, at helioradii $R < 1$ AU, allows us to determine a lower limit to the radial dependence of the 71–112 keV electron peak intensities measured along IMF lines. We find five events for which the nominal magnetic footpoint of *MESSENGER* was less than 20° apart from the nominal footpoint of a spacecraft near 1 AU. Although the expected theoretical radial dependence for the peak intensity of the events observed along the same field line can be approximated by a functional form $R^{-\alpha}$ with $\alpha < 3$, we find two events for which $\alpha > 3$. These two cases correspond to SEP events occurring in a complex interplanetary medium that favored the enhancement of peak intensities near Mercury but hindered the SEP transport to 1 AU.

Key words: acceleration of particles – shock waves – Sun: particle emission

1. INTRODUCTION

Time-intensity profiles of solar energetic particle (SEP) events observed at 1 AU are usually well organized in terms of the longitudinal distance between the parent solar event and the observer's magnetic footpoint (Cane et al. 1988). Events generated from the western hemisphere of the Sun (as seen from Earth) show, in general, rapid onsets to a maximum followed by slow decays. Events generated from eastern longitudes usually show gradual intensity increases with low-energy ($\lesssim$30 MeV) proton intensities peaking at the passage of shocks driven by coronal mass ejections (CMEs) or shortly after. High-energy ($\gtrsim$30 MeV) proton and near-relativistic ($\gtrsim$30 keV) electron intensities are usually dominated by acceleration processes occurring close to the Sun where CME-driven shocks are presumably efficient enough to accelerate particles at these high energies. Hence, the maximum high-energy proton and near-relativistic electron intensities are usually observed during the prompt component of the events, well before the arrival of any accompanying shock at the spacecraft. Near-Earth observations of a large number of SEP events (Cane et al. 1988), observations of individual SEP events by several spacecraft distributed in the inner heliosphere (e.g., Reames et al. 1996), and transport simulations of shocks and SEPs generated from various longitudes (e.g., Lario et al. 1998) have confirmed this general picture. Exceptions occur when an SEP event develops in a disturbed interplanetary medium, for example, due to the presence of interplanetary coronal mass ejections (ICMEs) from prior solar events (e.g., Richardson & Cane 1996), or in exceptional cases when SEP events are associated with widespread (∼300°) coronal shocks able to inject particles in a broad range of longitudes (e.g., Cliver et al. 1995, 2005).

The variability of energetic particle intensities observed from event to event is not only a consequence of the varying longitudinal distance between the parent solar event and the observer. The diversity of properties of the energetic particle sources, the different conditions for SEP acceleration and transport, and the possible existence of different SEP seed populations are among the factors that control the variability of the observed SEP intensities (e.g., Kahler 1999; Verkhoglyadova et al. 2012). In order to determine the radial and longitudinal dependences of particle intensities during SEP events, it is essential to have simultaneous observations of individual SEP events by spacecraft distributed throughout the heliosphere. Radial and longitudinal dependences of SEP intensities may be different in each individual event, hence statistical analyses over a large number of events are required to deduce average values of SEP intensity dependences.

Routine observations of SEP events from multiple vantage points in the inner heliosphere (at heliocentric distances $R \lesssim 1$ AU) were possible during solar cycle 21 with the presence of the two *Helios* spacecraft (at helioradii $0.29 \leqslant R \leqslant 0.98$ AU) and Earth-orbiting spacecraft such as the *Interplanetary Monitoring Platforms* (*IMP-7* and *IMP-8*) or spacecraft near 1 AU such as the *International Sun-Earth Explorer* (*ISEE-3*). Simultaneous measurements of SEP events from spatially distant vantage points have been made possible again with the launch of the two nearly-identical *Solar Terrestrial Relation Observatories* (*STEREO*) in 2006 October and the *MErcury Surface Space ENvironment GEochemistry and Ranging* (*MESSENGER*) spacecraft in 2004 August, along with near-Earth spacecraft. In this study, we use energetic particle observations from the fleet of spacecraft distributed in the inner heliosphere (at heliocentric distances $R \lesssim 1$ AU) during the rising phase of solar cycle

[4] Present address: Physics Department, University of Alcalá, Alcalá de Henares, E-28871 Spain.

24 (from 2009 December to the end of 2012 June) to obtain radial and longitudinal dependences of SEP peak intensities measured in the prompt component of SEP events. In particular, we use data from (1) *STEREO-A* (ahead of Earth in its orbit), (2) *STEREO-B* (trailing behind Earth in its orbit), (3) two spacecraft orbiting around the Sun–Earth L1 point (i.e., the *Advanced Composition Explorer*, *ACE*, and the *Solar and Heliospheric Observatory*, *SOHO*), and (4) the *Geostationary Operational Environmental Satellites* (*GOES*) around the Earth. This set of spacecraft, all located near 1 AU from the Sun, provides simultaneous observations of SEP events from well separated locations that allow us to determine the longitudinal dependence of SEP intensities. Additionally, we use energetic particle data from *MESSENGER* (initially en route to Mercury and finally inserted into an orbit about the innermost planet on 2011 March 8) to determine the radial dependence of near-relativistic electron peak intensities measured in the prompt component of SEP events observed simultaneously by *MESSENGER* (at $R < 1$ AU) and another spacecraft at $R \sim 1$ AU. We will compare the results obtained in the rising phase of solar cycle 24 with the longitudinal and radial dependences obtained in previous studies using *Helios* and *IMP* data.

We limit the study of the longitudinal and radial dependences of SEP peak intensities to: (1) the prompt component of the SEP events, understood as the maximum intensity measured shortly after the onset of the event (in terms of SEP field-aligned transit times) and far from the peaks associated with the arrival of interplanetary shocks (if observed) and (2) high-energy (>15 MeV) proton, near-relativistic (71–112 keV) electron, and relativistic (0.7–3.0 MeV) electron intensities. Whereas the absolute maximum intensity in an SEP event is determined by factors such as (1) the dynamic characteristics of the associated CME-driven shock such as speed, angular width, and strength; (2) the changing magnetic connection between the traveling CME-driven shock and the observers; (3) the evolving geometry of the shock with respect to the interplanetary medium; and (4) the different seed particle populations that the shock may encounter (e.g., Lario et al. 1998; Aran et al. 2005, 2011; Aran 2007; Verkhoglyadova et al. 2012, and references therein), the peak in the prompt component is usually reached when the associated CME-driven shocks are still close to the Sun and presumably able to accelerate protons and electrons to high energies. Therefore, by using the peak intensity during the prompt component of the events, we minimize the effect that the evolution of the CME-driven shock (traveling in the interplanetary medium and injecting particles at different longitudes) may have. The use of near-relativistic and relativistic electron intensities together with high-energy (>15 MeV) proton intensities also tend to minimize the number of events with local enhancements due to the passage of shocks. The specific energy ranges used in the present study result from the combination of the available data sets provided by the spacecraft listed above. In order to determine the longitudinal dependence of SEP peak intensities, we use (1) 71–112 keV electron, (2) 0.7–3.0 MeV electron, (3) 15–40 MeV proton, and (4) 25–53 MeV proton intensities measured by the spacecraft located near 1 AU. The limited available particle data from *MESSENGER* restricts us to the use of near-relativistic electron data (in this case 71–112 keV) in order to infer the radial dependences of SEP peak intensities.

The structure of the paper is as follows. Sections 2 and 3 provide a summary of previous studies dealing with longitudinal and radial dependences, respectively, of SEP intensities at distances $R \lesssim 1$ AU. In Section 4 we present the observations used in this study. The criteria used to select the SEP events to analyze are presented in Section 5. In Section 6 we discuss the longitudinal dependences of SEP peak intensities obtained from the SEP events simultaneously measured by two or more spacecraft near 1 AU. In Section 7 we present the radial dependences of SEP peak intensities obtained for those events observed simultaneously by two spacecraft with good nominal magnetic connection. We pay special attention to those specific SEP events that depart from the dependences deduced from nominal transport simulations and/or observational surveys. Finally, Section 8 summarizes the results of the present study.

2. LONGITUDINAL DEPENDENCE OF SEP PEAK INTENSITIES

From an Earth-orbiting spacecraft, well-connected events (i.e., generated from solar longitudes close to ∼W50°) tend to have peak intensities of both high-energy protons (Kahler 1982) and near-relativistic electrons (Decker & Armstrong 1979) that are larger than the peak intensities observed in poorly connected SEP events. At the lower energies, large proton intensities tend to be observed for events generated from longitudes close to the Sun–Earth line (e.g., Smart & Shea 1995) due to both the dominant contribution of the CME-driven shock in injecting low-energy protons as it propagates out from the Sun and the evolution of the magnetic connection along the shock front between the observer and the traveling shock (Cane et al. 1988; Lario et al. 1998). As described in the Introduction, the observed event-to-event variability leads to a large scatter of SEP peak intensities when plotted in terms of the longitude of the parent solar event (e.g., Figure 3 in Mewaldt et al. 2005; Figure 1 in Kahler 1982; or Figure 11 in Decker & Armstrong 1979).

Several analytical expressions have been used to describe the longitudinal dependence of SEP intensities. Kahler (1982) inferred an angular dependence as $I_p \sim \exp(-1.604\Delta\varphi)$ where I_p is the 20–40 MeV proton peak intensity and $\Delta\varphi$ is the angular distance (in radians) from a nominal well-connected longitude of W50°. Mewaldt et al. (2005) used a two-sided exponential function to describe the longitudinal dependence of >10 MeV proton peak intensities observed by *GOES* with an e-folding longitude of −45° or −25° for events generated at the west or east of the Central Meridian line, respectively. Shea et al. (1988) recommended scaling ion fluxes with longitudinal distance by a factor $10^{-(F-A)}$, where F is the heliographic longitude of the parent flare and A is the heliographic longitude of the spacecraft's magnetic footpoint (both F and A are expressed in radians). Ochelkov (1986) deduced that the 20–80 MeV proton intensity of SEP events at 1 AU decreases approximately 1 order of magnitude as the longitudinal distance between the observer's magnetic footpoint on the Sun and the parent solar flare site increases by 100°. In order to predict >10 MeV proton intensities at 1 AU from solar flare observations, Balch (1999) used a complex function of the angular distance between the observer's magnetic footpoint and the flare site that may be approximated by a decrease of 1 order of magnitude for every 100° in longitude.

Whereas all these studies have been based on near-Earth observations of a large number of events generated from different longitudes, few studies have quantified the longitudinal dependence of SEP intensities based on simultaneous measurements

of SEP events from multiple longitudes. McGuire et al. (1983a) studied the longitudinal variation of 11–60 MeV proton peak intensities for a limited number of SEP events observed simultaneously by *Helios 1/2* (at helioradii $0.29 \leqslant R \leqslant 0.98$ AU) and *IMP 7/8* (at helioradii $R \sim 1$ AU). Particle enhancements associated with the passage of interplanetary shocks were explicitly excluded. McGuire et al. (1983a) estimated that the peak intensities observed between 0.3 and 1 AU decrease an average of a factor of 20 per AU in terms of the radial distance. When peak intensities of the SEP events obtained at different radial and longitudinal positions were (1) normalized to make the intensities from the spacecraft best connected to the flare equal to one, (2) multiplied by the empirical factor of 20/AU to correct for the radial distance of the observer, and (3) plotted as a function of the longitudinal distance between the parent flare site and the magnetic connection of the observer, distributions nearly symmetric with respect to the longitudes east and west of the well connected longitudes were obtained. McGuire et al. (1983a) provided a range of values from 35° to 90° for the FWHM of the distributions. These values translate to the standard deviation, σ, of a Gaussian distribution centered around a flare site that varies between $\sigma = 15°$ and $\sigma = 38°$. For large longitudinal distances (more than 60° from the flare site) the peak intensities were estimated to decrease by a factor ranging from 50 to 500 for a 60° increase in longitudinal distance (Kunow et al. 1991).

Lario et al. (2006) used 4–13 MeV and 27–37 MeV proton intensities measured by *IMP-8* and the two *Helios* spacecraft to analyze the peak intensities of SEP events observed simultaneously by at least two of these spacecraft at different radial and longitudinal distances. In order to separate longitudinal and radial dependences, Lario et al. (2006) approximated the distribution of SEP peak intensities of the ensemble of the 72 events analyzed in that work by a functional form $j = j_0 R^{-\alpha} \exp[-k(\phi - \phi_0)^2]$, where R is the heliocentric radial distance of the spacecraft, ϕ is the longitudinal angular distance between the footpoint of the nominal field line connecting the observer to the Sun and the site of the active region that generated the event, ϕ_0 is the centroid of the distribution, and j_0 is the peak intensity at the centroid ϕ_0. The assumption that the radial and longitudinal dependences of j are completely separable may not be true, especially if particle injection is due to continuous acceleration by a CME-driven shock in the interplanetary medium where both the magnetic connection between shock and observer and the efficiency of the shock in particle acceleration vary as the shock propagates out from the Sun (Lario et al. 1998). However, the mathematic convenience of the form lies in $\ln j$ being expressed as a linear sum of the propagation parameters ($2k\phi_0$, k, α) when combining observations of pairs of spacecraft during the same event, thus enabling a simple least-squares fit to the data (see Equation (3) in Lario et al. 2006). Lario et al. (2006) concluded that the dominant parameter that determines the peak intensity of the SEP events is not the heliocentric radial distance but rather the longitudinal distance between the parent active region and the footpoint of the magnetic field line connecting the observer to the Sun. They found that, averaged over the collection of events, $\alpha = 2.1 \pm 0.3$, $k = 1.15 \pm 0.05$ rad^{-2}, $\phi_0 = -21° \pm 3°$, and $\alpha = 2.0 \pm 0.3$, $k = 1.23 \pm 0.06$ rad^{-2}, $\phi_0 = -11° \pm 3°$ for 4–13 and 27–37 MeV proton peak intensities measured in the prompt component of the events (i.e., without local enhancements due to shocks), respectively (cf. Table 3 in Lario et al. 2006). The values of k can be translated to the standard deviation of a Gaussian distribution as $\sigma = (2k)^{-1/2}$, resulting in $\sigma = 38°$ and $\sigma = 36°$ for 4–13 MeV and 27–37 MeV proton peak intensities, respectively.

Earlier, Kallenrode (1993) analyzed 39 SEP events (simultaneously observed by the two *Helios* spacecraft) and found that the 0.3–0.8 MeV electron peak intensity of the events decreases by one order of magnitude every 15° up to 60°, with a mean value of 29°, corresponding to an e-folding angle varying between 7° and 26°. Previously, Schellert et al. (1985) found an e-folding angle of about 23°, corresponding to an electron intensity decrease by one order of magnitude every 53°. More recently, Wibberenz & Cane (2006) after applying a correction factor of R^{-3} in events simultaneously observed by the *Helios* spacecraft and by *IMP-8* (and/or *ISEE-3*), obtained a Gaussian distribution for the 0.3–0.8 MeV electron peak intensities with standard deviation $\sigma = 30°$.

3. RADIAL DEPENDENCE OF SEP PEAK INTENSITIES

The study of the radial dependence of SEP peak intensities at helioradii $R < 1$ AU has important implications for the forthcoming missions of Solar Probe Plus and Solar Orbiter. Appropriate planning for instrument operation and radiation exposure budgets depends on predictions of the expected SEP intensities at $R < 1$ AU. Observational studies dealing with the radial dependence of SEP intensities are complicated because both radial and longitudinal effects are interrelated (e.g., McGuire et al. 1983a; Lario et al. 2006). In addition, SEP events that at 1 AU look like individual events produced by a single particle injection may appear as multiple events closer to the Sun due to multiple solar injections (e.g., Wibberenz & Cane 2006). Therefore, it is important to analyze isolated events with well identified solar origins.

In order to minimize the effect that the longitudinal dependence has on the SEP peak intensities observed at different heliospheric locations, it is desirable to analyze SEP events observed by two spacecraft at different helioradii but magnetically connected to the same source of SEPs. Therefore, particle intensities observed by these well-connected spacecraft depend on (1) how particles are injected onto the interplanetary magnetic field (IMF) line that connects both spacecraft, and (2) how energetic particles are transported from the source region toward the observers. Based on measurements of five SEP events observed simultaneously by a spacecraft near 1 AU and one of the *Helios* spacecraft at $R < 1$ AU, when the estimated connection longitudes of both observers were less than 35° apart, McGuire et al. (1983a) estimated, among a large variety of radial dependences (see their Figure 4), an averaged peak intensity of the prompt component of the events that increases a factor of 20 per AU with decreasing R. We understand this to be an exponential dependence $j = j_0 \exp(-R/L)$ with $1/L = \ln 20$ valid from 1 to 0.3 AU. This exponential dependence can be piecewise approximated by functional forms $R^{-\alpha}$ with $\alpha < 3$. Lario et al. (2006) showed three events for which the footpoints of the nominal field lines connecting *Helios-1* (at $R \sim 0.3$ AU) and *IMP-8* (at $R \sim 1$ AU) with the Sun were less than 20° apart (see their Figures 4–6). For these three events the radial dependences of the peak proton intensities measured at their prompt component were weaker than R^{-3}.

Modeling efforts used to study the radial dependences of SEP intensities and applied to determine the particle radiation environment at distances $R \leqslant 1$ AU include (1) Hamilton (1988) who used the spherically symmetric energetic particle transport model of Parker (1965) with a particle injection fixed at the Sun, (2) Lario et al. (2007) who solved the focused-diffusion

SEP transport equation (Ruffolo 1995) with a particle injection fixed at the Sun, and (3) Ruzmaikin et al. (2005), Aran et al. (2005, 2011), and Verkhoglyadova et al. (2012) who solved the focused-diffusion transport equation (Ruffolo 1995) with a mobile particle source located at a traveling shock. For particle sources fixed close to the Sun, pure diffusive transport predicts peak intensities that decay as R^{-3} (e.g., Vainio et al. 2007 and references therein). Because of the focusing effect due to the outward decreasing magnetic field, neither the diffusion model nor the model by Hamilton (1988) are applicable at distances $R < 1$ AU. In the context of the focused-diffusion transport (including solar wind convection, adiabatic deceleration, and pitch-angle scattering), the main factors determining the radial dependence of SEP peak intensities at $R < 1$ AU after a fixed point injection of particles from close to the Sun are the pitch-angle scattering processes undergone by the particles and the details of the particle injection (Lario et al. 2007). The radial dependences obtained by this method are in general weaker than R^{-3} (see details in Lario et al. 2007 and references therein). When the particle injection is dominated by a traveling shock that continuously injects particles as it travels from the Sun to the observer and beyond, the longitude of the parent solar event generating the CME-driven shock with respect to the observer's location and the shock speed, width, and strength, as well as the evolution of the particle injection as the shock expands are the main factors determining the radial variation of SEP peak intensities (Aran et al. 2005, 2011; Aran 2007). A recent modeling effort by Verkhoglyadova et al. (2012) showed that the radial dependence of the peak intensity may also depend on the shock obliquity, the properties of the seed particle populations, the particle energy, and the level of turbulence in the interplanetary medium. The reader is referred to the above references for details.

Note that all these models assume nominal undisturbed interplanetary conditions, usually represented by an Archimedean spiral magnetic field with superimposed IMF fluctuations. The effects that pre-existent transient solar wind structures, such as fast interplanetary shocks and/or ICMEs, may have on the transport of SEPs are not usually considered. The presence of these structures in the interplanetary medium introduces changes in the direction and strength of the IMF as well as an enhancement in the level of magnetic field turbulence in the downstream region of shocks (e.g., Hundhausen 1972; Vandas et al. 1996). Apart from an increase in the processes of pitch-angle scattering undergone by the energetic particles, SEPs injected into this disturbed medium also undergo processes of particle reflection, resulting in an efficient particle confinement within and around these structures (e.g., Roelof et al. 1992; Anderson et al. 1995; Vandas et al. 1996; Kallenrode 2002; Bieber et al. 2002; Lario et al. 2008; Tan et al. 2009; Agueda et al. 2010). Therefore, radial dependences measured in a more realistically disturbed interplanetary medium may differ from those predicted by the idealized models described above.

4. DATA SOURCES

We combine data sets provided by *STEREO-A*, *STEREO-B*, *ACE*, *SOHO*, *GOES,* and *MESSENGER* during the rising phase of solar cycle 24, in particular from 2009 December to the end of 2012 June. From this set of spacecraft, we choose energetic particle detectors that allow us to compare similar energy ranges. The Energetic Particle Spectrometer (EPS) on board *MESSENGER* measures electrons from ~25 keV to 1 MeV (Andrews et al. 2007). The DE (Deflected Electrons) detector of the Electron, Proton, and Alpha Monitor (EPAM) on board *ACE* measures electrons from ~35 keV to 315 keV (Gold et al. 1998). The Solar Electron and Proton Telescope (SEPT) of the In situ Measurements of Particles and CME Transients (IMPACT) investigation on *STEREO* measures electrons from ~45 keV to 425 keV (Muller-Mellin et al. 2008). Considering the different energy passbands used in these electron detectors, we decided to interpolate the electron spectra measured by the differential energy channels of *ACE*/EPAM/DE and *STEREO*/SEPT to generate a differential energy channel that matches the energy channel 71–112 keV of *MESSENGER*/EPS. In order to obtain this intermediate energy channel, we interpolate first-order and second-order polynomial functions to the logarithm of the intensities measured in the energy channels 53–103 keV and 103–175 keV of *ACE*/EPAM/DE, and the energy channels 65–75 keV, 75–85 keV, 85–105 keV, and 105–125 keV of *STEREO*/SEPT, respectively.

Similarly, the Electron Proton Helium Instrument (EPHIN) of the Comprehensive Suprathermal and Energetic Particle Analyzer (COSTEP) on board *SOHO* measures protons from ~4 MeV to more than 53 MeV and electrons from ~0.25 MeV to ~10.4 MeV (Muller-Mellin et al. 1995). The High-Energy Telescope (HET) of the IMPACT investigation on board *STEREO* measures protons from ~13 MeV to ~100 MeV and electrons from 0.7 to 4 MeV (von Rosenvinge et al. 2008). The large-aperture detector of the Energetic Particle Sensor (EPS) on board *GOES-11* and *GOES-13* measures protons from ~0.8 MeV to 500 MeV (Sauer 1993). Considering the different energy passbands of the energy channels used in each detector, we decided to interpolate between the proton differential energy channels of *STEREO*/HET in order to generate two differential energy channels matching the P4 channel (15–40 MeV) of *GOES-11*/EPS and *GOES-13*/EPS and the P25+P41 (25–53 MeV) channel of *SOHO*/COSTEP/EPHIN. Regarding relativistic electron data, the energy channels used in *SOHO*/COSTEP/EPHIN and *STEREO*/HET do not allow us to generate a perfectly matching energy channel. However, it is acceptable to compare the 0.7–3.0 MeV electron intensities measured by *SOHO*/COSTEP/EPHIN with the 0.7–4.0 MeV electron intensities from *STEREOs*/HET as long as the spectrum is not too flat. Hereafter we designate this channel as the 0.7–3.0 MeV electron channel.

We have used Level-2 data sets downloaded from the following Web sites: *ACE* (www.srl.caltech.edu/ACE/ASC/), *SOHO* (www2.physik.uni-kiel.de/SOHO/phpeph/EPHIN.htm), *STEREO*/SEPT (www2.physik.uni-kiel.de/stereo/), *STEREO*/HET (www.srl.caltech.edu/STEREO/), and *GOES*/EPS (www.swpc.noaa.gov/). Considering the different fields of view of each telescope, we decided to use directionally averaged intensities (using either the average of the intensities collected by the different telescopes of a given instrument when available or the spin-averaged intensity in the case of *ACE*).

Figure 1 shows the data selected for the study from 2009 December to the end of 2012 June. This time interval includes the rising phase of solar cycle 24. On 2009 December 1 *STEREO-A* was 63° in longitude ahead of Earth and *STEREO-B* 65° behind Earth, whereas on 2012 June 30 *STEREO-A* was 119° in longitude ahead of Earth and *STEREO-B* 115° behind Earth. The separation of the two spacecraft with respect to Earth increases by ~22°.5 per year. On 2009 December 1 *MESSENGER* was at heliocentric distance $R = 0.56$ AU and heliographic inertial longitude $\Psi = 195°$, whereas on 2012

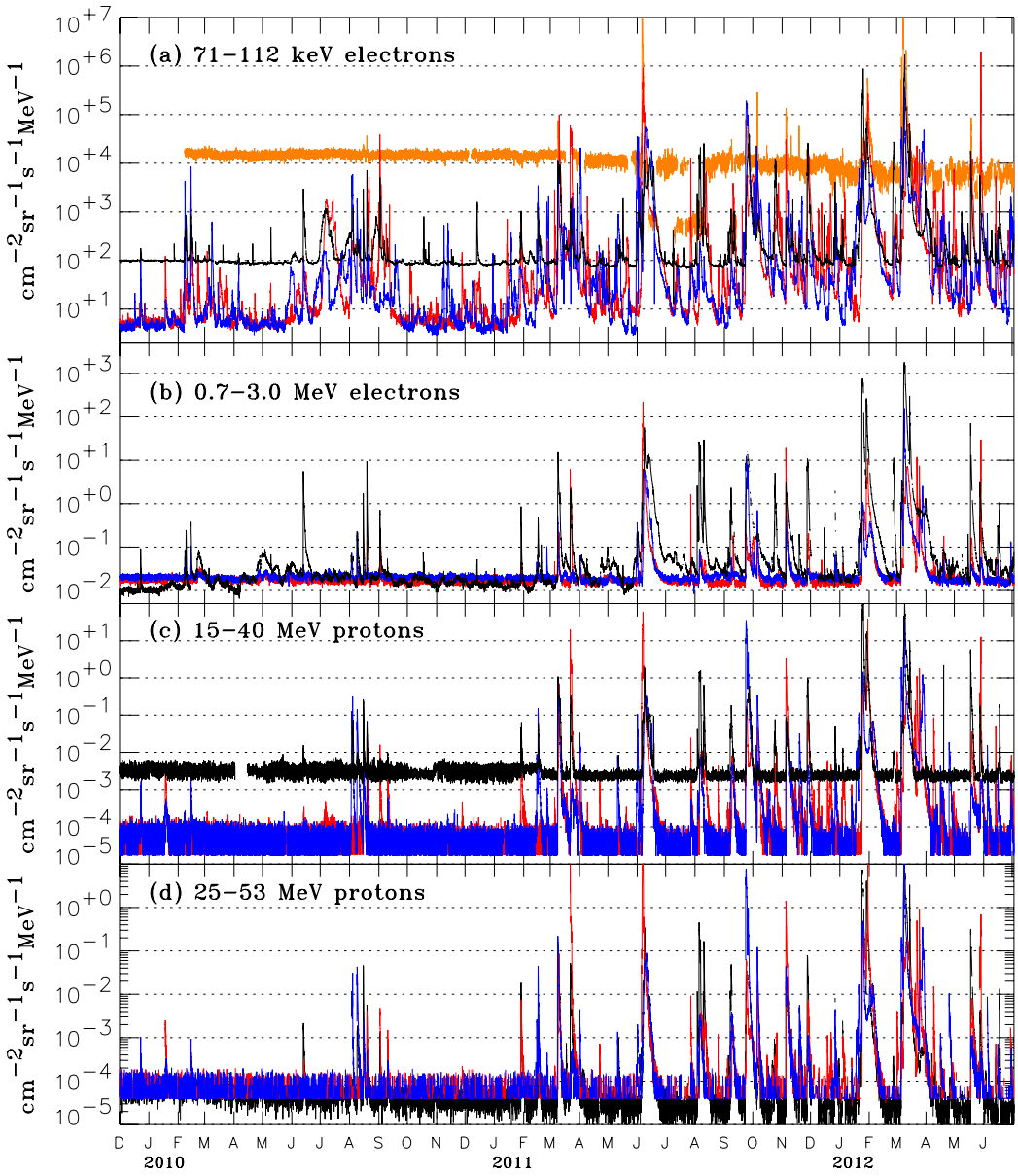

Figure 1. From top to bottom, hourly averages of (a) 71–112 keV electron intensities measured by *MESSENGER*/EPS (orange) and obtained from measurements by *ACE*/EPAM (black), *STEREO-A*/SEPT (red), and *STEREO-B*/SEPT (blue); (b) 0.7–3.0 MeV electron intensities measured by *SOHO*/COSTEP/EPHIN (black) and 0.7–4.0 MeV electron intensities measured by *STEREO-A*/HET (red) and *STEREO-B*/HET (blue); (c) 15–40 MeV proton intensities measured by *GOES-11* and *GOES-13* (black) and deduced from measurements by *STEREO-A*/HET (red) and *STEREO-B*/HET (blue); (d) 25–53 MeV proton intensities measured by *SOHO*/COSTEP/EPHIN (black) and deduced from measurements by *STEREO-A*/HET (red) and *STEREO-B*/HET (blue). The time interval covered is 2009 December 1 to 2012 June 30.

June 30 it was at $R = 0.45$ AU and $\Psi = 147°$ (Earth was at $\Psi = 353°$ on 2009 December 1 and $\Psi = 202°$ on 2012 June 30). On 2011 March 18 *MESSENGER* was inserted into a 12 hr orbit about Mercury (Zurbuchen et al. 2011).

Figure 1(a) shows hourly averages of the 71–112 keV electron intensities measured by *MESSENGER*/EPS (orange line) and those deduced from measurements by *ACE*/EPAM (black line), *STEREO-A*/SEPT (red line), and *STEREO-B*/SEPT (blue line). Figure 1(b) shows hourly averages of the 0.7–3.0 MeV electron intensity measured by *SOHO*/COSTEP/EPHIN (black line), *STEREO-A*/HET (red line), and *STEREO-B*/HET (blue line). Figure 1(c) shows hourly averages of the 15–40 MeV proton intensity as measured by *GOES*/EPS (black line) and the 15–40 MeV proton intensities deduced from *STEREO-A*/HET (red line) and *STEREO-B*/HET (blue line) measurements. Prior to 2010 April 14 we use corrected *GOES-11* data, whereas *GOES-13* data are used afterward. Figure 1(d) shows hourly averages of the 25–53 MeV proton intensities measured by *SOHO*/COSTEP/EPHIN (black line) and deduced from measurements by *STEREO-A*/HET (red line) and *STEREO-B*/HET (blue line). To be consistent with prior studies (e.g., Lario et al. 2006) we use hourly averages of the particle intensities. The 1 hr resolution may have some effect on the inferred radial dependences of peak intensities.

Not only is the actual maximum peak intensity at all distances lowered when using long time interval averages (e.g., Lario & Decker 2011), but also peak intensities at distances $R < 1$ AU are expected to be spikier than at 1 AU (e.g., Lario 2007; Lario et al. 2007). The use of hourly averages might produce a substantial reduction of the actual short-lived peaks at $R < 1$ AU, and hence the radial dependences obtained in this study should be considered lower limits of the actual radial dependence of SEP peak intensities.

Figure 1 shows that each instrument is affected differently by its instrumental background. There are significant backgrounds in the 71–112 keV electron intensities at *MESSENGER*/EPS, the 71–112 keV electron intensities at *ACE*/EPAM, and the 15–40 MeV proton intensities from *GOES*/EPS. During mid-2011, *MESSENGER*/EPS switched between several detection systems to maximize the electron detection geometric factor, so there are changes in instrument background level during these periods (Figure 1(a)). The sensitivity for detection of SEP intensity enhancements from each instrument depends on its intensity background level. In addition, comparison of intensities obtained from the different instruments requires the intercalibration of these instruments. Fortunately, the observation of SEP events during the beginning of the *STEREO* mission (when both spacecraft were still close to Earth) allows us to compare the intensities from the different spacecraft located at ∼1 AU when the longitudinal distance among the spacecraft still played a minor role.

The left panel of Figure 2(a) shows hourly averages of the 71–112 keV electron intensities during the events observed on 2007 January 23 and 24 by *ACE*/EPAM (black line), *STEREO-A*/SEPT (red line), and *STEREO-B*/SEPT (blue line). The right panel of Figure 2(a) shows the same intensities after subtracting pre-event intensity and dividing the *ACE*/EPAM intensities by an inter-spacecraft calibration factor of 1.3. The pre-event intensities used in the subtraction are obtained as the hourly averaged intensity measured at each spacecraft prior to the onset of each one of the three events shown in Figure 2(a). Similarly, the left panels of Figures 2(b)–(d) show the hourly averages of the (b) 0.7–3.0 MeV electron intensities measured by *SOHO*/COSTEP/EPHIN (black traces), *STEREO-A*/HET (red line), and *STEREO-B*/HET (blue line); (c) the 15–40 MeV proton intensities measured by *GOES*/EPS (black trace) and deduced from *STEREO-A*/HET (red line) and *STEREO-B*/HET (blue line) measurements; and (d) the 25–53 MeV proton intensities measured by *SOHO*/COSTEP/EPHIN (black traces) and deduced from *STEREO-A*/HET (red line) and *STEREO-B*/HET (blue line) measurements during the events on 2006 December 13 and 14 (days 347 and 348 of year 2006). The right panels of Figures 2(b)–(d) show the same data after pre-event background subtraction and applying (b) a dividing factor of 13 to the 0.7–3 MeV electron intensities measured by *SOHO*/COSTEP/EPHIN, (c) a dividing factor of 1.6 to the *GOES*/EPS data, and (d) a multiplying factor of 1.1 to the 25–53 MeV proton intensities measured by *SOHO*/COSTEP/EPHIN. The pre-event intensities used in the subtraction are obtained as the hourly averaged intensity observed prior to the onsets of the events early on day 347 and late on day 348 at each spacecraft.

The factors applied to the near-Earth (i.e., *ACE*, *SOHO*, and *GOES*) intensities in the right panels of Figure 2 result in intensities of the three spacecraft coinciding during the decay phase of the events. Considering the different field of view of the instruments on each spacecraft, and the fact that particle intensities during the decay phase of the event tend to be isotropic (e.g., Lario et al. 2004), we decided to normalize the time-intensity profiles to match the decay phases rather than peak intensities (wherein the intensities are still likely to be anisotropic). We will assume that these multiplicative factors applied to near-Earth observations (i.e., *ACE*/EPAM, *SOHO*/COSTEP/EPHIN, and *GOES*/EPS) are constant throughout the time interval under study, thus allowing us to compare intensities of SEP events measured by the selected instruments on board different spacecraft.

Unfortunately, SEP data from *MESSENGER*/EPS were not obtained when this spacecraft was still close to Earth, so direct intercalibration with 1 AU spacecraft was not possible. Nonetheless, similar electron intensities at *MESSENGER* and near 1 AU spacecraft have been observed in the decay phase of several events (e.g., Lario et al. 2011), indicating the presence of a reservoir effect in which comparable intensities are observed between distant spacecraft (McKibben 1972; Roelof et al. 1992; Lario 2010). This suggests to us that *MESSENGER* intensities are acceptably cross-calibrated. Therefore, we decided to compare *MESSENGER*/EPS data with near 1 AU data without applying any scaling correction factor.

5. EVENT SELECTION CRITERIA

We focus our attention on those SEP events that generate high-energy protons. In particular, the criteria used to select the events to analyze are the following: (1) the event has to show an increase in the 25–53 MeV proton channel in at least one spacecraft and (2) a single solar origin of the event has to be well identified with a distinctive site for either the parent solar flare or the parent filament eruption in such a way that the maximum peak intensity can be associated with such solar origin. An attempt to exclude those events clearly associated with multiple solar injections was made (e.g., the series of events in early March 2011 and 2012 were excluded). In order to be included in the analysis of the longitudinal dependences, an intensity enhancement in the different energy channels has to be observed by at least two spacecraft with an identifiable peak intensity during the prompt component of the event. As described by Lario et al. (2006), the peak intensity in the prompt component of the event is chosen as the maximum intensity reached shortly after the onset of the event and several hours or days before the particle enhancement commonly associated with the arrival of interplanetary shocks (if any), known as the energetic storm particle (ESP) component. For some events, the maximum intensity in the prompt component is observed in the form of a plateau in the time-intensity profile before the local enhancement associated with the passage of shocks (Reames & Ng 1998). In these cases, the peak intensity is taken as the value of the intensity plateau. Spacecraft observations for which particle intensity continuously increases until the arrival of the shock (if any), usually observed in the case of events generated from longitudes eastward of the spacecraft–Sun line, are not included in our statistical sample of events because no prompt component is identifiable. Events showing multiple intensity increases are only considered if the first intensity enhancement reaches a maximum and it can be associated with a single parent solar event.

As an example of how peak intensity and pre-event intensity are identified, Figure 3 shows (a) 71–112 keV electron and (b) 25–53 MeV proton intensities measured during the event on day 307 of 2011 by *MESSENGER* (orange trace), *STEREO-A* (red trace), *STEREO-B* (blue trace), *ACE* (black trace in Figure 3(a)),

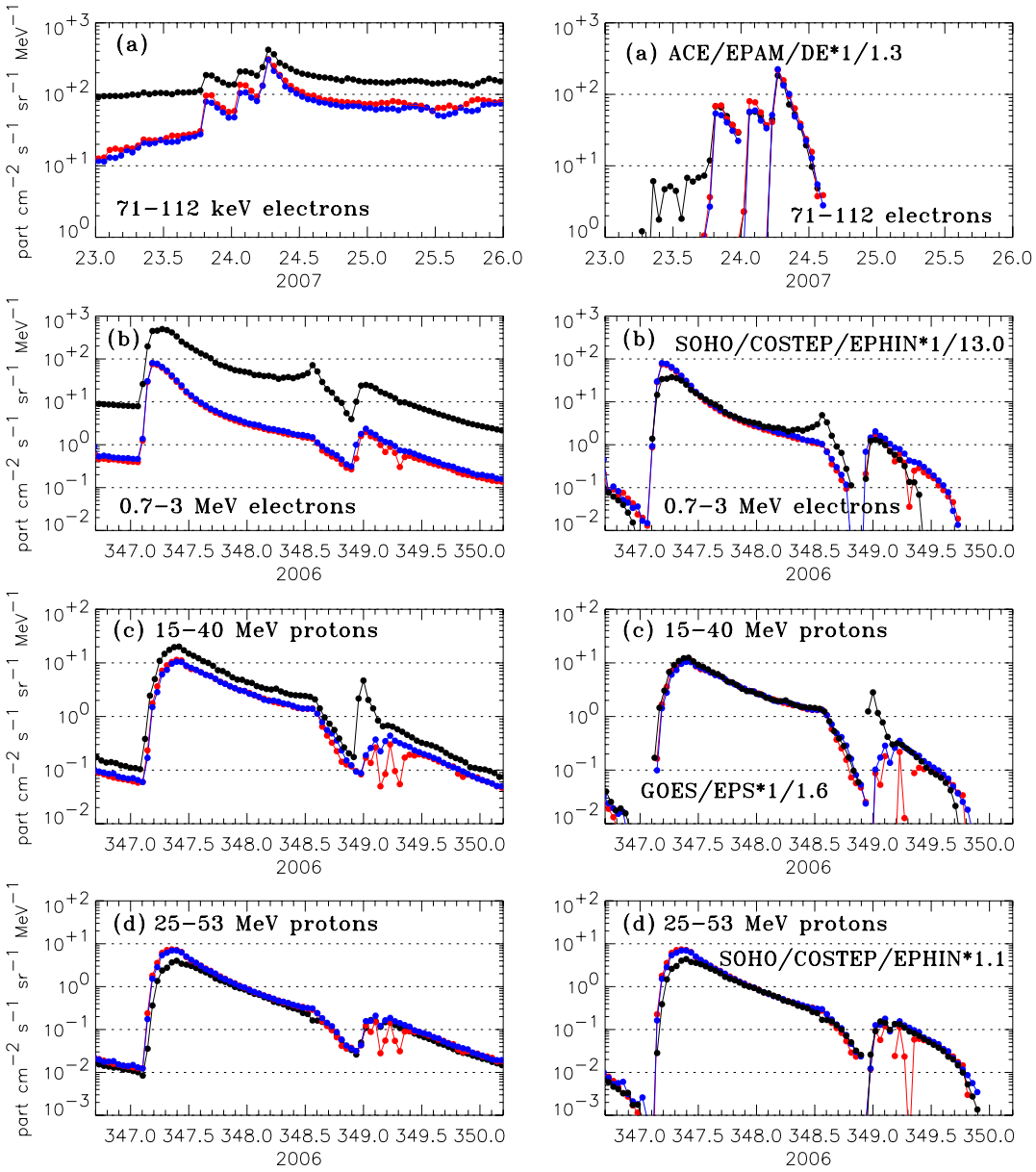

Figure 2. Left panels: hourly averages of the (a) 71–112 keV electron intensity during the events on 2007 January 23 and 24 obtained from measurements by *ACE*/EPAM (black), *STEREO-A*/SEPT (red) and *STEREO-B*/SEPT (blue); (b) 0.7–3.0 MeV electron intensities measured by *SOHO*/COSTEP/EPHIN (black) and 0.7–4.0 MeV electron intensities measured by *STEREO-A*/HET (red) and *STEREO-B*/HET (blue) during the events on 2006 December 13 and 14; (c) 15–40 MeV proton intensities measured by *GOES*/EPS (black) and *STEREO-A*/HET (red) and *STEREO-B*/HET (blue) during the events on 2006 December 13 and 14; (d) 25–53 MeV proton intensities measured by *SOHO*/COSTEP/EPHIN (black) and deduced from measurements by *STEREO-A*/HET (red) and *STEREO-B*/HET (blue) during the events on 2006 December 13 and 14. The right panels show the same data as the left panels after pre-event intensity subtraction and application of the indicated multiplicative factor to the near-Earth particle intensities to make the intensities of the three spacecraft coincide during the decay phase of the events. Fluctuations on the *STEREO-A* intensities and differences with respect to data from other spacecraft during the event on 2006 December 14 (day 349) were described by von Rosenvinge et al. (2009).

and *SOHO* (black trace in Figure 3(b)). The open circles identify the maximum intensity reached in the prompt component of the event at each spacecraft, and the solid horizontal lines the value of the pre-event intensity at each spacecraft (i.e., the hourly averaged intensity observed prior to the onset of the event). The dotted red and blue traces in Figure 3(a) identify time intervals with possible ion contamination in the electron channels of *STEREO*/SEPT. The absolute maximum 71–112 keV electron intensity at *STEREO-B* was reached in a period of ion contamination in association with the passage of an interplanetary shock. This absolute maximum intensity associated with the passage of a shock is not considered in our study, as it constitutes part of the ESP component, even if it would have occurred in a period without ion contamination.

A total of 35 SEP events during the period under study were selected (listed in Table 1). Column 1 of Table 1 identifies the year and the day of year when the onset of the event was observed. The following columns show the peak intensity measured at the prompt component of the event and in parentheses the pre-event intensity background of 71–112 keV electrons

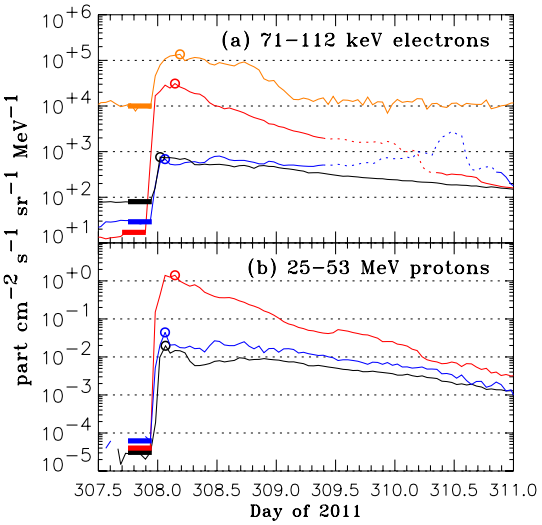

Figure 3. (a) 71–112 keV electron and (b) 25–53 MeV proton intensities measured during the event on day 307 of 2011 by *MESSENGER* (orange trace), *STEREO-A* (red trace), *STEREO-B* (blue trace), and *ACE* (black trace in Figure 3(a)) or *SOHO* (black trace in Figure 3(b)). The open circles identify the maximum intensity reached in the prompt component of the event at each spacecraft, and the solid horizontal lines the value of the pre-event intensity at each spacecraft. The dotted red and blue traces in Figure 3(a) identify time intervals with possible ion contamination in the electron channels of *STEREO*/SEPT. The absolute maximum 71–112 keV electron intensity at the *STEREO-B* is reached in association with the passage of an interplanetary shock. This maximum associated with the passage of a shock is not discussed in our study.

(Column 2), 0.7–3.0 MeV electrons (Column 3), 15–40 MeV protons (Column 4), and 25–53 MeV protons (Column 5) as measured by the indicated spacecraft (*STA* for *STEREO-A* and *STB* for *STEREO-B*). No intercalibration factor has been applied in the intensities listed in Table 1. The symbol NI indicates that no intensity enhancement was detectable above the pre-event background. NM indicates that we were not able to identify a maximum peak intensity during the event because of either irregular time-intensity profiles, a new SEP injection occurring before a peak intensity could be detected, or the event showing a gradual and continuous increase (as typically observed in events generated from eastern longitudes). IC indicates that 71–112 keV electron intensities at *STEREO* were affected by ion contamination and therefore not used in our analysis. The units for both the peak intensity and the pre-event background intensity are particles cm^{-2} s^{-1} sr^{-1} MeV^{-1}.

Table 2 lists the solar origin and spacecraft location for the selected events. The association between the origin of the SEP event and specific solar flares or CMEs is based on the temporal coincidence of their occurrence after examination of solar images from *STEREO* (cor1.gsfc.nasa.gov/catalog/) and *SOHO* (cdaw.gsfc.nasa.gov). Note that the association is made with the largest solar event occurring on the Sun; the possible existence of smaller synchronous eruptive activity capable of injecting particles at different longitudes is not considered in this study. For each event, Column 1 of Table 2 lists the date when the onset of the event occurred, Column 2 the NOAA active region (AR) where the associated flare occurred (FD indicates that a filament disappearance was associated with the origin of the event), and Column 3 the site of the associated solar event with respect to Earth and inferred from the solar images taken by *STEREO* and *SOHO*. When the site of the parent solar event is beyond Earth's visible part of the Sun, the numbering of the active region is established by following the solar rotation forward or backward until the active region appears on the visible side of the Sun (as seen from Earth). Column 4 of Table 2 indicates the onset time of either the soft X-ray solar flare emission (as reported at www.swpc.noaa.gov) or the type III radio bursts (as inferred from data posted at secchirh.obspm.fr) associated with the origin of the SEP event (in UT of the respective day). Columns 5, 6, and 7 list the heliocentric radial distance of Earth ($R_{\rm Earth}$), the heliographic inertial longitude of Earth ($\Psi_{\rm Earth}$), and the heliographic inertial longitude of the footpoint of the nominal magnetic field line connecting Earth with the Sun ($\phi_{\rm Earth}$). Similarly, Columns 8, 9, and 10 list the same parameters for *STEREO-A* ($R_{\rm STA}$, $\Psi_{\rm STA}$, and $\phi_{\rm STA}$) and Columns 11, 12, and 13 for *STEREO-B* ($R_{\rm STB}$, $\Psi_{\rm STB}$, and $\phi_{\rm STB}$). Units for the angles are degrees and for heliocentric distances AU. The magnetic footpoint of each spacecraft on the Sun is computed by assuming a Parker spiral for the interplanetary magnetic field with a constant solar wind speed of 400 km s^{-1}. The use of the actual solar wind speed instead of the constant value of 400 km s^{-1}, or the use of more accurate models to determine the longitude on the Sun that magnetically connects to each observer, does not guarantee a correct determination of the magnetic footpoint (MacNeice et al. 2011). Additionally, the associated CME is not necessarily centered on the flare site listed in Column 3 of Table 2. There could easily be a difference of ~10°–20° between the flare and the presumed CME direction (e.g., Ontiveros & Vourlidas 2009).

6. LONGITUDINAL DEPENDENCE: *STEREO* AND NEAR-EARTH OBSERVATIONS

Figure 4 shows the longitudinal distribution of the (a) 71–112 keV electron, (b) 0.7–3.0 MeV electron, (c) 15–40 MeV proton, and (d) 25–53 MeV proton peak intensities listed in Table 1 after subtraction of the pre-event background intensity and application of the inter-calibration factor described in Section 4. Horizontal axes of Figures 4(a)–(d) indicate the longitudinal distance ϕ between the parent solar flare and the footpoint of the field line connecting each spacecraft with the Sun ($\phi = \phi_{\rm Flare} - \phi_{\rm Foot}$). Well-connected events have ϕ close to 0°, whereas flares occurring at the west (east) of the footpoint are located at the right (left) of $\phi = 0°$. Black symbols indicate events observed by near-Earth observers (*ACE*, *GOES*, and *SOHO*), red symbols events observed by *STEREO-A*, and blue symbols events observed by *STEREO-B*. Magenta lines connect events simultaneously observed by two or three spacecraft, whereas the thin green lines connect those events in which one spacecraft did not detect any particle increase (those events are artificially plotted on the bottom horizontal axes of Figure 4). Because of the selection criteria and the difficulty in identifying a peak intensity during the prompt component of the events generated from heliolongitudes at the east of the observer, the vast majority of points in Figure 4 are located at the west of the central meridian line of each observer.

As expected, the largest intensities are observed from those spacecraft well connected to the parent solar event and decrease for large values of ϕ. Following the approach described by Lario et al. (2006), we use the functional form $j = j_0 \exp[-(\phi - \phi_0)^2/2\sigma^2]$ to describe the longitudinal distribution of peak intensities, for spacecraft near 1 AU (no radial dependence). By combining three pairs of spacecraft for those events observed by three spacecraft and one pair for those events observed by only two spacecraft (i.e., using only those points connected by magenta lines in Figure 4) we obtain (a) $\phi_0 =$

Table 1
Peak Intensity and Pre-event Intensity of the Selected SEP Events[a]

(1)	(2)			(3)			(4)			(5)		
Date	71–112 keV Electrons			0.7–3 MeV Electrons			15–40 MeV Protons			25–53 MeV Protons		
Year/Day	*ACE*	*STA*	*STB*	*SOHO*	*STA*	*STB*	*GOES*	*STA*	*STB*	*SOHO*	*STA*	*STB*
2009/356	1.8e2(9.9e1)	1.7e1(4.9e0)	1.6e2(4.8e0)	9.3e-2(9.0e-3)	NI(1.7e-2)	3.5e-2(2.1e-2)	NI(3.2e-3)	2.2e-4(6.0e-5)	1.3e-3(6.0e-5)	1.8e-4(5.5e-5)	NI(7.0e-5)	1.0e-3(6.0e-5)
2010/017	NI(9.9e1)	1.2e2(4.5e0)	1.6e1(4.2e0)	NI(1.2e-2)	NI(1.7e-2)	NI(2.1e-2)	NI(3.5e-3)	4.9e-3(5.0e-5)	5.5e-4(5.e-5)	NI(6.0e-5)	2.5e-3(6.5e-5)	3.3e-4(7.5e-5)
2010/043	8.9e2(2.9e2)	3.3e2(3.0e1)	8.5e3(1.4e3)	3.8e-1(1.1e-2)	NI(1.7e-2)	1.1e-1(3.3e-2)	NI(3.2e-3)	NI(6.2e-5)	1.9e-3(1.5e-4)	1.5e-4(6.0e-5)	NI(8.0e-5)	9.4e-4(7.5e-5)
2010/163	3.0e3(1.0e2)	1.3e2(1.1e1)	1.1e2(1.6e1)	5.6e0(2.3e-2)	4.0e-2(1.7e-2)	3.9e-2(1.8e-2)	1.6e-2(3.0e-3)	NI(4.5e-5)	NI(7.5e-5)	2.2e-3(4.5e-5)	NI(6.0e-5)	NI(7.5e-5)
2010/219	2.9e2(1.3e2)	NI(1.7e2)	1.9e3(2.3e1)	2.3e-1(1.2e-2)	NI(1.6e-2)	1.9e-1(1.9e-2)	1.0e-2(2.7e-3)	NI(7.0e-5)	1.4e-1(5.0e-5)	1.5e-3(4.0e-5)	NI(4.0e-5)	4.3e-2(4.2e-5)
2010/226	2.9e3(1.0e2)	6.7e1(3.0e1)	7.2e2(1.4e1)	1.7e0(1.5e-2)	NI(1.7e-2)	7.2e-2(1.9e-2)	2.6e-1(2.6e-3)	1.4e-3(4.5e-5)	9.4e-3(6.5e-5)	4.6e-2(4.5e-5)	6.4e-4(7.0e-5)	2.5e-3(7.0e-5)
2010/230	7.2e3(1.0e2)	4.6e3(2.2e1)	4.0e2(2.0e1)	9.4e0(2.2e-2)	1.4e-1(1.7e-2)	4.7e-2(2.2e-2)	5.9e-2(3.3e-3)	2.4e-2(5.5e-5)	2.7e-3(4.5e-5)	5.6e-3(5.3e-5)	4.2e-3(7.0e-5)	5.3e-4(6.0e-5)
2010/243	5.1e3(1.9e2)	3.9e4(6.4e2)	2.3e1(9.1e0)	7.1e-1(2.8e-2)	2.9e-1(2.0e-2)	NI(2.2e-2)	NI(3.6e-3)	1.6e-2(5.6e-5)	NI(4.0e-5)	1.3e-3(4.0e-5)	4.8e-3(7.2e-5)	NI(7.2e-5)
2010/251	2.8e2(9.8e1)	1.8e2(1.1e2)	2.2e1(1.5e1)	5.3e-2(2.0e-2)	NI(1.7e-2)	NI(1.9e-2)	9.7e-3(3.6e-3)	6.2e-3(3.6e-5)	6.2e-4(4.0e-5)	8.2e-4(4.2e-5)	1.5e-3(7.2e-5)	NI(7.0e-5)
2011/028	1.0e3(1.6e2)	6.3e2(4.4e1)	NI(5.4e1)	8.6e-1(1.4e-2)	4.5e-2(1.5e-2)	NI(2.0e-2)	4.8e-2(3.0e-3)	1.7e-2(5.0e-5)	NI(4.0e-5)	1.8e-2(5.2e-5)	7.3e-3(7.2e-5)	NI(6.2e-5)
2011/046	1.2e3(1.4e2)	NI(1.7e1)	3.5e3(7.0e2)	4.8e-1(5.0e-2)	NI(1.9e-2)	1.2e-1(3.1e-2)	6.2e-2(4.5e-3)	NI(6.0e-5)	1.5e-1(1.0e-3)	5.6e-3(5.5e-5)	NI(6.5e-5)	4.5e-2(2.2e-4)
2011/080	1.9e3(1.9e2)	6.2e4(1.1e2)	NM(9.0e1)	2.2e0(2.8e-2)	6.3e0(1.4e-2)	NI(1.9e-2)	3.4e-1(2.5e-3)	2.0e1(7.5e-5)	NI(1.0e-4)	5.2e-2(3.5e-5)	9.7e0(7.5e-5)	NI(7.5e-5)
2011/155A	6.1e2(2.1e2)	4.2e3(5.7e1)	NI(1.7e2)	2.0e-1(4.7e-2)	1.3e-1(2.0e-2)	NI(1.8e-2)	NM(2.5e-3)	1.7e-1(3.5e-5)	NI(5.5e-5)	6.1e-4(3.0e-5)	4.6e-2(6.0e-5)	NI(5.0e-5)
2011/155B[b]	2.4e3(1.4e2)	1.9e5(1.6e4)	5.6e4(6.5e1)	6.3e0(1.2e-1)	3.1e1(3.3e-1)	5.5e0(1.8e-2)	1.2e-1(3.5e-3)	1.7e1(8.5e-1)	2.1e-1(5.5e-5)	2.1e-2(8.0e-5)	8.4e0(7.0e-2)	4.4e-2(5.0e-5)
2011/214	2.4e3(8.5e1)	NI(5.5e0)	8.5e1(2.3e1)	2.6e0(2.5e-2)	NI(1.5e-2)	2.7e-2(1.7e-2)	4.4e-2(2.8e-3)	NI(3.0e-5)	9.9e-4(3.4e-5)	1.2e-2(2.1e-5)	NI(6.5e-5)	7.8e-4(1.2e-4)
2011/216	1.5e4(4.7e2)	3.6e2(1.1e1)	2.5e2(2.6e1)	2.7e1(1.4e-1)	7.7e-2(1.7e-2)	9.1e-2(1.9e-2)	1.4e0(4.3e-3)	6.9e-3(5.0e-5)	7.4e-3(2.5e-4)	4.5e-1(6.5e-4)	3.9e-3(7.5e-5)	3.5e-3(1.8e-4)
2011/221	2.5e4(1.3e3)	6.5e2(4.6e2)	IC(2.2e1)	3.0e1(3.8e-1)	5.0e-2(2.2e-2)	NI(1.9e-2)	6.5e-1(4.6e-3)	NM(1.5e-3)	NI(1.5e-4)	1.7e-1(8.6e-4)	NM(4.8e-4)	NI(1.4e-4)
2011/249A	4.6e2(9.3e1)	NM(2.2e1)	2.8e1(6.3e0)	7.2e-1(3.9e-2)	NI(1.5e-2)	NI(2.0e-2)	4.3e-2(2.1e-3)	NI(9.0e-5)	1.1e-3(5.1e-5)	1.2e-2(3.1e-5)	NI(7.7e-5)	6.8e-4(7.0e-5)
2011/249B	1.2e3(2.2e2)	NM(5.1e0)	1.1e2(3.6e1)	2.3e0(1.6e-1)	NI(1.5e-2)	5.7e-2(2.2e-2)	1.8e-1(2.4e-2)	NI(1.9e-4)	5.7e-3(1.9e-3)	4.9e-2(5.1e-3)	NI(7.7e-5)	3.9e-3(1.1e-3)
2011/264	3.4e2(8.6e1)	1.5e3(2.3e1)	NI(7.7e1)	4.1e-1(2.8e-2)	2.3e-2(1.3e-2)	NI(1.8e-2)	NI(2.4e-3)	3.5e-3(5.4e-5)	NI(4.0e-5)	4.8e-4(1.3e-5)	2.7e-4(3.9e-5)	NI(9.0e-5)
2011/265	1.3e4(1.7e2)	IC(7.7e2)	1.9e5 (1.3e2)	1.6e1(1.7e-1)	2.0e-1(2.1e-2)	1.2e1(2.0e-2)	2.6e-1(3.4e-3)	1.7e-1(1.2e-3)	3.5e1(1.7e-5)	3.5e-2(2.2e-4)	6.4e-2(3.1e-4)	7.7e0(8.3e-5)
2011/277[c]	9.3e2(3.3e2)	5.8e3(4.7e2)	1.1e4(7.6e2)	2.4e-1(1.4e-1)	2.6e-1(2.0e-2)	7.0e-1(2.3e-2)	NI(2.4e-3)	4.9e-2(1.8e-4)	3.6e-1(5.5e-5)	4.0e-4(4.64e-5)	1.6e-2(8.1e-5)	1.2e-1(3.9e-5)
2011/307	7.6e2(8.0e1)	3.1e4(1.7e1)	6.8e2(2.9e1)	3.0e0(2.2e-2)	1.9e1(1.4e-2)	5.2e-1(1.9e-2)	8.7e-2(2.2e-3)	3.5e0(3.6e-5)	7.6e-2(3.0e-5)	2.0e-2(3.1e-5)	1.4e0(4.0e-5)	4.4e-2(6.2e-5)
2011/321	2.8e2(9.9e1)	3.3e2(2.6e1)	6.9e2(2.5e2)	2.0e-1(2.4e-2)	NI(1.5e-2)	NI(2.1e-2)	NI(2.4e-3)	1.3e-3(3.7e-5)	3.2e-2(2.7e-4)	1.2e-4(2.7e-5)	5.8e-4(4.1e-5)	5.7e-3(4.3e-5)
2011/330	1.9e4(8.5e1)	1.7e4(1.9e2)	2.7e2(1.2e1)	1.1e1(2.0e-2)	2.0e-1(1.5e-2)	3.3e-2(1.8e-2)	1.0e0(2.6e-3)	1.1e-1(5.3e-5)	4.7e-3(3.6e-5)	7.9e-2(2.1e-5)	7.4e-3(1.6e-4)	1.1e-3(9.0e-5)
2012/012	NI(8.0e1)	3.2e1(1.5e1)	4.5e1(2.4e1)	NI(1.8e-2)	NI(1.5e-2)	NI(1.9e-2)	NI(2.4e-3)	1.4e-3(3.4e-5)	6.8e-4(3.4e-5)	NI(2.5e-5)	3.4e-4(6.0e-5)	2.0e-4(6.0e-5)
2012/019	1.6e3(1.1e2)	NM(5.3e0)	7.9e3(6.8e2)	6.9e-1(2.2e-2)	NI(1.6e-2)	2.7e-1(1.6e-2)	3.1e-2(2.7e-3)	NI(3.6e-5)	1.2e-1(5.1e-4)	7.3e-4(3.0e-5)	NI(4.0e-5)	1.7e-2(5.0e-5)
2012/023	1.8e5(9.3e2)	1.6e4(7.2e1)	1.2e4(1.1e3)	7.5e2(1.8e-1)	7.5e-1(2.0e-2)	1.1e0(2.3e-2)	7.1e1(1.3e-2)	8.5e-1(5.5e-5)	1.4e0(1.0e-2)	7.4e0(4.6e-4)	2.5e-1(4.2e-5)	4.9e-1(1.1e-3)
2012/027	7.3e4(4.7e3)	NM(9.5e3)	NI(6.8e2)	2.7e2(2.2e0)	4.0e0(1.5e-1)	NI(6.1e-2)	1.7e1(1.4e-1)	NM(1.3e-1)	NI(1.2e-2)	4.1e0(1.0e-2)	NM(2.5e-2)	NI(3.0e-3)
2012/060	NI(1.1e2)	8.8e2(3.0e2)	NI(6.3e1)	NI(2.3e-2)	3.5e-2(1.7e-2)	NI(1.9e-2)	NI(2.3e-3)	1.0e-2(1.1e-4)	NI(4.0e-5)	2.1e-4(2.4e-5)	4.1e-3(4.0e-5)	NI(4.0e-5)
2012/084	4.1e2(3.3e2)	2.0e4(4.1e2)	NM(6.7e2)	NI(4.8e-1)	7.5e0(6.1e-2)	5.1e-1(8.1e-2)	NI(2.4e-3)	1.8e0(2.1e-3)	4.3e-2(3.0e-3)	NI(2.2e-4)	9.1e-1(4.3e-4)	2.1e-2(8.2e-4)
2012/106	NI(7.7e1)	2.9e2(2.2e1)	6.9e2(8.3e1)	NI(2.1e-2)	2.5e-2(1.7e-2)	4.3e-2(2.0e-2)	NI(2.3e-3)	1.5e-3(3.1e-5)	4.6e-3(5.2e-5)	NI(2.1e-5)	6.9e-4(5.0e-5)	1.3e-3(9.5e-5)
2012/138	1.8e4(8.5e1)	NM(1.1e1)	6.0e1(9.9e0)	7.1e1(1.9e-2)	1.6e-1(1.7e-2)	4.1e-2(1.7e-2)	5.8e0(2.2e-3)	NM(1.8e-5)	1.4e-3(4.0e-5)	3.1e-1(1.6e-5)	NM(4.1e-5)	1.1e-3(8.2e-5)
2012/147[d]	5.6e3(9.2e1)	5.3e3(1.9e1)	NI(3.0e1)	3.1e0(3.0e-2)	5.2e-1(1.6e-2)	NI(1.7e-2)	1.8e-1(2.5e-3)	4.1e-1(1.2e-4)	NI(1.6e-4)	3.9e-3(4.1e-5)	1.2e-1(6.4e-5)	NI(6.4e-5)
2012/166	5.0e2(9.2e1)	NI(7.3e1)	3.7e2(9.1e1)	3.2e-1(4.8e-2)	NI(1.6e-2)	5.1e-2(1.7e-2)	NM(2.7e-3)	NI(2.9e-5)	3.1e-3(3.0e-5)	3.4e-4(1.2e-5)	NI(1.0e-5)	7.2e-4(4.5e-5)

Notes.
[a] Units are particles cm^{-2} sr^{-1} s^{-1} MeV^{-1}.
[b] The intensities listed for *STEREO-B* correspond to a particle increase with a ∼1 day of delay with respect to the onset at *STEREO-A* and near-Earth. Considering the nominal connection of *STEREO-B* that would correspond to one of the "extreme" propagation events described by Cliver et al. (1995, 2005). A CME seen by both *STEREO*s at 02:45 UT on day 156 (cor1.gsfc.nasa.gov/catalog) may have contributed to the particle intensities at *STEREO-B*. The particle intensities at *STEREO-B* are not considered in the ensemble distribution of peak intensities.
[c] The intensities listed for near-Earth observers may be compromised by the passage of an unrelated interplanetary shock. The particle intensities at near-Earth observers are not considered in the ensemble distribution of peak intensities.
[d] *STEREO-B* intensities increased later on day 2012/148 due to an unrelated CME at ∼5:25 UT on day 148 (cor1.gsfc.nasa.gov/catalog).

Table 2
Solar Origin and Spacecraft Location during the Selected SEP Events[a]

(1) Date	(2) AR	(3) Flare Site	(4) Time	(5) R_{Earth}	(6) Ψ_{Earth}	(7) ϕ_{Earth}	(8) R_{STA}	(9) Ψ_{STA}	(10) ϕ_{STA}	(11) R_{STB}	(12) Ψ_{STB}	(13) ϕ_{STB}
2009/356	11036	S26W46	04:50	0.98	14.2	72.7	0.97	78.1	136.0	1.05	307.0	3.0
2010/017	11041	S25E127	03:41	0.98	40.6	99.1	0.96	105.3	162.6	1.03	331.5	33.0
2010/043	11046	N26E11	11:19	0.99	67.1	126.2	0.96	132.4	189.7	1.01	356.3	56.3
2010/163	11081	N23W43	00:30	1.02	185.0	245.9	0.96	258.5	315.8	1.02	115.4	176.3
2010/219	11093	N11E34	17:55	1.01	238.3	298.6	0.96	317.6	14.9	1.06	167.1	230.4
2010/226	11099	N17W52	09:38	1.01	245.0	305.3	0.96	324.9	22.2	1.07	173.2	237.1
2010/230	11099	N14W100	04:45	1.01	248.9	309.2	0.96	329.1	26.4	1.07	176.7	240.6
2010/243	11100	~W144	20:55	1.01	261.5	321.8	0.96	342.6	39.9	1.08	188.0	252.5
2010/251	11105	N19W94	23:23	1.01	270.3	330.6	0.96	351.9	49.2	1.08	195.8	260.3
2011/028	11149	N16W92	00:44	0.98	51.6	110.1	0.96	138.2	195.5	1.04	319.3	21.4
2011/046	11158	S20W11	01:44	0.99	69.9	129.0	0.96	156.9	214.2	1.03	336.1	37.6
2011/080	11169	N16W130	02:15	1.00	104.2	163.9	0.96	192.4	249.7	1.01	8.9	69.2
2011/155A	11222	N16W145	~06:45	1.01	177.2	237.5	0.96	271.7	329.0	1.01	84.0	144.3
2011/155B	11222	N16W145	~21:45	1.01	177.2	237.5	0.96	271.7	329.0	1.01	84.0	144.3
2011/214	11261	N14W15	05:19	1.01	233.2	293.5	0.96	333.7	31.0	1.04	140.9	203.0
2011/216	11261	N19W36	03:41	1.01	235.2	295.5	0.96	335.8	33.1	1.04	142.7	204.8
2011/221	11263	N17W69	07:48	1.01	240.0	300.3	0.96	341.0	38.3	1.05	147.3	210.0
2011/249A	11283	N14W07	01:35	1.01	267.1	327.4	0.97	9.9	67.8	1.07	172.3	236.2
2011/249B	11283	N14W18	22:12	1.01	267.1	327.4	0.97	9.9	67.8	1.07	172.3	236.2
2011/264	11289	N25W108	22:24	1.00	281.8	341.5	0.97	25.3	83.2	1.07	185.4	249.3
2011/265	11302	N13E78	10:29	1.00	282.8	342.5	0.97	26.3	84.2	1.07	186.3	250.2
2011/277	11314	N22E155	12:45	1.00	294.7	354.4	0.97	38.7	96.6	1.08	196.6	261.1
2011/307	11347	N08E152	22:15	0.99	324.5	23.6	0.97	69.8	127.7	1.09	222.2	287.3
2011/321	11356	N15E110	20:36	0.99	338.5	37.6	0.97	84.3	142.2	1.09	234.1	299.2
2011/330	FD	N17W49	07:12	0.99	347.5	46.6	0.97	93.7	151.6	1.08	241.8	306.3
2012/012	11402	N30E115	08:24	0.98	35.0	93.5	0.96	142.8	200.1	1.07	282.8	346.7
2012/019	11402	N32E22	14:37	0.98	42.1	100.6	0.96	150.1	207.4	1.06	289.1	352.4
2012/023	11402	N28W21	03:34	0.98	46.2	104.6	0.96	154.3	211.6	1.06	292.7	356.0
2012/027	11402	N22W71	18:15	0.98	50.3	108.8	0.96	158.4	215.7	1.06	296.3	359.6
2012/060	11420	N12W140	~08:45	0.99	83.8	142.9	0.96	192.9	250.2	1.03	326.7	28.2
2012/084	11451	N18E165	~00:11	1.00	108.0	167.7	0.96	218.1	275.4	1.02	349.5	50.4
2012/106	11461	N15E100	02:10	1.00	129.7	189.4	0.96	241.4	298.7	1.01	10.9	71.2
2012/138	11476	N11W76	01:25	1.01	160.7	221.0	0.96	275.4	332.7	1.00	42.7	102.4
2012/147	11482	N16W122	~20:35	1.01	169.3	229.6	0.96	284.9	342.2	1.00	51.8	111.5
2012/166	11504	S17E06	12:52	1.02	187.3	248.2	0.96	305.0	362.3	1.00	70.9	130.6

Note. [a] Units are AU for heliocentric radial distances, degrees for the heliographic inertial longitudes Ψ and ϕ, and UT of the indicated day for the onset times of the parent solar event.

$-16^\circ \pm 3^\circ$ and $\sigma = 49^\circ \pm 2^\circ$ for 71–112 keV electrons, (b) $\phi_0 = -13^\circ \pm 3^\circ$ and $\sigma = 46^\circ \pm 2^\circ$ for 0.7–3.0 MeV electrons, (c) $\phi_0 = -12^\circ \pm 3^\circ$ and $\sigma = 43^\circ \pm 2^\circ$ for 15–40 MeV protons, and (d) $\phi_0 = -12^\circ \pm 3^\circ$ and $\sigma = 45^\circ \pm 1^\circ$ for 25–53 MeV protons. These latter values are directly comparable to previous studies performed with *Helios* and *IMP-8* data from solar cycle 21 that obtained $\phi_0 \sim -11^\circ \pm 3^\circ$ and $\sigma \sim 36^\circ \pm 2^\circ$ for 27–37 MeV protons (Lario et al. 2006). The slightly wider distributions obtained in the present study with all the observers close to 1 AU may be due to the fact that either we are using a different sample of events and/or that the events effectively spread in longitude with radial distance (see discussion below).

Figure 4 shows that the maximum values of peak intensity occur at values of ϕ close to about 0° or slightly negative (east of the nominal spacecraft's footpoint). This result was also found by Lario et al. (2006). Apart from the systematic errors due to the assumptions that CME-driven shocks (presumed to be responsible for particle acceleration) are centered on the flare site and that a Parker spiral IMF with a constant solar wind speed of 400 km s^{-1} represents the magnetic connection of the spacecraft to the Sun, there is the additional factor that CME-driven shocks propagate outward from the Sun before the maximum peak intensity is reached. This fact will indeed bias the longitude of peak intensities eastward. Estimates of the release time of both high-energy protons and near-relativistic electrons indicate that CMEs can already be at distances $\gtrsim 3\ R_s$ for electrons (Simnett et al. 2002) or even 5–15 R_s for high-energy protons (Kahler 1994). The motion of the point on the shock front that magnetically connects with the observer leads to an eastward bias, i.e., toward central meridian longitudes. The strongest portions of the shock front are located there when the shock is originated from longitudes at the east of the spacecraft's footpoint. Additionally, the effect of flux tube corotation, i.e., the longitudinal motion of the magnetic lines of forces rooted at the Sun (e.g., Lario et al. 1998; Giacalone & Jokipii 2012), together with the diffusive transport of energetic particles may favor the bias toward eastern longitudes. Consequently, the centroids of the distributions should slightly shift toward eastern longitudes, just as indicated by the values of ϕ_0.

7. RADIAL DEPENDENCE: *MESSENGER* OBSERVATIONS

The *MESSENGER* spacecraft provides contemporaneous observations of near-relativistic electrons from helioradii $R <$ 1 AU. We use 71–112 keV electron intensities measured by the EPS (Andrews et al. 2007). EPS is mounted on the back

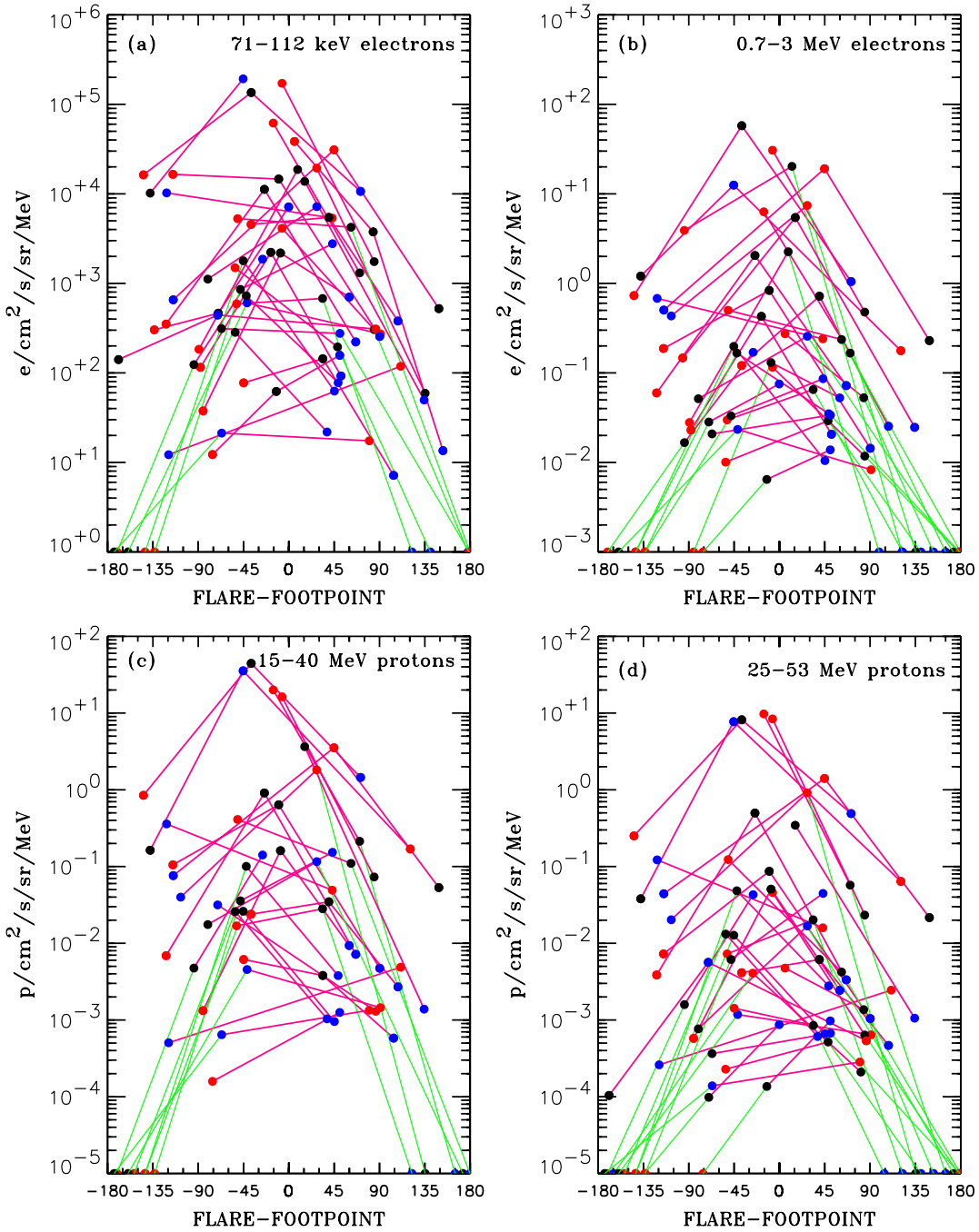

Figure 4. Longitudinal distribution of the (a) 71–112 keV electron, (b) 0.7–3.0 MeV electron, (c) 15–40 MeV proton, and (d) 25–53 MeV proton peak intensities as obtained from measurements by *STEREO-A* (red), *STEREO-B* (blue), and near-Earth spacecraft (black dots). Horizontal axes indicate the longitudinal distance between the parent solar flare and the footpoint of the nominal IMF line connecting each spacecraft to the Sun. Magenta lines connect events observed by two or three spacecraft. Thin green lines connect those events for which one spacecraft did not detect any particle increase (plotted as a dot on the bottom horizontal axis). Black symbols on the bottom horizontal axis of Figures 4(a) and (c) are omitted because the elevated background intensities of *ACE*/EPAM and *GOES*/EPS (see Figure 1) obscured the actual events at these spacecraft.

side of the spacecraft, so it has a field of view restricted to the antisunward direction. Therefore, EPS detects mostly particles moving in the sunward direction. Considering that closer to the Sun events tend to be more anisotropic than at 1 AU (e.g., Lario 2007), it is likely that *MESSENGER* misses the actual peak intensity of beam-like events. Therefore, *MESSENGER* observations provide only a lower limit to the actual peak intensities of the SEP events and overestimate the occurrence time of the peak of the event. Unfortunately, the large instrumental background of EPS means that only the most intense SEP events are observed by this spacecraft.

Table 3 lists the 71–112 keV electron events observed by *MESSENGER*/EPS during the period under study with (1) a maximum intensity identifiable during the prompt component

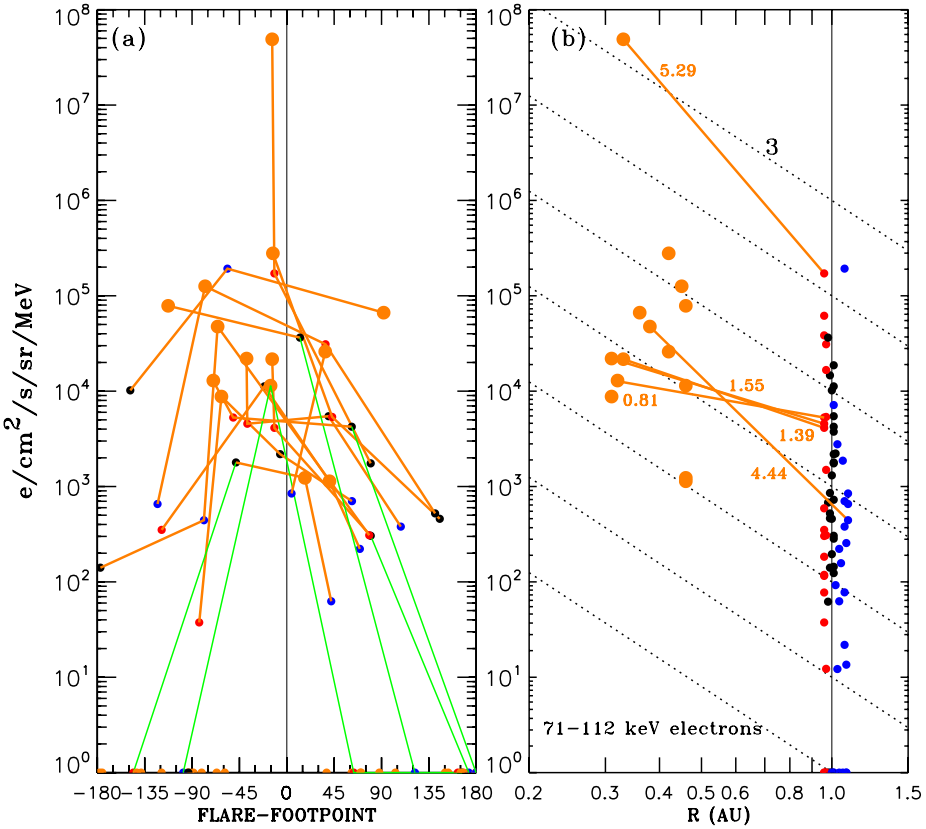

Figure 5. (a) The same as Figure 4(a) but for those events observed by *MESSENGER*/EPS listed in Table 3 (orange dots). (b) Distribution of the 71–112 keV electron peak intensities as a function of the heliocentric radial distance. The orange lines connect those events for which the nominal footpoints of *MESSENGER* and one of the spacecraft at ∼1 AU were separated by less than 20°. The dotted black lines indicate a R^{-3} radial dependence. The numbers in orange indicate the index α if a radial dependence $\propto R^{-\alpha}$ is assumed.

Table 3
MESSENGER/EPS 71–112 keV Electron Events

Date Year/Day	R_{MSGR} (AU)	Ψ_{MSGR} (°)	ϕ_{MSGR} (°)	Peak Intensity (Pre-event Background) (Particles cm^{-2} sr^{-1} s^{-1} MeV^{-1})
2010/226	0.31	342.6	1.1	2.5e4(1.6e4)
2010/230	0.31	8.6	27.1	3.7e4(1.5e4)
2011/155A	0.33	311.4	331.1	3.1e4(9.0e3)
2011/155B	0.33	311.4	331.1	4.9e7 (9.0e3)
2011/214	0.46	200.6	228.0	1.5e3(2.5e2)
2011/216	0.46	206.3	233.7	1.6e3(5.0e2)
2011/265	0.36	80.3	101.8	8.1e4(1.4e4)
2011/277	0.42	127.9	152.9	2.9e5(9.0e3)
2011/307	0.45	215.2	242.1	1.3e5(1.0e4)
2011/321	0.38	263.5	286.2	5.8e4(1.1e4)
2012/027	0.46	206.5	234.0	8.7e4(9.0e3)
2012/147	0.32	342.0	361.1	2.0e4(6.7e3)
2011/287	0.46	158.8	186	2.3e4(1.2e4)
2011/313	0.42	234.1	259	3.7e4(1.1e4)

of the event and (2) associated with only one parent solar event. Column 1 lists the date of the SEP event. Columns 2–4 list the heliocentric radial distance of *MESSENGER* R_{MSGR} (in units of AU), the heliographic inertial longitude of *MESSENGER* Ψ_{MSGR} (in degrees), and the heliographic inertial longitude of the footpoint of the nominal IMF line connecting *MESSENGER* with the Sun ϕ_{MSGR} (in degrees), respectively. The 71–112 keV peak intensity is listed in Column 5 whereas the pre-event intensities are listed in parentheses. The events on day 287 of 2011 and 313 of 2011, although observed by *MESSENGER*, did not meet the criteria described in Section 5 to select the events listed in Tables 1 and 2. For example, the event on 2011/287 was observed by *MESSENGER* but not by the other spacecraft; and the event on 2011/313 was observed by *MESSENGER* and only by *STEREO-B* at $R_{STB} = 1.09$ AU, $\Psi_{STB} = 227°$, $\phi_{STB} = 291°$.

Figure 5(a) shows the longitudinal distribution of 71–112 keV electron peak intensities for those events observed by *MESSENGER*/EPS (orange dots). The orange lines connect those events observed simultaneously by *MESSENGER* and one of the other spacecraft at ∼1 AU, whereas the green lines connect those events observed by *MESSENGER* while one or more of the other spacecraft did not detect any particle increase. The peak intensities for those spacecraft are artificially plotted on the bottom horizontal axis of Figure 5(a). We have also added on the bottom horizontal axis of Figure 5(a) those events of Table 1 for which *MESSENGER* did not observe any particle increase above its elevated background (indicated by orange dots). Owing to the elevated background of *MESSENGER*/EPS, the events for which this spacecraft detected intensity increases are above 10^3 electrons cm^{-2} sr^{-1} s^{-1} MeV^{-1}. Note that the two events observed by *MESSENGER* in 2011 August (days 214 and 216) correspond to time intervals when the geometrical factor of *MESSENGER*/EPS was modified allowing for a temporary detection of less intense events. As expected, the well-connected events show larger peak intensities than poor-connected events.

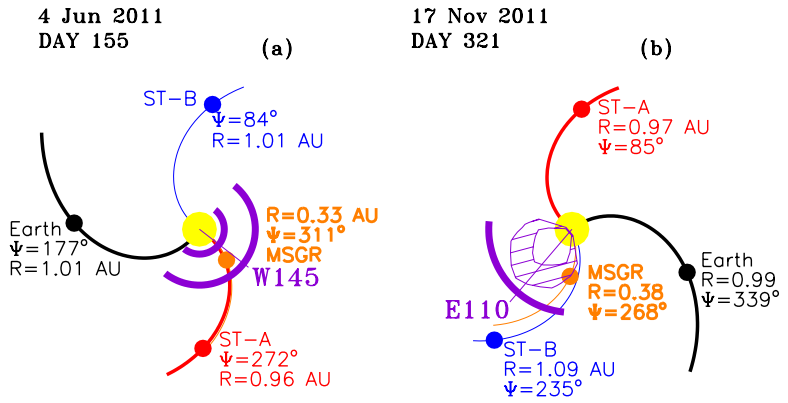

Figure 6. Schematic representation of the interplanetary configuration and spacecraft location (R = heliocentric radial distance; Ψ = heliospheric inertial longitude) during the events on (a) 2011 June 4 (2011/155B) and (b) 2011 November 17 (2011/321) as seen from the North ecliptic pole. Nominal IMF lines connecting each spacecraft with the Sun (orange for *MESSENGER*, black for *ACE*, red for *STEREO-A*, and blue for *STEREO-B*) and the longitude of the parent solar event (as seen from Earth) are indicated. The purple structures indicate the presence of interplanetary shocks (semi-circles) or ICMEs (hatched areas).

However, the radial dependence of peak intensities contributes also to the range of peak intensities displayed in Figure 5(a).

Figure 5(b) shows the distribution of peak intensities as a function of the heliocentric radial distance. Since the longitudinal distance of the observer with respect to the flare site has a stronger influence on the peak intensities than the radial distance of the observer (Lario et al. 2006), we focus our analysis on the events for which two spacecraft were nominally well connected, minimizing in this way the longitudinal effect on the SEP peak intensity gradient. As in Lario et al. (2006) we choose those events for which the nominal magnetic footpoints of *MESSENGER* and another spacecraft near 1 AU were separated by less than 20°. The orange lines in Figure 5(b) connect the peak intensities in the prompt component of these events, whereas the adjacent orange numbers indicate the index α if a radial dependence $R^{-\alpha}$ for the peak intensities is assumed. The black dotted lines show a R^{-3} radial dependence which is an upper limit obtained by the observational and modeling studies described in Section 3. Two events (2011/155B and 2011/321 in Tables 1 and 2) show stronger radial dependences than R^{-3}. The other three events (2010/230, 2011/155A, and 2012/147 in Tables 1 and 2) displayed radial dependences even weaker than R^{-3}. Because of the importance of the events with radial dependences stronger than R^{-3} for extrapolation of 1 AU particle measurements to the inner heliospheric distances that spacecraft such as the *Solar Orbiter* and *Solar Probe Plus* will explore (e.g., Lario & Decker 2011), we analyze these two events (2011/155B and 2011/321) in detail in the following section.

7.1. SEP Events with Radial Dependences Steeper Than R^{-3}

The two events with peak intensity dependences steeper than R^{-3} (and with nominal footpoints of *MESSENGER* and a near-1 AU spacecraft separated by less than 20°) occurred on (a) 2011 June 4 (day of year 155) and (b) 2011 November 17 (day of year 321). Figure 6 sketches the location of *MESSENGER* (MSGR; orange symbol), Earth (black symbol), *STEREO-A* (ST-A; red symbol), and *STEREO-B* (ST-B; blue symbol) as seen from the north ecliptic pole for each event. The heliocentric radial distance R and the heliographic inertial longitude Ψ of each spacecraft are indicated in the figure. Nominal IMF lines connecting each spacecraft with the Sun have been plotted, assuming a Parker spiral IMF with a solar wind of 400 km s^{-1}. The purple thin solid straight lines labeled with (a) W145 and (b) E110 indicate the longitudes of the parent solar events as seen from Earth. The purple structures indicate the presence of interplanetary shocks (semi-circles) or ICMEs (hatched areas) as described below. The distance between the nominal footpoints of *MESSENGER* and *STEREO-A* was only $\Delta\phi = 2°$ in the event 2011/155B, whereas the distance between the nominal footpoints of *MESSENGER* and *STEREO-B* was $\Delta\phi = 13°$ in the event 2011/321.

7.1.1. The Event on 2011 June 4

The most intense event observed by *MESSENGER* during the period of interest occurred on 2011 June 4 (Lario et al. 2013) when the spacecraft was already in orbit about Mercury at $R = 0.33$ AU. Figure 7 shows the *MESSENGER* (left) and *STEREO-A* (right) near-relativistic electron and magnetic field observations during this event. From top to bottom, Figure 7 shows: (a) 71–112 keV electron intensities, (b) magnetic field magnitude, and (c) and (d) polar and azimuth magnetic field angles in the RTN spacecraft centered coordinate system. We have subtracted from the measured particle intensities the intensity detected just prior to the onset of the most intense SEP event at the end of day 155.

Periodic increases in the *MESSENGER* magnetic field magnitude (Figure 7(b)) are caused by the close proximity of the spacecraft to Mercury. The structure of Mercury's magnetosphere has been described elsewhere (e.g., Anderson et al. 2007, 2010, 2011; Slavin et al. 2012). The vertical gray bars identify the time intervals when *MESSENGER* observed magnetic structures associated with Mercury's magnetosphere, whereas the periods between the gray vertical bars indicate that the spacecraft was immersed within the interplanetary medium. The red solid vertical lines in Figure 7 indicate the passage of interplanetary shocks identified by abrupt increases in magnetic field magnitude. The red vertical dashed lines indicate the time intervals with both enhanced magnetic field magnitude and magnetic field rotations (red dots in Figures 7(b)–(d)) typically observed in the downstream region of interplanetary shocks during the passage of ICMEs. In the case of *MESSENGER*, the observation of a magnetic field associated with the ICME is interrupted by the spacecraft's periapses close to Mercury. The magnitude and direction of the IMF is the dominant factor determining the intensity, configuration, and dynamic variations of the upstream and downstream structures in the Mercury's magnetosphere (e.g., Slavin et al. 2012). In particular, the compressed medium formed in the downstream region of the shocks clearly

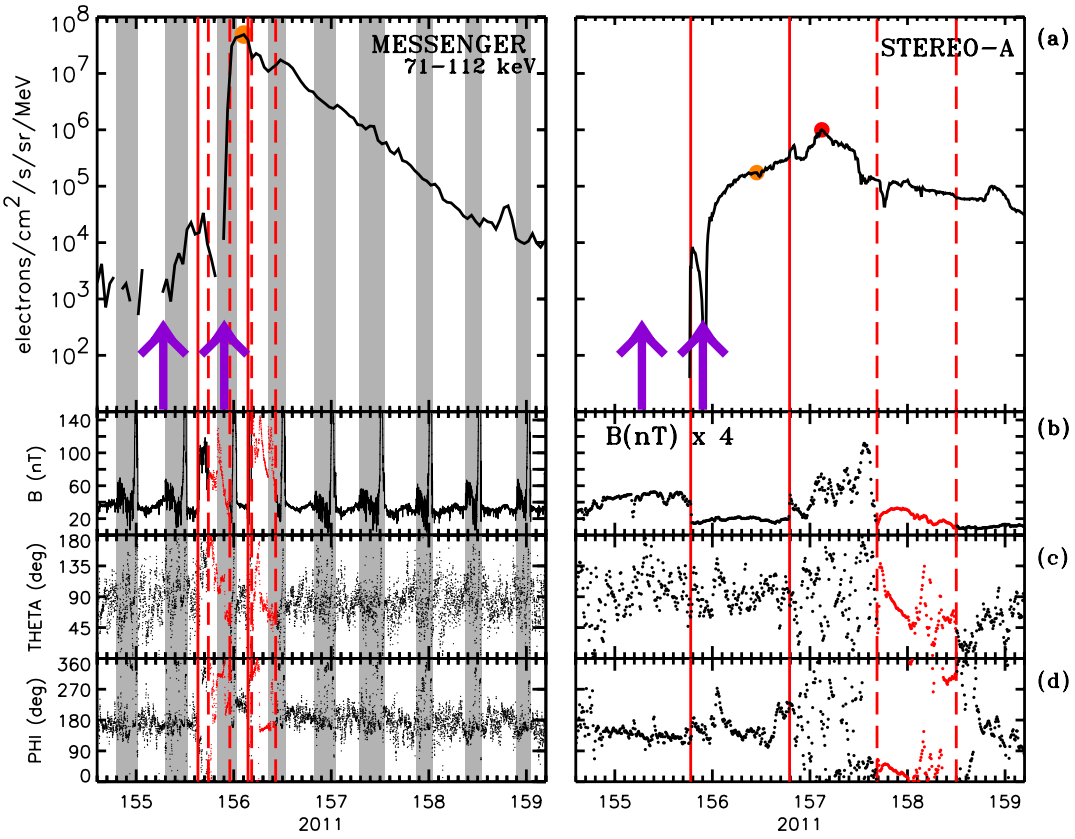

Figure 7. (a) 71–112 keV electron intensities, (b) magnetic field magnitude, (c) magnetic field polar angle, and (d) magnetic field azimuth angle in the RTN spacecraft centered coordinate system as observed by *MESSENGER* (left panels) and by *STEREO-A* (right panels) during the event on 2011 June 4 (2011/155B). The vertical gray bars in the left panels indicate the time intervals when *MESSENGER* observed magnetic field structures associated with Mercury's magnetosphere. The red vertical solid lines indicate the passage of interplanetary shocks and the dashed vertical lines limit the boundaries of the ICMEs. The purple arrows identify the solar events associated with the near-relativistic electron events as described in the text.

affects the properties of the planet's magnetosphere (e.g., Alexeev et al. 2008). Hence, the entry of the spacecraft into the magnetosphere after (or during) the passage of the interplanetary shocks shows larger magnetic field magnitudes and uncommon magnetic field orientations compared to those usually observed in orbits without the presence of shocks.

The arrows in Figure 7(a) identify the launch time of two fast halo CMEs originating from the same active region (Lario et al. 2013). These two halo CMEs were first seen in the C2 coronagraph of *SOHO*/LASCO (>2.5 R_s) at 06:48 UT on day 155 (associated with the origin of the event 2011/155A in Tables 1 and 2) and 22:05 UT on the same day (associated with the event 2011/155B) with plane-of-sky speeds of ~1400 km s^{-1} and ~2425 km s^{-1}, respectively (http://cdaw.gsfc.nasa.gov/CME_list/). As seen from EUVI 195 Å images taken by *STEREO-A* (http://cor1.gsfc.nasa.gov/catalog/), these two CMEs originated from the same active region at approximately ~N20W50 as seen from *STEREO-A* (or ~N20W145 as seen from Earth). Using the rotation rate of the Sun, we identify the active region where the flares temporally associated with the origin of the two CMEs originated from the old NOAA AR 11222 that crossed the west limb of the solar disk (as seen from Earth) on 2011 May 31 (day 151).

These two CMEs were well pointed to directly impact *MESSENGER*. By assuming that the first shock at *MESSENGER* (observed at 15:12 UT on day 155) was driven by the first CME, we imply a transit speed of ~1600 km s^{-1} to travel from the Sun to the spacecraft. By assuming that the second shock at *MESSENGER* (observed at 03:31 UT on day 156) was driven by the second CME, we deduce a transit speed of ~2345 km s^{-1}. Both transit speeds are in agreement with the LASCO plane-of-sky speeds quoted above. At the time of the second EUVI flare, the interplanetary shock driven by the first CME was located at a heliocentric distance of ~0.58 AU (assuming a constant travel speed of 1600 km s^{-1}, as inferred by the transit speed of the shock from the Sun to 0.33 AU), or ~0.50 AU (assuming a constant travel speed of 1400 km s^{-1} as obtained from LASCO CME observations). The peak intensity at *MESSENGER* was observed during a period of flat time-intensity profile between the passage of the two ICMEs. This is consistent with the scenario proposed by Kallenrode & Cliver (2001) to explain the most intense SEP events where energetic particles remain confined between two shocks. The elevated particle intensities are observed when the spacecraft (in this case *MESSENGER*) is located between the two shocks. By contrast, the presence of the first CME in the interplanetary medium (located beyond *MESSENGER*) and its associated shock may impede the transport of energetic particles to 1 AU (Lario et al. 2008), thus explaining the smaller particle intensities at *STEREO-A*. The orange dots in Figure 7 identify the peak intensity observed for the prompt component of the events. The radial dependence of the peak intensities obtained by using these values of the intensities (as indicated by the orange dots) is $R^{-5.29}$. The time-intensity profile at *STEREO-A* was clearly

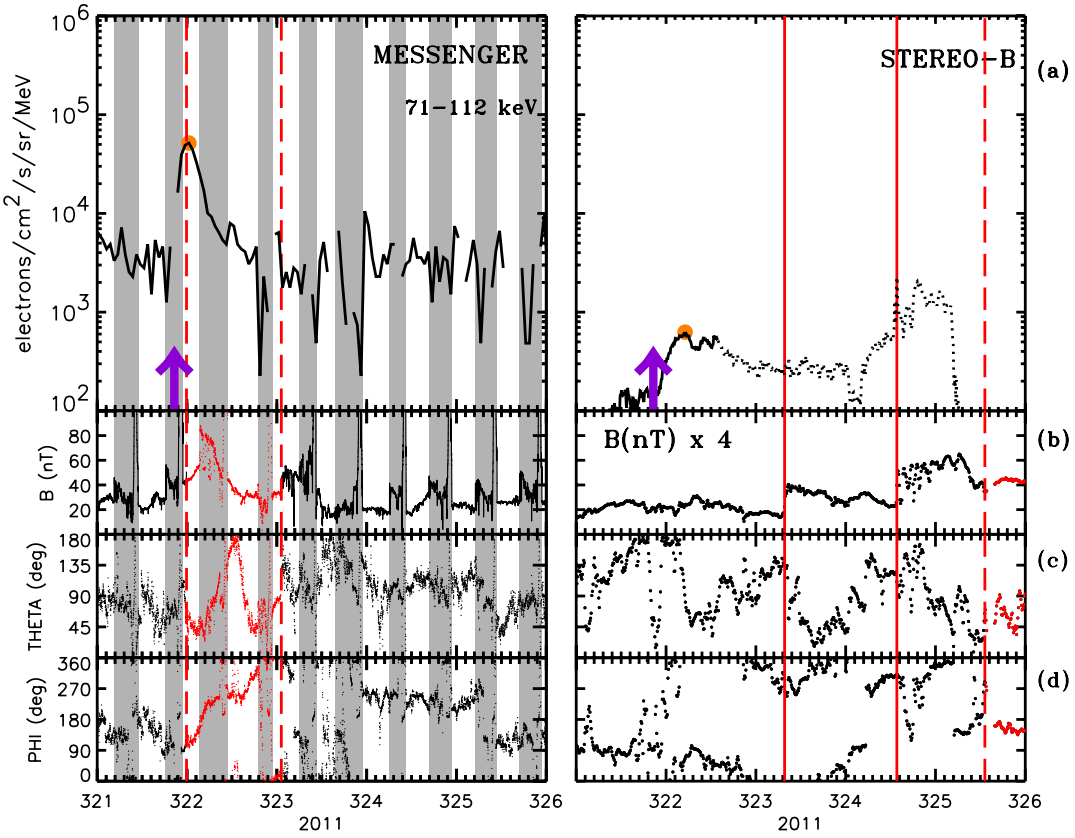

Figure 8. Same as Figure 7 but for the event on 2011 November 17 (2011/321).

affected by the passage of an interplanetary shock and an ICME, with an absolute peak intensity (red dot) observed during the passage of the sheath region formed in front of the ICME. The radial dependence obtained by using this peak intensity is $R^{-3.64}$.

7.1.2. The Event on 2011 November 17

Figure 8 shows, with the same format as Figure 7, particle and magnetic field observations during the event on day 321 of 2011. The origin of this event was associated with a halo CME detected by *SOHO*/LASCO (first seen in the C2 coronagraph at 20:36 UT on day 321) with a plane-of-sky speed of ~1040 km s^{-1} (http://cdaw.gsfc.nasa.gov/CME_list/). This halo CME was also detected by the *STEREO-B* coronagraphs at 20:45 UT (cor1.gsfc.noaa.gov/catalog/). The maximum CME speed observed by *STEREO-B* was similar to that derived from LASCO, 1041 km s^{-1}, as determined by the Computer Aided CME Tracking software (CACTus) (Robbrecht et al. 2009, secchi.nrl.navy.mil/cactus).

The origin of this CME was a few degrees east of the central meridian as seen from *STEREO-B* (Figure 6(b)). The purple arrows in Figure 8 indicate the launch of this CME. The onset of the SEP event at *MESSENGER* occurred when the spacecraft was immersed in Mercury's magnetosphere (indicated by gray bars in Figure 8(a)). The exit from the magnetosphere was characterized by an enhanced magnetic field magnitude and a day-long rotation of the magnetic field (red dots in the left panels of Figures 8(b)–(d)), suggesting the passage of a flux rope by *MESSENGER*. Presumably the passage of this ICME was preceded by an interplanetary shock; however the immersion of *MESSENGER* into the planet's magnetosphere prevented us from detecting the passage of this shock. The presence of a shock traveling toward *STEREO-B* (see the location of this spacecraft in Figure 6(b)) can also be inferred from in situ *STEREO-B* observations. Two shocks were observed by this spacecraft at 07:40 UT on day 323 and 13:40 UT on day 324 (red solid vertical lines in Figure 8). It is likely that the shock on day 324 at *STEREO-B* was associated with the CME launched from the Sun at 20:36 UT on day 321, implying an average transit speed of ~720 km s^{-1} between the Sun and *STEREO-B*. At the time of the injection of SEPs from the Sun late on day 321, the shock observed by *STEREO-B* on day 323 constituted an intervening structure located between the Sun and *STEREO-B*. Additionally, at the time of the onset of the SEP event at *STEREO-B*, the magnetic field was pointing northward, which may indicate that a transient structure swept by *STEREO-B* at the time of the electron event was affecting the propagation of electrons toward this spacecraft. The radial dependence obtained by using the peak intensity of the events indicated by orange dots in Figure 8 is $R^{-4.44}$. Note that electron intensities at *STEREO-B* were partially contaminated by ions (the period with unusable electron data and complete ion contamination is indicated by the dotted trace in the right panel of Figure 8(a)) which implies that the actual electron flux at *STEREO-B* would have been even smaller than those shown in Figure 8(a) and hence the resulting radial dependence would have been even steeper.

7.2. SEP Events with Radial Dependences Weaker Than R^{-3}

The three events with peak intensity dependences weaker than R^{-3} and nominal footpoints of *MESSENGER* and a near 1 AU

spacecraft separated by less than 20° occurred early on 2010 August 18 (event 2010/230; $\Delta\phi = 1°$; $R^{-1.39}$), early on 2011 June 4 (event 2011/155A; $\Delta\phi = 2°$; $R^{-1.55}$), and late on 2012 May 26 (event 2012/147; $\Delta\phi = 19°$; $R^{-0.81}$). The use of these weak radial dependences to extrapolate intensities measured at 1 AU to the inner heliosphere does not imply extreme radiation environments at $R < 1$ AU. Consequently, the interplanetary configuration under which these events developed is briefly sketched here. It should be remembered that *MESSENGER*/EPS cannot view the Sunward hemisphere and hence cannot detect the true prompt peak intensity in anisotropic events and therefore the actual radial dependence of the peak intensity of these events may be stronger than the values quoted in Figure 5(b).

In Section 7.1 we have seen that during the events 2011/155B and 2011/321, the presence of transient interplanetary structures between *MESSENGER* and 1 AU favored the enhancement of particle intensities at *MESSENGER* but hindered the transport of SEPs toward 1 AU. At the time of SEP injection from the Sun during the event 2010/230, transient structures were located beyond and around *STEREO-A*. A magnetic cloud passed through *STEREO-A* during the onset of the SEP event, allowing freshly injected SEPs to easily reach *STEREO-A* (Leske et al. 2012). This configuration favored the large particle intensities at *STEREO-A* and hence the weak radial dependence $R^{-1.39}$ obtained in this event (see details in Leske et al. 2012). The event 2011/155A at *STEREO-A* occurred within the passage of a high-speed solar wind stream bounded by a forward shock at 19:10 UT on day 153 (not shown here) and a reverse shock at 18:40 UT on day 155 (Figure 7(b)). Direct injection of particles into this corotating interaction region (CIR) may have led to particle re-acceleration by the CIR shocks and hence the large intensities at *STEREO-A* and the weak radial dependence $R^{-1.55}$ of this event. Finally, the event 2012/147 occurred when the nominal magnetic footprints of *MESSENGER* and *STEREO-A* were separated by ∼19° and the longitudinal effect may have played a role (*STEREO-A* was better connected to the flare site than *MESSENGER* whose nominal footpoint was ∼70° westward from the flare). The event 2012/147 was generated by the active region AR 11482. The event at *MESSENGER* was preceded one day earlier by the passage of an ICME (not shown here) that was not observed by *STEREO-A* on the subsequent days. The passage of this ICME by *MESSENGER* was not accompanied by any particle intensity increase and no CME-driven shock was observed in front of it. No SEP was observed prior to the passage of the ICME by *MESSENGER*. We presume that this ICME resulted from a slow CME at the Sun generated from an active region completely independent of the AR 11482. Whereas AR 11482 was well aligned with the Sun–*STEREO-A* line at the onset of the 2012/147 SEP event (see Table 2), the prior ICME (only observed by *MESSENGER* without any interplanetary shock in front of it) most likely changed the nominal magnetic connection assumed in this work between the spacecraft and the Sun, resulting in a reduction of the observed peak intensity at *MESSENGER* and hence the flat radial dependence obtained for the peak intensity in this event ($R^{-0.81}$).

8. SUMMARY

The simultaneous observations of SEP events by two or more spacecraft located at $R \sim 1$ AU during the rising phase of solar cycle 24 have allowed us to determine the longitudinal distributions of the SEP event peak intensities measured in the 15–40 MeV proton, 25–53 MeV proton, 71–112 keV electron, and 0.7–3 MeV electron intensities. We approximated the distributions of the peak intensities by Gaussian functions $\exp[-(\phi - \phi_0)^2/2\sigma^2]$ where ϕ is the longitudinal separation between the parent active region and the footprint of the nominal IMF line connecting each spacecraft with the Sun. A least-squares fit over the ensemble of observations allowed us to obtain the centroid ϕ_0 and the longitudinal gradient σ of the peak intensity distributions. We derived slightly negative values of ϕ_0 indicating that the maxima of the distributions are not exactly at the nominal well-connected longitudes but somewhat displaced toward central meridian longitudes as viewed from the spacecraft. This result suggests that the prompt component of the SEP events forms when the CME-driven shocks have already moved a significant distance outward from the solar surface, shifting the spacecraft magnetic connection to stronger portions of the shock fronts, and hence favoring longitudes closer to the central meridian of each observer. The negative values of ϕ_0 were first obtained by Lario et al. (2006) when combining *Helios* and *IMP-8* observations.

The values of σ obtained in the present work are slightly larger than those obtained by either McGuire et al. (1983a), Lario et al. (2006), or Wibberenz & Cane (2006) when combining *Helios* and *IMP* observations. The broader longitudinal distributions obtained here, with all observers at ∼1 AU, may result from the spreading of SEP events with radial distance. In fact, during solar cycle 23, large SEP events were simultaneously observed by both the *Ulysses* spacecraft (at distances $1.3 < R < 5.4$ AU) and near-Earth spacecraft regardless of the radial, longitudinal, and latitudinal distance between *Ulysses* and Earth (Simnett 2001). By contrast, a simultaneous observation of SEP events at $R < 1$ AU was not always shared by the two *Helios* spacecraft (e.g., Lario et al. 2006). The sample of events in the present study is also smaller than in the *Helios* study of Lario et al. (2006). Both the evolution of solar cycle 24 (after a long persistent solar minimum) and the imposed requirement that SEP events have (1) an increase in the 25–53 MeV proton channel observed by at least one spacecraft, (2) intensity enhancements observed by at least two spacecraft, (3) identifiable peak intensity during the prompt component of the event at least in two spacecraft, and (4) an identifiable distinct solar origin, limited us to using intense events observed when the two *STEREO* spacecraft were already distant in longitude, thus favoring broad angular distributions. Longitudinal distributions found for both electrons and protons are very similar, with only a larger eastward centroid offset and a slightly broader width for the near-relativistic electron longitudinal distribution, suggesting that the spread of near-relativistic electrons with longitudinal distances may be slightly more efficient than that of ∼25 MeV protons or relativistic electrons.

McGuire et al. (1983b) interpreted the longitudinal dependences of the peak intensities in terms of coronal diffusion of energetic particles injected from the flare site and neglected possible effects of shocks driven by CMEs. Those authors reproduced the longitudinal dependences obtained by McGuire et al. (1983a) by assuming that the longitudinal dependence of the particle injection was a Gaussian of a given width centered about the parent flare site. More recently, the association found between the longitudinal extent of the perturbation created in the corona by the lateral expansion of the flanks of a CME and the longitudinal extent of a specific SEP event in the heliosphere (e.g., Rouillard et al. 2012) suggests that the decrease of the particle intensities with longitudinal distance from the site

of the parent solar event is due to the weakening of the lateral expansion of the CME. Models that combined SEP transport of particles with injection from traveling interplanetary shocks already pleaded for the existence of (1) a longitudinal-dependent injection of particles near the Sun and (2) an injection of particles from an expanding shock in the interplanetary medium, both injections related to the same CME-driven shock (e.g., Heras et al. 1995, Lario et al. 1998). Alternatively, the multi-spacecraft observations of SEP events from distant points in longitude may also be described in terms of particle sources of a finite longitudinal width close to the Sun together with particle transport in the interplanetary medium including perpendicular diffusion (e.g., Dresing et al. 2012). The longitudinal dependence of peak intensities would result then from particle transport across IMF lines. Such models attempt to reproduce not only the arrival time of the first particles at the different observers but also the observed particle anisotropies as well as the longitudinal dependences of the SEP events.

The *MESSENGER* spacecraft, first during cruise toward Mercury and later in orbit around the planet, has allowed us to estimate the radial dependence of near-relativistic electron peak intensities. For those events with a nominal good connection between *MESSENGER* and near 1 AU spacecraft, we fit the radial dependence of 71–112 keV electron peak intensities along IMF lines by $R^{-\alpha}$. We obtain three events for which α is below 3 and two events for which α is above 3. The two events with $\alpha > 3$ occurred during complex interplanetary configurations where intervening interplanetary structures favored the larger SEP intensities close to Mercury while hindering the transport of SEPs toward 1 AU, resulting in large SEP peak intensities close to the Sun but depressed particle intensities at 1 AU. These types of configurations may lead to the largest particle intensities and extreme radiation environment that future spacecraft such as *Solar Orbiter* and *Solar Probe Plus* traveling in the innermost part of the heliosphere will experience.

We acknowledge the use of *SOHO*, *ACE*, *STEREO*, and *GOES* data provided through the indicated Web sites. The *MESSENGER* project is supported by the NASA Discovery Program under contracts NAS5-97271 to The Johns Hopkins University Applied Physics Laboratory and NASW-00002 to the Carnegie Institution of Washington. The *STEREO*/SEPT project is supported under grant 50 OC 0902 by the German Bundesministerium fuer Wirtschaft through the Deutsches Zentrum fuer Luft- und Raumfahrt (DLR). D.L. acknowledges support from NASA under grants NNX09AG30G and NNX11A083G. R.G.H. acknowledges financial support from the Spanish Ministerio de Ciencia e Innovación under project AYA2011-29727-C02-01. A.A. acknowledges support from the Spanish Ministerio de Economía y Competitividad under the project AYA2010-17286. E.C.R. acknowledges NASA support under the ACE grant NNX10AT75G.

REFERENCES

Agueda, N., Vainio, R., Lario, D., & Sanahuja, B. 2010, A&A, 519, A36
Alexeev, I. I., Belenkaya, E. S., Yu. Bobrovnikov, S., Slavin, J. A., & Sarantos, M. 2008, JGR, 113, A12210
Anderson, B. J., Acuña, M. H., Korth, H., et al. 2010, SSRv, 152, 307
Anderson, B. J., Acuña, M. H., Lohr, D. A., et al. 2007, SSRv, 131, 417
Anderson, B. J., Slavin, J. A., Korth, H., et al. 2011, P&SS, 59, 2037
Anderson, K. A., Sommers, J., Lin, R. P., et al. 1995, JGR, 100, 3
Andrews, G. B., Zurbuchen, T. H., Mauk, B. H., et al. 2007, SSRv, 131, 523
Aran, A. 2007, PhD thesis, Univ. of Barcelona, www.am.ub.es/∼blai/
Aran, A., Sanahuja, B., & Lario, D. 2005, AnG, 23, 3047
Aran, A., et al. 2011, in AGU Fall Meeting 2011, Abstract SH33B-2051A
Balch, C. C. 1999, Radiat. Meas., 30, 231
Bieber, J. W., Dröge, W., Evenson, P. A., et al. 2002, ApJ, 567, 622
Cane, H. V., Reames, D. V., & von Rosenvinge, T. T. 1988, JGR, 93, 9555
Cliver, E. W., et al. 1995, in Proc. 24th ICRC, vol. 4, ed. N. Iucci & E. Lamanna (London: IUPAP), 257
Cliver, E. W., et al. 2005, in Proc. 29th ICRC, vol. 1, ed. B. Sripathi Acharya, S. Gupta, P. Jagadeesan et al. (Mumbai: Tata Institute of Fundamental Research), 121
Decker, R. B., & Armstrong, T. P. 1979, JGR, 84, 7334
Dresing, N., Gómez-Herrero, R., Klassen, A., et al. 2012, SoPh, 281, 281
Giacalone, J., & Jokipii, R. J. 2012, ApJL, 751, L33
Gold, R. E., Krimigis, S. M., Hawkins, S. E., III, et al. 1998, SSRv, 86, 541
Hamilton, D. C. 1988, in Proc. Interplanetary Particle Environment Conf., ed. J. Feynman & S. Gabriel (JPL Publ. 88-28; Pasadena, CA: JPL), 86
Heras, A. M., Sanahuja, B., Lario, D., et al. 1995, ApJ, 445, 497
Hundhausen, A. J. 1972, in Coronal Expansion and Solar Wind, Vol. 5, ed. A. J. Hundhausen (Physics and Chemistry in Space; Berlin: Springer), 181
Kahler, S. W. 1982, JGR, 87, 3439
Kahler, S. W. 1994, ApJ, 428, 837
Kahler, S. W. 1999, in Proc. 26th ICRC, vol. 6, ed. D. Kieda, M. Salamon, & B. Dingus (London: IUPAP), 248
Kallenrode, M.-B. 1993, JGR, 98, 5573
Kallenrode, M.-B. 2002, JATP, 64, 1973
Kallenrode, M.-B., & Cliver, E. W. 2001, in Proc. 27th ICRC, vol. 8, ed. W. Droge, H. Kunow, & M. Scholer (London: IUPAP), 3314
Kunow, H., Wibberenz, G., Green, G., Müller-Mellin, R., & Kallenrode, M.-B. 1991, in Physics of the Inner Heliosphere II, ed. R. Schwenn & E. Marsch (New York: Springer), 243
Lario, D. 2007, in Proc. Second Solar Orbiter Workshop, ed. E. Marsch, K. Tsinganos, R. Marsden, & L. Conroy (ESA SP-641; Noordwijk: ESA)
Lario, D. 2010, in AIP Conf. Proc. 1216, Twelfth Int. Solar Wind Conf., ed. M. Maksimovic, K. Issautier, N. Meyer-Vernet et al. (Melville, NY: AIP), 625
Lario, D., Aran, A., Agueda, N., & Sanahuja, B. 2007, AdSpR, 40, 289
Lario, D., & Decker, R. B. 2011, SpWea, 9, S11003
Lario, D., Decker, R. B., & Aran, A. 2008, in AIP Conf. Proc. 1039, Particle Acceleration and Transport in the Heliosphere and Beyond: Proc. 7th Ann. Astrophys. Conf., ed. G. Li, Q. Hu, O. Verkhoglyadova et al. (Melville, NY: AIP), 156
Lario, D., Decker, R. B., Roelof, E. C., Reisenfeld, D. B., & Sanderson, T. R. 2004, JGR, 109, A01107
Lario, D., Ho, G. C., & Roelof, E. C. 2011, ACE News 139, www.srl.caltech.edu/ACE/ACENews/
Lario, D., Kallenrode, M.-B., Decker, R. B., et al. 2006, ApJ, 653, 1531
Lario, D., Sanahuja, B., & Heras, A. M. 1998, ApJ, 509, 415
Lario, D., et al. 2013, JGR, 118, 63
Leske, R. A., Cohen, C. M. S., Mewaldt, R. A., et al. 2012, SoPh, 281, 301
MacNeice, P., Elliott, B., & Acebal, A. 2011, SpWea, 9, S10003
McGuire, R. E., van Hollebeke, M. A. I., & Lal, N. 1983a, in Proc. 18th ICRC, vol. 10 (Bombay: Tata Institute of Fundamental Research), 353
McGuire, R. E., van Hollebeke, M. A. I., & Lal, N. 1983b, in Proc. 18th ICRC, vol. 10 (Bombay: Tata Institute of Fundamental Research), 357
McKibben, R. B. 1972, JGR, 77, 3957
Mewaldt, R. A., Cohen, C. M. S., Mason, G. M., et al. 2005, in Proc. Solar Wind 11-SOHO 16 Connecting Sun and Heliosphere, ed. B. Fleck, T. H. Zurbuchen, & H. Lacoste (ESA SP-592; Noordwijk: ESA) 67
Muller-Mellin, R., Böttcher, S., Falenski, J., et al. 2008, SSRv, 136, 363
Muller-Mellin, R., Kunow, H., Fleißner, V., et al. 1995, SoPh, 162, 483
Ochelkov, Y. P. 1986, Geomag. Aeron., 26, 851
Ontiveros, V., & Vourlidas, A. 2009, ApJ, 693, 267
Parker, E. N. 1965, P&SS, 13, 9
Reames, D. V., Barbier, L. M., & Ng, C. K. 1996, ApJ, 466, 473
Reames, D. V., & Ng, C. K. 1998, ApJ, 504, 1002
Richardson, I. G., & Cane, H. V. 1996, JGR, 101, 27521
Robbrecht, E., Berghmans, D., & Van der Linden, R. A. M. 2009, ApJ, 691, 1222
Roelof, E. C., Gold, R. E., Simnett, G. M., et al. 1992, GeoRL, 19, 1243
Rouillard, A. P., Sheeley, N. R., Tylka, A., et al. 2012, ApJ, 752, 44
Ruffolo, D. 1995, ApJ, 442, 861
Ruzmaikin, A., Li, G., Zank, G., Feynman, J., & Jun, I. 2005, in Proc. Solar Wind 11-SOHO 16 Connecting Sun and Heliosphere, ed. B. Fleck, T. H. Zurbuchen, & H. Lacoste (ESA SP-592; Noordwijk: ESA), 441
Sauer, H. H. 1993, in Proc. 23rd ICRC, vol. 3, ed. D. A. Leahy, R. B. Hickws, & D. Venkatesan (Singapore: World Scientific), 250
Schellert, G., Wibberenz, G., & Kunow, H. 1985, in Proc. 19th ICRC, vol. 4 (N85-34729 23-92; Baltimore, MD: NASA Goddard Space Flight Center), 305

Shea, M. A., Smart, D. F., Adams, J. H., Jr., et al. 1988, in Proc. Interplanetary Particle Environment Conf., ed. J. Feynman & S. Gabriel (JPL Publ. 88-28; Pasadena, CA: JPL), 3
Simnett, G. M. 2001, SSRv, 97, 231
Simnett, G. M., Roelof, E. C., & Haggerty, D. K. 2002, ApJ, 579, 854
Slavin, J. A., Anderson, B. J., Baker, D. N., et al. 2012, JGR, 117, A01215
Smart, D. F., & Shea, M. A. 1995, in Proc. 24th ICRC, vol. 4, ed. N. Iucci & E. Lamanna (London: IUPAP), 313
Tan, L. C., Reames, D. V., Ng, C. K., Saloniemi, O., & Wang, L. 2009, ApJ, 704, 1753
Vainio, R., Agueda, N., Aran, A., & Lario, D. 2007, in ESWW2, Space Weather: Research Towards Applications in Europe, ed. J. Lilenstein (ASSL, vol. 344; Dordrecht: ESA), 27
Vandas, M., Fischer, S., Geranios, A., et al. 1996, JGR, 101, 21589
Verkhoglyadova, O. P., Li, G., Ao, X., & Zank, G. P. 2012, ApJ, 757, 75
von Rosenvinge, T. T., Reames, D. V., Baker, R., et al. 2008, SSRv, 136, 391
von Rosenvinge, T. T., Richardson, I. G., Reames, D. V., et al. 2009, SoPh, 256, 443
Wibberenz, G., & Cane, H. V. 2006, ApJ, 650, 1199
Zurbuchen, T. H., Raines, J. M., Slavin, J. A., et al. 2011, Sci, 333, 1862

JOURNAL OF GEOPHYSICAL RESEARCH, SUBMITTED XX JANUARY 2014

W. Dröge[1], Y. Y. Kartavykh[1,2], N. Dresing[3], B. Heber[3], and A. Klassen[3]

Wide longitudinal distribution of interplanetary electrons following the 7 February 2010 solar event: observations and transport modeling

Abstract. We analyze a solar electron event that was observed simultaneously by STEREO-A, STEREO-B, and ACE on 7 February 2010. A method to reconstruct the full electron pitch angle distributions from the four SEPT sensors on STEREO-A/B and the EPAM instrument on ACE in the energy range of approximately 60 - 300 keV for periods of incomplete angular coverage is presented. A transport modeling based on numerical solutions of a three-dimensional particle propagation model which includes pitch angle scattering and focused transport is applied to the intensity and anisotropy profiles measured on all three spacecraft. Based on an analysis of intensity gradients observed between the three spacecraft we find that the lateral transport of the electrons occurs partially close to the Sun and partially in the interplanetary medium. For the mean free paths characterizing the electron diffusion parallel and perpendicular to the interplanetary magnetic field we derive values of $\lambda_{\parallel} \sim 0.1$ AU and $\lambda_{\perp} \sim 0.01$ AU. In comparison with results from other particle events we had previously analyzed in a similar manner we discuss whether the diffusion mean free paths parallel and perpendicular to the average magnetic field might be related with each other, and whether the particle transport perpendicular to the average magnetic field is more likely due to particles following meandering magnetic field lines, or due to particles being scattered off individual field lines.

1. Introduction

Solar energetic particles (SEPs) carry fundamental information about properties of the region in which they are accelerated, about the nature of particle acceleration processes in astrophysical plasmas, and about the mechanisms governing their propagation in the interplanetary medium. Observed intensity-time profiles, anisotropies, energy spectra, and elemental and ionic charge compositions are determined by a combination of the above effects. However, by the time the energetic particles have propagated to some distance from the Sun, these effects generally cannot be uniquely unfolded when observed with only one spacecraft, and multi-spacecraft observations of SEPs are therefore of great interest. Such investigations which allowed multipoint measurements with spacecraft located at different longitudes, latitudes and radial distances became possible following the launch of the Voyager and Helios missions in the 1970's and the Ulysses mission in 1990 [e.g., *Dalla et al.*, 2003; *Lario et al.*, 2006]. Multi-spacecraft studies prior to the launch of the STEREO mission in 2006 had the disadvantage that remote sensing measurements were only available from observation points close to the Earth, and that it was thus impossible to identify the active region for all SEP events. The multipoint measurements with the twin spacecraft STEREO-A and STEREO-B with almost identical instrumentation, their separation in solar longitude increasing by $\sim 44°$ per year, the combination with near-Earth particle measurements (e.g., by ACE, SOHO, or Wind) and, in comparison to the earlier missions, much improved remote sensing capabilities from three distinct observation points provide a novel tool for a disentanglement of the above processes.

Generally SEPs are attributed to two distinct acceleration mechanisms [e.g., *Reames*, 1999]: in gradual events particles are energized by large-scale shocks driven by coronal mass ejections (CMEs), whereas in impulse events SEPs are energized on short time scales by magnetic reconnection and/or turbulence in a compact source associated with a solar flare, and are subsequently released into the interplanetary medium without much delay. Impulsive events are also characterized by enhanced ratios of ^{3}He/^{4}He, and of electron-to-proton ratios which can be much larger as those typically observed in gradual events. While the observed wide lateral spread of particles in gradual events can be quite naturally understood in the above picture as due to their acceleration taking place over a large range of magnetic field lines as the shock intersects them close to the Sun, the lateral spread of particles in impulsive events seems to be more intricate. *Reames* [1999] noted that the locations of flares associated with impulsive events are narrowly confined to the western limb of the solar disk, and *Haggerty and Roelof* [2002] found from an examination of ~ 80 impulsive near-relativistic beamlike electron events observed on ACE that the majority of those events were associated with Hα flares observed between W30° and W80°. Both of these findings suggest that in impulsive events particles are injected from the Sun over a limited angular range and follow the Parker spiral magnetic field lines without much lateral propagation in the interplanetary medium. In contrast, *Wibberenz and Cane* [2006] found in a study combining Helios-1/2 and IMP-8 data that energetic electrons associated with impulsive flares could be observed over more than 80° in heliographic longitude. Similar results were reported by *Dresing et al.* [2012] who analyzed simultaneous STEREO-A/B and ACE electron observations following an impulsive flare which occurred on 17 January 2010, and by *Wiedenbeck et al.* [2013] who presented observations of ^{3}He ions which were detected by the two STEREOs and ACE on

[1]Institut für Theoretische Physik und Astrophysik, Universität Würzburg, Würzburg, Germany.
[2]Ioffe Physical-Technical Institute, St. Petersburg, Russia.
[3]Institut für Experimentelle und Angewandte Physik, Universität Kiel, 24118 Kiel, Germany.

0148-0227/14/$9.00

7 February 2010 when a total range in longitudes of $\sim 136°$ was spanned by the three spacecraft. If we assume that magnetic field configurations in the regions surrounding impulsive flares do not differ strongly from one event to another the question arises whether the apparent differences in the longitudinal spread of particles is not caused by varying propagation conditions in the interplanetary medium. The stochastic component of the particle transport in the heliospheric magnetic field is on the one hand determined by pitch-angle scattering which gives rise to spatial diffusion along the field and can be characterized by a parallel mean free path $\lambda_\parallel$, and on the other hand by diffusion perpendicular to the average magnetic field (characterized by a perpendicular mean free path $\lambda_\perp$) due to particles following meandering field lines or due to particle motion across the field by turbulent drift or scattering. For solar particles $\lambda_\perp$ can be determined from simultaneous observations on several spacecraft distributed in heliospheric longitude and latitude and some assumptions about the lateral variation of their injection at the Sun, or from intensity gradients perpendicular to the mean magnetic field convected with the solar wind past a single spacecraft.

The amount of perpendicular diffusion of particles moving in the heliospheric magnetic field is often discussed in terms of the ratio $\lambda_\perp/\lambda_\parallel$. Single spacecraft observations of sharp cross field gradients in the intensity profiles of low-energy ions in impulsive solar particle events which are observed as 'dropouts' [e.g., *Mazur et al.*, 2000; *Chollet and Giacalone*, 2011] and 'cutoffs' [*Dröge et al.*, 2010] indicate ratios of the order of $\sim 10^{-4}$. The modulation of galactic cosmic rays, observations of Jovian electrons [*Conlon78*, 1978] have suggested a ratio of $\sim 10^{-2}$. Recent numerical simulations also seem to indicate larger values of $\lambda_\perp/\lambda_\parallel \sim 0.02 - 0.05$ [e.g., *Matthaeus et al.*, 2003]. Even ratios as large as ~ 1, deduced from anisotropy measurements during co-rotating interaction region events [*Dwyer et al.*, 1997] have been reported. The considerations of the perpendicular mean free path in terms of ratios of $\lambda_\perp$ to $\lambda_\parallel$, and suggestions from advanced transport models [e.g., *Shalchi*, 2013, and references therein] may create the impression that $\lambda_\perp$ generally increases monotonically with $\lambda_\parallel$, and that the above variations could be explained by a proportionality factor relating the two parameters which varies between solar events, as a function of radial distance from the Sun, or of the particles' rigidity. However, one might ask whether that concept would reflect the true nature of diffusion parallel and perpendicular to the average magnetic field, or whether other relations between $\lambda_\perp$ and $\lambda_\parallel$ could be possible. In this context it is interesting to note that the occurrence of sharp intensity gradients across the field in solar particle events seems to be correlated with large parallel mean free paths, and that the observed values of $\lambda_\parallel$ in the wide-spread events analyzed by *Wibberenz and Cane* [2006] and *Dresing et al.* [2012] are, for electrons, comparatively small, in contrast to the beam-like electrons reported in the study by *Haggerty and Roelof* [2002]. Multi-spacecraft observations of solar particle events offer the possibility to study $\lambda_\perp$ and $\lambda_\parallel$ *independently* of each other, and thus can be employed to elucidate the nature of the transport perpendicular to the interplanetary magnetic field. Electrons from impulsive flares are particularly suited for this task because they, unlike ions of which the transport is often strongly influenced by CMEs and coronal and interplanetary shock waves, have a reasonably high probability that their transport takes place in a more or less regular heliospheric magnetic field. A period during which the above criteria were fulfilled occurred in the first two weeks of February 2010 when a series of electron events were observed by the two STEREOs and ACE. In this work we present a detailed analysis of the event on 7 February which provided the best overall data coverage on all three spacecraft.

The structure of the paper is as follows. In Section 2 we give an overview of the particle detectors on ACE and STEREO used for this study. In Section 3 we present observations of interplanetary electron fluxes, solar wind parameters, and of electromagnetic radiation from the Sun made during the particle event of 7 February 2010. In Section 4 we discuss a method on how to reconstruct pitch-angle distributions and omnidirectional intensities for periods of incomplete angular coverage of the particle detectors. In Section 5 we introduce the formalism to describe the three-dimensional pitch-angle dependent transport of solar particles in the inner Heliosphere. In Section 6 we present results of the transport modeling for two scenarios of the lateral spread of the electrons. Finally, Section 7 discusses the implications of our results with regard to a possible relation between the particles' diffusion coefficients parallel and perpendicular of the magnetic field and summarizes our conclusions.

2. Instrumentation

The particle data used in this work are from the SEPT instrument [*Müller-Mellin et al.*, 2008] of the IMPACT suite [*Luhmann et al.*, 2008] on board STEREO and from the EPAM instrument on board ACE [*Gold et al.*, 1998]. The Solar Electron and Proton Telescope (SEPT), one of four instruments of the Solar Energetic Particle (SEP) suite for the IMPACT investigation on board STEREO, is designed to provide the three-dimensional distribution of energetic electrons and protons with good energy and time resolution. This knowledge is essential for characterizing the dynamic behaviour of CME associated and solar flare associated events.

SEPT consists of two dual double-ended magnet/foil particle telescopes which cleanly separate and measure electrons in the energy range from 30 - 400 keV and ions from 60 keV/n to 7 MeV/n. The dual set-up (sketched in Fiure. 1 top) refers to two adjacent sensor apertures for each of the four view directions: one for ions, one for electrons. The double-ended set-up refers to the detector stack with view cones in two opposite directions: one side (electron side) is covered by a thin foil (marked in red in Figure 1), the other side (ion side) is surrounded by a magnet (magenta block in Figure 1).

Each double-ended telescope has two solid state detectors (SSDs) which are operated in anti-coincidence (green bars in Figure 1). One SSD looks through an absorption foil and its partner through the air gap of a magnet system. The foil leaves the electron spectrum essentially unchanged but stops ions of energies less than ~ 400 keV/n. The magnet is designed to sweep away electrons below 400 keV, but leaves ions unaffected. In the absence of > 400 keV/n ions, the foil SSD only detects electrons, and the magnet SSD only detects ions. Ions from 400 keV/n to 7 MeV/n will stop in the magnet SSD and their fluxes will be cleanly measured. The contribution of > 400 keV/n ions to the foil SSD can then be computed and subtracted to obtain the electron fluxes. Each SSD is equipped with its own guard ring for background reduction.

Anisotropy information on a non-spinning spacecraft is acquired in four look directions: SEPT-E observes in the ecliptic plane along the nominal Parker spiral magnetic field direction both forward and backward, SEPT-N/S observes perpendicular to the ecliptic plane towards North and South. To warrant unobstructed fields of view, the full angle of the viewing cones is limited to 52 degrees and SEPT-N/S is mounted on its own mounting bracket. The view cones of the four telescopes on a sphere are shown in the bottom of Figure 1. The geometrical factor for each of the four magnet telescopes is 0.17 cm^2 sr, and for each of the four foil telescopes 0.13 cm^2 sr.

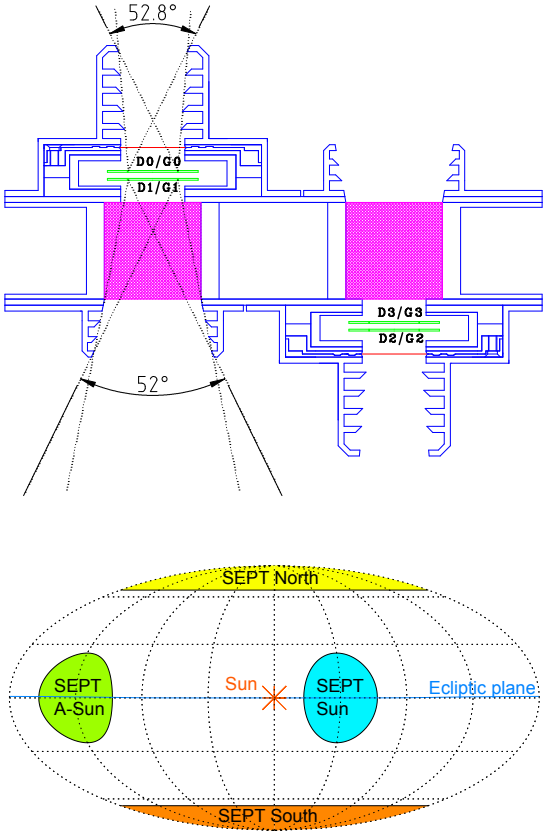

Figure 1. Upper panel: schematic outline of the SEPT telescopes on board STEREO. Detection elements are silicon detectors (D0 - D3, green) with guard rings (G0 - G3), Parylene foils (red), and magnetic fields perpendicular to the drawing plane (magenta). Lower panel: fields of view of the SEPT North/South and Sun/Anti-Sun telescopes (adopted from *Müller-Mellin et al.* [2008]).

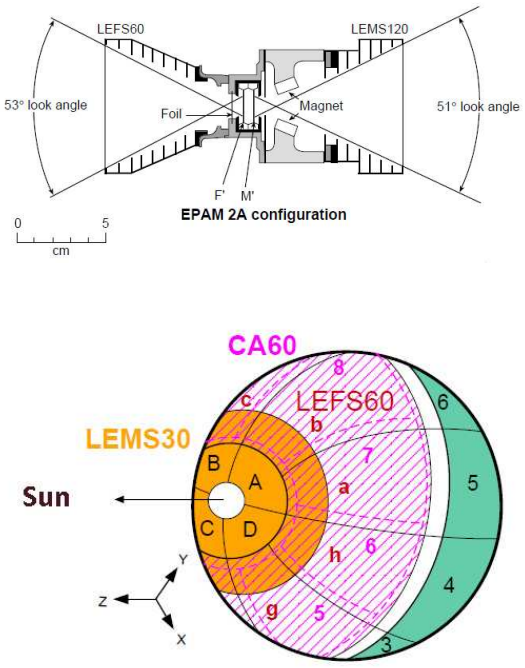

Figure 2. Upper panel: schematic outline of the LEFS60 and LEFS150 telescopes of the EPAM instrument onboard ACE. Lower panel: fields of view of the EPAM telescopes (adopted from *Gold et al.* [1998]).

Electron measurements close to Earth used in this work have been obtained with the EPAM instrument [*Gold et al.*, 1998] on board the Advanced Composition Explorer (ACE). ACE is a spin-stabilized spacecraft which rotates about an axis directed within 20° of the Sun and a spin period of 12 s. EPAM is designed to make measurements of ions and electrons over a broad range of energy and intensity with five separate solid-state detector telescopes that provide nearly full coverage of the unit sphere. In this study we use high-resolution electron data obtained by the LEFS60 telescope which deploys an aluminized Parylene foil, nominally 0.35 mg cm^{-2} thick, to absorb ions with energies below approximately 350 keV/n while allowing electrons with energies above 45 keV to pass through to a solid-state detector. A schematic of the LEFS60 and LEMS120 telescope is shown in Figure 2 (top). The LEFS60 telescope provides four electron channels between 45 and 312 keV and eight directional sectors The bottom of the figure shows the view cones covered by the different sensors of EPAM on a sphere.

3. Observations

A sequence of interplanetary particle events was produced in the beginning of February 2010 by active region (AR) 11045 which emerged rapidly with increased activity on the solar disc at the end of February 5, showing a very fast developing from few small spots to a large sunspot group on February 7. Figure 3 shows observations of energetic electrons and solar wind parameters obtained on STEREO-B, ACE, and STEREO-A during the period of February 7 through February 10. The events were observed by all three spacecraft, with decreasing intensity from STEREO-B over ACE to STEREO-A following the wider longitudinal separation to the parent AR as displayed in Figure 4 (left panel). Below the energetic electron intensities, the panels show magnetic field azimuthal and longitudinal angles, magnetic field magnitude, solar wind density and solar wind speed, respectively. STEREO-B and ACE observations during the period between February 7 to 10 indicate a slow and quiet solar wind with speeds $\leq$ 500 km/s. STEREO-B observed also low solar wind densities and magnetic field strengths, not showing any ICME or CIR associated structures or in-situ shocks. Although STEREO-A detected higher solar wind speeds up to $\sim$ 600km/s, and higher density and magnetic field strengths during the beginning of the period, no specific structures can be identified in the data. Only a small density increase is observed during the onset of the electron event on early 7 February. In contrast to the STEREO observations the solar wind conditions are more complicated at ACE. A small compression in density at the end of 7 February followed by a rotation in magnetic field angles and increasing magnetic field magnitude lasting up to the end of 9 February, appears as signature of a transient structure. This structure is also listed in the ACE ICME (interplanetary CMEs, www.srl.caltech.edu/ACE/ASC/DATA-/level3/icmetable2.htm) list as an ICME propagating with a speed of 370 km/s. Due to this rather low speed and the absence of an in-situ shock we suspect this ICME to play a minor role for the events. ACE solar wind density data have been complemented by SOHO/CELIAS data (orange trace) to fill the data gaps in ACE observations.

In the following we focus on the event on 7 February 2010 which provided the best overall electron observations

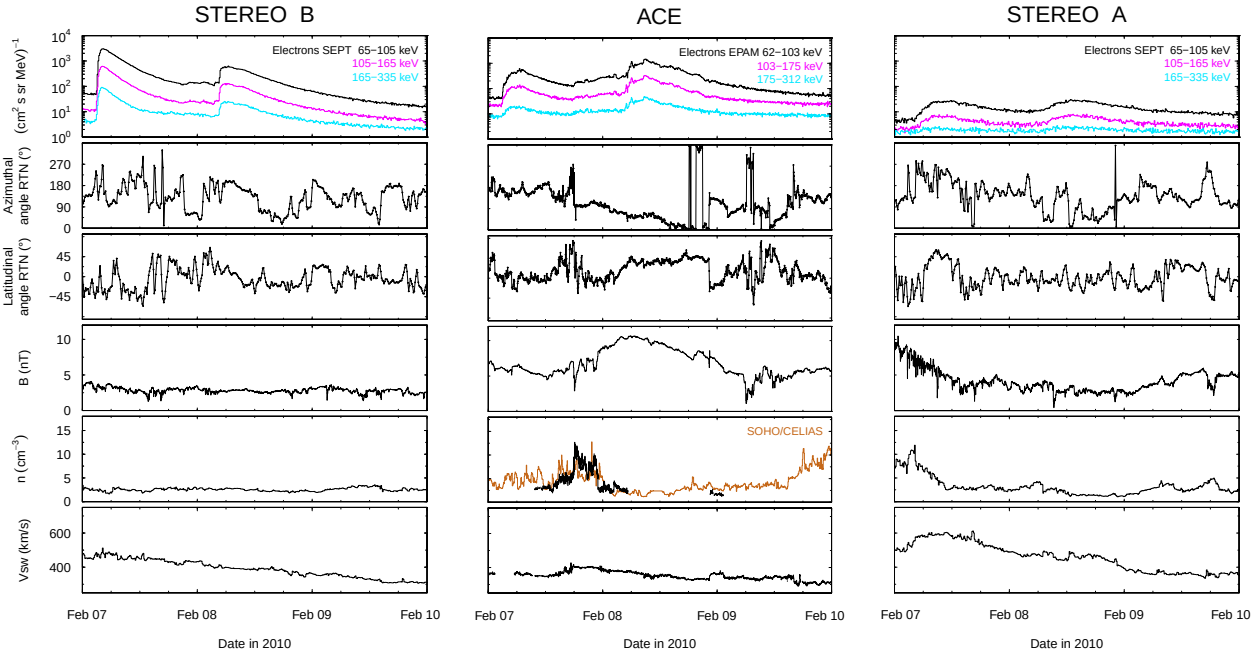

Figure 3. In-situ measurements by STEREO-B (left), ACE (middle) and STEREO-A (right). From top to bottom: electron intensities, magnetic field azimuthal and latitudinal angles, magnetic field magnitude, solar wind density and speed. Due to data gaps in ACE solar wind density, SOHO/CELIAS measurements have been added.

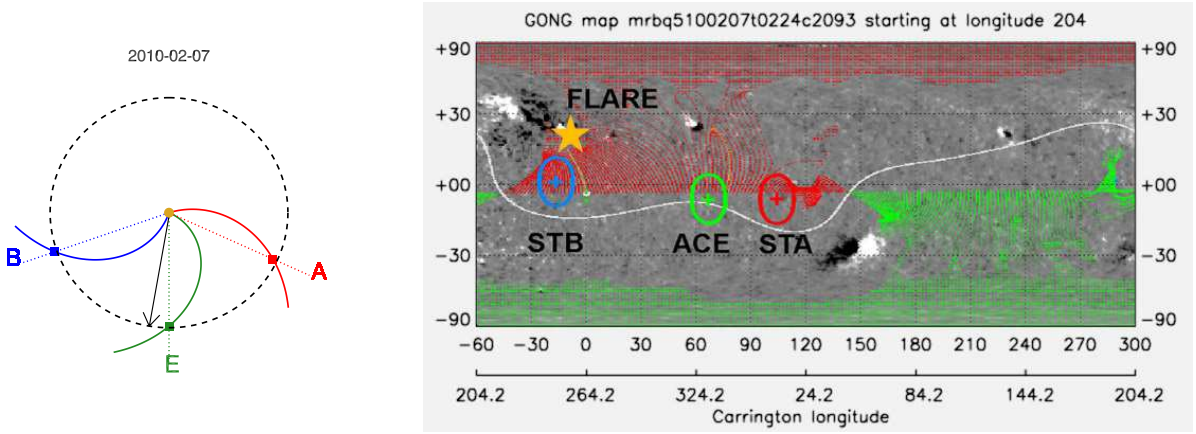

Figure 4. Left panel: Longitudinal positions of ACE, STEREO-A and STEREO-B on 7 February 2010. The flare longitude is marked by the black arrow. Right panel: Synoptic Ecliptic Plane Field Plot overlying a magnetogram map by the Global Oscillation Network Group (GONG) for Carrington rotation 2093. Also marked are the estimated positions of the magnetic footpoints of the three spacecraft and the position of the flare.

on the three spacecraft. The sketch in the left panel of Figure 4 shows the positions of the three spacecraft at this time, spanning 136° in longitude. Also shown are the magnetic field lines connecting the Sun and the spacecraft which were obtained assuming a Parker magnetic field. Similarly, the longitudes Φ of the magnetic footpoints were determined according to $\Phi = \Phi_0 + \Omega \cdot r/V_{SW}$, where r and Φ_0 denote the radial distances and projected longitudes of the spacecraft, respectively, Ω is the solar rotation frequency, assumed to correspond to a siderial rotation period of 25.5 days, and V_{SW} is the solar wind speed taken at the time of the event onset at the respective spacecraft. The right panel of Figure 4 shows a Potential Field Source Surface (PFSS) Carrington map overlying a magnetogram map of Carrington rotation 2093, provided by the Global Oscillation Network Group (GONG, http://gong.nso.edu/). The white wavy line represents the neutral sheet, separating the negative polarity sector (marked in red) from the positive polarity sector (marked in green). The plus signs mark the extrapolated positions of the magnetic footpoints for the STEREOs and ACE, respectively, the surrounding circles indicate the uncertainty in the extrapolation [cf., *Nolte and Roelof*, 1973]. The particle event on 7 February 2010 was associated with an M6.4/1N X-ray/optical flare at ∼ N21 E10 (see Figure 5, marked by the orange star in Figure 4), an EIT wave, a slow halo CME as observed from LASCO/SOHO and a filament loop-like cold plasma eruption seen mainly in 304 Åfrom STEREO-A/B.

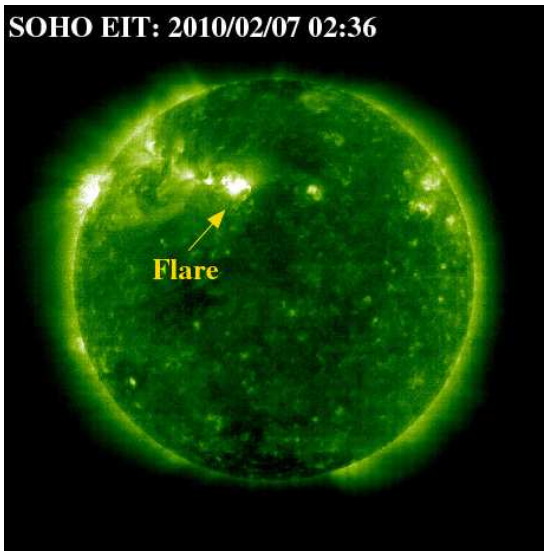

Figure 5. SOHO EIT extreme ultraviolet observations during the flare maximum on 7 February 2010 at 02:36 UT. The location of the flare is indicated by the arrow.

At that time STEREO-A and STEREO-B were separated from the Earth-Sun line at 65 and 71 degrees, respectively. The flare, located close to the east/west limb for STEREO-A/STEREO-B (see Figure 4), and close to the central meridian for SOHO was first detected at 02:23 UT by the EUVI instrument on STEREO-B in the 195 Åband. While the CME observed from LASCO/SOHO - due to the projection effect - shows a halo structure moving with a speed of 420 km/s, the CME angular width as viewed from STEREO-A/B, was rather narrow ($\leq$ 75 degrees, see Figure 6) with a slightly higher speed of 570 km/s, practically without a projection effect. According to the LASCO CME catalog (http://cdaw. gsfc.nasa.gov/CME_list/), at least five CMEs were launched from the Sun during the three days before the February 7 particle event occurred. All the preceding CMEs had mostly small angular widths below 97 degrees and low velocities below 659 km/s. The fastest CME (with V=659 km/s) on February 5 was very narrow, with an angular width of 7 degrees. The broadest CME (97 degrees) on February 6 was very slow with a speed of 240 km/s, and originated from the same AR as the CME associated with the SEP event discussed here. According to Jian et al. (http://www-ssc.igpp.ucla.edu/forms/stereo/stereo_level_3.html) and the SOHO Proton Monitor shock list (http://umtof.umd.-edu/pm/FIGS.HTML) no in-situ shocks were observed on STEREO and SOHO during the period from February 5 - 13. A flare associated EIT wave was detected from all three s/c, propagating mainly towards the south-west direction from the flare site. During its propagation the EIT wave crossed the magnetic footpoint connecting the flare site with STEREO-B. While it weakened rapidly it arrived at the magnetic footpoint of ACE, and disappeared well before it could have arrived at the footpoint of STEREO-A. The flare was also accompanied by coronal and IP type III radio bursts occurring between 02:30 and 02:41 UT (as will be shown in Figure 9) at frequencies below 150 MHz, and by a drifting type IV radio burst at 02:38-03:05 UT above 150 MHz (not shown). Radio signatures of a type II burst were detected neither in the corona nor in the interplanetary medium, suggesting that the associated CME was too slow to drive a shock wave.

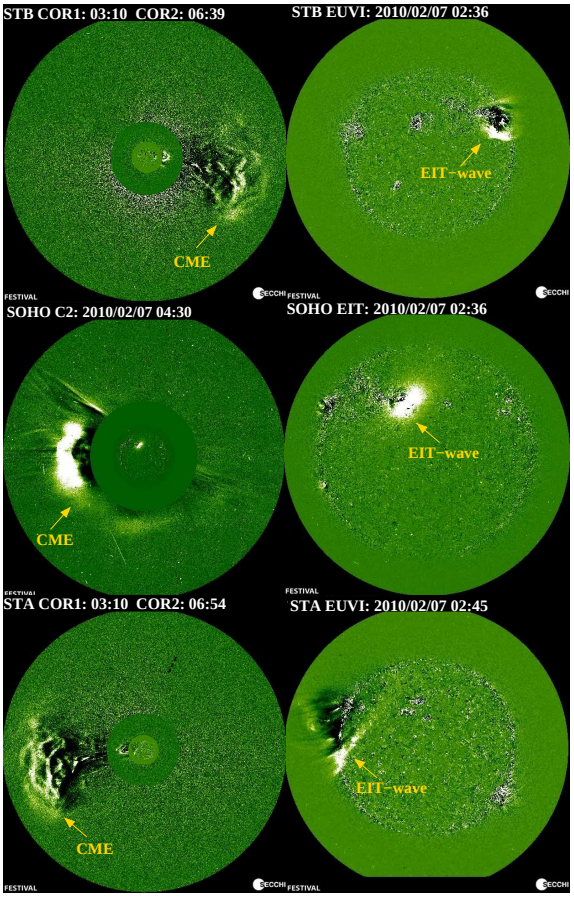

Figure 6. STEREO and SOHO observation of the EIT wave and the CME on 7 February 2010. Left: EUVI 195 A, EIT 195 A, COR1, LASCO C2 and COR2 from STEREO-B, SOHO and STEREO-A running difference images showing the CME structure. Right: EIT 195 A running difference images of the EIT wave.

4. Data Analysis

For resolving the various effects which determine the transport of the energetic electrons from their source at the Sun to the three spacecraft it would not be sufficient to only to consider sector averaged intensities. We have to make an attempt to reconstruct - as best as possible - the pitch angle distributions (PADs) at the locations of the involved spacecraft. With $\mu = \cos\vartheta$ as the particle's pitch angle cosine and $f(\mu, t)$ as the local pitch angle distribution, the omnidirectional intensity can be computed by integrating $f(\mu, t)$ over the range -1 $\leq \mu \leq$ 1, and a first-order anisotropy parallel to the mean magnetic field can be defined as

$$A_{1p}(t) = \frac{3\int_{-1}^{+1} d\mu\, \mu\, f(\mu, t)}{\int_{-1}^{+1} d\mu\, f(\mu, t)} \qquad (1)$$

Figure 2 shows that the LEFS60 telescope on board ACE samples an annulus centered at 60° ($\pm$ 25°) to the ACE spin axis. As a result the LEFS60 telescope, unlike similar instrumentation on e.g., the Wind spacecraft [3DP solid state telescopes, *Lin et al.*, 1995] does not always provide a full coverage in pitch angle space. A nearly complete coverage is only achieved when the average local magnetic field direction is approximately perpendicular to the ACE spin axis.

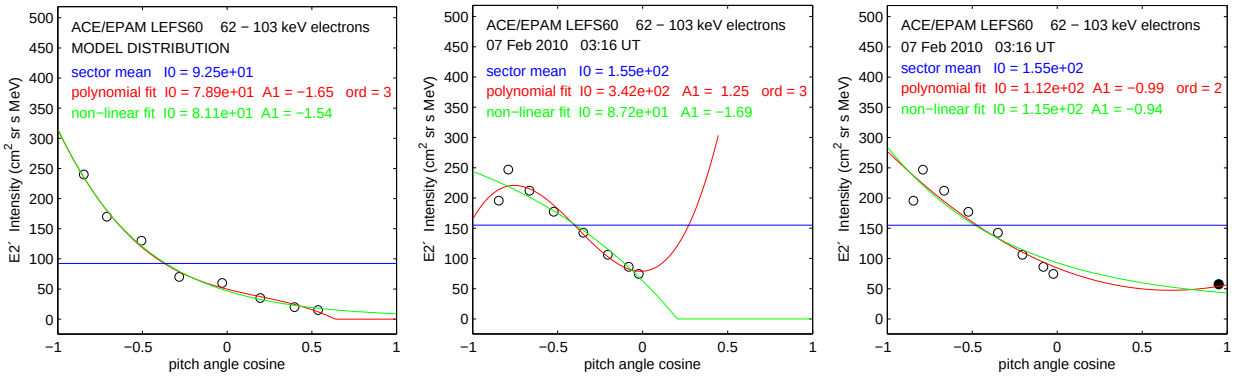

Figure 7. Reconstruction of ACE/EPAM electron pitch angle distributions. Left panel shows a pitch angle distribution which is typical for the onset of solar electron events and which was observed at a time for which the pitch angle coverage was good. Middle panel shows a pitch angle distribution which was observed at a time for which the pitch angle coverage was incomplete (only the hemisphere in which particles are streaming away from the Sun) and fits do not give meaningful results. Right panel shows resconstructed pitch angle distribution obtained by adding an artificial ninth data point at $\mu = 0.95$.

For a nominal interplanetary magnetic field ($\sim 45°$ angle between the magnetic field direction and the ACE spin axis the pitch angle coverage is already significantly reduced, and for an interplanetary magnetic field direction close to the spin direction an evaluation of pitch angle distributions is not possible anymore. For reconstructing the pitch angle distributions, and to infer omnidirectional intensities and first order anisotropies from them, we have tried to fit them with polynomials of second and third order, and also with a non-linear function with two linear (c_1, c_2) and one nonlinear parameter (c_3) of the form

$$f(\mu) = c_1 + c_2 \cdot \exp(c_3 \cdot \mu) \qquad (2)$$

which resembles properties of theoretical predictions [e.g., *Kunstmann*, 1979]. It is interesting to note that - above a certain threshold - the relative size of the wiggles in the observed ACE/STEREO intensity profiles (cf., Figure 3) does not decline in a way as one would expect due to the increasing count statistics after the onset of the event. It seems likely that these intensity fluctuations, and related fluctuations in the angular distributions, are rather caused by fluctuations in the solar wind magnetic field perpendicular to the mean direction, leading to different parallel propagation conditions for the particles in neighboring flux tubes, as they are swept past the spacecraft. For our fitting method this has the consequence that we cannot reasonably assign error bars to the intensity values at the various pitch angle bins. Therefore we decided to give each intensity value the same statistical weight in the fit.

Figure 7 (left panel) shows a pitch angle distribution which is typical for the onset of solar electron events and for a good pitch angle coverage. Polynomial and nonlinear fits to the pitch angle distribution and the calculations of the resulting omnidirectional intensities and anisotropies were performed by approximating the integral in equation (1) by a sum over 200 grid points. To avoid unphysical results, negative intensity values were set to zero. Both 3rd-order polynomial and non-linear fit resemble the shape of the pitch angle distribution well. The omnidirectional intensities predicted by the fits are $\sim 15\%$ lower than the sector averages which are not equally distributed in pitch angle and give larger intensity values a higher statistical weight. The predicted anisotropies from both fits are in good agreement.

The middle panel of Figure 7 shows a pitch angle distribution observed by ACE/EPAM during the rising phase of the 7 February 2010 event. Here the data points only cover the range $-1 < \mu < 0$, and both of the above test functions do not give meaningful fits. To find out whether in general fits with polynomials of order 2 or 3, or with the non-linear function (2) would give better results, we performed a study with pitch angle distributions for which we required that there were at least two data points in each hemisphere. However, no clear picture about which of the three fit functions would be best suited emerged. We therefore attempted a fitting procedure which assumes that the particle flux is always directed away from the Sun. This implies that the particles are injected close to the Sun, and that downstream of the observer there are neither particles which are reflected at an obstacle nor particles which reach the connecting field line due to perpendicular diffusion and move in the solar direction. In this case the pitch angle distributions are always monotonic, with a minimum towards the solar and a maximum towards the anti-solar direction. In accordance with the above hypothesis we added an artificial data point to the distribution at $\mu = 0.95$, with an intensity obtained from the average of the nearest (in μ) data point and the pre-event background, assumed to be isotropic. We found that in almost all cases of incomplete coverage this method stabilized the fit (see Figure 7, right panel), and allowed to obtain omindirectional intensities and anisotropies in a reproducible manner. In the case of good coverage the additional data point usually did not change the fit significantly.

Similar problems with the pitch angle coverage also arise in the reconstruction of pitch angle distributions observed by the SEPT instrument on the two STEREO spacecraft. Due to the viewing directions of the four particle telescopes the coverage is always symmetric with respect to $\mu = 0$. However, varying directions of the interplanetary magnetic field with respect to the spacecraft orientation can result in differing widths of the coverage, and in differing spacings between the two data points at positive and negative values of $\mu = 0$, respectively. The pitch angle distribution shown in the left panel of Figure 8, recorded on STEREO-B during the rising phase of the 7 February 2010 event, exhibts a coverage which allows a good reconstruction of the omnidirectional intensity and the anisotropy, by both the polynomial and the non-linear fit. The middle panel of the figure shows a pitch angle distribution recorded on STEREO-A where the non-linear fit obviously produces an unphysical result, and the polynomial fit also does not provide an optimal reconstruction of the pitch angle distribution. To stabilize

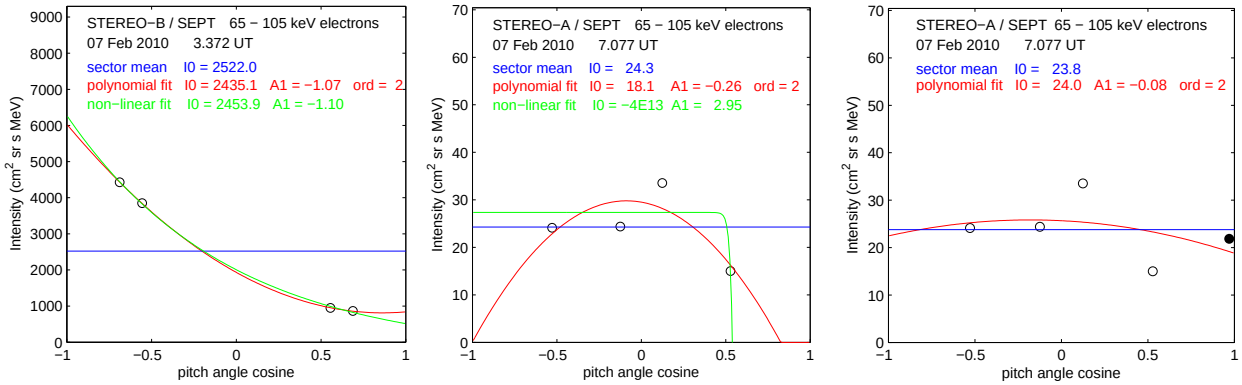

Figure 8. Reconstruction of STEREO-SEPT electron pitch angle distributions. Left panel shows a pitch angle distribution which is typical for the onset of solar electron events and which was observed at a time for which the pitch angle coverage was good. Middle panel shows an observation at a time during which the the pitch angle distribution was inhomogeneous, the coverage was incomplete (only central region), and fits do not give meaningful results. Right panel shows a resconstructed pitch angle distribution obtained by adding an artificial fifth data point at $\mu = 0.95$.

the fit, we have added an artificial fifth data point to the STEREO/SEPT pitch angle distribution, in a similar manner as for the reconstruction of the ACE/EPAM pitch angle distributions (right panel of Figure 8).

5. Interplanetary Transport

The properties of solar particle events observed in the inner Heliosphere reflect the combination of a number of physical processes. For particles originating from solar flares these processes include acceleration in the flaring region, some kind of lateral transport in the solar corona to a magnetic field line connected with the observer, and transport in the solar wind. In the undisturbed solar wind, i.e., in the absence of CMEs and shocks, the latter can usually be described as adiabatic motion along the average interplanetary magnetic field [assumed to be an Archimedian spiral, see *Parker*, 1963] and pitch angle scattering off the fluctuations superimposed on the field. Particle drifts perpendicular to the average field arise due gradients and curvature in the field, and bye the action of an induced electric field, $\boldsymbol{E} = \boldsymbol{V}_{sw} \times \boldsymbol{B}$, where $\boldsymbol{V}_{sw}$ is the solar wind velocity and $\boldsymbol{B}$ denotes the magnetic field [co-rotation, *Ng and Gleeson*, 1971]. Diffusion perpendicular to the average magnetic field is caused by interactions with magnetic fluctuations which scatter the particles' gyrocenter from one field line to another, and due to particles propagating along meandering field lines [e.g., *Jokipii and Parker*, 1969; *Matthaeus et al.*, 2003]. *Marsh et al.* [2013] suggested that also the combined effects of drifts and pitch angle scattering can lead to diffusion across the magnetic field. Depending on particle species and energy, also convection and energy losses in the interplanetary medium can be of importance for the transport process. In recent years it has become clear [e.g., *Dröge*, 2005] that during most impulsive solar particle events interplanetary scattering is weak and a theory based on pitch angle dependent transport, rather than on spatial diffusion, should be used to describe the particle transport along the interplanetary magnetic field. Transport equations for the evolution of the particle's gyro-averaged phase space density $f(\boldsymbol{r}, p, \mu, t)$ (where $\boldsymbol{r}$ is the location in the Heliosphere relative to the center of the Sun, t is the time, and p and $\mu = \cos\vartheta$ denote the particles' momentum and pitch angle cosine, respectively) which include all the above effects have been presented by *Zhang et al.* [2009] and *Dröge et al.* [2010].

Note that $f(\boldsymbol{r}, p, \mu, t)$ is proportional to the measured flux or intensity of the particles, $I(\boldsymbol{r}, E, \mu, t)$, here formulated as function of the kinetic energy E, which is usually the observable. In the most general case the quantitative treatment of the evolution of the particle's gyro-averaged phase space density $f(\boldsymbol{r}, \mu, p, t)$ at the location $\boldsymbol{r}$ can be cast into the form

$$\frac{\partial f}{\partial t} = -\mu v \boldsymbol{b}\cdot\boldsymbol{\nabla} f - \frac{1-\mu^2}{2L} v \frac{\partial f}{\partial \mu} - \frac{\partial}{\partial \mu}\left(D_{\mu\mu}(\mu)\frac{\partial f}{\partial \mu}\right) + Q(\boldsymbol{r}, \mu, p, t) \quad (3a)$$

$$- (\boldsymbol{V}_{sw} + \boldsymbol{V}_d)\cdot\boldsymbol{\nabla} f - \left[\frac{\mu(1-\mu^2)}{2}(\boldsymbol{\nabla}\cdot\boldsymbol{V}_{sw} - 3\boldsymbol{bb} : \boldsymbol{\nabla}\boldsymbol{V}_{sw})\right]\frac{\partial f}{\partial \mu} \quad (3b)$$

$$+ \left[\frac{1-\mu^2}{2}(\boldsymbol{\nabla}\cdot\boldsymbol{V}_{sw} - \boldsymbol{bb} : \boldsymbol{\nabla}\boldsymbol{V}_{sw}) + \mu^2 \boldsymbol{bb} : \boldsymbol{\nabla}\boldsymbol{V}_{sw}\right] p\frac{\partial f}{\partial p} \quad (3c)$$

$$+ \boldsymbol{\nabla}\cdot(\boldsymbol{D}_\perp \boldsymbol{\nabla} f) \quad (3d)$$

Here v is the particle speed, $\mu = \cos\vartheta$ the particle pitch angle cosine, t the time, and $\boldsymbol{b} = \boldsymbol{B}/B$ a unit vector in the direction of the average magnetic field $\boldsymbol{B}$. The focusing of particles due to the divergence of the magnetic field is described by $L(\boldsymbol{r}) = -(\boldsymbol{b}\cdot\boldsymbol{\nabla}\ln B(\boldsymbol{r}))^{-1}$. The stochastic forces are taken into account through the pitch angle diffusion coefficient $D_{\mu\mu}(\mu)$ and the tensor $\boldsymbol{D}_\perp(\boldsymbol{r}, p, \mu)$ which describes the diffusion of particles in the two dimensions perpendicular to the average magnetic field direction. The injection of particles close to the Sun is given by $Q(\boldsymbol{r}, \mu, p, t)$. The symbol " : " denotes a tensor contraction, e.g., $\boldsymbol{bb} : \boldsymbol{\nabla}\boldsymbol{V} = b_i b_j \partial V_i/\partial x_j$ where a summation is performed over similar indices. Higher-order terms in V_{sw}/v have been neglected in equation (3), and the variables are written in mixed reference frames, with the spatial coordinates in a fixed frame, and particle momentum and pitch

angle in the solar wind frame [e.g., *Ruffolo*, 1995]. If the scattering is sufficiently strong, $f(\boldsymbol{r},\mu,p,t)$ adjusts rapidly to a nearly isotropic distribution, and the solutions of equation (3) become similar to those of a spatial diffusion model [*Parker*, 1965]. The mean free path $\lambda_\parallel$ which relates the pitch angle scattering rate to the spatial diffusion parallel to the ambient magnetic field is given by [*Hasselmann and Wibberenz*, 1968]

$$\lambda_\parallel \;=\; \frac{3v}{8}\int\limits_{-1}^{+1} d\mu\;\frac{(1-\mu^2)^2}{D_{\mu\mu}(\mu)} \tag{4}$$

The mean free path is often used as a convenient parameter to characterize the varying degrees of scattering from one solar particle event to another, even when it adopts values close to or larger than the observers's distance from the Sun and the transport process can not be considered as spatial diffusion. A radial mean free path can be defined in a similar manner as $\lambda_r = \lambda_\parallel \cos^2\psi$, where $\psi(r)$ is the angle between the radial direction and the magnetic field. For modelings of observed particle data often a power law dependence of the pitch angle diffusion coefficient, or the corresponding mean free path, as a function of radial distance from the Sun is assumed, e.g., $\lambda_r \propto r^b$. A *pitch-angle dependent* perpendicular mean free path $\Lambda_\perp(\mu)$, and a related perpendicular diffusion coefficient $D_\perp(\mu)$ can be defined from the diagonal elements of $\boldsymbol{D}_\perp(\boldsymbol{r},p,\mu)$ according to [*Schlickeiser*, 2002]

$$\Lambda_\perp(\mu) = 3/v\cdot D_\perp(\mu) = 3/v\cdot[D_{xx}(\mu)+D_{yy}(\mu)] \tag{5}$$

The *spatial* perpendicular diffusion coefficient $K_\perp$ and mean free path $\lambda_\perp$ which are used in diffusion-convection transport models for isotropic distribution functions, and describe the combined transport effects due to magnetic field line and gyro-center diffusion, are then given by the μ-average

$$K_\perp \;=\; \frac{v\lambda_\perp}{3} \;=\; \frac{1}{2}\int\limits_{-1}^{+1} d\mu\; D_\perp(\mu) \tag{6}$$

Besides trying to solve equation (2) with numerical methods, it is also possible to treat the transport problem by means of Monte-Carlo simulations. For this purpose the Fokker-Planck equation (3) has to be recast in a number of corresponding Ito stochastic differential equations [SDEs, cf., *Gardiner*, 1983]. The resulting three SDEs, one each for the pitch-angle, spatial and momentum transport can then be solved with Euler or Runge-Kutta schemes. Their solutions can be viewed as trajectories of quasi-particles, and the number of quasi-particles which are present in a volume element around a location $\boldsymbol{r}$ during a time period from t to $t+\Delta t$ is a measure for $f(\boldsymbol{r},\mu,p,t)$. Somewhat different approaches in the implementation of the stochastic processes and in the treatment of momentum losses in the pitch-angle dependent transport of solar particles have been used. *Qin et al.* [2006] studied parallel transport using a time-backward Markov stochastic process method. Here particles are injected at $(\boldsymbol{r},t)$, traced back to the initial time, and only those particles in the source region at that time then contribute to the statistics. Momentum changes are treated explicitely through the corrsponding SDE. Further investigations of pitch-angle dependent transport parallel to $\boldsymbol{B}$ [e.g., *Kocharov et al.*, 1998; *Kartavykh et al.*, 2007; *Dröge and Kartavykh*, 2009] used a time-forward stochastic process method where particles are injected at the source and counted at $(\boldsymbol{r},t)$. Here the particles are traced in two reference frames: the local solar wind frame, in which the particles are scattered at magnetic fluctuations which are assumed to be static, and a corotating frame in which advection and focusing are considered. The effects of adiabatic losses in a diverging flow of scattering centers and of convection due to the isotropization of the particle distribution in the system moving with the solar wind are treated implicitely by obeying the proper Lorentz transformations between the different systems for the quasi-particle.

The effects of diffusion perpendicular to the magnetic field on intensity-time profiles at locations with various longitudinal and latitudinal distances to the injection region at the Sun were studied by *Zhang et al.* [2009] who used a time-backward stochastic process with an explicite scheme, and *Dröge et al.* [2010] who used a time-forward stochastic process with an implicite scheme. We find that the second of the two SDE approaches outlined above is better suited to get an overview about the spatial distribution of flare particles in the inner heliophere, and therefore have adopted it in this study. Accordingly, the SDE for the momentum transport is omitted and only the following two SDEs are left:

$$d\boldsymbol{r}(t) = \mu v dt\boldsymbol{b} + \sqrt{2\boldsymbol{D}_\perp}\,d\boldsymbol{W}_\perp(t) + \boldsymbol{\nabla}\boldsymbol{D}_\perp dt \tag{7}$$

$$d\mu(t) = \sqrt{2D_{\mu\mu}}\;dW_\mu(t) + \left[\frac{v}{2L}(1-\mu^2) + \frac{\partial D_{\mu\mu}}{\partial\mu}\right]dt \tag{8}$$

which can be solved by means of Monte-Carlo simulations. $W_\mu(t)$ and $\boldsymbol{W}_\perp(t)$ denote one- and two-dimensional Wiener processes, respectively. Our simulations require transformations between several coordinate systems: i) the Heliocentric Inertial (HCI) system in which Z is the solar rotation axis, X the solar ascending node on the ecliptic, and Y the third orthogonal axis. We assume that in this system the Sun rotates as a rigid body with an angular velocity Ω, corresponding to a rotation period of 25.5 days, and that the resulting interplanetary magnetic field has the form of Archimedian spirals [*Parker*, 1963]. ii) the co-rotating system which rotates around the Z-axis of system i) with the angular velocity Ω. In this system the solar wind velocity is parallel to the magnetic field. iii) the co-moving system which moves with the solar wind velocity in system ii). In this system one axis is tangential to the magnetic field line at a given location, the second is normal to the field line and the third orthogonal to the former two. iv) the Heliocentric Earth Equatorial (HEEQ) system in which compared to the HCI system the coordinate X is replaced by the intersection of the solar equator and the solar meridian as seen from Earth. The effects of convection and adiabatic energy losses in the expanding solar wind can be accounted for by obeying the correct kinematic transformations between the above coordinate systems, although we neglect them here because of the high speeds of the electrons considered, compared to the solar wind speed. We do take into account the effect of corotation. For further details on the implementation of the simulation we refer the reader to the paper by *Dröge et al.* [2010].

6. Modeling

We attempt to reconstruct the transport of energetic electrons during the 7 February 2010 event from the acceleration site, assumed to be a flaring region in the solar chromosphere at $\sim$ N21 E10, to STEREO-A/B and ACE by considering two possible scenarios. In the Scenario I we assume that the electrons first undergo lateral transport away from the flare site in complex magnetic fields in the solar corona, a process which has been referred to as coronal propagation or coronal diffusion [*Reid*, 1964]. Once the electrons reach an open magnetic field line they start to propagate in the

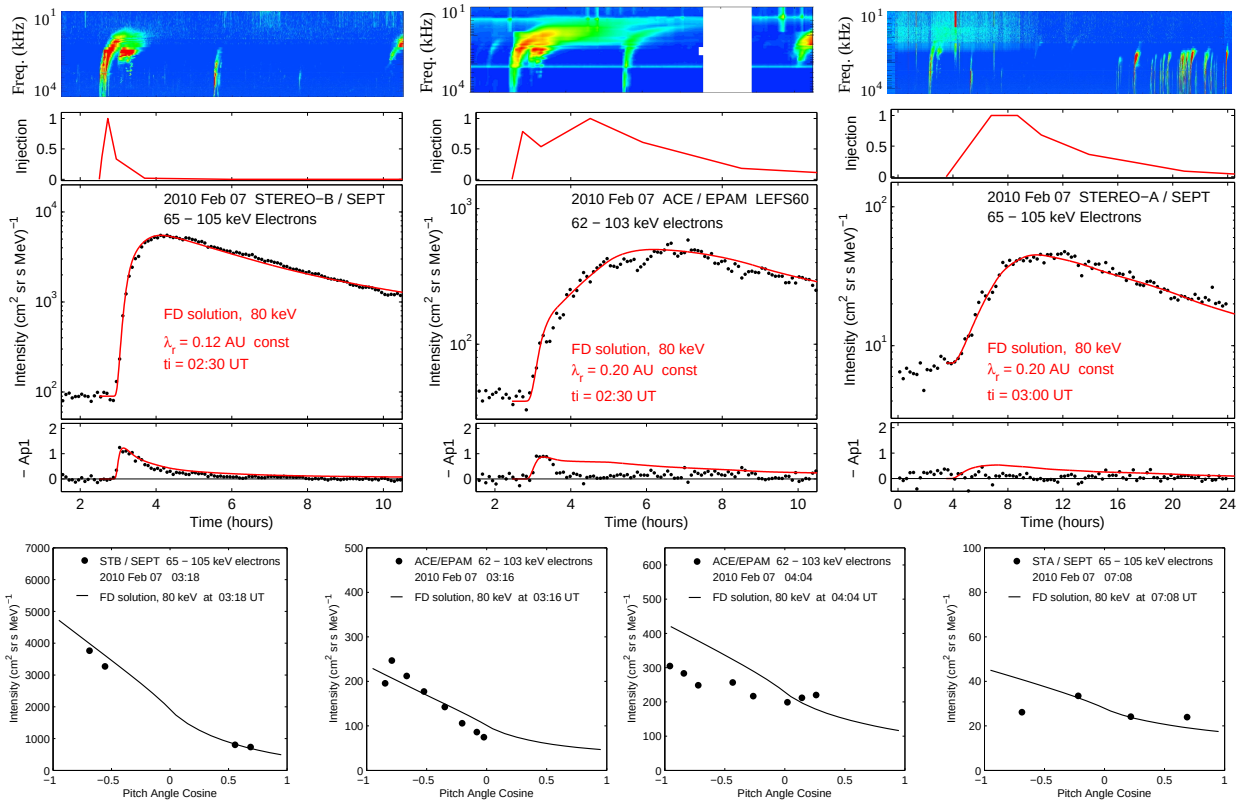

Figure 9. a) - c), upper row left to right: results of one-dimensional (Scenario I) transport modeling of *STEREO-A/B* and *ACE* electron observations on 7 February 2010. Panels from top to bottom: type-III radio bursts which are a proxy for the onset of the electron injection, injection profiles derived from the modeling (normalized to unity), intensity and anisotropy profiles. Lower row: d) comparison of observed and predicted pitch-angle distribution at the time of the event onset for *STEREO-B*, e) same as before for *ACE*, f) pitch angle distributions on ACE at the time after the flattening of the intensity rise, g) pitch angle distributions at the time of the event onset for *STEREO-A*.

solar wind. In this scenario we assume that transport along the interplanetary magnetic field is the dominating process, and neglect other processes. In Scenario II we study the fully three-dimensional transport of the electrons which includes also the effects of corotation and transport perpendicular to the interplanetary magnetic field. As the speed of the electrons considered here is large compared to the solar wind speed, convection and energy losses are neglected in both scenarios. Because our numerical model to solve the full equation (3) currently can handle only a symmetric Parker field with a constant solar wind speed throughout the Heliosphere, we set V_{SW} to 413 km/s which corresponds to a solar wind speed averaged over the three spacecraft from 7 February throughout 10 February (see Figure 3).

6.1. Scenario I: One-dimensional Transport

The propagation of the electrons in Scenario I can then basically be considered as one-dimensional spatial transport along a given magnetic field line (or in a magnetic flux tube), characterized by the arc length s, and the quantitative treatment of the evolution of the particle's reduced phase space density $f(s, \mu, t)$ is described completely by equation (3a), which we here solve with a finite-differences schemes [e.g., *Ng and Wong*, 1979; *Ruffolo*, 1991; *Dröge*, 2003]. An inner reflecting boundary at r=0.05 AU and an outer absorbing boundary at r=3 AU is assumed. For simplicity, equation (3a) is solved for monoenergetic electrons at 80 keV which approximately corresponds to the center of the electron energy interval considered here. The injection function $Q(s, \mu, t)$ absorbs processes which the particles undergo during their propagation in complex coronal magnetic fields to the connecting interplanetary field line. For the pitch angle diffusion coefficient we make a product ansatz of the form

$$D_{\mu\mu}(s, E, \mu) \;=\; \kappa_0(s, E) \cdot \left\{ |\mu|^{q-1} + H \right\} \; (1 - \mu^2) \qquad (9)$$

which partially resembles the result of standard quasi-linear theory [QLT, cf., *Jokipii*, 1966] and additionally introduces a parameter H which can phenomenologically describe an enhancement of scattering through $\mu = 0$ by non-resonant and non-linear effects. The parameter q denotes the spectral index of the magnetic fluctuations along the field, which is here assumed to be a single power law in wave number. Typical values are $q = 1.67$ for a Kolmogorov spectrum, and a variation of H between 0.05 and 0.5, corresponding to weaker to stronger scattering through $\mu = 0$ due to the above mentioned effects. In the work presented here we have assumed $q = 1.67$ and $H = 0.5$. Information about the spatial variation of the scattering and of its dependence on the particle energy E (which we use from now on instead of the momentum for a more direct relation to the energy ranges of the electron observations) is absorbed in the coefficient $\kappa_0(E, s)$.

Solutions of the above transport equation have been widely used to model in-situ observations of SEP events with the goal of deriving the injection function and the interplanetary transport parameters. To achieve this it is important to not only model the isotropic part of the distribution function but also make use of the information contained in its

angular dependence, or the first-order anisotropy parallel to the magnetic field (equation 1). Different fitting/modeling techniques have been used to extract information from the particle data about the transport process, including the traditional method of "fitting by eye" [e.g., *Dröge*, 2003; *Dröge and Kartavykh*, 2009], with an emphasis on the early phase of the event, an automated piecewise linear fitting method which minimizes a χ^2 value [*Ruffolo*, 1998], or by procedures that use an estimator of the goodness of the fit [e.g., *Agueda et al.*, 2008]. Comparison between the various methods have shown that they give similar results in most cases. Here we adopt the "by eye"-method and will refer to it, because it is not based on a rigorous mathematical treatment, as "modeling" rather than "fitting".

Figure 9a shows the result of a modeling of the 65 - 105 keV electron fluxes observed on STEREO-B. The modeling of the intensity and anisotropy (equation. 3) together is crucial for deriving the injection profile of the particles. Otherwise, effects of prolonged injection could not be separated from diffusive delays in the interplanetary medium. The time dependence of the injection on the modeling of the observed intensity- and anisotropy-time profiles was performed utilizing a convolution of the impulsive solution I_0 with a time dependent source function $Q(s, E, \mu, \tau)$:

$$I(s, E, \mu, t) \; = \; \int_0^t d\tau \; I_0(s, E, \mu, t-\tau) \; Q(s, E, \mu, \tau) \quad (10)$$

The best overall agreement with the observed intensity and anisotropy-time profiles was obtained for a piecewise linear injection function as shown in the second panel of Figure 9a, and a spatially constant radial mean free path $\lambda_r = 0.12$ AU which can be related to the parallel mean free path according to $\lambda_r = \lambda_\parallel \cos^2\psi$, where $\psi(r)$ is the angle between the radial direction and the magnetic field. At 1 AU this would here correspond to a value of $\lambda_\parallel = 0.24$ AU. The time profile of the derived injection function resembles well that of a type III radio burst observed on STEREO-B (upper panel of Figure 9a), which indicates the emission of an electron beam close to the Sun. Observed and predicted pitch-angle distribution at the time of the event onset (Figure 9d) are in good agreement. It appears that the assumptions underlying Scenario I can give a good reproduction of the STEREO-B observations. A modeling of the 62 - 103 keV electron intensity and anisotropy on ACE is shown in Figure 9b. The observed intensity profile is characterized by a fast rise during the first 40 minutes of the event which is accompanied by a significant anisotropy. This phase of the event is consistent with a modeling assuming a spatially constant radial mean free path $\lambda_r = 0.2$ AU, and a triangular injection profile with a width of $\sim$ 30 minutes at half intensity which is matched with a type III radio burst observed by Wind/Waves. Observed and predicted pitch-angle distributions (Figure 9e) at the time of the maximum intensity also agree resonably well. The flatter increase in the electron intensity after $\sim$ 03:30 UT towards a maximum around 06:00 UT would require a second, long-lasting injection period in the one-dimensional transport model. This in turn would lead to a long-lasting anisotropy which is not observed, and predicted pitch-angle distributions which do not agree with the observed ones (cf., Figure 9f).

An alternative explanation could be that the majority of the electrons observed on ACE after 04:00 UT would not origin from an injection close to the solar corona. Instead, these electrons would rather access the connecting field line at some distance from the Sun where adiabatic focusing is already rather weak and resulting pitch-angle distributions then cannot be strongly anisotropic. The absence of long-lasting type III radio bursts at high frequencies after 03:30 UT would also support the hypothesis that no electrons were injected close to the Sun during this period. Observations of 65 - 105 keV electron fluxes observed on STEREO-A and results of a transport modeling are shown in Figure 9c. With an injection profile as indicated in the figure and the same mean free path as for ACE a good modeling of the observed intensity profile is possible. However, the long-lasting small but finite anisotropy predicted by the modeling is not matched by the observations, which show no significant anisotropy throughout the event (see also the pitch-angle distribution in Figure 9g). We also note that during the rising phase of the event no corresponding type III radio emission was observed on STEREO-A.

6.2. Scenario II: Three-dimensional Transport

Following the arguments presented above, we conclude that only a small fraction of the electrons observed on STEREO-A were injected on the connecting field line close to the Sun, and that the majority of the electrons must have accessed the connecting field line at some distance from the Sun. This indicates that for a realistic modeling of the electron fluxes observed on the three spacecraft a three-dimensional interplanetary propagation model would be required which combines the effects of focused transport along the interplanetary magnetic field, spatial diffusion of the electrons perpendicular to the field, and an injection from the solar corona into the interplanetary medium which does not origin from a point source but is rather distributed in latitude and longitude with respect to the acceleration site. *Dröge et al.* [2010] argued that the assumption of a radially constant $\lambda_\perp/\lambda_\parallel$ in the inner Heliosphere, even if it is very small, would result in a spatial distribution of particles at 1 AU that is much wider than typically observed for impulsive solar ion events, due to efficient perpendicular diffusion close (on scales << 1 AU) to the Sun. As a possibly more realistic assumption for the variation of the perpendicular diffusion in the inner Heliosphere they suggested that the perpendicular mean free path scales with the gyroradius of the particle, i.e., with the magnetic field strength and with the particle's pitch angle:

$$\Lambda_\perp(r, \psi, \mu) = \alpha \cdot \lambda_\parallel(r) \cdot (r/1\mathrm{AU})^2 \cdot \cos\psi(\mathrm{r}) \cdot \sqrt{1-\mu^2} \quad (11)$$

where α is a parameter to model the relative contributions of parallel and perpendicular diffusion. The strong adiabatic focusing at small radial distances, keeping μ close to 0, would then efficiently inhibit lateral transport close to the Sun. To compare the above μ-dependent perpendicular mean free path with those formulated for diffusion-convection models, and to obtain the resulting ratio of $\lambda_\perp$ to $\lambda_\parallel$ at 1 AU, we would have to calculate $\psi(r)$ for a given solar wind speed in a Parker magnetic field and average equation (11) over μ for an appropriate pitch angle distribution. A different effect of the particle's pitch angle on $\lambda_\perp$ might be expected if the diffusion perpendicular to the average field would be mainly due to magnetic field line wandering. At this stage we do not attempt to distinguish between the various possibilities for perpendicular diffusion and restrict ourselves to equation (11) for the modeling.

Contrary to STEREO-A observations, the significant anisotropies on STEREO-B and ACE during the onsets of the electron events indicate that a part of the electrons detected on these spacecraft had direct access to the connecting field lines, rather than reaching them predominantly by perpendicular diffusion. We therefore hypothesize that lateral transport in the solar corona as well as in the interplanetary medium had a non-negligible influence on the appearance of the electron events at the locations of each of the three spacecraft, whereby the former effect was dominating

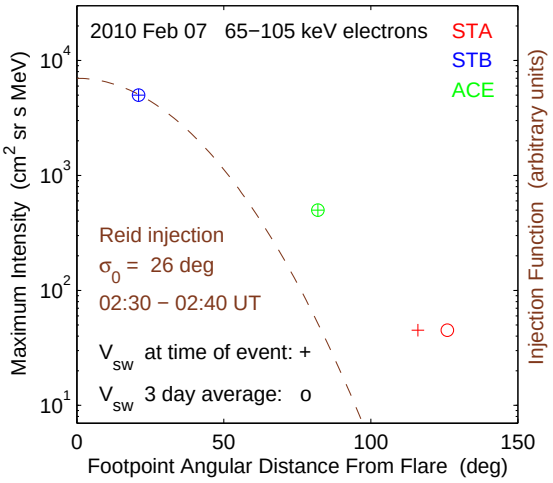

Figure 10. Angular dependence of electron injection from the solar source surface into the interplanetary medium assumed for the modeling (dashed brown line) and of maximum intensities observed on the three spacecraft for a solar wind speed observed at the onset times (crosses) and averaged over three days (circles).

on STEREO-B, and the latter on STEREO-A. For the angular propagation of the electrons close to the Sun we employ the *Reid* [1964] model which provides an approximate solution of the problem of particles diffusing on a sphere, and undergoing escape from the sphere, without making any specific assumptions about the nature of these processes. As a further simplification we consider an electron injection with a constant rate from 02:30 to 02:40 UT, according to a power law energy spectrum over the range from 62 to 105 keV, and arrive at an injection function

$$Q(r{=}\,0.05\mathrm{AU},\sigma,\mathrm{E}) = \mathrm{Q}_0\ \mathrm{E}^{-3}\ \exp\left\{-\frac{\sigma^2}{2\sigma_0^2}\right\} \qquad (12)$$

where σ is the total angular distance from the acceleration site (assumed to be the location of the flare at N21 E10), and σ_0 characterizes the spread of the electrons on the injection surface close to the Sun. Assuming an isotropic injection at an inner reflecting boundary located at r = 0.02 AU, and an escape boundary at r = 4.5 AU simulations for various combinations of the modeling parameters $\lambda_\parallel$, α, and σ_0 were performed. We assumed that the above parameters would not vary in energy over the range stated above.

We find that for an injection with $\sigma_0 = 26°$, $\lambda_\parallel = 0.08/\cos^2\psi(\mathrm{r})$ AU (equivalent to a radially constant $\lambda_r = 0.08$ AU) and α=0.13 a good overall agreement with the electron observations made on the three spacecraft can be reached. At a distance of 1 AU the parallel and perpendicular mean free paths, and their ratio ϵ adopt values of $\lambda_\parallel^0 = 0.16$ AU, $\lambda_\perp^0 = 0.011$ AU, and $\epsilon = 0.07$, respectively, which we will use in the following for comparisons with results from other observational studies and theoretical predictions. The injection is shown in Figure 10 as a function of angular distance from the flare, in comparison with the maximum electron intensities observed at the three spacecraft. Figure 11 shows a comparison of the electron observations with with the results of the modeling. The simulated intensity and anisotropy profiles were determined by counting quasi-particles in a box which is centered at the location of the respective spaceraft, and which extends 0.01 AU away from the location of the spaceraft along the axes of the

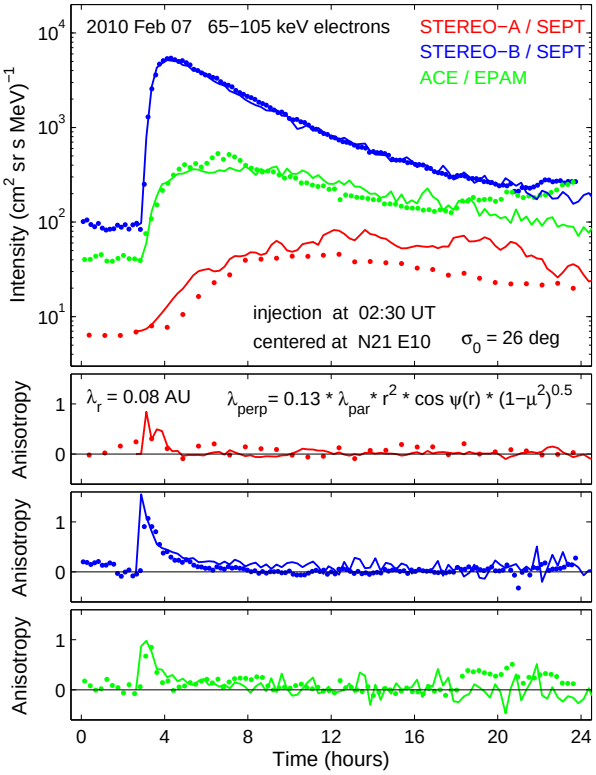

Figure 11. Results of the three-dimensional modeling for electron intensity and anisotropy profiles at the locations of *STEREO-A/B* and *ACE* (solid lines) in comparison with electron observations (dotted lines). For details see text.

HEEQ system. The observations on STEREO-B and ACE are well reproduced by the modeling. Our simulation also correctly predicts the low anisotropy observed on STEREO-A. We note that the predicted intensity for STEREO-A rises too early, and its maximum value is a factor of ~ 2 too high compared to the observed one. This deviation might be attributed to the fact that the inherent uncertainty in the estimation of the footpoint positions, and the simplifying assumptions for the solar wind velocity field and the resulting heliospheric magnetic field geometry would have the largest effect for STEREO-A. The predicted spatial distribution of the electrons in the solar equatorial plane four hours after the injection is shown in Figure 12, with a resolution of 0.05 AU. For the presentation of the simulation results we have assumed a spatially constant background electron flux with a peak intensity of 0.1% of that of the maximum intensity observed on STEREO-B, indicated by the gray color. For a direct comparison with the observed spatial distribution we have to take into account that the event on 7 February was preceeded by two smaller electron events on 5 and 6 February, respectively. The background electron fluxes in the inner Heliosphere were thus not homogeneous, as is also evident from the upper panel of Figure 11. It can be seen from Figure 12 that transport along the magnetic field lines is the fastest process, but also that four hours after the $\sim$ 02:30 flare at N21 E10 electrons had already spread around the Sun by an amount of almost 180° at a distance of 1 AU. With the spatial resolution used for the figure, the effects of corotation are not visible at this time, although they were considered in the simulation.

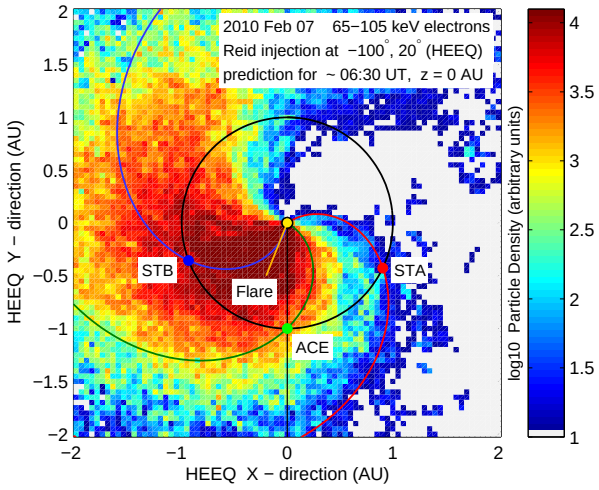

Figure 12. Results of the three-dimensional modeling for the spatial distribution of energetic electrons in the solar equatorial plane following the flare on 7 February 2010. For details see text.

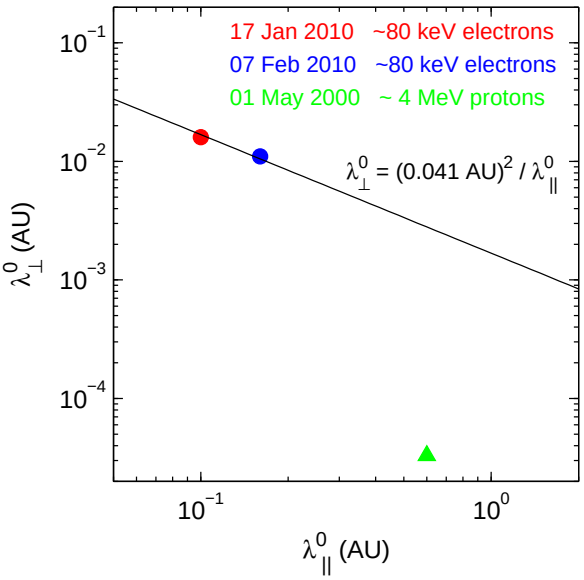

Figure 13. Perpendicular mean free path $\lambda_\perp^0$ vs. parallel mean free path $\lambda_\parallel^0$ for three solar particle events which we have modeled with our three-dimensional anisotropic transport code. The solid line indicates a possible correlation between the two transport parameters for the electron events suggested by hard-sphere type scattering models.

7. Discussion and Summary

A comparison of the outcomes obtained from the two scenarios discussed above shows that the three-dimensional transport modeling of Scenario II predicts a noticeably smaller value of $\lambda_\parallel$ as the one-dimensional modelings of Scenario I. A possible explanation for this result could be the fact that significant perpendicular diffusion of the electrons from densely populated magnetic field lines with a close connection to the acceleration site to less densely populated field lines originating at a larger distance to the flare leads to a faster drop of the intensity after the maximum, compared to the situation when the electrons remain in the magnetic flux tube into which they have been injected. To make up for the faster intensity decline, a smaller mean free path would have to be assumed in the modeling. The expected slower intensity rise due to a smaller value of $\lambda_\parallel$ is balanced by the shorter injection time assumed in the three-dimensional modeling (02:30 to 02:40 UT). Although we are not able to make any quantitative statements here about a possible correlation of the type III radio burst observed on the three spacecraft with the injection profiles of the electrons (see upper two rows of panels in Figure 9) it appears that there is a better overall agreement with the predictions of Scenario II.

The estimate for the parallel mean free path obtained from our modeling ($\lambda_\parallel^0 = 0.16$ AU) is not unusually low, although it seems that more frequently solar electrons with energies of ~ 80 keV exhibit a beam-like behaviour [*Haggerty and Roelof*, 2002] in events which are not associated with major CMEs and interplanetary shocks, resulting in values for $\lambda_\parallel$ of the order of 1 AU [e.g., *Dröge*, 2005]. The basic processes determining the transport parallel to the magnetic field (advection, focusing and pitch-angle diffusion) are well defined and can be quantitatively related to magnetic field fluctuations observed during particle events. For strong pitch-angle scattering Gaussian spatial diffusion parallel to the magnetic field is obtained for the various turbulence geometries currently under discussion. We are therefore confident that our modeling describes the parallel transport of the electrons in the 7 February 2010 event reasonable well, despite some simplifications we had to make with respect to the lateral variation of solar wind and transport parameters. Finding a similarly comprehensive approach for the random component of particle transport perpendicular to the average magnetic field seems to have so far proved elusive. This cross-field diffusion is assumed to be composed of two physical processes: one due to the departure of the particle's guiding center from an individual field line caused by pitch-angle scattering or stochastic gradient/curvature drift ('microscopic' diffusion), and the other from the particles following field lines that meander due to large-scale turbulence [e.g., *Fraschetti and Jokipii*, 2011]. Considerable effort has been spent in recent years to perform analytical calculations and numerical simulations to determine $\lambda_\perp$ for a variety of turbulence geometries, dynamical properties of the fluctuations, and non-linear and non-Markovian aspects of perpendicular diffusion. It still appears to be more intricate than in the case of parallel transport to relate the predictions of the above models to observations of lateral transport and magnetic fluctuations during solar particle events, and to differentiate between the effects of mircoscopic perpendicular diffusion and field line random walk.

One might conjecture that for the case of vanishing turbulence $\lambda_\parallel \to \infty$ and $\lambda_\perp \to 0$, as there would be no pitch-angle scattering and also no perpendicular diffusion, neither on a 'microscopic' level nor due to field line random walk. For an increasing turbulence level, $\lambda_\parallel$ would then decrease and $\lambda_\perp$ would increase, leading to an anticorrelation between the two transport parameters. As mentioned above, in other applications of particle transport such as the modeling of the propagation of galactic and anomalous cosmic rays, and of Jovian electrons in the Heliosphere, the perpendicular mean free path is often taken to be a fixed fraction of the parallel mean free path, i.e., $\lambda_\perp = \epsilon \cdot \lambda_\parallel$, where ϵ is a constant typically taken to be in the range 0.005 - 0.05. Also, there seems to be a general trend that values of $\lambda_\perp$ predicted from advanced transport models increase monotonically with $\lambda_\parallel$ [e.g., *Bieber et al.*, 2004; *Shalchi*, 2013, and references therein]. To search for clues about a possible relation between the two parameters we have plotted in Figure 13 $\lambda_\perp$ vs. $\lambda_\parallel$ for the three solar particle events

for which we have so far determined them with our three-dimensional anisotropic transport model, and unlike as in earlier studies, rather *independently* of each other. Besides the event considered here this comprises electron observations in the same energy range made by STEREO-A/B and ACE during the wide spread particle event of 17 January 2010 [*Dresing et al.*, 2012], and $\sim$ 4 MeV proton observations during the event of 1 May 2000 [*Dröge et al.*, 2010]. Parallel and perpendicular mean free paths in the former event were determined in a similar way as in this study, although due to the small observed anisotropies with a lesser accuracy. In the 1 May 2000 event $\lambda_\perp$ was estimated from a sharp spatial gradient convected past a single spacecraft. A positive correlation, being aware of the small number of the events and the different methodologies used, does not seem to be indicated by Figure 13. A formula in diffusion theory which would formally allow an anticorrelation between $\lambda_\perp$ and $\lambda_\parallel$ is that of classical (hard-sphere) scattering theory [e.g., *Gleeson*, 1969]:

$$\lambda_\perp = \frac{\lambda_\parallel}{1 + (\lambda_\parallel / l_c)^2} \tag{13}$$

where the scale length l_c would correspond to the particle's gyroradius r_g. For the limit $l_c \ll \lambda_\parallel$ equation (13) becomes $\lambda_\perp \approx l_c^2/\lambda_\parallel$. It is obvious that for the gyroradii of the electrons considered here ($\sim$ 200 km for a magnetic field of 5 nT) the resulting value of the perpendicular mean free path would be much smaller than the observed values. However, if we take l_c as a free parameter we can model the data points in Figure 13 with a value of $l_c = 0.041$ AU, which is of the order of observed correlation length scales of solar wind turbulence at 1 AU [e.g., *Wicks*, 2010]. Note that a possible anticorrelation between the two mean free paths would not be in contradiction to the parametrization used in equation (11) where we merely scaled $\lambda_\perp$ in fractions of $\lambda_\parallel$. Some support for the above assumptions is provided by the quasilinear theory of field line random walk [e.g., *Matthaeus et al.*, 1999] which predicts a perpendicular mean free path $\lambda_\perp \propto \left\langle \Delta x^2 \right\rangle / \Delta z = (\delta B_x^2 / B_0^2) l_x$, where x and z are the directions perpendicular and parallel, respectively, to the average magnetic field B_0, δB_x^2 is the turbulent power in the fluctuations perpendicular to B_0, and l_x is the correlation length of B_x in the z-direction along B_0. It might not be unreasonable to assume that for other processes leading to particle diffusion perpendicular to the average magnetic, i.e., diffusion of the gyrocenter away from the field line, a similar expression holds. Similarly, particle diffusion along the average magnetic field due to pitch-angle scattering should scale inversely with the turbulent power, $\lambda_\parallel \sim (B_0^2/\delta B_x^2) \cdot l_\parallel$. Upon eliminating $\delta B_x^2 / B_0^2$ we arrive at

$$\lambda_\perp \;\sim\; \frac{l_x \; l_\parallel}{\lambda_\parallel} \tag{14}$$

which resembles the asymptotic form of equation (13). Here l_x and $l_\parallel$ denote the correlation length scales of the magnetic field fluctuations characteristic for transport parallel and perpendicular to the field, respectively, which one might try to relate to, e.g., the slab or 2D components of the solar wind turbulence. The normalized turbulent power $\delta B_x^2 / B_0^2$ also constitutes the curve parameter - the quantity which would vary in this picture from one electron event to another - in Figure 13, ranging from low values in the lower right to high values in the upper left corner. As possible effects due to an energy/rigidity dependence of the particle transport parallel and perpendicular to B_0, and due to the shapes of the power spectral densities are absorbed in the scaling parameters δB and l, the true connection between $\lambda_\perp$ and $\lambda_\parallel$ will likely be more complicated, but the general tendency for an anticorrelation might well persist. We have identified $\sim$ 10 electron events during the period 2010 to 2012 which were observed simultaneously on Wind/ACE and one or both of the two STEREO spacecraft, and for which the propagation conditions were not heavily affected by interplanetary disturbances. There seems to be a tendency in that sample that beam-like events, characterized by a large anisotropy, are not as widely distributed in longitude as the more diffusive events. We expect that a modeling of these events, in a similar way as presented here for the 7 February 2000 event, will contribute to resolve the question whether a systematic relationship between $\lambda_\perp$ and $\lambda_\parallel$ in solar electron events exists. It appears that the data point in Figure 13 for the 4 MeV protons in the 1 May 2000 event does not fit into the scheme outlined above, due to its very small perpendicular mean free path. An explanation for this finding could be that in that event $\lambda_\perp$ was not determined by comparing intensity gradients between longitudinally distributed spacecraft - which would hardly allow to measure values of $\lambda_\perp$ below 10^{-4} AU - but by the convection of a step-like intensity decrease ('cutoff') marking a separation between field lines which are connected to the particle source and those which are not past a single spacecraft [*Dröge et al.*, 2010]. Similarly small values of $\lambda_\perp$ were also found in the 'dropout' events [*Mazur et al.*, 2000], intermittent abrupt depletions in the fluxes of low energy ions which exhibit no velocity dispersion. The dropout phenomenon is likely the result of magnetic flux tubes not connected to the particle source at the Sun having mingled with the flux tubes filled by solar particles. However, the edges of the dropouts show some structure and it was suggested by *Chollet and Giacalone* [2011] that this could be related to particles scattering off field lines. We find it quite possible that the phenomenologically derived value of $\lambda_\perp$ in the 1 May 2000 event also corresponds to cross-field diffusion rather than to magnetic field line diffusion. Both dropout and cutoff events seem to have in common that their observation would require a relatively large parallel mean free path and a relatively small amount of field line mixing. In contrast, particle propagation in wide-spread electron events would be determined by comparatively small parallel mean free paths and strong field line diffusion. Future studies of particle propagation in multi-spacecraft events, which we also plan to extend to ion observations in events which are not severely affected by disturbances in the solar wind, can be expected to provide more information about the relative importance of the various mechanisms leading to lateral transport of solar particles, and possible relations between the transport parallel and perpendicular to the interplanetary magnetic field.

Acknowledgments. We acknowledge the STEREO PLASTIC, IMPACT, SECCHI, EIT and Wind and ACE teams for providing the data used in this paper. The STEREO/SEPT and SOHO/EPHIN projects are supported under Grant 50 OC 0902 by the German Bundesministerium für Wirtschaft through the Deutsches Zentrum für Luft- und Raumfahrt (DLR). The research leading to these results has received funding from the European Unions Seventh Framework Programme (FP7/2007-2013) under grant agreement No 262773 (SEPServer). This work utilizes data obtained by the Global Oscillation Network Group (GONG) Program, managed by the National Solar Observatory, which is operated by AURA, Inc. under a cooperative agreement with the National Science Foundation. The data were acquired by instruments operated by the Big Bear Solar Observatory, High Altitude Observatory, Learmonth Solar Observatory, Udaipur Solar Observatory, Instituto de Astrofsica de Canarias, and Cerro Tololo Interamerican Observatory. The authors benefited from discussions with R. Vainio.

References

Agueda, N., R. Vainio, D. Lario, and B. Sanahuja (2008), Injection and interplanetary transport of near-relativistic electrons: modeling the impulsive event on 2000 May 1, *Astrophys. J., 675*, 1601–1613.

Bieber, J. W., W. H. Matthaeus, A. Shalchi, and G. Qin (2004), *Geophys. Res. Let. 31*, L10805.

Conlon, T. F. (1978), The interplanetary modulation and transport of Jovian electrons, *J. Geophys. Res. 83*, 541–552.

Chollet, E. E., and J. Giacalone (2011), Evidence of confinement of solar-energetic particles to interplanetary magnetic field lines, *Astrophys. J., 728*, 64–67.

Dalla, S., et al. (2003), Properties of high heliolatitude solar energetic particle events and constraints on models of acceleration and propagation, *Geophys. Res. Lett.,30*(19), 8035, doi:10.1029/2003GL017139.

Dresing, N., R. Gómez-Herrero, A. Klassen, B. Heber, Y. Y. Kartavykh, and W. Dröge (2012), The Large Longitudinal Spread of Solar Energetic Particles During the 17 January 2010 Solar Event, *Solar Phys., 281*, 281–300.

Dröge, W. (2003), Solar particle transport in a dynamical quasi-linear theory, *Astrophys. J., 589*, 1027–1039.

Dröge, W. (2005), Probing heliospheric diffusion coefficients with solar energetic particles, *Adv. Space. Res., 35*, 4, 532–542.

Dröge, W., and Y. Y. Kartavykh (2009), Testing Transport Theories with Solar Energetic Particles, *Astrophys. J., 693*, 69–74.

Dröge, W., Y. Y. Kartavykh, B. Klecker, and G.A. Kovaltsov, (2010), Anisotropic three-dimensional focused transport of solar energetic particles in the inner heliosphere, *Astrophys. J., 709*, 912–919.

Dwyer J. R., G. M. Mason, J. E. Mazur, J. R. Jokipii, T. T. von Rosenvinge, and R. P. Lepping, (1997), Perpendicular Transport of Low-Energy Corotating Interaction Region–associated Nuclei, *Astrophys. J., 490*, L115

Fraschetti, F., and J. R. Jokipii, (2011), Time-dependent Perpendicular Transport of Fast Charged Particles in a Turbulent Magnetic Field, *Astrophys. J., 734(2)*, article id: 83, 8, doi:10.1088/0004-637X/734/2/83

Gardiner, C.W. (1983), Handbook of Stochastic Methods (Berlin: Springer).

Gleeson, L. (1969), The equations describing the cosmic-ray gas in the interplanetary region, *Planet. Space Sci., 17*, 31–47.

Gold, R. E., S. M. Krimigis, S. E. Hawkings III, D. K. Huggerty, D. A. Lohr, E. Fiore, T. P. Armstrong, G. Holland, and L. J. Lanzerotti (1998), Electron, Proton, and Alpha Monitor on the Advanced Composition Explorer spacecraft, *Space Sci. Rev., 86*, 541–562.

Haggerty, D. K., and E. C. Roelof (2002), Impulsive near-relativistic solar electron events: delayed injection with respect to solar electromagnetic emission, *Astrophys. J., , 579*, 841–853.

Hasselmann, K., and G. Wibberenz (1968], Scattering of charged particles by random electromagnetic fields, *Zeitschrift für Geophys., 34*, 353–388.

Ho, G. C., E. C. Roelof, G. M. Mason, D. Lario, and J. E. Mazur (2003), Onset study of impulsive solar energetic particle events, *Adv. Space. Res., 32*, 12, 2679–2684.

Jokipii, J. R., (1966), Cosmic-Ray Propagation. I. Charged particles in a random magnetic field, *Astrophys. J., 146*, 480–487.

Jokipii, J. R., and E. N. Parker (1969), Stochastic aspects of magnetic lines of force with application to cosmic-ray propagation, *Astrophys. J., 155*, 777–498.

Kartavykh, Y. Y., W. Dröge, W., B. Klecker, G. M. Mason, E. Möbius, E., M. Popecki, and S. Krucker (2007), Evidence of a Two-Temperature Source Region in the ^{3}He-Rich Solar Energetic Particle Event of 2000 May 1, *Astrophys. J., 671*, 947–954.

Kocharov, L., R. Vainio, G. A. Kovaltsov, and J. Torsti (1998), Adiabatic deceleration of solar energetic particles as deduced from Monte Carlo simulations of interplanetary transport, *Solar Phys., 182*, 195–215.

Kunstmann, J. E. (1979), A new transport mode for energetic charged particles in magnetic fluctuations superposed on a diverging mean field, *Astrophys. J., 229*, 812–820.

Lario, D., M.-B. Kallenrode, R. B. Decker, E. C. Roelof, S. M. Krimigis, A. Aran, and B. Sanahuja (2006), Radial and longitudinal dependence of solar 4-13MeV and 27-37MeV proton peak intensities and fluences: Helios and IMP 8 observations, *Astrophys. J., 653*, 15311544.

Lin, R. P., K. A. Anderson, S. Ashford, C. Carlson, D. Curtis, R. Ergun, D. Larson, J. McFadden, M. McCarthy, G. K. Parks et al. (1995), A three-dimensional plasma and energetic particle investigation for the Wind spacecraft, *Space Sci. Rev., 71*, 125–153.

Luhmann, J. G., et al. (2008), STEREO IMPACT Investigation Goals, Measurements, and Data Products Overview, *Space Sci. Rev., 136*, 117–184.

Marsh, M. S., S. Dalla, J. Kelly, and T. Laitinen, (2013), Drift-induced Perpendicular Transport of Solar Energetic Particles, *Astrophys. J., 774(1)*, article id: 4, 9, doi:10.1088/0004-637X/774/1/4.

Matthaeus, W. H., C. W. Smith, and J. W. Bieber, (1999), Correlation lengths, the Ultrascale, and the spatial structure of interplanetary turbulence, in Ninth Int. Solar Wind Conf., AIP Conference Proceedings, 471, 511–514.

Matthaeus, W. H., G. Qin, J. W. Bieber, G. P. Zank, (2003), Nonlinear collisionless perpendicular diffusion of charged particles, *Astrophys. J., 590*, L53–L56.

Mazur, J. E., G. M. Mason, J. R. Dwyer, J. Giacalone, J. R. Jokipii, and E. C. Stone, (2000), Interplanetary magnetic field line mixing deduced from impulsive solar flare particle, *Astrophys. J., 532*, L79–L82.

Müller-Mellin, R., et al. (2008), The Solar Electron and Proton Telescope for the STEREO Mission, *Space Sci. Rev., 136*, 363–389.

Ng, C. K., and L. J. Gleeson, 1971, The propagation of Cosmic-Ray Bursts *Solar Phys., 20*, 166–185.

Ng, C. K., and K. Y. Wong, 1979, Solar particle propagation under the influence of pitch-angle diffusion and collimation in the interplanetary magnetic field, *Proc. 16th Internat. Cosmic Ray Conf. (Kyoto), 5*, 252–255.

Nolte, J. T., and E. C. Roelof, (1973), Large-Scale Structure of the Interplanetary Medium, I: High Coronal Source Longitude of the Quiet-Time Solar Wind, *Solar Phys., 33*, 241–257.

Parker, E. N. (1963), Parker, E. N. 1963, Interplanetary Dynamical Processes (New York: Wiley).

Parker, E. N. (1965), The passage of energetic charged particles through interplanetary space, *Planet. Space Sci., 13*, 9–49.

Qin, G., M. Zhang, and J. Dwyer (2006), Effect of adiabatic cooling on the fitted parallel mean free path of solar energetic particles, *J. Geophys. Res., 111*, ID A08101.

Reames, D. V. (1999), Particle acceleration at the Sun and in the heliosphere, *Space Sci. Rev., 90*, 413–491.

Reid, G. C. (1964), A Diffusive Model for the Initial Phase of a Solar Proton Event, *J. Geophys. Res. 69*, 2659–2667.

Roelof, E. C. (1969), Propagation of solar cosmic rays in the interplanetary magnetic field, *in Lectures in High Energy Astrophysics, ed. H. Ögelmann, and J. R. Wayland (NASA SP-199)*, 111–136.

Ruffolo, D. (1991), Interplanetary transport of decay protons from solar flare neutrons, *Astrophys. J., 382*, 688–698.

Ruffolo, D. (1995), Effect of adiabatic deceleration on the focused transport of solar cosmic rays, *Astrophys. J., 442*, 861–874.

Ruffolo, D. (1998), T. Khumlumlert, and W. Youngdee (1998), Deconvolution of interplanetary transport of solar energetic particles, *J. Geophys. Res., 103*, A9, 20591–20602.

Schlickeiser, R. (2002), *Cosmic Ray Astrophysics*, Springer, Berlin, 519 p.

Shalchi, A. (2013), Simple Analytical Forms of the Perpendicular Diffusion Coefficient for Two-component Turbulence. I. Magnetostatic Turbulence, *Astrophys. J., 774(1)*, article id: 7, 6, doi:10.1088/0004-637X/774/1/7.

Wibberenz, G., and H. V. Cane (2006), Multi-Spacecraft Observations of Solar Flare Particles in the Inner Heliosphere, *Astrophys. J., 650*, 1199–1207.

Wicks, R. T., M. J. Owens, and T. S. Horbury, (2010), The Variation of Solar Wind Correlation Lengths Over Three Solar Cycles, *Solar Phys., 262*, 191–198.

Wiedenbeck, M. E., G. M. Mason, C. M. S. Cohen, N. V. Nitta, R. Gómez-Herrero, and D. K. Haggerty, (2013), Observations of Solar Energetic Particles from ^{3}He-rich Events over a Wide Range of Heliographic Longitude, *Astrophys. J., 765(1)*, article id: 54, 9, doi:10.1088/0004-637X/762/1/54.

Zhang, M., G. Qin, and H. Rassoul, (2009), Propagation of solar energetic particles in three-dimensional interplanetary magnetic fields, *Astrophys. J., 692*, 109-132.

DANKSAGUNG

Meinem Doktorvater Prof. Dr. Bernd Heber möchte ich hier an erster Stelle für die Aufgabenstellung dieser Arbeit und die enthusiastische Betreuung danken. Ich habe mich stets gefördert und gut beraten gefühlt und weiß das entgegengebrachte Vertrauen sehr zu schätzen.

Ein goßer Dank gebührt auch Dr. Andreas Klassen und Dr. Raúl Gómez-Herrero, die mich wie zwei 'Doktoronkel' betreut und unterstützt haben. Die weitreichende wissenschaftliche Zusammenarbeit und die vielen Diskussionen habe ich sehr genossen.

Den Kollegen in der Gruppe Extraterrestrik/Heliosphärische Astroteilchenphysik möchte ich für das gute Klima danken; ich habe mich hier immer sehr wohl gefühlt.
Für sehr wertvolle Korrekturen dieser Arbeit möchte ich neben den oben genannten folgenden Menschen herzlich danken: Dr. Anne Wellbrock, Dr. Jan Köhler, Dr. Christian Drews, Herrn Dipl. Phys. Jan Gieseler und Herrn Dipl. Phys. Thies Peleikis. Vielen Dank auch für eure mentale Unterstützung, von jedem auf seine Weise, und den vielen Spaß am Arbeitsplatz.

Zuletzt möchte ich meiner Familie für den Stolz und die Unterstützung danken und meinem lieben Partner Jan Gieseler; du bist großartig!

EIDESSTATTLICHE ERKLÄRUNG

Ich versichere an Eides Statt, dass ich die vorliegende Dissertation in Form und Inhalt eigentständig angefertigt habe. Abgesehen von der Beratung durch meine Betreuer und der angegebenen Literatur wurde die Arbeit ohne fremde Hilfe erstellt. Ich versichere, dass ich keine andere als die angegebene Literatur verwendet habe. Diese Versicherung bezieht sich auch auf alle in dieser Arbeit enthaltenen Grafiken und bildlichen Darstellungen.
Die Arbeit als Ganzes wurde bisher keiner anderen Prüfungsbehörde vorgelegt. Teile der Arbeit wurden bereits in Fachzeitschriften veröffentlicht und sind als solche gekennzeichnet. Die Quellennachweise der in den einzelnen Veröffentlichungen referenzierten Inhalte finden sich in der jeweiligen Veröffentlichung selbst und werden nicht zusätzlich im Quellennachweis dieser Arbeit aufgeführt. Für das Einbinden der Veröffentlichungen in diese Arbeit wurde die ausdrückliche Genehmigung der publizierenden Fachzeitschrift eingeholt.
Ich erkläre abschließend, dass die Arbeit unter Einhaltung der Regeln guter wissenschaftlicher Praxis der Deutschen Forschungsgemeinschaft entstanden ist.

Kiel, April 2014

Nina Dresing